CRANFIELD UNIVERSITY

NATALIA DI MATTEO

Optimal Design and Numerical Analysis of a Morphing Flap Structure

SCHOOL OF ENGINEERING
Department of Aerospace Engineering

PhD THESIS
Academic Year 2011-2012

Supervisor: Dr Shijun Guo
October 2012

This page is intentionally left blank.

CRANFIELD UNIVERSITY

SCHOOL OF ENGINEERING

Department of Aerospace Engineering

PhD THESIS

Academic Year 2011-2012

NATALIA DI MATTEO

Optimal Design and Numerical Analysis of a Morphing Flap Structure

Supervisor: Dr Shijun Guo

October 2012

This thesis is submitted for the award of Doctor of Philosophy

Abstract

Over the next few years the aviation industry will face the challenge to develop a new generation of air vehicles characterised by high aerodynamic efficiency and low environmental impact. The technologies currently available, however, are inadequate to meet the demanding performance requirements and to comply with the stringent regulations in terms of polluting emissions.

An innovative and very promising solution is offered by airframe morphing technologies. Morphing wing structures, internally actuated and able to change their shape smoothly to adapt to different loading conditions, would be able to achieve near-optimal lift and drag profiles throughout all the different phases of the flight. This would enhance the aircraft aerodynamic performance and contribute to a significant reduction of the fuel consumption, polluting emissions and noise.

The present study has been conducted as part of the European Commission founded Seventh Framework Program called "Smart High Lift Device for the Next Generation Wing" (SADE).

The aim of this research is the development of an effective design of a morphing flap with flexible trailing edge for a commercial aircraft wing. The investigation focused on morphing concepts which are suitable for large transport aircraft and which can be effectively developed and become operational within the next 20 years. For these reasons, the morphing was limited to the high lift devices of the wing, while the conventional wing box structure was retained.

The objectives of the current research are the design of a suitable internal actuation mechanism for a morphing flap device and its integration into a tailored flap structure, the analysis of the structural behaviour of the morphing device under the effect of static and dynamic loading to demonstrate the feasibility and the effectiveness of the proposed design and the optimisation of the morphing structure to meet the shape requirements.

In the first stage of this research, attention was focused on the design of an internal actuation mechanism to smoothly deflect the flexible rear part of the flap to achieve a specified target shape. An actuation system based on the principle of the eccentuation was designed. Significant changes were made to the conventional flap structure in order to integrate the actuation mechanism into the flap and to achieve the desired morphed configuration.

In the second stage of the research, attention was paid to the modelling of the proposed design in order to assess its structural behaviour. The morphing flap was analysed using the finite element method and a nonlinear static analysis was conducted to determine the flap deflection and to evaluate the stress and strain in the skin due to the morphing. The dynamic behaviour of the flap structure was also assessed and the natural frequencies and the response to transient input loads were evaluated to show that the proposed morphing structure can compete with the conventional configurations.

Lastly, the interaction between the flexible flap structure and the surrounding air flow was analysed and the proposed design concept was optimised to meet the morphing requirements.

This study demonstrates that a feasible design for a flap with morphing trailing edge for a large commercial aircraft can be achieved. The proposed actuation mechanism has the capability to effectively deflect the structure into the desired morphed shape and the structural modifications implemented were able to preserve the strength of the morphing structure. Moreover, the optimisation of the design parameters ensured that morphing was achieved with minimum weight penalty. The use of the morphing flap has the potential to improve aircraft efficiency and represents a significant contribution towards the development of the next generation of high performance and environmentally friendly air vehicles.

Acknowledgements

I clearly remember my first day in Cranfield. Sitting at my new desk, I was full of hopes and determined to make the most of my experience as a research student. Still, somehow, I felt slightly worried and unable to foresee what to expect from it, as if the thick fog which engulfed the nearby airfield was hiding not only the runway but also my future. Now that my PhD studies are approaching the end, I can say that that day was the beginning of an amazing experience. The years in Cranfield have been a pleasant and challenging journey. I would like to convey my appreciation to the many people I have met and who have contributed to my professional and personal growth.

First and foremost I would like to express my deepest gratitude for my supervisor Dr Shijun Guo, who has encouraged my efforts and inspired me to always push the boundaries of my studies. His patient guidance has helped me to overcome many doubts and many challenges encountered on my path. Without his continuous support and technical advice this research work and this thesis would have never been accomplished.

I acknowledge all the members of the SADE Consortium, whom I have had the pleasure to work with in the past years, for giving me the chance to challenge my research study during our meetings for the SADE project, and the European Commission for the financial support to my studies.

I would like to thank Dr Xiang Zhang for her insightful feedback and suggestions on my research, for her support in many aspects of my academic life and for making me feel welcome at Cranfield.

It is also a pleasure to acknowledge Dr Daochun Li, Barry Walker, Reynolds Premji Issac and Thibault Deligni for their help with the experimental model.

I would like to give a special thank you to Ryoko Morishima, for helping me in many ways to settle into my new life abroad, for her friendship and for all the happy moments spent together, and to Cinzia Taccoli, for sharing with me many laughs and tears and for easing the burden of the long evenings spent working.

I am thankful to Luca Camosi, Marco Nunez, Marco Boscolo, Pierre-Daniel Jameson, Vis Sripawadkul, Varun Datta, Mudassir Lone and Max Starr for the countless lunches and coffees we have had together and for their company in the Forum. A big thank you goes also to Vincent Fu, Shakeel Ahmed, Melanie Peiris and Yang Da Qing for the many pleasant times in the office discussing work and life in front of a cup of tea.

Finally, I would like to give an heartfelt thank you to my parents, my sisters Maria and Anna and to my boyfriend Riccardo. They have always encouraged me to pursue my aspirations and have patiently put up with me during many difficult moments. I would have not come this far without their love, continuous support and confidence in me.

This page is intentionally left blank.

Contents

This page is intentionally left blank.

List of Figures

This page is intentionally left blank.

List of Tables

Nomenclature

E	Young's Modulus for Isotropic Materials
E_1	Longitudinal Young's Modulus
E_2	Transverse Young's Modulus
G	Shear Modulus for Isotropic Materials
G_{12}	Ply Shear Modulus
S	Shear Strength
X_c	Longitudinal Compressive Strength
X_t	Longitudinal Tensile Strength
Y_c	Transverse Compressive Strength
Y_t	Transverse Tensile Strength
ϵ_1	Ply Local Fibre Strain
ϵ_2	Ply Local Off-Fibre Strain
ϵ_x	Direct Strain in the x Axis
ϵ_y	Direct Strain in the y Axis
γ_{12}	Ply Local Shear Strain
γ_{xy}	Direct Shear Strain in the xy Plane
ν_{12}	Major Poisson's Ratio
σ_1	Ply Local Fibre Stress
σ_2	Ply Local Off-Fibre Stress
σ_x	Direct Stress in the x Axis
σ_y	Direct Stress in the y Axis
τ_{12}	Ply Local Shear Stress
τ_{xy}	Direct Shear Stress in the xy Plane
α	Inclination of Neutral Axis to the Reference Coordinate System
β	Angle of deflection of the handle in the demonstrator

ϕ	Angle between the Tangential Displacement v_t and the x Axis
ρ	Density
σ_z	Stress
θ	Rotation in the xy Plane
ξ	Distance from Neutral Axis
B	Bi-moment
$B_{1,2}$	Boom Areas 1, 2
C_w	Cross Sectional Warping Constant
FML	Fibre-reinforced Metal Laminates
$GLARE$	Glass Reinforced Aluminium Laminate
I	Second Moment of Area
J	Moment of Inertia
M	Bending Moment
$MTOW$	Maximum Take Off Weight
OEW	Operating Empty Weight
q	Shear Flow
SMA	Shape Memory Alloy
T	Torque
t	Thickness
t_D	Direct Stress Carrying Thickness
u	Displacement in the x Direction
V	Shear Force
v	Displacement in the y Direction
v_t	Tangential Displacement
WRP	Wing Reference Plane
CFRP	Carbon Fibre Reinforced Plastic
EBAM	Eccentric Beam Actuation Mechanism
FE	Finite Element
GFRP	Glass Fibre Reinforced Plastic
MPC	Multi Point Constraint
TE	Trailing Edge

This page is intentionally left blank.

CHAPTER 1

Introduction

1.1 Overview

Over the next few years the aviation industry will face the challenge to develop a new generation of air vehicles characterised by high performance and low environmental impact. Following the guidelines of the Vision 2020 report [1] by the European Commission for Research, in the next few years the main objective of aircraft design will be the development of aircraft technologies able to satisfy the rising demand for lower travel costs, better service quality and high safety standard, while achieving a significant reduction in the perceived noise generated and a drastic cut to the fuel consumption and polluting emissions.

The need for a significant reduction in polluting emissions and noise caused by commercial aircraft, however, seems to be in contrast with the constantly rising demand for high performance. Conventional design solutions are unable to provide a satisfactory trade off betweeen these two conflicting requirements and, for this reason, there is great interest in the exploration and development of different design approaches.

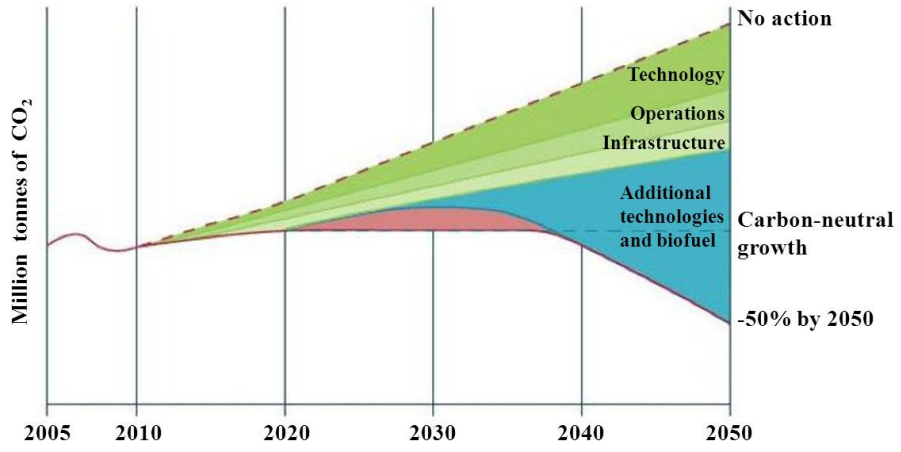

Figure 1.1: Impact of new technologies on CO_2 emissions [2]

Figure 1.1 presents a likely forecast for the CO_2 emissions by 2050: the graph shows that a simple improvement of existing technologies, operations and infrastructures is not sufficient to determine a reduction in the CO_2 emissions and innovative technologies are the key to achieve carbon-neutral growth.

Morphing airframe technologies represent a very promising area of investigation in the field of aircraft structural design. Aircraft wings are usually designed to suit all the different segments of the vehicle's mission. However, they cannot achieve the optimum airframe configuration for any single flight condition, as this changes between the different phases of the flight (cruise, take off and landing) and it depends on several parameters such as altitude, velocity and mass. In order to partially reduce the loss of performance in the sub-optimal configurations, modern commercial aircraft are equipped with high lift devices, able to modify in a favourable way the shape of the wing and to improve the performance achievable. The conventional devices mounted on a transport aircraft typically consist of slats and flaps driven by specific mechanisms. They significantly improve the aerodynamic behaviour of the wing but, on the other hand, they also increase the weight and the complexity of the structure and represent one of the main sources of noise from the aircraft due to the presence of the slots.

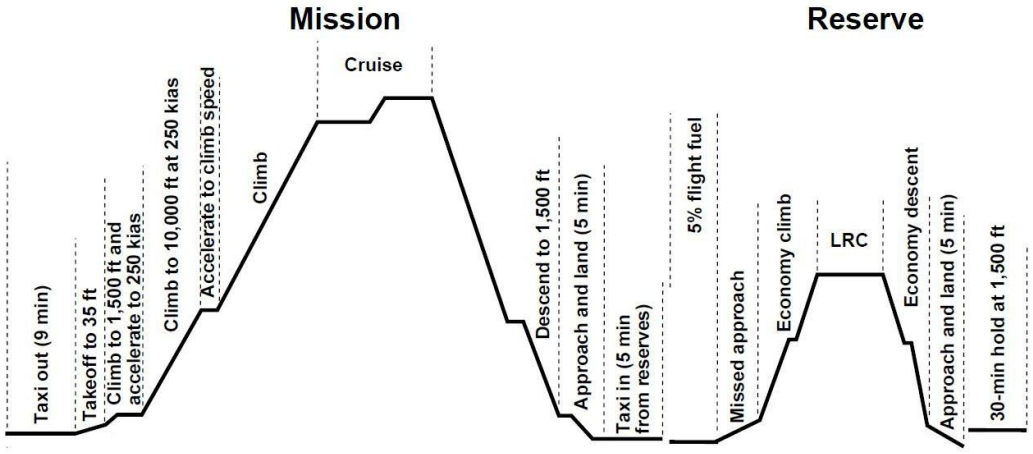

Figure 1.2: Typical mission profile of a transport aircraft [3]

The use of morphing technologies instead of the conventional high lift devices would offer several advantages. The possibility to smoothly deflect the wing surfaces to meet certain shape requirements would enable the aircraft to fly in the optimal configuration during all the phases of the flight, achieving higher aerodynamic efficiency and generating less off-design effects. The lower number of gaps in the airframe structure would allow a more laminar air flow over the wing surface during take-off and landing. The laminarisation of the air flow around the airfoil, in turn, would reduce drag and lead to a reduced fuel consumption. Finally, the use of a gapless structure would reduce the noise emission from the aircraft.

Several morphing concepts have been proposed in recent years. However, most of them are not suitable for large commercial aircraft and their applicability is limited to Micro Aerial Vehicles (MAVs), Unmanned Aerial Vehicles (UAVs) and Unmanned Combat

Aerial Vehicles (UCAVs). For such types of vehicles, it is relatively easy to obtain a change in shape due to the reduced dimension of the wings. The reason lies mainly in the low energy required to perform morphing of a small structure. Different actuation systems embedded or not in the structure can be used and also smart materials for actuation such as piezoelectric devices and shape memory alloys (SMAs) can be successfully implemented. Different techniques have been tested and have proven to be effective.

Designing smooth morphing high lift devices for a large vehicle is a much more challenging goal due to the stringent strength requirements involved. One of the main issues during the design process is the correct selection of the actuation mechanism and of the skin materials. The actuation system has to be efficient in terms of power consumption and, of course, able to deflect the morphing structure to reach the target shape. Actuation should be performed using a small number of moving parts to guarantee high reliability and attention should be paid also to the overall weight of the system. The skin material should be stiff enough to keep the desired shape while undergoing the external aerodynamic loads, but it should also be flexible to follow the deflection imposed by the actuation system as smoothly as possible. Stresses and strains arising in the skin and in the other structural components should be low enough to guarantee the structural strength and integrity is preserved. From this point of view, also the aeroelastic interaction between the morphing structure and the aerodynamics has to be carefully investigated, to prevent undesired effects. Finally, nonlinear phenomena due to the presence of loose hinges, to friction between moving parts and to aerodynamic phenomena such as gusts and vortex shedding from the structure should be kept into account.

1.2 The SADE Project

The research study presented in this thesis is part of a wider research project called 'Smart High Lift Devices for the Next Generation Wing' (SADE), conducted within the European Union Seventh Framework Programme. The SADE project aims to investigate and develop morphing concepts for the high lift devices of future aircraft wings. The main objective pursued by SADE has been the development of a Smart Leading Edge and a Smart Single Slotted Flap to replace the conventional slats and flaps found on commercial aircraft wings. The use of a smart, gapless leading edge device would contribute to achieve laminar flow over the wing and would help to reduce the noise and drag generated. Moreover, the use of a smart flap having morphing capabilites would increase the lift to drag ratio and hence the efficiency of the aircraft.

Thirteen different partners were involved in the Programme, in order to cover all the different aspects and phases of the design, analysis and testing of the morphing devices. The research activity was divided into four separate Work Packages:

- Work Package 1: *Integration*. This Work Package aims to investigate the integration of the high lift devices in the aircraft and to assess the impact of the morphing on the overall wing behaviour.
- Work Package 2: *Smart Leading Edge*. Different morphing concepts for the leading edge have been proposed and analysed. The study comprises the initial mechanical design and the structural and aerodynamic analysis. Several concepts were

assessed in terms of their design feasibility, performance offered and readiness of the technology involved.

- Work Package 3: *Smart Single Slotted Flap*. Similarly to Work Package 2, different morphing concepts for the trailing edge flap have been proposed and analysed. The study comprises the initial mechanical design and the structural and aerodynamic analysis. Several concepts were assessed in terms of their design feasibility, performance offered and readiness of the technology involved.

- Work Package 4: *Wind Tunnel Tests*. The morphing concept selected in the Work Package 2 for the smart leading edge has been designed, manifactured and tested in the wind tunnel.

This current research study focuses on the Work Package 3 activities on the Smart Single Slotted Flap. Various morphing concepts were reviewed and an innovative design for a gapless and hingeless internal actuation mechanism for the flap was selected. The flap structure with internal actuation mechanism was subsequently designed in detail and modelled using finite elements. A geometrical nonlinear structural analysis was conducted on the flap to assess its structural behaviour and to evaluate the effectiveness and feasibility of the proposed actuation solution.

1.3 Research Objectives

Flaps are commonly used to increase lift during take-off and landing and are nowadays available in a variety of configurations to suit the needs of any commercial vehicle. However, the existing flap designs do not allow to overcome the limits of a fixed and rigid wing configuration. The aim of this research study is to design a morphing flap with a flexible end, hingeless and internally actuated, capable to replace the existing rigid design and to achieve at least the same aerodynamic benefits.

The objectives of this thesis can be summarized as:

- To develop a suitable design concept for a morphing trailing edge device to increase the performance of a large transport aircraft
- To demonstrate the feasibility of the design concept
- To analyise the structural behaviour of the morphing trailing edge device under static and dynamic loading
- To investigate the possibility of optimising the structural design

In order to fulfill these objectives the state of art solutions in the field of morphing structures were researched to identify the basic principles and methods applied and to understand the challenges arising in the design of a morphing high lift device. A new concept for the actuation mechanism of the morphing trailing edge was developed. The mechanism was fully integrated with the trailing edge skin and a geometrically nonlinear

finite element analysis was conducted to investigate its structural behaviour under the effect of the mechanical and aerodynamic loads. Some modifications to the conventional internal structure of the flap were suggested and included in the analysis in order to achieve a uniform deflected shape. Finally, the interaction of the trailing edge flap with the airflow was investigated and some design improvements were proposed in order to optimise the morphing flap structure.

1.4 The Scope

Several morphing concepts and innovative wing configurations have been proposed in the last decades to improve the performance and to extend the operative range of an aircraft. Many of these concepts have been initially developed for military applications, such as small UAVs, hence they are not able to meet the design and strength requirements for commercial aircraft and lie outside of the area of investigation of this thesis. On the other hand, some very promising concepts would require drastical changes to the conventional wing configurations and, since the level of readiness of such techniques is generally very low, they are not suitable for analysis within the SADE project, which focuses on morphing structures that can be realised effectively within the next two decades.

In this current study, the traditional basic wing structure, represented by a central wing box connected to moveable parts, is retained in order to have a favourable strength to weight ratio. Within the SADE Project, the investigation has been restricted to concepts suitable for the moveable parts such as the high lift devices. Moreover, only internal actuation mechanisms able to provide a uniform and gapless deflected airfoil shape have been considered in order to meet the stringent aerodynamic requirements of a transport aircraft.

1.5 Research Novelty and List of Publications

The current research work presents the innovative design, modelling, analysis and optimisation of a morphing flap device for a next generation commercial aircraft.

Despite the increasing interest for morphing structures, no previous work available in literature offers a comprehensive investigation of morphing applied to large scale commercial vehicles. The research work conducted has contributed in adding new knowledge in this area.

A novel concept for the internal actuation mechanism of a morphing trailing edge flap has been developed in order to improve the aerodynamic performance of the wing. Attention has been paid to ensure that the structure was flexible enough to meet the deflection requirements while preserving its strength and load carrying capability. Great effort has been made to identify suitable modelling techniques for the morphing structure with limited guidance available from previous studies. Lastly, the interaction of the flexible structure with the airflow has been investigated and the problem to extend conventional optimisation techniques to internally actuated morphing structures has been addressed.

Please refer to Chapter 9 of this thesis for a detailed description of the results of this investigation.

The following list of papers demonstrates the originality of the work:

- Di Matteo, N., Guo, S., Morishima, R., Optimization of leading edge and flap with actuation system for a variable camber wing, 53^{rd} *AIAA/ASME/ASCE/AHS/ASC Structures, Structural Dynamics, and Materials Conference*, 23-26 April 2012, Honolulu, Hawaii

- Di Matteo, N., Guo, S., Morishima, R., Aeroelastic modelling and analysis of a wing with morphing high lift devices, *International Forum of Aeroelasticity and Structural Dynamics (IFASD)*, 26-30 June 2011, Paris, France

- Di Matteo, N., Guo, S., Li, D., Morphing trailing edge flap for high lift wing, 52^{nd} *AIAA/ASME/ASCE/AHS/ASC Structures, Structural Dynamics, and Materials Conference*, 4-7 April 2011, Denver, Colorado

- Di Matteo, N., Guo S., Ahmed, S., Li, D., Design and analysis of a morphing flap structure for high lift wing, 51^{st} *AIAA/ASME/ASCE/AHS/ASC Structures, Structural Dynamics, and Materials Conference*, 12-15 April 2010, Orlando, Florida

- Li, D., Guo, S., Xiang, J., Di Matteo, N., Control of an aeroelastic system with control surface nonlinearity, 51^{st} *AIAA/ASME/ASCE/AHS/ASC Structures, Structural Dynamics, and Materials Conference*, 12-15 April 2010, Orlando, Florida

- Guo, S., Morishima, R., Di Matteo, N., Ahmed, S., A composite wing structure with morphing high lift devices, 17^{th} *ICCE Conference*, 26 July - 01 August 2009, Hawaii, USA

- Morishima, R., Guo, S., Di Matteo, N., Ahmed, S., A composite wing structure with morphing leading edge and flap, *World Journal of Engineering*, Vol. 7, No.4, 2010, pp.186-193

1.6 Structure of the Thesis

A description of the thesis structure is herein provided to guide the reader and to present how the research was conducted. The content of the following chapters is outlined below.

- Chapter 2 - Literature Review

  This chapter illustrates the state of the art in the study of morphing structures. In the first part, the role of morphing in the developments of future aircraft is discussed. A variety of morphing concepts is presented in the framework of their respective research programmes and critically reviewed on the basis of the performance achieved and feasibility. Other issues strictly connected to the design of morphing structures are also introduced, such as the need for smart skin materials,

the importance of the aeroelastic interactions for a flexible structure and the benefits and challenges in the optimisation of morphing structures.

- Chapter 3 - Theoretical Background

  This chapter introduces the theoretical background of the current research study. The basic principles for the study of thin walled structures are recalled. The principles of the classical laminate theory for composite materials are also described. The finite element modelling was briefly recalled with emphasis on the finite element analyses conducted in this current research.

- Chapter 4 - The Wing with Morphing Hihg Lift Devices

  Chapter 4 provides a description of the baseline wing structure considered for the analysis and illustrates the geometry and the material properties of the wing box, leading edge device and flap. The target deflected shape for the high lift devices is presented and discussed on the basis of aerodynamic considerations and the aerodynamic pressure distribution over the selected airfoil in various configurations is also given.

- Chapter 5 - Design and Modelling Approach for the Morphing Trailing Edge Flap

  Chapter 5 presents the novel concept developed to deflect the morphing trailing edge of the flap, called Eccentric Beam Actuation Mechanism (EBAM) and based on the principle of the eccentuation. In order to integrate the EBAM in the flap structure and to meet the deflected shape requirement, the internal structure of the flap was substantially modified. The design improvements, such as the use of an open sliding trailing edge and the inclusion of additional connections in the structural model, are discussed in detail. A new procedure for the determination of the actuation load required to deflect the structure is also set up. Finally, the feasibility of the EBAM concept is demonstrated using a flap demonstrator model.

- Chapter 6 - Nonlinear Static and Dynamic Analysis of the Morphing Trailing Edge Flap

  Chapter 6 presents the results of a nonlinear static stress and strain analysis conducted on the trailing edge flap with integrated actuation system using the finite element method. The analysis was carried out first on a 1 m spanwise section of the flap trailing edge and subsequently extended to the whole inboard flap structure. In the final part of the chapter, the structural dynamic properties of the flap are presented in terms of natural frequencies, mode shapes and frequency response functions. The transient response to a 1-cos gust type input was also calculated for different values of the input frequency to assess the dynamic behaviour of the flap.

- Chapter 7 - Aeroelastic Analysis of the Trailing Edge Flap

  This chapter investigates the methods of analysis of the interaction between the trailing edge flap structure and the aerodynamic pressure loads. The aerodynamic load on a deflected trailing edge surface is initially evaluated using a simple analytic approach proposed by Howe and ESDU approved methods. The results are compared with the pressure distribution obtained with panel method and CFD analysis. A Fortran-based software able to iteratively interface the Nastran structural solver with the commercial software Xfoil for panel method analysis has been developed. A case study was conducted on the morphing flap to show the effect of the progressive deflection on the air pressure load until an equilibrium configuration is reached.

- Chapter 8 - Optimisation of an Actuated Morphing Structure

  Chapter 8 investigates the possibility to optimise the design of the morphing trailing edge flap by acting on the characteristics of the actuation mechanism and on the mechanical properties of the skin materials. An iterative analysis was implemented by coupling the Nastran structural solver to the NASA optimisation tool ADS. Different design configurations for the Eccentric Beam Actuation Mechanism are proposed and evaluated in terms of deflection shape and actuation load. An optimised design for the morphing trailing edge device is also presented.

- Chapter 9 - Conclusions and Future Work

  This last chapter summarises the main findings of the research work on the morphing trailing edge device and states the main contribution to the knowledge of this study. Possible further investigations which are not part of this thesis due to the time constraints of a research work are also indicated and some guidelines for future research work are suggested.

CHAPTER 2

Literature Review

This chapter presents an overview of the current technologies and future trends in the field of aircraft design and provides an introduction to the study of morphing structures. In the first part of the chapter, the current status of the aviation industry is briefly outlined and the challenging targets set for the next few years are presented. The high lift devices mounted on the conventional modern wings are reviewed in Section 2.2, with emphasis on the limitations of the existing designs in achieving further performance improvements. In Section 2.3, morphing technologies are introduced as a very promising solution for the development of the next generation of aircraft structures. The potential advantages and disadvantages of morphing are discussed for the case of a commercial transport aircraft and an overview of the various research projects which have focused on active wings in recent years is given. The literature review evidenced that, despite the great research efforts, a comprehensive and unified approach to the study of morphing airframe technologies is still missing. An attempt at a classification of the different types of morphing was made in Section 2.3.2, where several morphing concepts are reviewed. In Section 2.4, some considerations about skin materials for the morphing structures are presented and the possibility to use composite materials and innovative smart materials is discussed. In the final part of this chapter, selected studies on the aeroelastic behaviour of the wing are presented due to the importance that the interaction of aerodynamic loads and elastic bodies acquires for flexible morphing structures. Structural optimisation methods are also discussed to identify their applicability and the potential benefits they offer to the design of morphing structures .

2.1 Historical Developments and Future Trends in Aircraft Design

Aircraft design is a continuously evolving discipline, where new concepts, materials and technologies are constantly being developed in order to meet the demanding requirements of a highly competitive market.

According to [1], air travel is nowadays experiencing the fastest growth among all modes of transport. The aviation industry is under tremendous pressure to deliver aircraft characterised by high performance, high efficiency, low costs and, at the same time, low impact on the environment. On one hand, airlines and aircraft manufacturing companies push for highly efficient and performing structures, in order to reduce the fuel consumption and to achieve low production and operative costs. On the other hand, polluting emissions and noise from the aircraft have raised concern among the governments and the scientific community about the impact that high volumes of air transport could have on the environment. Since 1977, the International Civil Aviation Organization (ICAO) has developed standards and measures to regulate the emissions. More recently, the European Union has set very ambitious targets to reduce the environmental issues connected to an increased number of flights. The Vision 2020 report [1], by the European Commission for Research, specifies stringent requirements, which include a consistent reduction of carbon dioxide and nitrogen oxides emissions,as well as of the noise caused by the aircraft, to be achieved in the next few years.

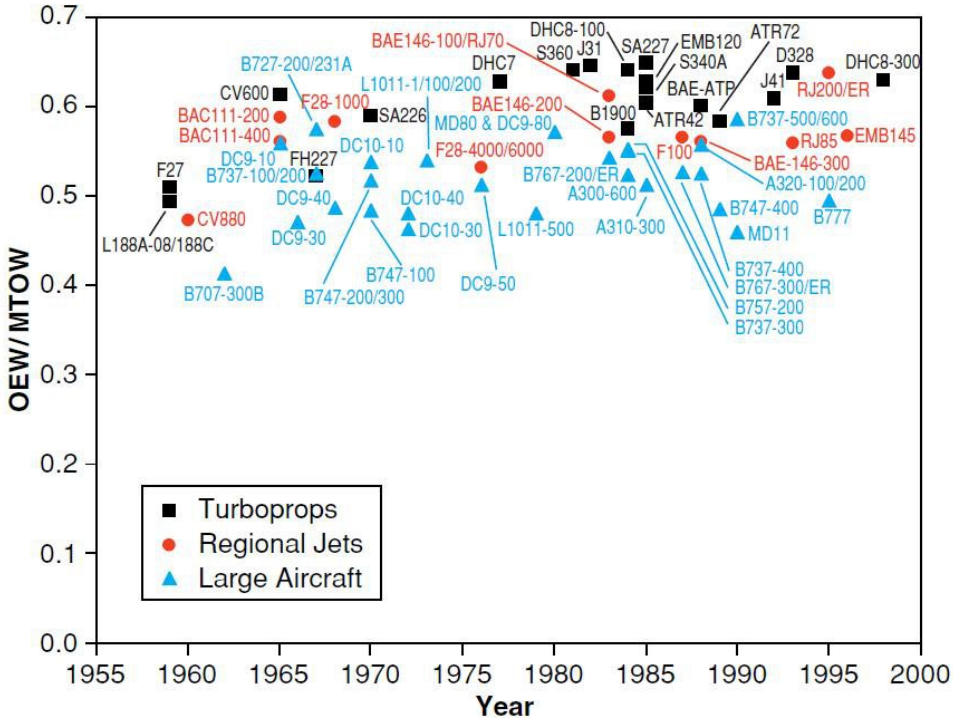

Figure 2.1: Structural efficiency of modern airliners [4]

Over the past 50 years, there has been a continous increase in aircraft performance and capabilites. Propulsion systems have evolved from propellers to turbofans, while the capacity of transport aircraft has gone from less than 100 people to up to the 850 passengers for some Airbus A380 configurations. Perhaps the more evident improvements concern the cruise speeds of modern aircraft; planes in the 1940s had average speeds of 100 knots, while today's turbofans cruise at average speeds of around 500 knots (and, although now dismissed, the Concorde was able to operate in the supersonic regime). The flight range of commercial vehicles has been considerably extended and nowadays the conventional cruise altitude is between 10.5 and 11 km of altitude, in order to obtain more efficient cruise performance, as opposed to the 3 to 7.5 km of the beginnings.

Despite the gradual and continuous improvements, however, modern airliners are, in principle, still very similar to the older aircraft introduced decades ago. As discussed by Babikian et al. in [4], if the ratio between the Operating Empty Weight (OEW) and the Maximum Take Off Weight (MTOW) is taken as a measure of the structural efficiency of the aircraft, the graph in Figure 2.1 shows that, over the past 70 years, this parameter has not changed much. Moreover, after several years of use, the conventional design concepts and methodologies are already fully optimised and have reached their maximum potential. For these reasons, the current technologies are unable to meet the ambitious performance targets and the stringent requirements set for the next few years.

The scientific community has always understood the need for a radically new approach. In 1997 Dan Goldin, then one of NASA's heads, gave a public speech entitled "The Three Pillars for Success for Aviation and Space Transportation in the 21st Century" [5]. One of the three pillars that Goldin mentioned was 'a revolutionary technology leap', allowing significant improvements in the field of aviation. Since then, many research programmes have been conducted and have laid the foundations for the modern design analyses, as will be shown in the following Sections.

As highlighted by a report from the US National Research Council [6] published in 1998, there are three main areas of research and development most likely to allow this technology leap. These are:

- Radically different configurations
- Improvement of existing subsystems
- Major breakthroughs in manufacturing or design processes

The development of radically different configurations has the potential to transform air transportation, but the changes would require a very long time to be implemented. The improvement of existing subsystems, on the contrary, would allow to retain the basic traditional configurations and to reduce the time needed to achieve some performance improvements. Progress in manufacturing or design processes, on the other hand, would have a direct impact on the costs of producing an aircraft. A combination of these improvements would be extremely beneficial.

In all the cases, the main driver for the design innovation is the need to expand the performance and capabilties of the aircraft. During its life, the aircraft operates over a wide range of flight conditions and its wing configuration will have to suit all the different segments of a typical mission. However, once a design has been selected, the conventional rigid wings can achieve only relatively small in-flight shape changes. As a consequence, the wing will be in a non-optimal configuration during large part of the flight, leading to a reduced efficiency and low cost effectiveness, as pointed out by Spillman [8].

The state of the art solution to this problem is represented by the use of high lift devices, able to improve the wing performance during take off and landing. These devices, however, cannot eliminate all the limitations connected to a rigid wing and present a series of disadvantages, such as the additional weight, complexity and noise due to eventual gaps in the structure.

An innovative, very promising solution is represented by morphing wing technologies. Morphing can be defined as the capability of a wing to achieve a continuous shape change upon a specific actuation. The use of morphing could allow the wing to adapt its shape smoothly under different loading conditions, to achieve near-optimal lift and drag profiles throughout all the different phases of the flight. The main advantages of this would be a reduced fuel consumption and a higher aerodynamic efficiency. Additional benefits coming from morphing could be an improved control of the aircraft during flight and a better airload distribution over the wing.

The following sections offers a review of the various high lift devices mounted on modern aircraft and a selection of the different morphing concepts which have been developed over the years is presented. Subsequently, the main aspects to take into account when attempting to design an innovative wing configuration are discussed. The importance of aeroelastic and aeroservoelastic phenomena is highlighted and the possible onset of nonlinear effects is also illustrated.

2.2 High Lift Devices

Modern commercial airliners are equipped with high lift devices for both the leading and the trailing edge. These devices are mainly used during take-off and landing to reduce the vehicle speed while still generating the lift necessary to safely maintain flight. They also offer a series of additional benefits and improve the aircraft flying capabilities to such an extent that they have become indispensable and routinely mounted on almost any modern air vehicle.

Leading and trailing edge devices both determine a change of the original clean shape of the wing. Over the years, the development of high lift devices has been influenced by the increase of the aircraft cruise speed following the introduction of more powerful engines and of some innovative design features such as wing sweep. The original basic high lift designs have evolved into complex geometries in order to keep up with the increasing demand for high performance and manoeuvrability of the aircraft.

2.2.1 Conventional High Lift Devices for the Leading Edge

High lift devices are mounted on the leading edge of commercial aircraft in order to safely operate at higher angles of attack. They contribute to increase the lift coefficient and, as a consequence of this, allow the aircraft to fly at lower speeds. These devices are typically used to improve manoeuvrability and avoid stall at high angles of attack, and during take off and landing, to reduce the distances needed on the runway. They also help to maintain roll effectiveness and delay or suppress control reversal phenomena [7] and, when used in conjunction with trailing edge devices (see next Section), they reduce the pitching moment generated by the latter.

Fixed Slot
The fixed slot, schematically shown in Figure 2.2, has been successfully mounted on airplanes with small cruise speed and short takeoff and landing (STOL) vehicles. The high drag generated by the device, however, makes it unfit for civil transport aircraft.

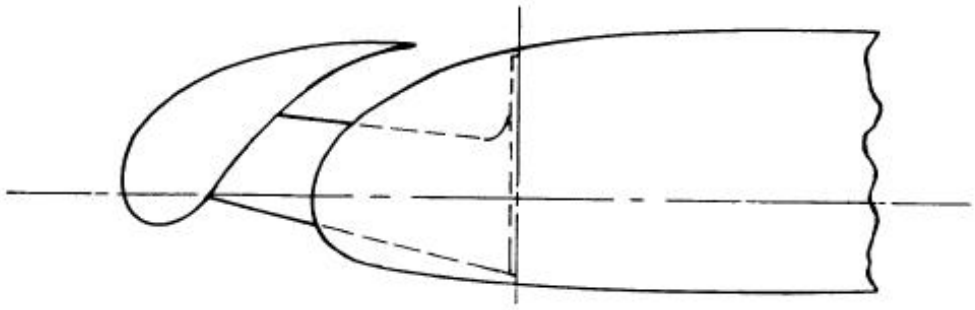

Figure 2.2: Fixed slot for the leading edge [10]

Simple Krueger Flap
The simple Krueger flap is a panel hinged on the lower side of the wing leading edge, shown in Figure 2.3. This panel is able to rotate downward and forward up to an angle of 80°. This device is one of the simplest leading edge devices ever mounted on modern transport aircraft. It offers a good performance for the inboard wing section, however it is unable to adapt to various angles of attack.

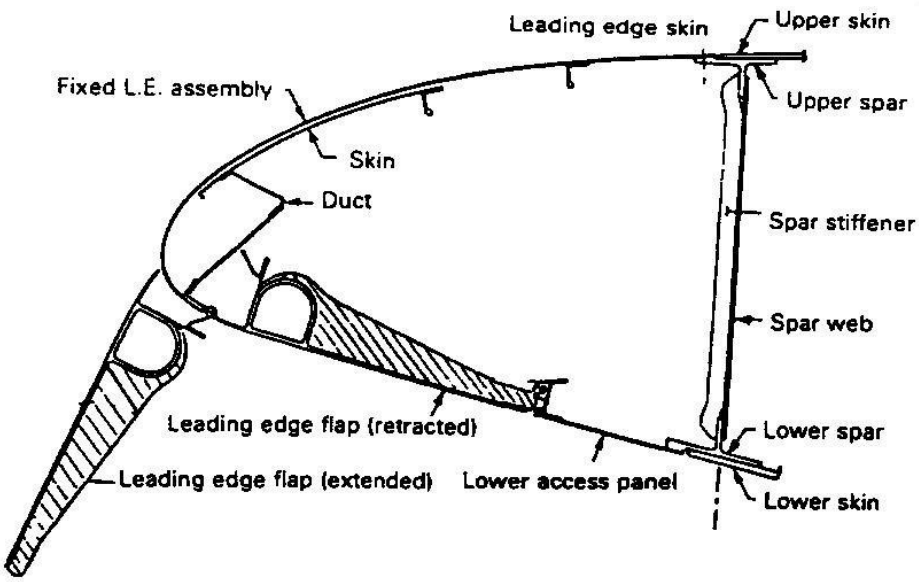

Figure 2.3: Simple Krueger flap [10]

Folding Krueger Flap
The folding Krueger flap (also known as bull-nose Krueger flap) is a modification of the simple Krueger flap characterised by the addition of a folding bull nose at the end of the flap panel. The nose, having a D-shaped cross section, improves the performance of the simple Krueger flap by maintaining the flow attached over a wider range of angles of attack.

Variable Camber Krueger Flap
In the Variable Camber (VC) Krueger flap, the Krueger flap panel is changed from a rigid to a flexible one, with consequent improvements of the airfoil shape and aerodynamic performance. This design, however, presented several disadvantages. The linkages required to actuate the VC Krueger flaps, in fact, are much more complex than the simple Krueger flaps and the flexible panel tends to distort under the air pressure loads.

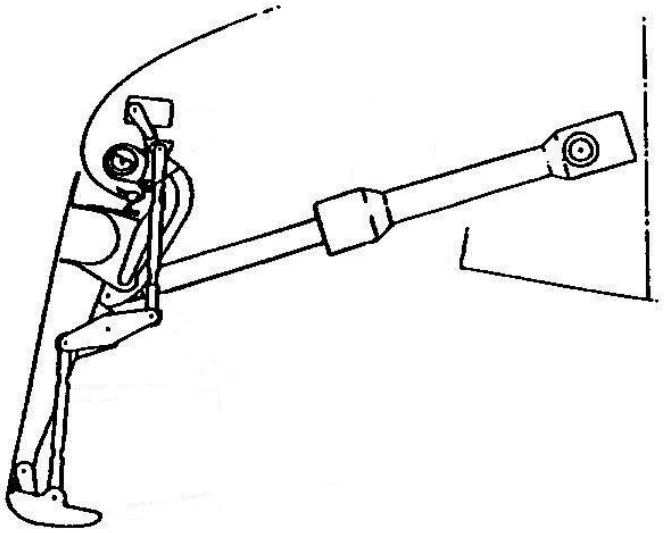

Figure 2.4: Folding Krueger flap [10]

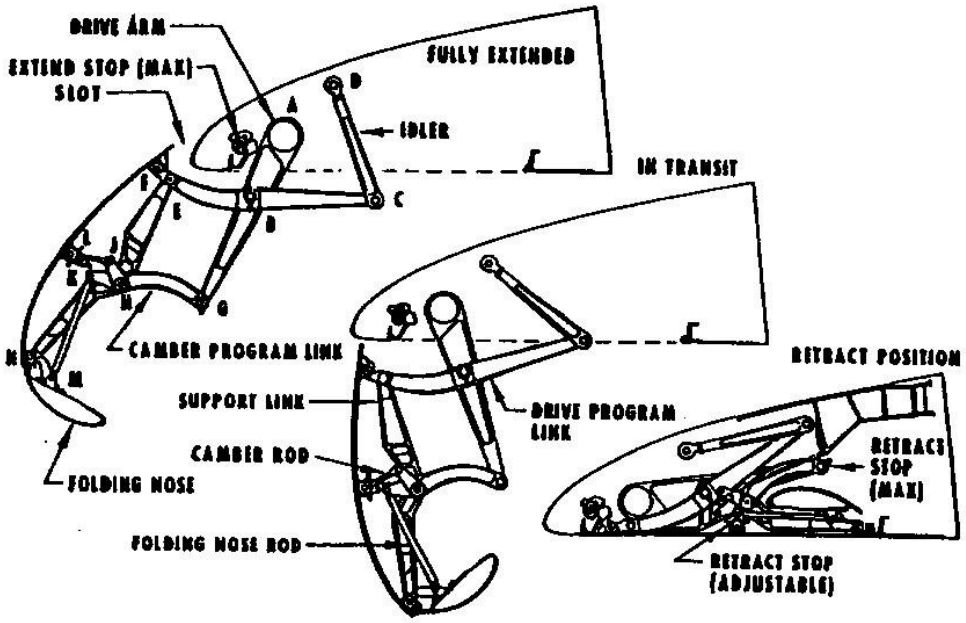

Figure 2.5: Variable camber Krueger flap [10]

Two and Three Positions Slat

The slat is very common on modern civil transport airliners. The slats are in retracted position during cruise flight and are mounted on curved traks to move forward and downwards during low speed flight. The two-position slat has one stowed and one deployed configuration, while for the three-position slat two deployed positions are possible: a intermediate take off position, where the slat end is sealed against the surface of the fixed leading edge, and a fully deployed landing position, where the slat forms a slot with the fixed leading edge structure.

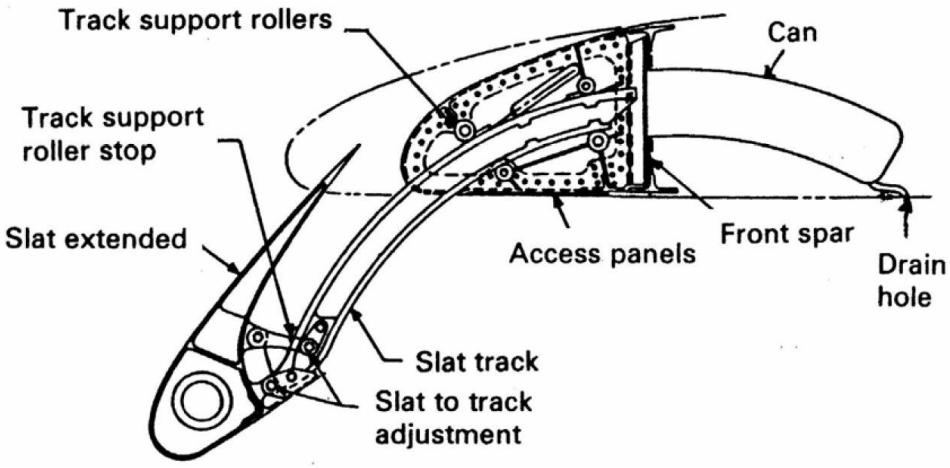

Figure 2.6: Slat Device with Curved Track [10], [11]

Droop nose (Hinged Leading Edge)

The droop nose is obtained by rigidly deflecting the leading edge structure around a hinge placed close to the front spar. This mechanism, however, is characterised by a tight radius of curvature on the upper wing surface, which causes flow separation unacceptable for a commercial aircraft. On the contrary, this concept has been used for supersonic fighter airplanes, where a high leading edge sweep angle gnerates a stable vortex on the upper surface and eliminates the negative effects of the hinge.

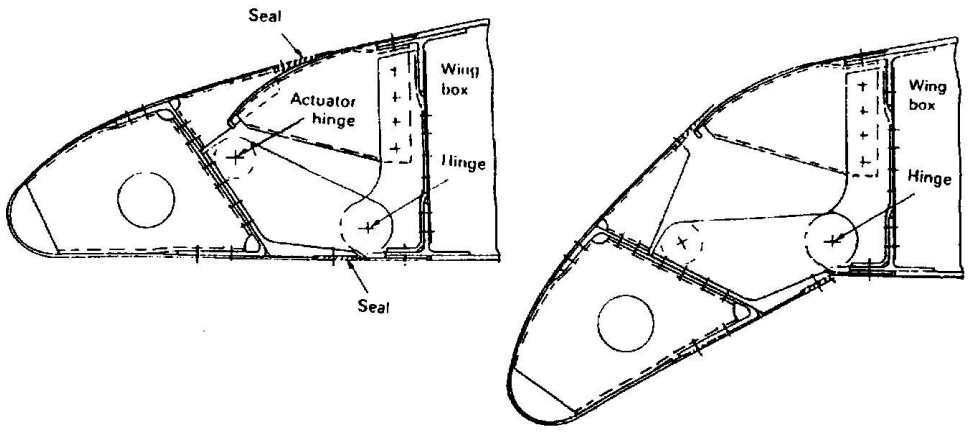

Figure 2.7: Hinged Leading Edge [10]

2.2.2 Conventional High Lift Devices for the Trailing Edge

The high lift devices for the trailing edge are commonly called "flaps". The use of flaps increases the wing camber and planform area, leading to higher values of the lift coefficient and to a reduction of the stall velocity of the aircraft. According to Szodruch [12], flaps also improve the lift distribution over the span. During takeoff, the use of flaps reduces the runway distance and the climb rate required. During landing, when the flaps are typically fully extended, the additional drag generated contributes to a shorter landing. Flaps also allow a better glide-slope control and improve the pilot's vision over the nose during landing by reducing the aircraft attitude ([10], [11]).

Over the years, as the cruise speed and wing loading increased, flaps evolved from early designs, such as the split flap, simply hinged to the final part of the wing, to the more complex Fowler flaps with single, double, and even triple slots. Smith, in his paper "High Lift Aerodynamics" [13] demonstrated that a flap with $N + 1$ elements is more effective than one with N elements. Nowadays the tendency in high-lift system development has been to achieve high levels of lift with simpler devices in order to reduce maintenance costs, design complexity and to minimize the risk of failure.

Split Flap
In this design, at the wing trailing edge a portion of the lower surface was hinged to the main structure and was able to rotate downwards, while the upper surface remained in the same position. The split flap represents a very early design which has been nowadays abandoned because it does not allow significant lift increase. It has been used on military airplanes as a speed brake, able to generate drag without losing lift.

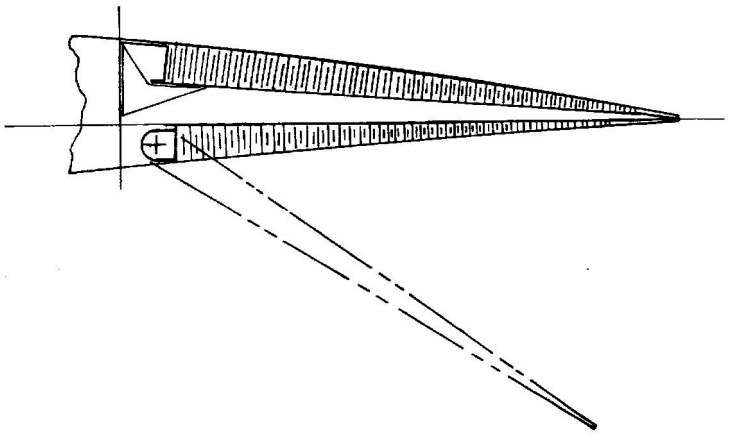

Figure 2.8: Split Flap [10]

Plain Flap
The plain flap consists of a device situated at the rear part of the airfoil, hinged at its front and able to rotate downwards. The flap has a rounded leading edge, so that during the rotation no slot is created between the fixed and the moveable structures. This device can be deflected up to a maximum of 20°, as beyond this value flow separation on the upper surface would occur, consequently reducing the lift increase generated by the flap. Plain flaps are no longer used on commercial planes.

Simple Slotted Flap
In this design the flap is mounted on pivots below the lower wing surface and is able

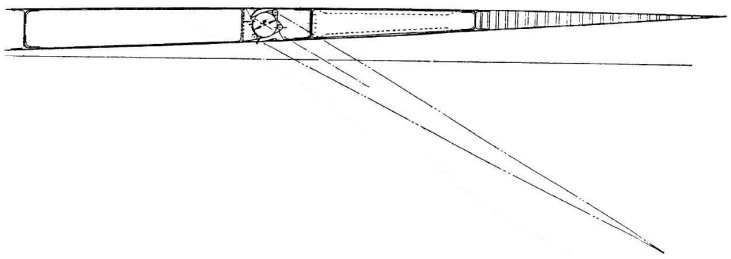

Figure 2.9: Plain Flap [10]

to deflect up to 35°. During the deployment, a gap between the flap and the wing is created and high pressure air from below the wing is forced over the flap, contributing to maintain the airflow attached to the flap. The slotted flap generates a significant lift increase thanks to the high-speed air around the leading edge of the flap, which increases the velocity of the air around the airfoil. The same principle can be extended to have multiple slots to further increase the lift.

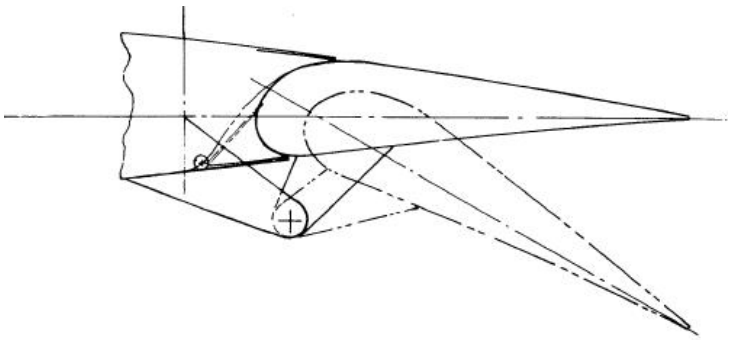

Figure 2.10: Simple slotted flap [10]

Single Slotted Fowler Flap
This flap is similar to a simple slotted flap, only with a significant overlap between the flap and the upper cover panel from the main wing structure (see Figure 2.11). When the flap is in fully deployed position, the overlap is converted in a chordwise movement of the flap, called Fowler motion from the name of its inventor. The additional benefit of a Fowler flap is represented by the increase in the wing area due to the motion. Slotted Fowler Flaps represent the most widespread design currently adopted on commercial aircraft due to their good performance and medium level of complexity.

2.2.2.1 The Deployment Mechanisms

A very important role in determining the performance of the trailing edge high lift system is played by its deployment mechanism. A review of the most common deployment mechanisms fitted on transport aircrafts can be found in [10] and [11]. The key parameters that influence flap performance are the deflection angle, Fowler motion and flap gap. If the plane that goes through the leading edge of the wing and the trailing edge of the flap in the stowed position is assumed as the wing reference plane (WRP), then the flap angle is defined as the angle between the WRP in the stowed position and the one in the deployed position. The flap Fowler motion, on the other hand, is defined as

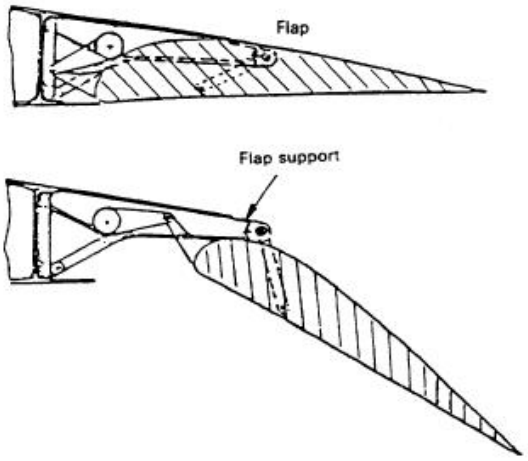

Figure 2.11: Single slotted Fowler flap [10]

the translation of the flap aft from the stowed position in the direction parallel to the WRP. This translation increases the chord of the wing and contributes to the increase of the lift. As pointed out by Rudolph [11], however, considering the projected chord variation makes the Fowler motion of many flaps negative because the rotation shortens the projected flap chord. This is even more evident if a smart flexible device is considered, because the progressive deflection emphasizes the negative Fowler motion. An alternative definition of Fowler motion was hence proposed. According to [11], Fowler motion can be seen as the increase in developed wing chord, which means chord in space and not just the wing chord projected into the wing reference plane. As a general guideline stated in [11], a good flap mechanism should provide the major part of its total Fowler motion in the initial phases of deployment, when deflection angles are low, resulting in an optimal lift/drag ratio (see also [11], [10], [14], [15]). Other desirable requirements include a good development of the gap between the flap and the main wing, low complexity, small fairings and light weight.

Figure 2.12 compares the Fowler motion progression for several flap mechanisms. Simple solutions, like hinged flaps, fail to meet the requirements of large commercial vehicles because the Fowler motion is generally too low. On the other hand, one of the best flap mechanisms proved to be the link-track type, shown in Figure 2.13, which offers good performance despite the large size of its fairing, as pointed out in [11], [10] and [16]. A link-track mechanism is currently fitted into the A320 Series trailing edges. Another promising mechanism is the Upside Down Four Bar Linkage, which is used on Boeing 747, although its higher complexity makes it more problematic from a structural and aerodynamic point of view.

Many other combinations of slots and linking mechansim have been experimented, as recalled by Smith [13]. Complex designs, however, must be carefully assessed. The greater number of moving parts increases the risk of failure of the assembly and requires additional links and supporting members. Moreover, the presence of the slots is responsible for considerable aerodynamic losses. There is, in fact, a limit to the increase of performance achievable with the use of conventional high lift devices. Other solutions, such as morphing airframe technologies, must be introduced in order to dramatically improve aircraft performance.

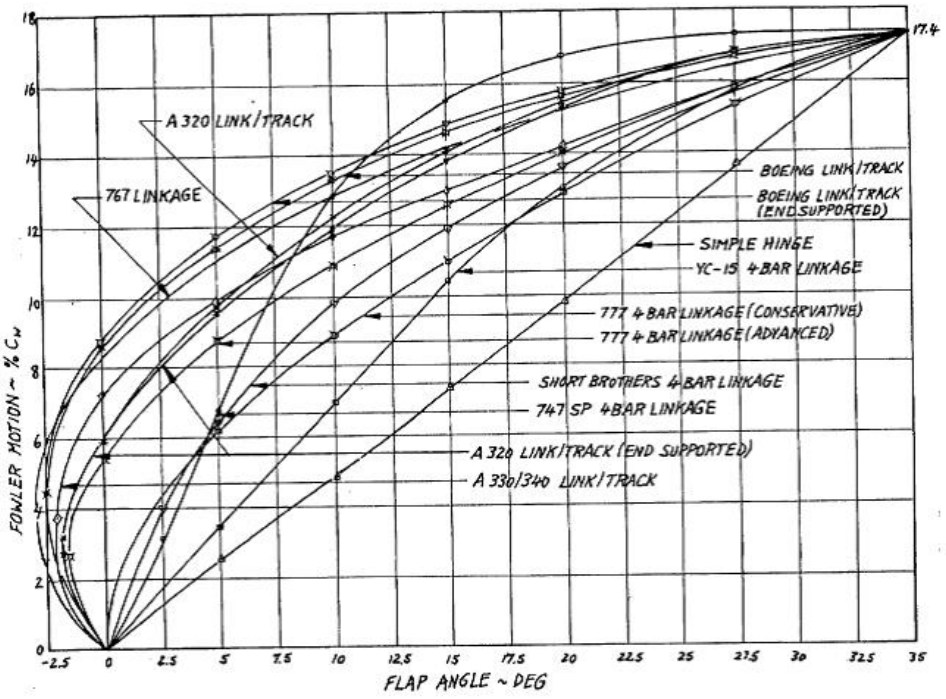

Figure 2.12: Fowler motion progression for different flap deployment mechanisms [11]

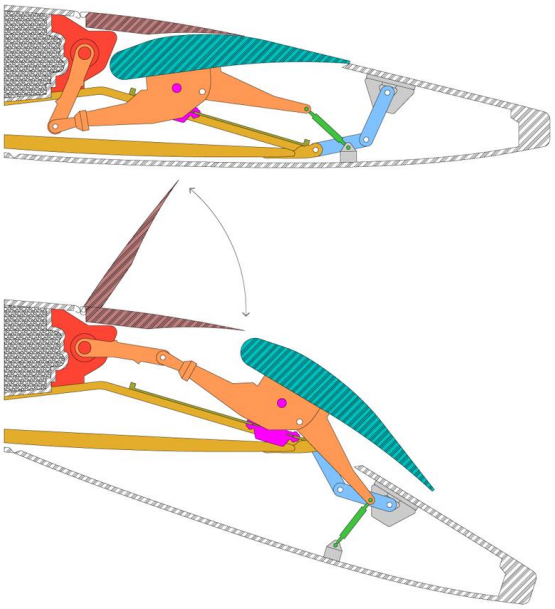

Figure 2.13: A320 Link-track flap deployment mechanism [17]

2.3 Morphing Wing Technologies

Morphing technologies have been used since the beginning of the history of aviation to change the wing planform, in order to control the airplane during flight and to obtain aerodynamic advantage. In 1903 the Wright brothers, in their first heavier-than-air machine flight, used flexible wings equipped with pulleys and cables to twist the wingtips [18], using wing warping to control the structure; few years later, in 1916, the first variable camber wing was built.

In recent years, several research programmes have been conducted having as main objective the design of a flexible wing capable to drastically change its shape but maintaining, at the same time, its structural integrity and a high aerodynamic efficiency [19], [20]. Many of the proposed solutions exploit aeroelasticity to improve aircraft performance while and different design approaches have been proposed to actuate the morphing components.

2.3.1 Active Aeroelastic Wing Projects

In 1979 the Mission Adaptive Wing (MAW) programme lead to the development of a wing with variable chord and camber, later dismissed because of high complexity, weight and limited aerodynamic performance of the morphing devices [21]. The MAW wing, shown in Figure 2.14 was one of the first examples of wing with continuously deformable leading and trailing edge, without any discrete control surface, as pointed out by Weisshaar in [22].

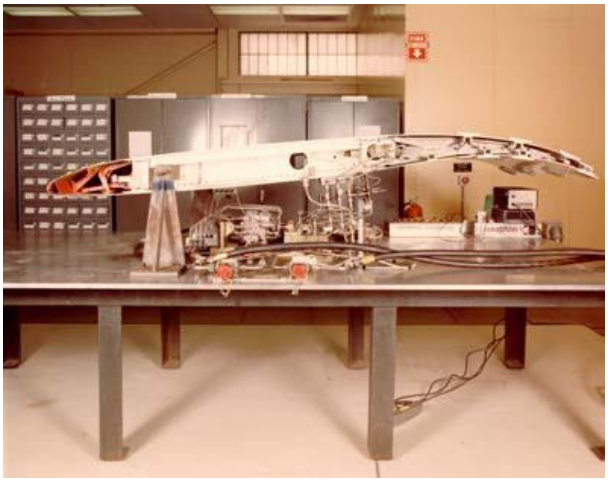

Figure 2.14: MAW airfoil cross-section in deformed position [22]

In the 1990s the Active Aeroelastic Wing (AAW) research programme by US Air Force Laboratories showed the potential benefits of wing flexibility in terms of increase in control power and drag reduction together with an enlargement of the flight envelope [23]. The aeroelastic deformation was exploited to reduce induced drag and maneuver loads and to improve the control the aircraft [24]. Later, the NASA's Morphing Project focused on structural morphing applied to micro air vehicles and on biologically-inspired flight systems [25].

Particularly important was the two-phase Smart Wing programme [26], [27], [28] by the US Defence Advanced Research Projects Agency (DARPA), in which two gapless and hingeless control surfaces for the leading and the trailing edge were designed and successfully tested on a scaled model.

Another relevant programme in the DARPA framework was Morphing Aircraft Structures (MAS), whose main objective was to extend the flight envelope of the aircraft by radical in-flight shape changes obtained trough smart actuation techniques (see [29] and [30]). In 1999 a European project called ADIF investigated the effect of variable camber at cruise condition [31]. In 2002, another project, the Active Aeroelastic Aircraft Structures (3AS) promoted studies to improve aircraft efficiency by exploiting aeroelastic deformations of the structure [32].

2.3.2 Morphing Concepts

The design of morphing structures presents several challenges due to the conflicting requirements that such structures have to satisfy. From a structural point of view, for instance, morphing wings should have high flexibility to enable shape changes, but also enough stiffness to withstand the external aerodynamic loads. A careful analysis of the trade off between these two parameters is of paramount importance to ensure a safe design. The need for both flexibility and strength is only one of the many possible examples of issues that need to be addressed in the study of morphing technologies. Barbarino et al. [35] offered a comprehensive review of morphing concepts developed over the past decades and a clear analysis of advantages and disadvantages connected to the use of morphing technologies.

Moreover, the traditional principles followed in aircraft design will have to be extended in order to enable researchers and engineers to develop new design concepts. An example of this is provided by Moorhouse, Sanders et al. in their article [33], where it is pointed out that additional parts, such as actuators, connections and moving parts, will be required in order to actuate the morphing structure, leading to an increased weight of the wing, to power consumption from the actuators and to an overall increase of the complexity of the structure. As noted in [33], however, the weight penalty of a morphing wing compared to a conventional non morphing one is not necessarily a totally negative parameter, as it contributes to the overall performance increase. Again, a careful examination of all the parameters involved is fundamental to determine whether the improved performance of a morphing wing will exceed the disadvantages of a heavier, more complicated structure.

In recent years, however, the term “morphing wings” has been referred to more significant transformations of the wing shape. As recalled in [34], the Defence Advanced Research Projects Agency (DARPA) has provided a technical definition of morphing referred to a wing as “the capability to perform either a 200% change in aspect ratio, a 50% change in wing area, a 5% change in wing twist or a 20 deg change in wing sweep”. This definition, however, does not specify in which way these changes are obtained.

Table 2.1 provides a summary of the main morphing concepts proposed over the years and offers a possible classification. Two main characteristics of the concepts are considered: the type of morphing pursued, either mechanical or through elastic deformation, and the class of air vehicles the concept can be applied to. Different ideas have been developed for

Type of Morphing	MAVs	UAVs	Commercial Aircraft
Mechanical	Wing folding Tail folding	Telescopic spar Wing folding	Variable sweep
Elastic	Piezoelectrics SMAs Wing twisting Stiffness tailoring	Piezoelectrics SMAs Wing twisting Stiffness tailoring	Eccentuator Active flexible rib Rotating rib Vertebrae like rib Belt rib

Table 2.1: Possible classification of morphing concepts

Unmanned Aerial Vehicles (UAVs) and Unmanned Combat Aerial Vehicles (UCAVs), as presented in [36] and [37], as well as for Micro Air Vehicles (MAVs), shown in [25], and for large transport aircraft (see [38], [39], [40] and [41]). It should be noted that many of the concepts present in the literature are at a theoretical stage and their feasibility has not yet been demonstrated ([42] and [43]). Moreover, morphing techniques that have proved to be successful for small vehicles cannot be transferred directly to large aircraft. On the other hand, it is interesting to study how the morphing is actually achieved. A fundamental distinction that can be done is between morphing obtained using mechanical devices and morphing obtained taking advantage of the elastic deformation of the structures.

Morphing by Mechanical Actuation
Morphing obtained through mechanical devices comprises wing sweep variation, variable span performed by using telescopic wings, wings with moving spars and wings or tail folding.

Morphing by Elastic Deformation
Morphing using elastic deformation is still achieved by using some moving part, but the change of shape is mainly associated to considerable elastic deformation. Typically, the moving parts provide the actuation needed to deflect the structural components. In the restricted field of analysis of morphing concepts through elastic deformation for large vehicles, it is possible to identify at least three groups of concepts. The first sub-type of morphing obtained by elastic deformation is represented by morphing through compliant skins internally supported. Other concepts provide a very good support to the skin but they do not allow a satisfying deformation of the morphing device. These concepts, part of the second group, are the elastomeric skin - flexcore ([44], [45]) and the belt-rib [39] concepts.

2.3.3 Active Wing Concepts

Variable sweep [22]
Mechanisms allowing a variation of the wing sweep consent to achieve good performance at both low and high speed. However, these devices are very complex and heavy and their use has been limited to military applications such as the Bell X-5, the F14 Tomcat and the F111.

Variable span [37]
Wings with variable span were initially developed for long range cruise missiles and later

Figure 2.15: Bell X-5 variable sweep wing [22]

applied to UAVs and UCAVs. According to Bae et al. in [37], an increase in the wing span significantly reduced induced drag and allowed a better control of roll motion. However, the severe aeroelastic deformation of the wing due to the high bending moments at the root required an increase in the wing bending stiffness.

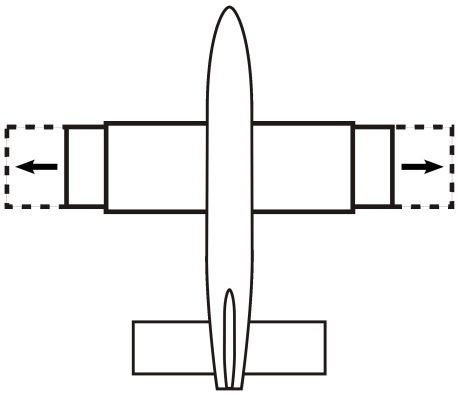

Figure 2.16: Variable span wing

Moving spar ([32], [39], [47] and [46])
Within the 3AS programme [32], a number of changes to the internal wing structure in order to control wing bending and twisting has been investigated. In particular, the amount of twist induced by aerodynamic forces is strictly connected to the position of the elastic centre of the wing section and to the torsional stiffness of the skin. The moving spar concept aimed to change the elastic centre location and the bending and torsional stiffness of a wing by changing the chordwise position of one or more spars, as shown in Figure 2.17, or by rotating the spar in the wing plane. Flight tests have shown that moving the spar allows it to act on the natural frequencies of the wing and also to control effectively the roll motion without adding any weight to the structure.

Wing and tail folding ([25], [29] and [44])
This morphing concept deals with shape changes out of the plane of the wing. For the moment only small scale models have been built to demonstrate the feasibility of the concept, whose application is limited to small UAVs and MAVs. An example of wing

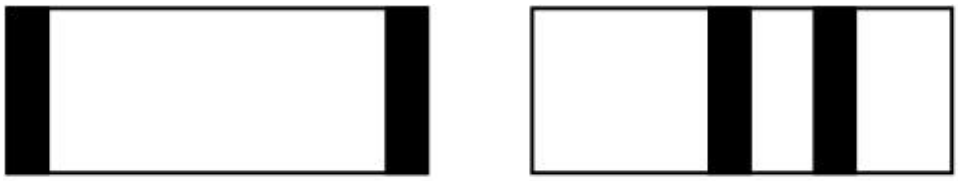

Figure 2.17: Moving spars for the control of wing torsional stiffness [46]

folding is provided by a small UAV for US Air Force missions also known under the name of Z-wing, shown in Figure 2.18.

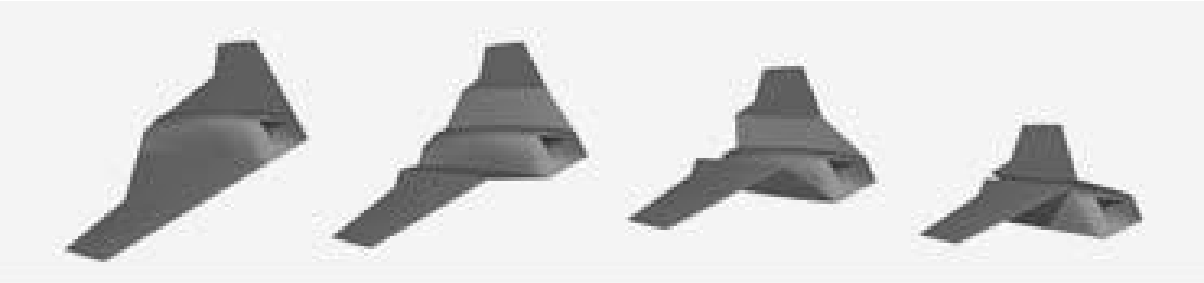

Figure 2.18: Z-wing morphing concept [44]

2.3.4 Morphing Leading Edge Devices

Dornier Droop Nose [48]
The Dornier Company developed and patented a concept for the droop nose of a transport aircraft. The internal actuation mechanism consisted of a bar located at the nose, connected to both upper and lower skins and set into rotation by an arm connected to the front spar. During the rotation, the bar allowed a change in camber and curvature of the leading edge, with beneficial aerodynamic effects.

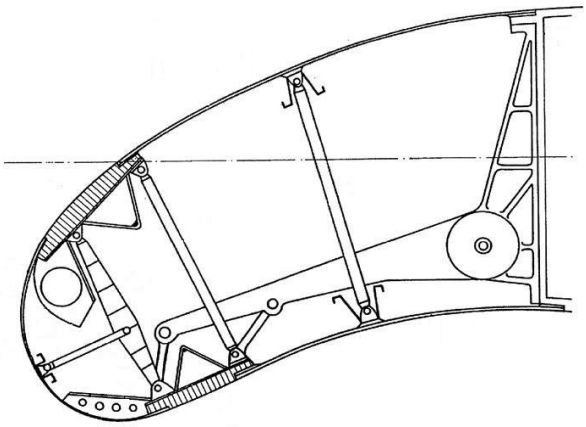

Figure 2.19: The Dornier Droop Nose [48]

Airbus Droop Nose [49]
Another concept for a droop nose was developed by Airbus to replace the conventional slat on the A380 aircraft. The concept consists of an internal mechanism composed of

hinged arms moved by rotary actuators. The droop nose is able to deflect without any gap and has achieved significant drag reduction.

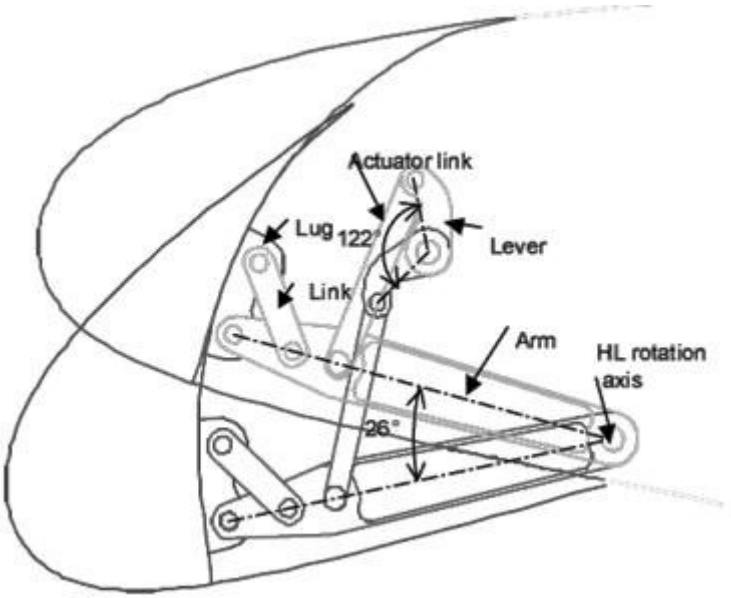

Figure 2.20: Droop Nose proposed by Airbus [49]

Boeing Discontinuous Droop Nose

In 1982 Boeing patented the design concept for a deflecting leading edge featuring a discontinuous lower skin surface. This approach was able to reduce the high strains in the leading edge skin associated with the deflection, however it reduced the structural stiffness of the nose and it required a complex internal kinematic mechanism to be actuated.

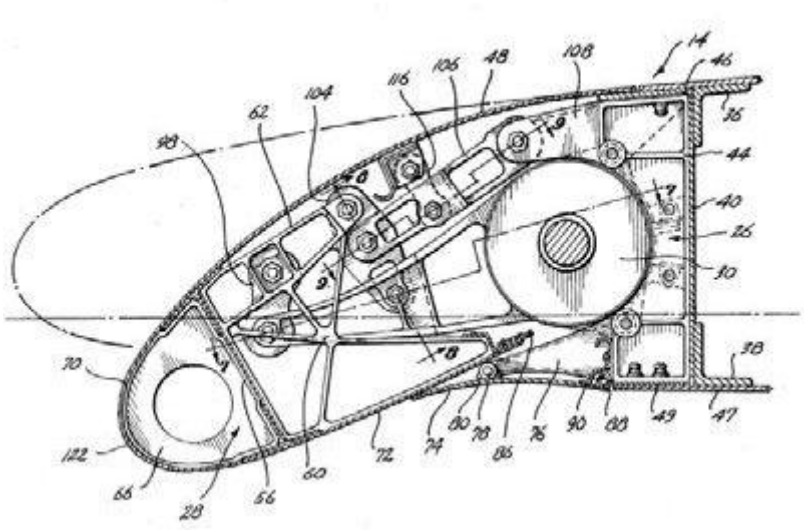

Figure 2.21: Discontinuous Droop Nose proposed by Boeing

Bent Tube Mechanism

In this concept, a bent tube located in the nose is rotated and allows to change the airfoil shape according to its curvature (see [50]). This idea is similar to the eccentric actuation principle developed within the DARPA project [26].

2.3.5 Morphing Trailing Edge Devices

As shown by Carlsson and Cronander [47] and reported by Monner [38], [41], achieving a camber variation at the trailing edge maximizes the efficiency of the shape change from a structural and aerodynamic point of view. In fact, in order to obtain an efficient control, "distributed control surfaces should be used in the regions where the effect of the surfaces is likely to be reversed in the speed envelope considered" [47].

Morphing by multi-hinge internal actuation
To the first group belong the active flexible rib (finger rib) ([38], [41]), the modified active rib (rotating rib) [40] and the vertebrae-like concepts [51]. They are all characterised by moving elements able to transfer the motion one to the other. On one hand, these concepts allow good deflection and they can also be easily implemented on large vehicles. On the other hand, the large number of moving parts reduces the reliability and increases the overall weight of the structure. Moreover, the skins have to be highly compliant and anisotropic to follow the deformation of the inner parts and some kind of support should be added to prevent bubbling of the skin itself under the action of the external loads.

Active flexible rib ([38], [41])
The active flexible rib concept (also called "finger rib") developed by the German Aerospace Centre (DLR) allows a smooth chordwise as well as spanwise differential camber. As shown in Figure 2.22, the conventional inflexible rib was replaced by active plate like elements connected to each other with revolute joints. An actuator starts the rotation of the driven segment and the motion is then transferred gradually from element to element. Linear slide bearings ensure the connection between the rib segments and the upper and lower skins.

Rotating rib [40]
This morphing concept is very similar to the active flexible rib. The concept is illustrated in Figure 2.23: the final part of the rib can rotate with respect to a hinge and the upper and lower skins, connected to the rib by means of some linear slides, can glide over the rib contour. At the trailing edge, upper and lower skins are not rigidly connected but they are allowed to glide into a slide bearing. Unfortunately, a large amount of torque is required to obtain the desired rotation of the rib and to make the skins slide gaining friction forces. Other disadvantages include the slow actuation velocity and the small camber variations obtainable.

Vertebrae like elements [51]
Some vertebrae-like units, connected along their axis of symmetry, have been proposed instead of plates in order to reduce the weight penalty and to provide enough space to accommodate the actuation system. Push-pull rods and rotary actuators were proposed to generate the motion.

All composite, electric, hinged trailing edge [52]
An hinged trailing edge design has been proposed by Wildschek et al. [52] for the flaps and ailerons of a Blended Wing Body (BWB) aircraft. A system of hinges distributed chordwise and connected to the skin stringers is able to deflect the composite trailing edge skins. The device is powered by an electric actuator and provides both the flap and aileron modes at the same time.

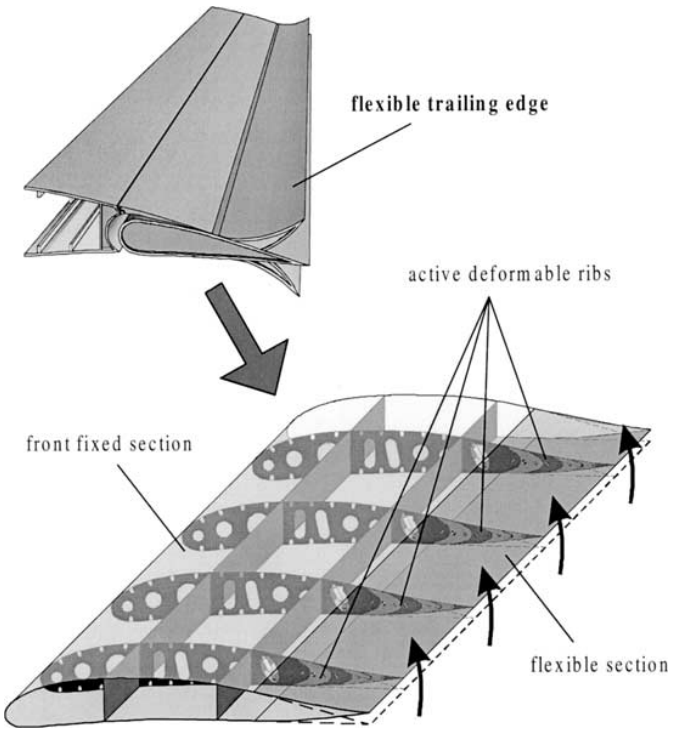

(a) Active deformable ribs to achieve spanwise differential camber capability

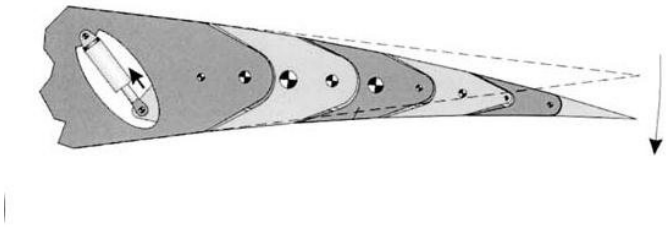

(b) Detail of the trailing edge

Figure 2.22: Active flexible wing concept [38], [41]

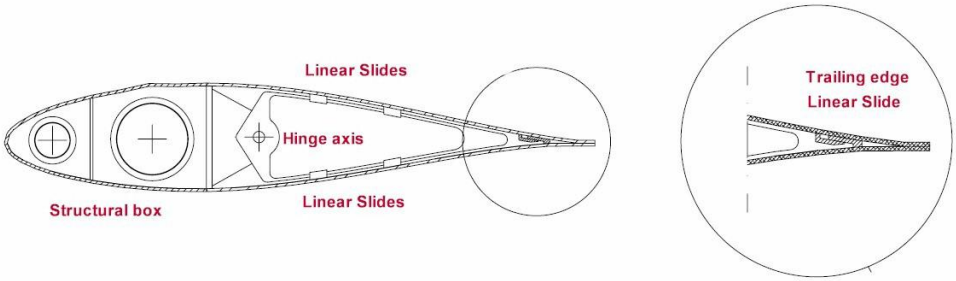

Figure 2.23: Rotating rib [40]

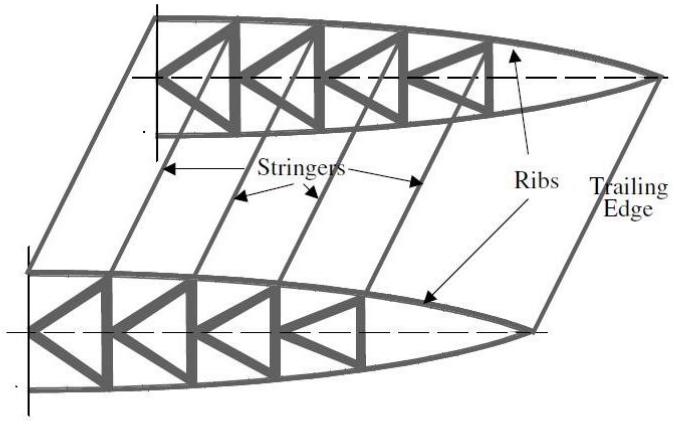

Figure 2.24: Vertebrae-like elements [51]

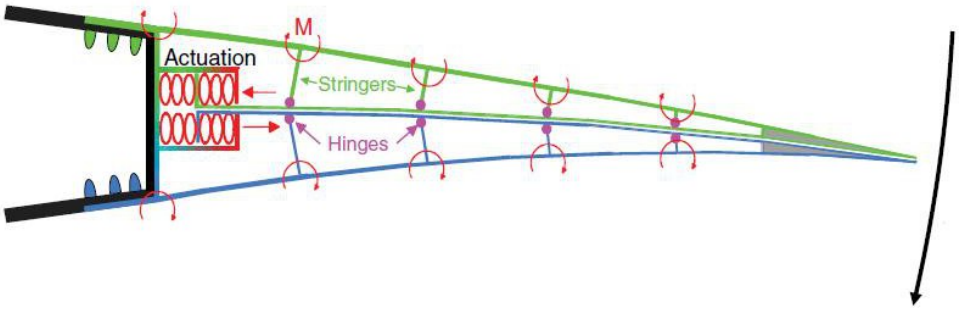

Figure 2.25: All composite, electric, hinged trailing edge flap for Blended Wing Body aircraft [52]

Morphing by eccentric actuation

A morphing device capable of providing both a powerful actuation system and enough support for the skins is represented by the eccentuator, first mentioned in [27], [44] and [45]. This concept was originally proposed by Musgrove ([53], [54]) and subsequently developed within the DARPA project [26]. The eccentuator is a bent beam able to convert a rotary input motion into a vertical and lateral translation at the output end. The beam is connected to rectangular plates which push the skin up or down and deflect the trailing edge to the desired shape, as shown by Bartley-Cho et al in [27]. It is possible to control structural bending and twisting simply by changing the direction of rotation of the beam. Figure 2.26 presents an example of trailing edge actuated by eccentuators and illustrates its working principle. This system offers the advantage that the actuator and the substructure share the external loads.

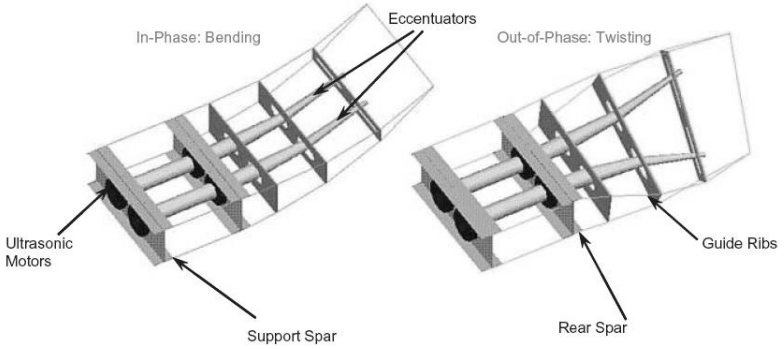

Figure 2.26: Morphing by eccentric actuation [27], [44] and [45]

In the ADIF Adaptive Wing Project, mentioned by Stanewsky [31] and discussed in detail by Muller [55], a horn-shaped arm was adopted to deflect the trailing edge of a large wing. In this case, the load transfer from the actuator to the skins was ensured by a series of spanwise webs at different chordwise locations. The horn was positioned in holes created in the webs and both the webs and the horn contributed to the stiffness of the trailing edge structure (see Figure 2.27).

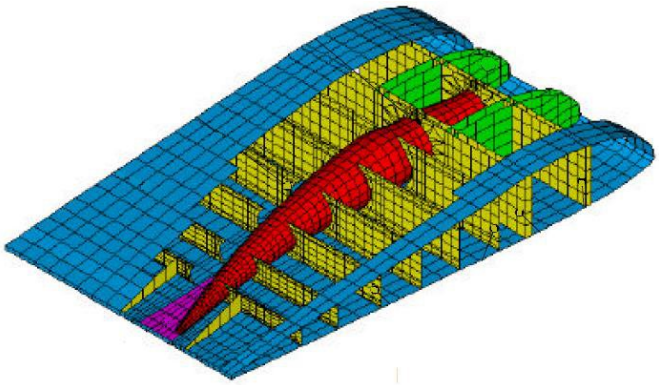

Figure 2.27: Horn concept from the ADIF Adaptive Wing Project [55]

Another application of the eccentuation principle was provided by Perera and Guo in [56] for the design of a hingeless flexible wing trailing edge for a small air vehicle.

Morphing concepts using elastic flexible materials

The use of advanced materials for morphing structures is a wide topic which will be

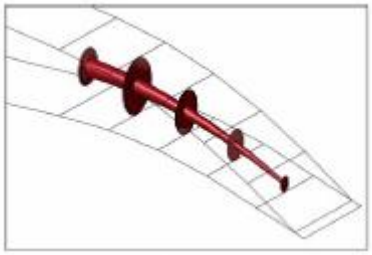

Figure 2.28: Eccentric beam actuation system for a small air vehicle [56]

addressed in the next Section 2.4. In this paragraph, some interesting morphing concepts reviewed by Thill et al. [44] and Ghandi et al. [45] and relying mainly on their flexible skin materials to achieve the desired deflection are presented.

Elastomeric skin - flexcore ([44], [45])
A device consisting in a flexible sandwich structure for the trailing edge is shown in Figure 2.29. A fibreglass laminate was used as inner part to attach the aluminium tip and the actuation system. An aramid honeycomb core provided the required stiffness in thickness direction and supported the silicone skin.

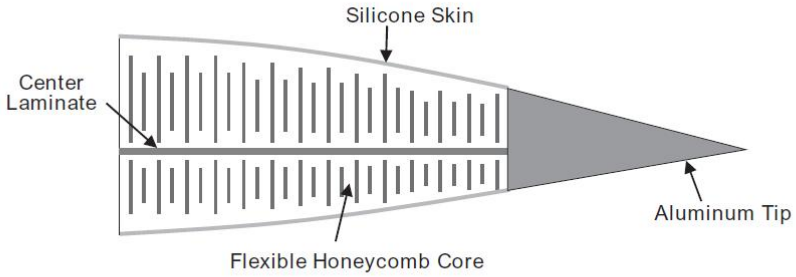

Figure 2.29: Elastomeric skin - flexcore [44]

Belt rib [39]
The belt rib concept was proposed within the ADIF Adaptive Wing Project by Campanile et al. ([39], [31]). Its main advantage consists in eliminating the moveable parts to realize camber variations using only flexible elements distributed through the wing section. The conventional rib was replaced by a closed belt like shell reinforced with some stiffeners, as illustrated in Figure 2.30. The stiffeners were connected to the belt by hinges. Morphing is achieved without moving any mechanical part.

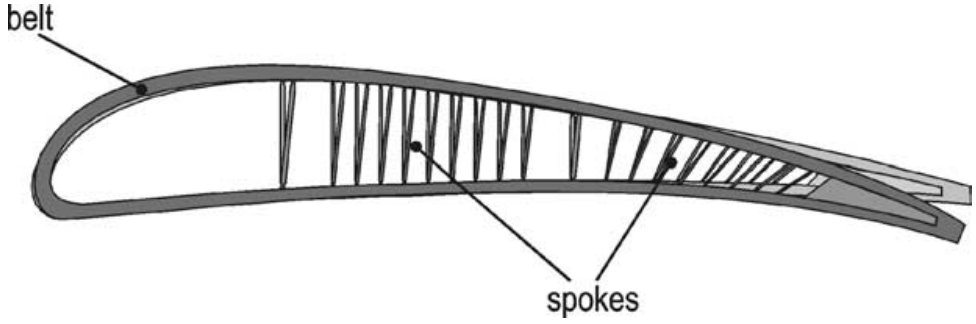

Figure 2.30: Belt-rib concept [39]

2.4 Morphing Skins

Morphing structures require special skins with highly anisotropic characteristics to comply with the deflection required, usually in chordwise direction, while ensuring the structural strength of the morphing parts is not compromised. Kikuta [57] first outlined the requirements for the skins of morphing wing structures. These are:

- high flexibility in chordwise direction to allow low force actuation
- moderate stiffness in spanwise direction to withstand aerodynamic loads
- toughness
- high strain capability and high strain recovery rate
- resistance to different environmental conditions, to abrasion and chemicals
- fatigue resistance

Gandhi et al. [45] showed that the ideal skin for chordwise morphing wings should have a low in-plane axial stiffness and a high out-of-plane flexural stiffness. In [45] they also established a lower limit for the axial stiffness as the value beyond which the deflection due to the aerodynamic load alone is no longer acceptable. A high flexural stiffness, on the contrary, is required to prevent excessive deformation, local bending or "bubbling" of the skin between the supporting points. In some cases elastomers have been proposed as skin materials.

Composite materials, which have already been used on conventional non morphing parts of the aircraft, have a good potential as morphing skins due to the possibility to tailor their mechanical properties based on the design requirements. To further enhance the morphing capabilities of a structure, other types of material have also been introduced and tests conducted on demonstrators have shown promising results.

In the DARPA Smart Wing Programme [27] a flexible silicone skin supported by a honeycomb flexcore was adopted. The inner honeycomb structure provided the necessary out-of plane stiffness while the flexible skin allowed high deformation under small loads. Unfortunately, as outlined by Thill et al. [44], elastomers exhibit several negative properties (elastic properties variable with strain, strain rate and temperature and also viscoelasticity, i.e. strain is time dependent) that make them not suitable to carry high aerodynamic

loads and to transfer them to the underlying support structures. Other materials proposed for morphing purposes are the auxetic materials, reviewed in [45] and [44], characterised by a negative Poisson ratio (they become wider if stretched and vice-versa). Auxetic materials have been used to enhance properties of conventional composites or as filling materials.

A very promising type of material for future aircraft structures are the Fibre Metal Laminates (FML), investigated by Botelho et al. in [58] and consisting of thin, high strength aluminium alloy sheets alternately bonded to plies of fibre-reinforced epoxy adhesive . They provide an ideal combination of properties of metals and composites and allow a substantial weight saving if compared to current metallic structures. Moreover, they exhibit good fatigue behaviour, damage tolerant properties and resistance to corrosion [58].

2.4.1 Composite Materials for Aircraft Structures

Composite materials are characterized by a high specific strength and show the potential for a considerable weight reduction for aircraft structures. Moreover, they can be engineered so to have specific material properties along the desired directions, in order to better adapt their structural behaviour to the design requirements.

The use of composites in the aviation industry is relatively recent. One of their first applications was for the empennages of the F14 and F15 fighters in the late 1960s. Subsequently, composites were adopted on the secondary structures of many civil aircraft, allowing weight savings of the order of 40%. Today their use has extended also to primary structures such as wings and fuselages. Composite materials, for instance, constitute almost 50% of the Boeing 787, with average weight savings of 20%.

The full potential of composite materials, however, is still not exploited in current aircraft structures. The reason for this lies in the fact that composites are relatively young materials and many aspects of their structural behaviour remain uncertain despite the large number of studies which have focused on composite structures in recent years. Rather than simply replacing the metallic alloys, composites materials require a review and an extension of the design principles to include aspects not encountered in the analysis of isotropic materials. The uncentainity in the use of composites is strictly connected to the high number of factors that affect their structural behaviour and make the modelling very complicated. The laminate stacking sequence, for instance, is an important design parameter as it significantly influences the overall laminate structural properties and the magnitude of the interlaminar normal and shear stresses. Moreover, the choice of the combination of fibers and resins and manufacturing issues must all be carefully evaluated. The fracture behavior of composites is not yet well understood and modelled if compared with the problem of fracture in metals and the fatigue life of the composite is a very complex process which involves several damage modes, including fiber/matrix de-bonding, matrix cracking, delamination and fiber fracture. The complexity of the design process, however, is widely compensated for by the mass savings and improvements that composite materials can offer.

In addition to the favorable high specific strength and stiffness, fibre reinforced composite materials offer the possibility to achieve a desirable aeroelastic behaviour by acting on

the fibre orientation with minimum weight penalty. Several applications of the composite skin tailoring to the optimisation of the laminate stacking sequence to obtain a desirable aeroelastic behaviour have been proposed ([31], [33], [59]). The most notable examples of this are the increase of the divergence speed of a forward swept composite wing, presented in [21] and [60], and the use of the elastic coupling produced by unsymmetrical laminate layups to act on the dynamic aeroelastic behavior of a composite wing, as discussed by Iannucci and Fontanazza in [62]. Guo in [61] has investigated an optimal design for an aerobatic aircraft wing structure to meet lightweight, strength and aeroelastic design requirements.

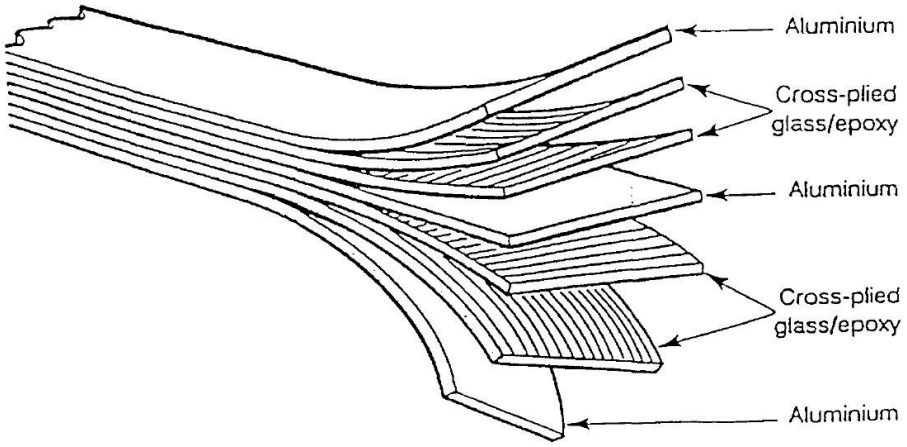

Figure 2.31: Build-up of a cross-ply GLARE laminate

Hybrid solutions have been also proposed to exploit the advantages of both metallic and composite materials. A new class of materials, called Fibre-reinforced Metal Laminates (FML) has been developed to have high strength in the direction of the fibres and to benefit from the tensile properties of the metal in the transverse direction. The most famous example of FML is represented by GLARE (glass reinforced aluminium laminate), which is composed of thin aluminium sheets bonded together with prepreg sheets of high-strength glass fibers. As shown by Wu and Yang [63] and by Asundi and Choi [64], GLARE offers very good fatigue resistance, high fracture resistance and a desirable impact behaviour while allowing weight savings of between 15% and 30% over aluminium alloy.

2.4.2 Smart Materials for Active Actuation

Smart materials can be used as actuators to induce the desired deformations of the structural components. The most common types of smart materials are piezoelectric materials and shape memory alloys.

Piezoelectric materials ([65], [66])
Piezoelectric materials show the property to undergo a certain degree of deformation when subjected to an electric field. These materials have an inner structure constituted by electric dipoles arranged in random directions. During the manufacturing process it is possible to align these dipoles trough a process called poling, in order to obtain the desired macroscopic deformation when electrically excited. A schematic representation of their behaviour is given in Figure 2.32. Piezoelectric materials are a very promising class

of actuators due to their light weight and their versatility. Their use has been however limited only to small application because of their brittleness, low tensile strength and also because they exhibit a shift from linear response to hysteresis when the excitation level is increased above a certain threshold.

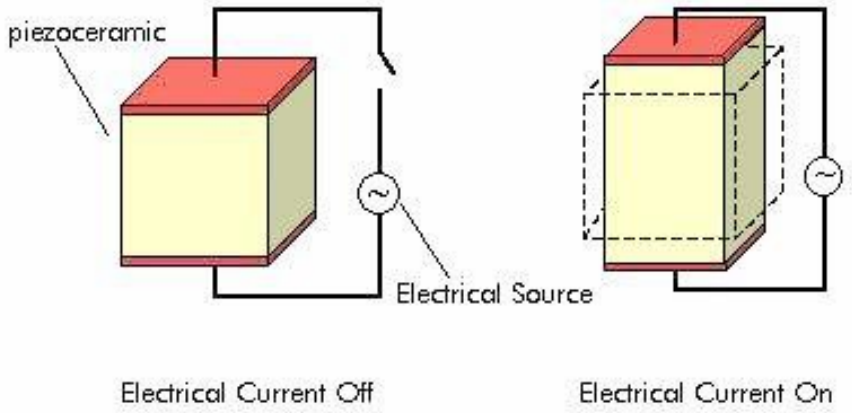

Figure 2.32: Behaviour of piezoelectric materials

Shape memory alloys [65]
Shape memory alloys (SMA) exhibit the interesting property of remembering a certain deformed shape and to recover that shape at high temperature. SMAs undergo a phase transformation in solid state, which means that although both the initial and final phases of the transformation are solid, a change to their crystallographic structure has taken place (see Figure 2.33). The phase change is triggered by a change of temperature or by applying a mechanical load. This capability has been exploited to develop some internal actuators embedded in the structure, with good performance in terms of small size, light weight and possibility to undergo cyclic loading.

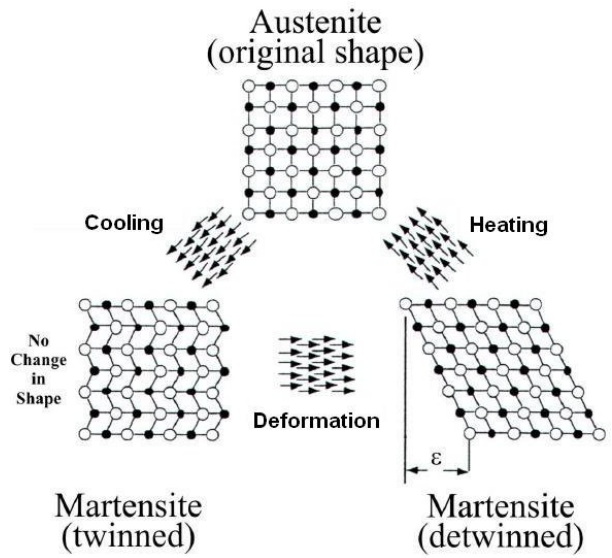

Figure 2.33: Shape Memory Effect in Shape Memory Alloys

The main disadvantages presented by SMAs include the possibility to be used only within some ranges of temperature and the need to heat them to perform the morphing with consequent high energy consumption. Moreover, SMAs are not suitable for those applications requiring a fast response time.

Berton [67] has shown the possibility to apply SMAs to the shape control of the trailing edge of a UAV. Keefe and Carman [68] have shown that it is possible to manufacture SMA torque tubes able to replace rods and have investigated the thermo-mechanical response of the alloys. The use of SMAs has been investigated also as part of the SADE project [93], however the idea has been abandoned due to the limited performance of SMAs for the morphing of a large vehicle. A similar investigation has been conducted also by Barbarino et al. [69], who conceptually studied the possibility to use SMA to build the internal architecture of a flap with variable camber capabilities for a larger aircraft and offered useful design guidelines.

2.5 Interactions between Aerodynamics and Elastic Bodies

2.5.1 Aeroelasticity

According to Bisplinghoff et al. [70], aeroelasticity is "the science that studies the mutual interaction between aerodynamic, elastic and inertial forces, and the influence of this interaction on airplane design".

Aeroelasticity represents a key discipline in the field of aircraft design because the interaction between the wing structure and the surrounding airflow can potentially lead to significant off-design effects or to catastrophic failure of the aircraft.

Two classes of aeroelastic phenomena can be identified: static and dynamic. Static aeroelastic phenomena arise from the interaction between the elastic forces acting on the structure and a steady state aerodynamic field. The most common examples of static aeroelastic effects include the redistribution of the aerodynamic load over the wing, but also torsional divergence of the wing and control reversal. Dynamic aeroelastic phenomena, on the other hand, involve not only aerodynamic and elastic forces, but also the inertia of the structure. They have the effect to induce oscillations in the structural components, which could be critical if the frequency of the oscillations approaches the structural natural frequency. Flutter, buffeting and dynamic response are all examples of dynamic aeroelastic effects. The basic aeroelastic principles and effects mentioned above are discussed in many textbooks (see Bisplinghoff et al. [70], Fung [71], Dowell [72] and Megson [73].

Aeroelastic phenomena are strongly dependent on the structural stiffness of the wing and, for conventional wing structures, a stiffness increase represents a common way to reduce negative aeroelastic effects. When dealing with morphing wings, conversely, since the structural stiffness has been deliberately reduced in order to perform a specified shape change, aeroelastic effects become predominant. Many studies have been conducted to correctly model the aeroelastic behaviour of morphing components. Battoo in 1999 published an interesting review of the most relevant papers dealing with aeroelasticity and

its applications [74] and smart morphing devices occupy a relevant part of the list.

In the past, aeroelastic phenomena such as divergence, flutter, control reversal and changes in the load distribution have caused undesired aircraft behaviour during flight or even catastrophic effects and structural failure. For these reasons, for a long time aeroelastic effects have been seen as purely negative for the structure.

2.5.2 Aeroservoelasticity

According to the definition provided by Wright and Cooper [75], aeroservoelasticity is the discipline that "extends the study of the aeroelastic interaction between aerodynamic, elastic and inertial forces to include control systems".

As pointed out by Noll [76], one of the first programs devoted to the study of the aeroservoelastic interactions of an aircraft was the Active Flexible Wing (AFW) program, initiated at the NASA Langley Research Centre in 1985. The main goal of this project was to demonstrate that the integration of active controls with a highly flexible and aerodynamically advanced wing design was able to enhance the aircraft performance as well as to increase stability and reduce structural weight [76]. Some of the areas of investigation included flutter suppression and rolling manoeuvre load alleviation [77].

As a result of these early studies, modern commercial vehicles are nowadays normally equipped with flight control systems to improve flight performance and stability, as well as devices to alleviate gust and manoeuvre loads. These control systems usually include some sensors and a control input, applied via the control surfaces.

In order to predict the behaviour of the coupled aeroservoelastic system with a good degree of accuracy, a detailed representation of the flexible structure, of the steady and unsteady aerodynamic forces acting on it and of the control system is required. In [78], Librescu et al. investigated the dynamic aeroelastic response of a composite wing modelled as an anisotropic thin-walled beam and a new control approach was developed to perform active suppression of flutter and other aeroelastic instabilities. Azoulay and Karpel in [79] reviewed and compared various methods to evaluate gust response of an aeroservoelastic system.

One of the main concerns of a safe aeroservoelastic design is to avoid any form of coupling between the structure and the control system. In fact, if the sensors detect not only the rigid body motions of the structure but also the flexible ones, these vibrations are fed back into the control system and they can affect the input given via the control surfaces, which in turn can act on the flexible modes, causing the aircraft to vibrate further and leading to unstable behaviour as explained by Wright and Cooper in [75]. Moreover, nonlinearities arising in the structure and in the control surfaces have required the development of models capable to take into account nonlinear effects. Gold and Karpel in [80] presented a methodology to obtain the aeroservoelastic equations of motion with large local structural nonlinearities for a UAV with control surface freeplay. Dimitriadis and Cooper in [81] successfully designed a nonlinear control law to increase flutter speed of a simple nonlinear aeroservoelastic system. They also found that moderate friction could improve the stability of the system and induce limit cycle oscillations instead of flutter.

The use of smart structure technologies can strongly affect the dynamic stability and response of the aircraft. Moulin and Karpel in [82] and [83] showed that if piezoelectric actuators are embedded into the structure to achieve morphing, nonlinear effects due both to the actuator response and to the mechanical connections between actuators and structure might arise.

2.5.3 Nonlinear Effects

Classical theories for the study of the various aircraft components usually assume linear aerodynamics and structures. However, in some cases, nonlinearities present in the aircraft can significantly affect the dynamic behaviour of the aeroelastic system and a nonlinear model is of paramount importance to fully understand the characteristics of the deflection ([94], [95]).

Nonlinearities present in an aeroelastic system can arise from aerodynamic, inertia or structures [94]. Shock waves, viscosity, separated flow, turbulence and transonic flows cause aerodynamic nonlinearities, while fuel consuming or fuel sloshing cause inertial ones. Structural nonlinearities generally arise from worn hinges of control surfaces, loose linkages or from material behaviour. However, it is very difficult to predict their presence even though the materials and the moving parts present in the structure are known. Structural nonlinearities can be divided into distributed or concentrated ones ([94], [95], [96]). The first ones depend on the elastodynamic deformation of the whole structure, while the second ones usually act locally in the moving parts of a mechanism or a linkage. Another cause of nonlinearities is solid friction. The most common types of structural concentrated nonlinearities are freeplay, friction, hysteresis and springs with a hardening or softening behaviour. Freeplay nonlinearities usually occur in control surfaces or parts with loose connections. Outside a specific dead zone (zone 2 in Figure 2.34), the control surface hinge moment is proportional to the rotation angle depending on the stiffness of the system. If the rotation angle falls inside the dead zone, the hinge moment is zero and the control surface is free.

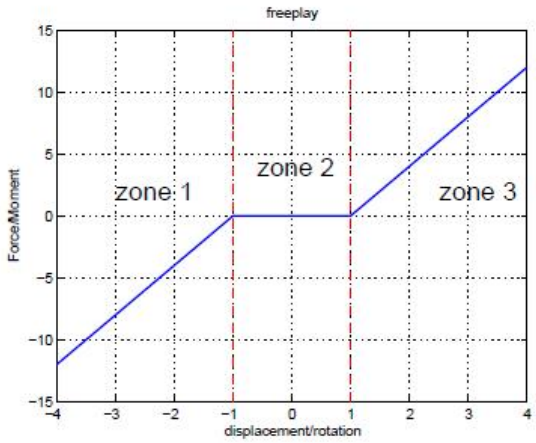

Figure 2.34: Freeplay nonlinearity [96]

In case of friction nonlinearities (Figure 2.35), the system is characterized by a threshold

value for the force that keeps two bodies in contact. This nonlinearity is often present in rotating joints and cable guides.

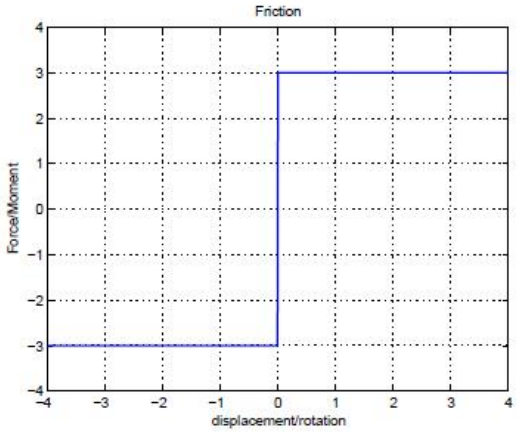

Figure 2.35: Friction nonlinearity [96]

Hysteresis nonlinearities show four different linear profiles for the moment when the rotation is changed. Outside of the hysteretic cycle ABCD shown in Figure 2.36, the restoring moment is linear with two different linear branches. As the displacement is increased, the restoring moment switches from one linear branch to the other via constant linear branch BC. On the other hand, if the displacement is decreased, the moment goes back to the first linear branch via a different constant linear branch DA. This type of nonlinearity causes a gain or a loss of stiffness of the system when the displacement is changed.

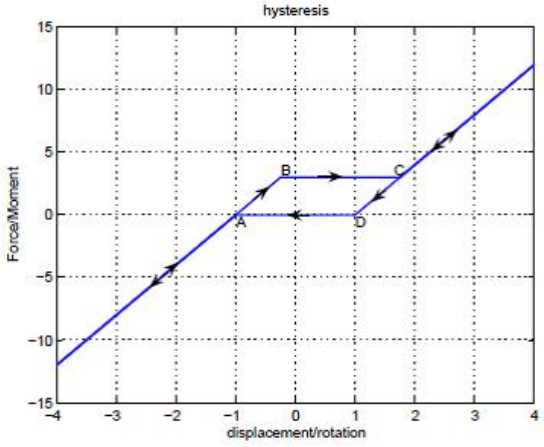

Figure 2.36: Hysteresis nonlinarity [96]

Thin wings and propeller blades will likely behave as a cubic hardening spring (see Figure 2.37) when twisted, with their stiffness increasing as the angle of twist increases.

Among all the structural nonlinearities, freeplay and hysteresis are usually the most dangerous ones, because they can trigger the appearance of limit cycle oscillations (LCOs) in the aeroelastic behaviour of control surfaces ([97], [98], [99], [100]). As reported by Lee and Price [94], LCOs were recently the main cause of the high vibration level in the aft

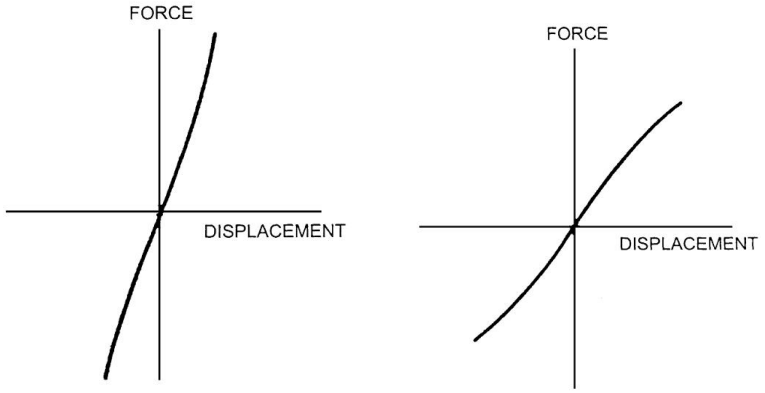

(a) Hardening behaviour (b) Softening behaviour

Figure 2.37: Nonlinear spring behaviour [94]

cabin of the Model A320 series airplanes, and the Model B737 also exhibited vibration of the aileron tabs due to freeplay.

2.6 Structural Design Optimisation

Structural optimisation methods have been traditionally employed in the aerospace industry with the primary objective to minimize the structural weight without compromising the load carrying capability of the structure. Vanderplaats in his paper "Thirty years of modern structural optimisation" [84] offers a review of the history of structural optimisation and details the most valuable moments of the development of this discipline.

In the 1950s, the basic approach adopted for the structural optimisation of aircraft components was the so-called "simultaneous failure design optimisation" method. The idea was to size the structural components so that several failure modes became critical simultaneously and, based on a careful choice of the constraints, this often resulted also in a minimum weight design. In his review papers, Vanderplaats [84] and Gartmeier [85] mention an earlier study conducted by Schmit in 1960, "Structural Design by Systematic Synthesis", which is considered a landmark of modern structural optimisation. As Vanderplaats recalls in [84], Schmit for the first time showed that full stressing of a structural component is not necessary in order to achieve an optimum minimum weight design. This notion gave new impulse to the research into structural optimisation. Schmit also introduced the idea to couple the finite element method with mathematical nonlinear programming to obtain the accurate solution of a wide range of structural optimisation problems. Unfortunately, due to the long computational times required for such analyses, coupled methods were deemed unpractical. Other methods, such as the optimality criteria methods and fully stressed concepts continued to be used between 1960 and 1970. Both the approaches of optimality criteria and mathematical programming used gradient-based methods. The optimality criteria methods can deal with a large number of design variables but only a limited number of constraints. The mathematical programming school, on the other hand, used some classical gradient-based methods and suffered from the high computational cost of each iteration. To increase the computational efficiency of these methods, several approximations were proposed for stress constraints and

displacement response functions in order to reduce the number of iterations needed to reach the optimum, leading to the so called "Formal Approximation Concepts" [84].

The progress in computer science achieved in the 1070s and 1980s and the wide diffusion of design software based on finite elements method, such as NASTRAN, contributed to the development of the modern structural optimisation discipline. The finite element analysis of the structure and the accurate evaluation of displacements and stresses gave the possibility to extend the optimisation process also to large, complex structures. A variety of design packages combining optimisation and finite element methods were implemented, as reviewed by Sikiotis et al [86]. The ADS/NASOPT software coupled the ADS optimization subroutine and the NASTRAN structural solver. Other similar packages included CSAR/OPTIM, CSAR/SIZING, NISAOPT, STARS, STARSTRUC. Balling [87] in 1986 has presented a variety of methods to interface analysis software to optimisation software. Vanderplaats has conducted extensive studies on design optimisation [88] and on methods to automate the calculations. In particular, in his report "ADS - A Fortran program for automated design synthesis" [89], he presented a general purpose optimisation subroutine which can be used as an optimisation tool for a variety of structural optimisation problems.

Nowadays multidisciplinary design optimisation (MDO) is commonly applied to structural aircraft design to find the optimal solution for a combination of problems, involving several relevant disciplines at the same time rather than a sequence of subsequent problems.

In recent years, the introduction of innovative techniques to enhance aircraft performance has further increased the complexity of the design process and new objectives, other than weight minimisation, have to be considered in any structural optimisation process.

For morphing wing structures, the objective of the optimisation procedure is not only the minimisation of the structural weight but also the achievement of a target deflected shape, possibly with minimum actuation, under stress constraints. The development of new optimisation procedures integrated with a detailed study of the structural behaviour is hence required for the optimisation of morphing structures.
Friswell et al. [90] have given an overview of the techniques applicable to optimise morphing structures, focusing on the aeroelastic tailoring of a composite skin. They also introduced the idea of using a hierarchical approach, modelling the structural problem using different scales and showing that the optimisation of the lower levels contributes to the high level structural optimisation.

Skillen et al. [91] investigated the possibility to accurately predict the weight of a morphing wing in the early stages of design for structural optimisation purposes, showing that many uncertainties arise on the prediction of the actuation system weight and on the identification of the failure modes. From 2010, the European project OMSAMA (Optimisation of Multi-scale Structures with Applications to Morphing Aircraft) [92] is studying innovative methods for the optimisation of morphing structures based on the combination of models having different fidelities. This will allow a more accurate design and evaluation of the benefit introduced by morphing technologies.

CHAPTER 3

Theoretical Background

This chapter introduces the structural analysis methods underlying the study presented in this thesis. The complete derivation of the theories applied to the study of modern aircraft structures can be found in many textbooks and is outside the scope of this chapter, which intends to offer a brief outline of the approach and assumptions adopted.

Aircraft structures present many peculiar characteristics if compared to to other structures for civil applications. The need to achieve high strength and durability while maintaining a low weight has led to the use of shell structures stiffened by additional structural elements, while the introduction of composite materials has further contributed to increase the specific strength of aircraft structural components. Section 3.1 introduces the use of the thin walled theory and the application of classical laminate theory for the analysis of aircraft components under different types of loading. The use of the finite element method (FEM) for the accurate computation of deformations and stresses in the structure is discussed in Section 3.3. Finally, the aerodynamic theories for the calculation of the in-flight loads are presented in Section 3.4.

3.1 Structural Analysis of Composite Aircraft Components

Aircraft structures have the role to maintain an aerodynamic shape and to resist the loads encountered during the flight and on the ground, while at the same time providing a safe environment for the passengers and the payload of the aircraft.

There are two classes of loads to be considered during the operative life of an aircraft: *ground loads*, experienced during movement and transportation on the ground, and *air loads*, which are generated during flight by the air pressure distribution over the aircraft surfaces, by manoeuvres and gusts. As a result of the air loads generated by the differential pressure distribution on the aerodynamic sufaces, and of concentrated loads coming from the presence of actuation devices, engine attachements and many other elements,

the aircraft structures are subject to bending, shear and torsion loads, often combined one to the other.

In the modern approach, two types of design have been used for aircraft structures: *monocoque* structures, which rely entirely on their skins to resist the loads, and *semi-monocoque* structures, where the skins are supported by longitudinal and transverse stiffening members. Each structural component has a specific role and contributes to the overall load carrying capability of the aircraft. The wing skin forms an impermeable surface so that the wing is able to generate lift and transmits the loads generated by the aerodynamic pressure distribution to the other structural components, mainly the ribs, the spars and the stringers. The skins and the spar webs contribute to resist the shear and torsional loads, while the skins and stringers react the axial and bending loads. Stringers are attached to the skins in order to increase the buckling load by dividing the skins into smaller panels, rather than increasing the thickness with consequent weight increase.

3.1.1 Analysis of Thin Walled Structures [73]

Aircraft components can be considered as "thin walled structures" since their thickness t is considerably smaller than the cross-sectional dimensions. The theory of thin walled beams is based on a series of assumptions:

- the beam cross sections are assumed rigid in their own planes but are allowed to warp out of their original planes. This statement is verified for aircraft structures since the presence of transverse stiffening members such as the ribs allows to maintain the cross-sectional shape.
- the transverse shear strains are uniform over the cross-section
- the wall thickness of the structure is small compared to its radius of curvature

Moreover, the small thickness of the walls allows to make some simplifying assumptions in the study of the stresses and deflections under the applied loadings:

- the stresses are considered to be constant across the thickness
- squares and higher powers of t are neglected

3.1.2 Bending of Open and Closed Thin Walled Sections of Beams [73]

A beam of arbitrary cross section is considered, and a system of coordinates axes xy having its origin in the centroid C of the cross section is defined. When the beam is subject to bending moments M_x and M_y about the axes x and y, it will bend about its neutral axis. We consider an element of area δA at a point (x, y), located at a distance ξ from the neutral axis. If α is the inclination of the neutral axis to the reference coordinates system, then

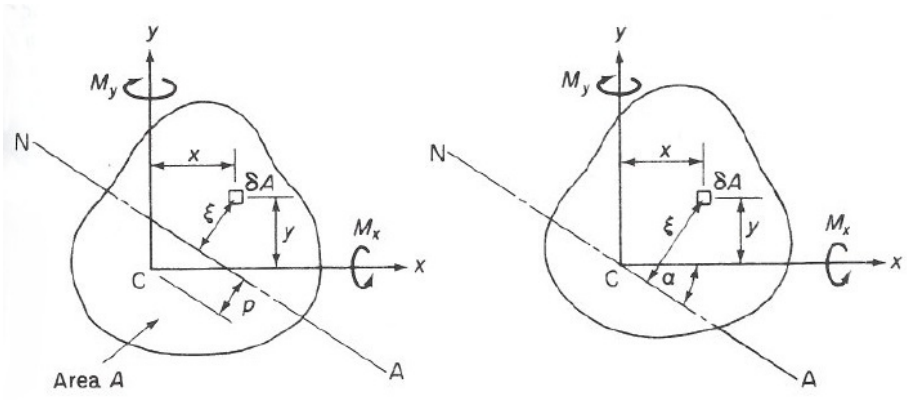

Figure 3.1: Determination of stresses due to bending [73]

$$\xi = xsin\alpha + ycos\alpha \tag{3.1.1}$$

The stress σ_z arising over δA is:

$$\sigma_z = E\epsilon_z \tag{3.1.2}$$

and

$$\epsilon_z = \frac{\xi}{\rho} \tag{3.1.3}$$

where ρ is the radius of curvature of the beam about the neutral axis.

Hence,

$$\sigma_z = \frac{E\xi}{\rho} = \frac{E}{\rho}\left(xsin\alpha + ycos\alpha\right) \tag{3.1.4}$$

The moment resultant of the stress distribution is equal to the applied moments, hence:

$$M_x = \int_A \sigma_z y dA \tag{3.1.5}$$

and

$$M_y = \int_A \sigma_z x dA \tag{3.1.6}$$

Remembering the definition of the second moment of area

$$I_{xx} = \int_A y^2 dA \qquad I_{yy} = \int_A x^2 dA \qquad I_{xy} = \int_A xy dA$$

and substituting the expression 3.1.4, we obtain the moments M_x and M_y as:

$$M_x = \frac{Esin\alpha}{\rho} I_{xy} + \frac{Ecos\alpha}{\rho} I_{xx} \tag{3.1.7}$$

and

$$M_y = \frac{Esin\alpha}{\rho} I_{yy} + \frac{Ecos\alpha}{\rho} I_{xy} \tag{3.1.8}$$

Rearranging this equation to express the stress σ_z (see Equation 3.1.4) we have

$$\sigma_z = \left(\frac{M_y I_{xx} - M_x I_{xy}}{I_{xx} I_{yy} - I_{xy}^2} \right) x + \left(\frac{M_x I_{yy} - M_y I_{xy}}{I_{xx} I_{yy} - I_{xy}^2} \right) y \tag{3.1.9}$$

The assumption of thin walled section comes into play in the evaluation of the second moments of area. In fact, since the thickness t of a thin walled section is assumed to be small compared to the cross sectional dimensions, squares and higher powers of t can be neglected and it can be assumed that the section is represented by the mid-line of its wall. Moreover, stresses may be considered constant across the thickness.

If we consider an element of beam having length δz subject to bending moments and, in addition, shear forces and a distributed load w_y, the equilibrium of the forces and moments can be written as:

$$\left(S_y + \frac{\partial S_y}{\partial z} \delta z \right) + w_y \delta z - S_y = 0 \tag{3.1.10}$$

$$\left(M_x + \frac{\partial M_x}{\partial z} \delta z \right) - \left(S_y + \frac{\partial S_y}{\partial z} \delta z \right) \delta z - w_y \frac{\delta z^2}{2} - M_x = 0 \tag{3.1.11}$$

These expressions, rearranged, lead to the known relations between distributed loads, shear and bending moments:

$$w_y = -\frac{\partial S_y}{\partial z} \quad \text{and} \quad S_y = \frac{\partial M_x}{\partial z}$$

3.1.3 Shear of Open and Closed Thin Walled Sections of Beams [73]

The bending theory recalled in 3.1.2 is based on the assumption that plane sections remain plane after bending. This hypothesis is verified only if the bending moments M_x and M_y are constant along the beam, as a variation of the bending moments would imply the presence of shear loads, which generate shear stresses.

An element $\delta s \times \delta z \times t$ of the beam wall is considered. The element undergoes direct stresses σ_z generated by bending moments or by the bending effect of the shear loads, and shear stresses due to shear or torsion. The shear stresses are indicated as $\tau_{sz} = \tau_{zs} = \tau$. The hoop stress σ_s is usually assumed equal to zero unless the structure is loaded by internal pressures.

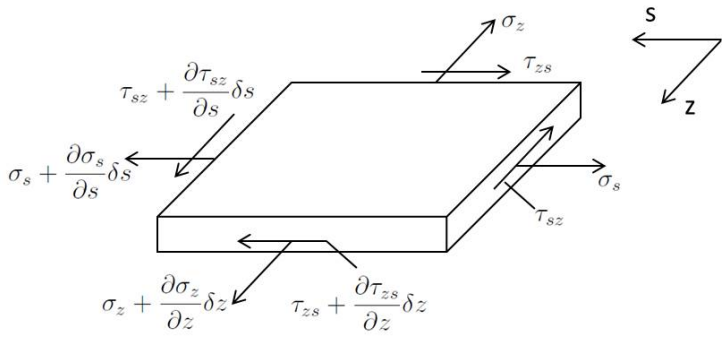

Figure 3.2: Stresses on a element of a thin walled beam

It is possible to define the shear flow q over a section having thickness t as $q = \tau t$ and to write the equilibrium of the element as:

$$\left(\sigma_y + \frac{\partial \sigma_z}{\partial z}\delta z\right) t\delta s - \sigma_z t\delta_s + \left(q + \frac{\partial q}{\partial s}\delta s\right)\delta z - q\delta z = 0 \tag{3.1.12}$$

which can be rewritten into two equations along z and s:

$$\frac{\partial q}{\partial s} + t\frac{\partial \sigma_z}{\partial z} = 0 \tag{3.1.13}$$

$$\frac{\partial q}{\partial z} + t\frac{\partial \sigma_s}{\partial s} = 0 \tag{3.1.14}$$

Since it has been assumed that the section moves rigidly in its own plane, the displacement of any point is fully defined by two translations u and v and a rotation θ. The tangential displacement v_t of a generic point, forming an angle ϕ with the direction of the displacement u, can be expressed as:

$$v_t = p\theta + ucos\phi + vsin\phi \tag{3.1.15}$$

Open Section
An open section beam of arbitrary section with shear loads S_x and S_y applied through the shear centre is considered.

The equilibrium equations for the generic element of the section, Equation 3.1.13 is recalled:

$$\frac{\partial q}{\partial s} + t\frac{\partial \sigma_z}{\partial z} = 0 \tag{3.1.16}$$

The direct stress σ_z, derived from the bending theory, is substituted into Equation 3.1.13 to obtain:

$$\frac{\partial q}{\partial s} = -\frac{(S_x I_{xx} - S_y I_{xy})}{I_{xx} I_{yy} - I_{xy}^2} tx - \frac{(S_y I_{yy} - S_x I_{xy})}{I_{xx} I_{yy} - I_{xy}^2} ty \tag{3.1.17}$$

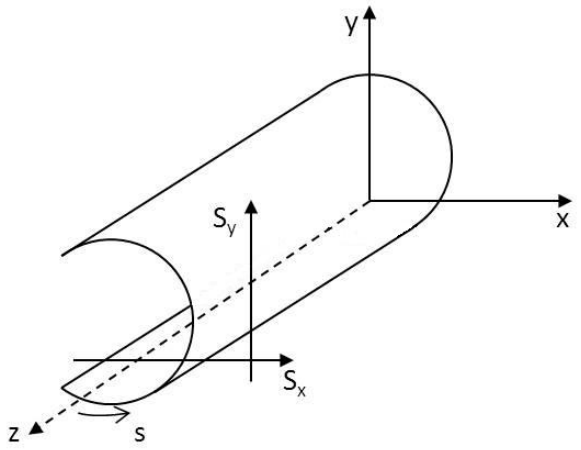

Figure 3.3: Open section under shear loads

If the origin of the s coordinate is taken at the open edge of the section then, for $s = 0$, $q = 0$. Integrating with respect to s from the origin $s = 0$ to a generic point s along the section, the shear flow q_s can be expressed as:

$$q_s = -\frac{(S_x I_{xx} - S_y I_{xy})}{I_{xx} I_{yy} - I_{xy}^2} \int_0^s t x ds - \frac{(S_y I_{yy} - S_x I_{xy})}{I_{xx} I_{yy} - I_{xy}^2} \int_0^s t y ds \tag{3.1.18}$$

Equation 3.1.18 can be further simplified for sections symmetric with respect to the x or y axis, which are characterised by $I_{xy} = 0$:

$$q_s = -\frac{S_x}{I_{yy}} \int_0^s t x ds - \frac{S_y}{I_{xx}} \int_0^s t y ds \tag{3.1.19}$$

Closed Section

A beam having closed cross-section can be studied in a similar way as the open section one. However, in this case it is possible to apply the shear loads in a point other than the shear centre. A torque T will be generated, resulting in an addtional shear flow on the section.

Equation 3.1.17 still holds for closed section beams, however in this case it is not possible, in general, to find a location s where the value of the shear flow is known. The integration of Equation 3.1.17 then leads to:

$$q_s - q_{s,0} = -\frac{(S_x I_{xx} - S_y I_{xy})}{I_{xx} I_{yy} - I_{xy}^2} \int_0^s t x ds - \frac{(S_y I_{yy} - S_x I_{xy})}{I_{xx} I_{yy} - I_{xy}^2} \int_0^s t y ds \tag{3.1.20}$$

where $q_{s,0}$ is the value of the shear flow for $s = 0$. Equation 3.1.20 shows that the shear flow in the closed section can be expressed as the sum of the shear flow for the open section plus an additional term q_b.

$$q_s = q_{s,0} + q_b \tag{3.1.21}$$

where the additional shear flow q_b is equal to the right end side of Equation 3.1.20.

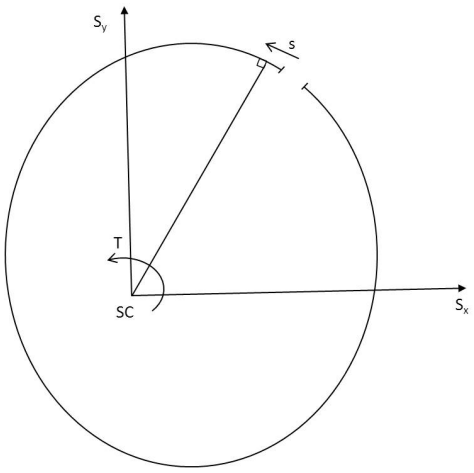

Figure 3.4: Shear flow in a closed section

In order to calculate q_b, the cross section is "cut" at some convenient location and the value of the shear flow for $s = 0$ is derived from the equilibrium of the moments.

The shear loads not applied through the shear centre will generate out of plane displacements of the cross-section, causing the section to twist and warp. Remembering that $q = \tau t$ and $\tau = G\gamma$, where $\gamma = \frac{\partial w}{\partial s} + \frac{\partial v_t}{\partial z}$ by definition, is it possible to derive the warping displacement w for the shear loaded section.

The shear flow

$$q_s = Gt(\frac{\partial w}{\partial s} + \frac{\partial v_t}{\partial z}) \tag{3.1.22}$$

can be rewritten as

$$\frac{q_s}{Gt} = \frac{\partial w}{\partial s} + p\frac{\partial \theta}{\partial z} + \frac{\partial u}{\partial z}cos\phi + \frac{\partial v}{\partial z}sin\phi \tag{3.1.23}$$

and integrating with respect to s:

$$\int_0^s \frac{q_s}{Gt}ds = \int_0^s \frac{\partial w}{\partial s}ds + \frac{\partial \theta}{\partial z}\int_0^s pds + \frac{\partial u}{\partial z}\int_0^s cos\phi ds + \frac{\partial v}{\partial z}\int_0^s sin\phi ds \tag{3.1.24}$$

$$w_s - w_0 = \int_0^s \frac{q_s}{Gt}ds - \frac{A_{0s}}{A}\oint_0^s \frac{q_s}{Gt}ds - \frac{\partial u}{\partial z}(x_s - x_0) - \frac{\partial v}{\partial z}(y_s - y_0) \tag{3.1.25}$$

If the origin of the s coordinate coincides with the centre of twist of the section, the last two terms of Equation 3.1.25 are zero.:

$$w_s - w_0 = \int_0^s \frac{q_s}{Gt}ds - \frac{A_{0s}}{A}\oint_0^s \frac{q_s}{Gt}ds \tag{3.1.26}$$

.

Integrating Equation 3.1.24 over all the cross section yelds

$$\oint_0^s \frac{q_s}{Gt} ds = 2A \frac{d\theta}{dz} \tag{3.1.27}$$

3.1.4 Torsion of Open and Closed Thin Walled Sections of Beams [73]

Closed Section
The application of a pure torque T to a closed beam section generates a constant shear flow in the beam wall.

The torque generated by the shear flow acting on an element ∂s of the beam wall is $pq\partial s$. Hence, for the whole section:

$$T = \oint pqds \tag{3.1.28}$$

Since q is constant, the torque generated is equal to:

$$T = 2Aq \tag{3.1.29}$$

Equation 3.1.29 is known as the *Bredt-Batho formula*. The shear flow q has been expressed in Equation 3.1.22 as

$$q_s = Gt \left(\frac{\partial w}{\partial s} + \frac{\partial v_t}{\partial z} \right) \tag{3.1.30}$$

Differentiatin this expression, and remembering that q is constant:

$$\frac{\partial q}{\partial z} = Gt \left(\frac{\partial^2 w}{\partial z \partial s} + \frac{\partial^2 v_t}{\partial z^2} \right) = 0 \tag{3.1.31}$$

The longitudinal strain $\partial w/\partial z = \epsilon_z$ is zero in the absence of direct stresses. This leads to $\partial^2 v_t/\partial z^2 = 0$. Decomposing v_t as already done for Equation 3.1.23

$$p\frac{\partial^2 \theta}{\partial z^2} + \frac{\partial^2 u}{\partial z^2} cos\phi + \frac{\partial^2 v}{\partial z^2} sin\phi = 0 \tag{3.1.32}$$

Noting that to have $\partial^2 v_t/\partial z^2 = 0$ all its terms have to be zero, we derive that θ, u and v are all linear functions of z.

The rate of twist obtained for a shear loaded closed beam section, Equation 3.1.27 is also valid for constant shear flow, hence

$$\frac{d\theta}{dz} = \frac{1}{2A} \oint \frac{q_s}{Gt} ds \tag{3.1.33}$$

The warping distribution for constant q, also derived in Equation 3.1.26 for shear loaded beams, is $w_s - w_0 = \int_0^s \frac{q_s}{Gt} ds - \frac{A_{0s}}{A} \oint_0^s \frac{q_s}{Gt} ds$.

Defining

$$\delta = \oint \frac{ds}{Gt} \tag{3.1.34}$$

and

$$\delta_{Os} = \int_0^s \frac{ds}{Gt} \tag{3.1.35}$$

and replacing q from the Bredt-Batho formula, Equation 3.1.29, the warping distribution in a close section generated by a torque T is:

$$w_s - w_0 = \frac{T\delta}{2A}\left(\frac{\delta_{Os}}{\delta} - \frac{A_{Os}}{A}\right) \tag{3.1.36}$$

From Equation 3.1.36, the condition for zero warping at a section is:

$$\frac{\delta_{Os}}{\delta} - \frac{A_{Os}}{A} = \frac{1}{\delta}\oint \frac{ds}{Gt} - \frac{1}{2A}\int_0^s p_R ds = 0 \tag{3.1.37}$$

which leads to

$$p_R Gt = \frac{2A}{\delta} = constant \tag{3.1.38}$$

Equation 3.1.38 defines a so called *Neuber beam*, that is a beam which does not warp. Examples of this are beams of circular section having constant thickness, rectangular sections of sides a and b for which $t_a b = t_b a$.

Open Section
An open thin walled section can be considered as a thin strip. The shear stress τ_{zs} can be written as:

$$\tau_{zs} = 2Gn\frac{d\theta}{dz} \tag{3.1.39}$$

and its maximum value will be

$$\tau_{zs,max} = \pm Gt\frac{d\theta}{dz} \tag{3.1.40}$$

while τ_{zn} will be zero.

The torsion constant of the thin section is given by

$$J = \frac{1}{3}\int t^3 ds \tag{3.1.41}$$

and the relation between the rate of twist and the torque will be given by

$$T = GJ\frac{d\theta}{dz} \tag{3.1.42}$$

An open section beam under torsion experiences two types of warping, respectively warping of the cross section and warping across its thickness The first type of warping is called

primary warping, while the second one is called *secondary warping* and in general is considerably less than the first one and is in general ignored in aircraft structures.

The warping across the thickness, similar to what happens for a thin rectangular strip, can be expressed as:

$$w_t = ns\frac{d\theta}{dz} \tag{3.1.43}$$

To obtain the warping of the cross section, remembering that

$$\gamma_{zs} = \frac{\partial w}{\partial s} + \frac{\partial v_t}{\partial z} \tag{3.1.44}$$

If R is the centre of twist of the cross section , the tangential displacement can be expressed as:

$$\frac{\partial v_t}{\partial z} = p_R\frac{d\theta}{dz} \tag{3.1.45}$$

Substituting Equation 3.1.45 into Equation 3.1.44 and multiplying by the shear modulus G, we obtain

$$\tau_{sz} = \left(\frac{\partial w}{\partial s} + p_R\frac{d\theta}{dz}\right)G \tag{3.1.46}$$

and the stress τ_{sz} is zero on the the midline of the section wall.

The primary warping w_s can be written as:

$$w_s = -\frac{d\theta}{dz}\int_0^s p_R ds \tag{3.1.47}$$

or, in terms of the applied torque, as

$$w_s = -2A_R\frac{T}{GJ} \tag{3.1.48}$$

3.1.5 Warping Theory [73]

A torque applied to a thin walled structure can generate not only shear stresses but also axial stresses. This phenomenon, called warping torsion, arises in thin walled structures when the axial displacements of the cross sections are restrained (for instance, if a beam is clamped at one of its ends). Sections which are axisymmetric or have straight intersecting members do not warp: this is the case for circular, L, T and X cross sections for instance.

If M and V are the bending moment and shear force on a thin walled beam, related by

$$V = \frac{dM}{dx} \tag{3.1.49}$$

and h is the vertical dimension of the cross section, then the torque T is given by:

$$T = Vh = \frac{dM}{dx}h \tag{3.1.50}$$

and remembering that

$$M = EI\frac{d^2w}{dx^2} \tag{3.1.51}$$

from beam theory, the torque T can be expressed as

$$T = hEI\frac{d^3w}{dx^3} \tag{3.1.52}$$

For a beam undergoing torsion, the relation between the rotation and the displacement is given by:

$$w = -\phi\frac{h}{2} \tag{3.1.53}$$

which leads to

$$T = -\frac{h^2}{2}EI\frac{d^3w}{dx^3} = -EC_w\frac{d^3w}{dx^3} \tag{3.1.54}$$

The quantity $C_w = -\frac{h^2}{2}I$ represents the cross sectional warping constant of the beam.

It is possible to superimpose the effect of the standard St. Venant torque to the warping torsion to obtain the total torque T_{tot}:

$$T_{tot} = GJ\frac{d\phi}{dx} - EC_w\frac{d^3\phi}{dx^3} \tag{3.1.55}$$

In the theory of warping torsion, it is convenient to define an auxiliary quantity called bi-moment B:

$$B = EC_W\phi'' \tag{3.1.56}$$

The bi-moment B is the analogous of the bending moment M for the bending loading conditions. In fact, it is possible to obtain an expression similar to $M = EI\frac{d^2w}{dx^2}$ for the bi-moment in warping torsion theory:

$$B = Mh = EI\frac{d^2w}{dx^2}h = \frac{h^2}{2}EI\frac{d^2\phi}{dx^2} = EC_w\phi'' \tag{3.1.57}$$

Since both the bending and the warping torsion are formulated in terms of axial stresses, it is possible to combine them together.

3.1.6 Idealization of Stiffened Thin Walled Structures [73]

In a semi monocoque structure, the longitudinal stiffeners contribute significantly to withstand axial loadings. While their presence does not affect much the torsional behaviour of the section, it greatly influences shear flow distribution. In fact, the shear flow will vary continuously along the walls in correspondence of the skin panels and will experience a jump in correspondence of a stiffener, wich depends on its cross sectional area and position.

In real aircraft structures, the analysis of a typical wing or fuselage section would be extremely laborious due to the use of complicated cross sectional geometries and a large

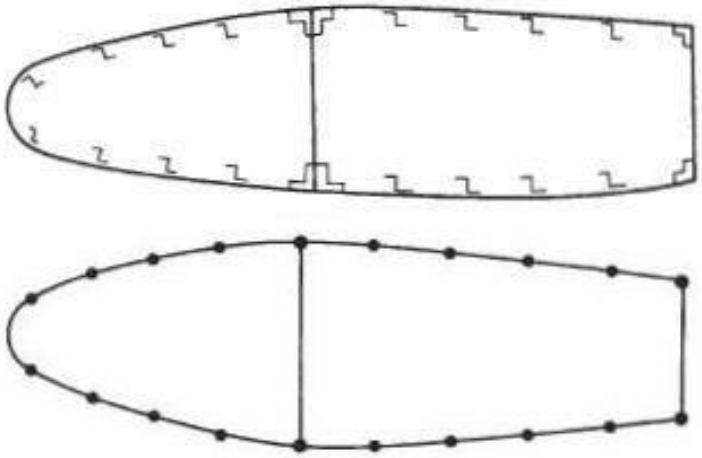

Figure 3.5: Typical wing section and its idealisation

number of structural components. The real complex sections are hence idealised into simpler mechanical models by separating the contributions of each component to the overall structural behaviour under loading.

In structures like the wing section of Figure 3.5 the longitudinal stiffeners and the spar flanges resist mainly bending loads, while the skins undergo mainly shear. The stiffeners and spars can be replaced by concentration of areas, called *booms*, over which the axial stress is constant and it can be assumed that all the direct stresses are carried by the booms while the skins contribute only in shear. It is possible to account for the skin stress carrying capability by increasing the area of the booms in proportion to it. The skins become subject only to shear flows which are constant between two consecutive booms.

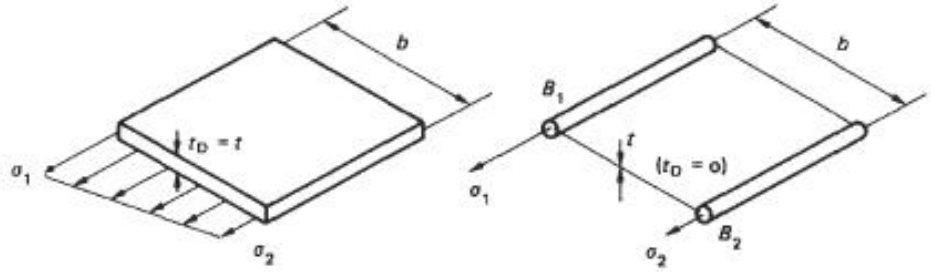

Figure 3.6: Idealisation of a panel

Considering the real and idealised panels shown in Figure 3.6, the linear stress distribution on the actual panel is replaced by two loads σ_1 and σ_2 on the booms, exactly equal to the stresses at the two ends of the panel. By equating the moments about the right end side of each panels

$$\sigma_2 t_D \frac{b^2}{2} + \frac{1}{2}(\sigma_1 - \sigma_2) t_D b \frac{2}{3} b = \sigma_1 B_1 b \tag{3.1.58}$$

where B_1 and B_2 are the boom areas and t_D the real thickness of the panel.

Hence

$$B_1 = \frac{t_D b}{6}\left(2 + \frac{\sigma_2}{\sigma_1}\right) \tag{3.1.59}$$

and

$$B_2 = \frac{t_D b}{6}\left(2 + \frac{\sigma_1}{\sigma_2}\right) \tag{3.1.60}$$

The ratio of the stresses can be assumed in many applications. For a pure axial loading, $\sigma_1/\sigma_2 = 1$, while for a pure bending moment, $\sigma_1/\sigma_2 = -1$, leading to different boom areas for different loading conditions.

The idealisation of a structure leads to some modifications to the analysis of open and closed cross section beams. In fact, the neutral axis position and the sectional properties must be referred to the direct stress carrying areas and will be modified by the presence of the booms.

3.1.7 Classical Lamination Theory ([101], [102])

The structural behaviour of composite materials is different from isotropic materials and the determination of deformations and stresses depends on several additional parameters. A ply is a thin sheet of fibres arranged in a matrix material. A stack of plies having different orientation and usually bonded by the same matrix is called a laminate. The classical lamination theory allows the calculation of the stiffness properties of a laminate based on the study of the single plies that compose it. When dealing with a single ply, it is convenient to adopt a local coordinates system, where the axes are arranged in directions parallel and perpendicular to the fibre direction (directions 1 and 2). On the other hand, when the laminate is considered, a global coordinates system is adopted (directions x and y).

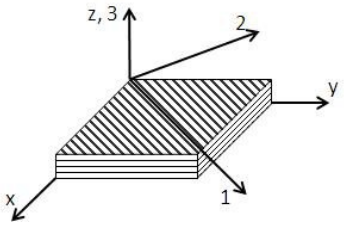

Figure 3.7: Ply and Laminate Reference Frames

The classical lamination theory is based on some preliminary assumptions :

- The bonding between the plies that compose the laminate is assumed to be perfect, infinitesimally thin as well as non-shear-deformable. Therefore, the displacements are continuous across the laminate and no ply can slip relative to another.
- Deflections and strains are small compared to the thickness of the laminate.
- Plane sections that are initially normal to the mid-plane of the laminate remain normal to the mid-plane after deformation. This assumption is equivalent to ignoring the shear strains γ_{xz} and γ_{yz} and to consider them equal to zero.
- The stress normal to the mid-plane, σ_z, is small compared to the other stress components and can be neglected.

- The strain perpendicular to the middle surface is ignored, therefore $\epsilon_z = 0$.

The reduced stiffness matrix Q for an orthotropic ply is symmetric about its leading diagonal and depends on four independent elastic constants: the elastic moduli E_1 and E_2 in the 1 and 2 direction, the in-plane shear modulus G_12 and the Poisson's ratio ν_{12}. Expressed in the local coordinates system:

$$Q = \begin{bmatrix} Q_{11} & Q_{12} & 0 \\ Q_{12} & Q_{22} & 0 \\ 0 & 0 & Q_{66} \end{bmatrix}$$

where:

$$Q_{11} = \frac{E_1}{1-\nu_{12}\nu_{21}}, \quad Q_{22} = \frac{E_2}{1-\nu_{12}\nu_{21}}$$
$$Q_{12} = \frac{\nu_{12}E_2}{1-\nu_{12}\nu_{21}}, \quad Q_{66} = G_{12}$$

For an orthotropic ply, the stress-strain relation is given by:

$$\begin{bmatrix} \sigma_1 \\ \sigma_2 \\ \tau_{12} \end{bmatrix} = \begin{bmatrix} Q_{11} & Q_{12} & 0 \\ Q_{12} & Q_{22} & 0 \\ 0 & 0 & Q_{66} \end{bmatrix} \begin{bmatrix} \epsilon_1 \\ \epsilon_2 \\ \gamma_{12} \end{bmatrix}$$

It is possible to switch from the local to the global coordinates system by considering a coordinates transformation matrix. Defining as θ the angle between the local and the global axes and $m = cos\theta$, $n = sin\theta$, the transformation matrix is given by:

$$T = \begin{bmatrix} m^2 & n^2 & 2mn \\ n^2 & m^2 & -2mn \\ -mn & mn & m^2 - n^2 \end{bmatrix}$$

The stresses and strains in Equation (3.1.7) can be rewritten as:

$$\begin{bmatrix} \sigma_1 \\ \sigma_2 \\ \tau_{12} \end{bmatrix} = T \begin{bmatrix} \sigma_x \\ \sigma_y \\ \tau_{xy} \end{bmatrix}$$

and

$$\begin{bmatrix} \epsilon_1 \\ \epsilon_2 \\ \epsilon_{12} \end{bmatrix} = T \begin{bmatrix} \epsilon_x \\ \epsilon_y \\ \epsilon_{xy} \end{bmatrix}$$

where ϵ_{xy} is the tensor strain, which can be converted into the engineering strain $\gamma_{xy} = 2\epsilon_{xy}$

For each ply, the in-plane forces and moments per unit width applied to a generic point in the laminate can be obtained by integrating the stresses through the thickness:

$$\begin{bmatrix} N_x \\ N_y \\ N_{xy} \end{bmatrix} = \int_{-h/2}^{h/2} \begin{bmatrix} \sigma_x \\ \sigma_y \\ \tau_{xy} \end{bmatrix} dz$$

$$\begin{bmatrix} M_x \\ M_y \\ M_{xy} \end{bmatrix} = \int_{-h/2}^{h/2} \begin{bmatrix} \sigma_x \\ \sigma_y \\ \tau_{xy} \end{bmatrix} z dz$$

The strain ϵ in each ply is a function of z and can be expressed as:

$$\begin{bmatrix} \epsilon_x \\ \epsilon_y \\ \epsilon_{xy} \end{bmatrix} = \begin{bmatrix} \epsilon_x^0 \\ \epsilon_y^0 \\ \epsilon_{xy}^0 \end{bmatrix} - z \begin{bmatrix} \kappa_x \\ \kappa_y \\ \kappa_{xy} \end{bmatrix}$$

where ϵ^0 is the mid-plane strain and κ is the curvature of the mid-plane.

By using the stress-strain relation and adding up in all the plies 1 to N, Equations 3.1.7 and 3.1.7, can be rewritten as:

$$\begin{bmatrix} N_x \\ N_y \\ N_{xy} \end{bmatrix} = \begin{bmatrix} A_{11} & A_{12} & A_{13} \\ A_{12} & A_{22} & A_{23} \\ A_{13} & A_{23} & A_{33} \end{bmatrix} \begin{bmatrix} \epsilon_x^0 \\ \epsilon_y^0 \\ \epsilon_{xy}^0 \end{bmatrix} + \begin{bmatrix} B_{11} & B_{12} & B_{13} \\ B_{12} & B_{22} & B_{23} \\ B_{13} & B_{23} & B_{33} \end{bmatrix} \begin{bmatrix} \kappa_x^0 \\ \kappa_y^0 \\ \kappa_{xy}^0 \end{bmatrix}$$

and

$$\begin{bmatrix} M_x \\ M_y \\ M_{xy} \end{bmatrix} = \begin{bmatrix} B_{11} & B_{12} & B_{13} \\ B_{12} & B_{22} & B_{23} \\ B_{13} & B_{23} & B_{33} \end{bmatrix} \begin{bmatrix} \epsilon_x^0 \\ \epsilon_y^0 \\ \epsilon_{xy}^0 \end{bmatrix} + \begin{bmatrix} D_{11} & D_{12} & D_{13} \\ D_{12} & D_{22} & D_{23} \\ D_{13} & D_{23} & D_{33} \end{bmatrix} \begin{bmatrix} \kappa_x^0 \\ \kappa_y^0 \\ \kappa_{xy}^0 \end{bmatrix}$$

where the coefficients A, B and D are defined in terms of the ply stiffness as:

$$A_{ij} = \sum_{k=1}^{N} (\overline{Q}_{ij})_{(k)} (z_k - z_{k-1})$$

$$B_{ij} = \frac{1}{2} \sum_{k=1}^{N} (\overline{Q}_{ij})_{(k)} (z_k^2 - z_{k-1}^2)$$

$$D_{ij} = \frac{1}{3} \sum_{k=1}^{N} (\overline{Q}_{ij})_{(k)} (z_k^3 - z_{k-1}^3)$$

The resultants and moments for a laminated plate in function of the in-plane strains and curvature are given by:

$$\begin{bmatrix} N_x \\ N_y \\ N_{xy} \\ M_x \\ M_y \\ M_{xy} \end{bmatrix} = \begin{bmatrix} A_{11} & A_{12} & A_{16} & B_{11} & B_{12} & B_{16} \\ A_{12} & A_{22} & A_{26} & B_{12} & B_{22} & B_{26} \\ A_{16} & A_{26} & A_{66} & B_{16} & B_{26} & B_{66} \\ B_{11} & B_{12} & B_{16} & D_{11} & D_{12} & D_{16} \\ B_{12} & B_{22} & B_{26} & D_{12} & D_{22} & D_{26} \\ B_{16} & B_{26} & B_{66} & D_{16} & D_{26} & D_{66} \end{bmatrix} \begin{bmatrix} \epsilon^0_{xx} \\ \epsilon^0_{yy} \\ \gamma^0_{xy} \\ \kappa_x \\ \kappa_y \\ \kappa_{xy} \end{bmatrix}$$

or, in a condensed form, by:

$$\begin{bmatrix} N \\ M \end{bmatrix} = \begin{bmatrix} A & B \\ C & D \end{bmatrix} \begin{bmatrix} \epsilon \\ \kappa \end{bmatrix}$$

The ABD matrix describes the elastic behaviour of the laminate. Matrix **A** represents the in-plane stiffness matrix and its terms A_{16} and A_{26} are responsible for the coupling between in-plane tension and in-plane shear. Matrix **B** is the coupling matrix between the in-plane and flexural behaviour of the laminate, in particular B_{11}, B_{12} and B_{22} couple the in-plane behaviour to the bending, while B_{16} and B_{26} to the twisting. This means that a in-plane tension on the laminate will generate also a curvature or warping.This effect can be avoided by using laminates symmetric about the midplane, which have all the terms in the coupling matrix **B** equal to zero. Finally, matrix **D** is the flexural stiffness matrix, which realises the coupling between bending and twisting through its terms D_{16} and D_{26}.

3.2 Extension to Thin Walled Composite Beams

The classical theory for thin walled structures presented in Section 3.1.1 can be extended to thin walled beams made of composite materials.

In this case, the walls of the beams may consist of a single layer or of several layers, each layer may be made of composite materials. As shown in Figure 3.8, the beams wall consists of k flat segments 1 to K which are initially considered separately.

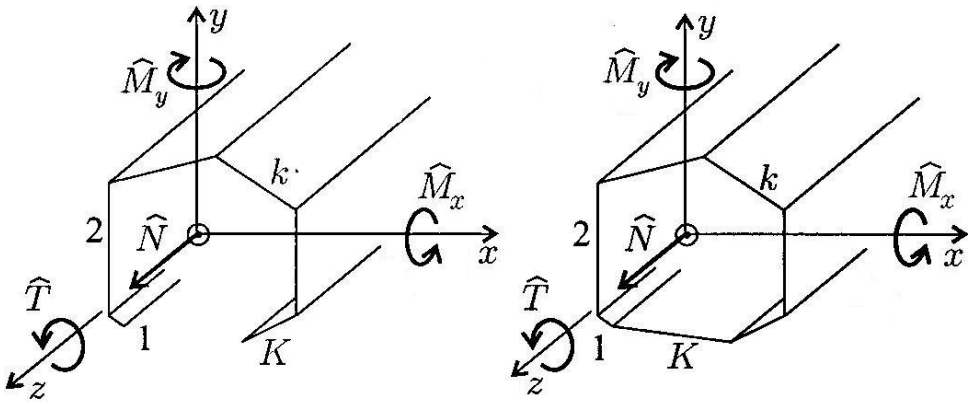

Figure 3.8: Open and closed section of a composite thin walled beam

The cross-sections of beams with arbitrary layup do not remain plane under a generic loading. Nonetheless, in a long body, such as a beam, the strains may be considered to

be constant in the axial direction, and the plane-strain condition can be applied similarly to what has been done in Section 3.1.1.

Remembering that $E_z = E_x$ and that E_z is likely to vary from each laminate, the cross sectional properties can be redefined to include the effective elastic modulus in the member Z-direction as:

$$I_{xx}^{'} = E_z I_{xx} \qquad I_{yy}^{'} = E_z I_{yy} \qquad I_{xy}^{'} = E_z I_{xy}$$

And the stress σ_z acting on the laminate in the beam z-direction due to the applied moments M_x and M_y will be

$$\sigma_z = E_z \left(\frac{M_y^{'}}{I_{yy}^{'}} x + \frac{M_x^{'}}{I_{xx}^{'}} y \right) \tag{3.2.1}$$

where $M_y^{'}$ and $M_x^{'}$ will be given respectively by

$$M_y^{'} = \frac{M_y I_{xx}^{'} - M_x I_{xy}^{'}}{I_x^{'} x I_y^{'} y - I_{xy}^{'2}} \tag{3.2.2}$$

and

$$M_x^{'} = \frac{M_x I_{yy}^{'} - M_y I_{xy}^{'}}{I_{xx}^{'} I_{yy}^{'} - I_{xy}^{'2}} \tag{3.2.3}$$

When all the n laminates of the section are considered the sectional properties are given by the sum on all the layers of the $I_{xx}^{'}$, $I_{yy}^{'}$ and $I_{xy}^{'}$.

The thin-walled theory and the laminate theory presented in this section provide the theoretical background for the analysis developed in the next chapters. Although the expressions presented in Section 3 have not been directly used in the calculations, they are built in the FE package and represent the theoretical basis of the analysis.

3.3 Finite Elements Analysis

The finite elements method allows the calculation of stresses and deformations for structural components and loading conditions which cannot be studied with the analytical methods. This approach has proved extremely useful for the study of aircraft structures, where the complexity of the structures and the variety of loading conditions to be assessed make standard methods of analysis inadequate.

The first step for the solution of a structural problem is the discretisation of the structure. The real, continuous structure, having an infinite number of degrees of freedom, is represented using a finite number of smaller components, called *elements*, connected one to the other in specific points called *nodes*. The solution of the original problem is

transformed into the solution of a system of algebraic equations with a finite number of unknowns, which are the nodal displacements. The displacement of each point of the structure is defined as a function of the nodal displacements. From the displacements it is possible to calculate the deformation, and hence the stresses, at every point. Different types of element can be used, in order to represent the real structure in a correct and accurate way. Each type of element is characterised by a different displacement function. The elements can be monodimensional, bi-dimensional or three-dimensional. The elements can also be divided into linear and non-linear ones. Finite elements with linear displacement functions represent the displacements, deformations and stresses in each element as linear. For this reason, structures with areas having strong gradients in the stress distribution (like areas with section variations or notches) need a very fine division into elements. Elements with higher order shape functions, for such cases, would give more accurate results.

Several finite element commercial software have been developed. In the following sections, some aspects of the FEM analysis will be addressed, considering in particular the approach followed by the NASTRAN software.

3.3.1 Linear and Nonlinear Static Analysis ([103]-[107])

Many structural problems exhibit a certain degree of nonlinearity. Common examples of nonlinear behaviour are permanent deformations, cracks, the distortion of open section beams, buckling, high temperatures et cetera. For all these cases, the linearized theories developed for the structural analysis lead to inaccurate results.

Three main kinds of structural nonlinearities can be indentified: geometric, material and boundary condition nonlinearities. Geometric nonlinearities arise when the stiffness of the structure depends on the displacements it undergoes; material nonlinearities interest materials with a nonlinear stress/strain relation, while boundary condition nonlinearities are described through changes to the stiffness of the structure such as in contact problems, when parts of the structure come into contact or separate one from each other, staged analyses, where material is removed from the solution, or when the initial restraints are changed during the analysis.

Nonlinearities increase the complexity of the finite element analysis because many basic principles adopted during linearization no longer apply. This is the case, for instance, of the principle of superposition, in which the resultant deflection, stress, or strain in a system due to several forces is simply the algebraic sum of their effects when separately considered.

In order to capture the nonlinear behaviour, usually more refined finite element meshes than for linear analysis are required. In the FEM linear analysis the displacement under certain loading conditions are obtained by performing the inversion of the stiffness matrix, which remains constant independently from the magnitude of the loading. In the FEM nonlinear analysis, on the other hand, the displacements are no longer proportional to the applied load and the approach used in the finite element solver is to apply the load in a series of steps or increments. The size of the increments used and the degree of nonlinearity encountered determines how well the solution will predict the true structural behaviour. The construction and inversion of the stiffness matrix at each step considerably increases

the computational costs of a nonlinear analysis. This is especially true for models with a large number of degrees of freedom or a large number of loading increments. In the standard Newton-Raphson method the stiffness matrix is reformed at each iteration of each increment in the process. Several solution procedures have been developed through the years, the standard and modified Newton-Raphson methods, Strain Correction Methods, Secant or Conjugate-Gradient Methods and Direct Substitution Methods are among the most widespread. Incremental nonlinear FE solutions are often referred to as quasi-static. In these solutions, the loading is applied progressively in a number of increments and the analysis provides the structural response over time, while any inertia effect is neglected (such as in creep analysis or fire analysis).

3.3.2 Dynamic Analysis ([103]-[107])

The three common types of dynamic analysis are:

- Real eigenvalue analysis
- Linear frequency response analysis
- Linear transient response analysis

The real eigenvalue analysis is used to determine the basic dynamic characteristics of a structure by assessing the undamped free vibration and determining the natural frequencies and mode shapes. Frequency response analysis evaluates the steady-state response to sinusoidal excitation, while transient response analysis computes the response to time-varying loads.

Real Eigenvalue Analysis
The natural frequencies and mode shapes of the structure characterize its basic dynamic behaviour. Assuming damping is present and no load is applied, the natural frequencies of the structure can be determined by solving the equation of motion for damped free vibration:

$$[M]\left\{\ddot{x(t)}\right\} + [B]\left\{\dot{x(t)}\right\} + [K]\{x(t)\} = 0 \tag{3.3.1}$$

where $[M]$, $[B]$ and $[K]$ are the mass, damping and stiffness matrices, $\{x\}$ is the displacement and $\{\ddot{x}\}$ and $\{\dot{x}\}$ the vectors of the acceleration and velocity.

The solution of Equation 3.3.1 is in the form of:

$$\{x\} = \{\phi\}\,\xi\,(\omega)\,e^{j\omega t} \tag{3.3.2}$$

where $\{\phi\}$ represents the eigenvector or mode shape, $\xi\,(\omega)$ are the modal coordinates, used to uncouple the equations of motion one from the other and to obtain a system of uncoupled single degree of freedom equations, and ω is the circular natural frequency.

Substituting 3.3.2 into 3.3.1, the eigenequation for the determination of the structural eigenvalues is obtained:

$$\left[-\omega^2 M + j\omega B + K\right]\{x\} = 0 \tag{3.3.3}$$

The relation between the i-th natural frequency f_i and the eigenvalue ω_i is given by:

$$f_i = \frac{\omega_i}{2\pi} \tag{3.3.4}$$

Several methods are available in Nastran for the calculation of the natural frequencies and modes shapes. The methods can be divided into transformation methods, where the eigenvalue equation is transformed into a special form easily solvable, and the tracking methods, where the eigenvalues are extracted one at a time using an iterative procedure. Nastran recommends the use of the Lanczos method due to its accuracy and efficiency. It requires that the mass matrix be positive semidefinite and the stiffness be symmetric.

Linear Frequency Response Analysis
Frequency response analysis is a method used to compute structural response to steady-state oscillatory excitation. In frequency response analysis the excitation is explicitly defined in the frequency domain. All of the applied forces are known at each forcing frequency. Forces can be in the form of applied forces and/or enforced motions (displacements, velocities, or accelerations).

Two different methods of analysis can be implemented: direct and modal. In the direct frequency response analysis (Nastran Sol 108), the structural response is obtained by solving the damped forced equations of motion at discrete excitation frequencies.

The forced vibrations under harmonic excitation in presence of damping are described by:

$$[M]\left\{\ddot{x(t)}\right\} + [B]\left\{\dot{x(t)}\right\} + [K]\{x\} = \{P(\omega)\}\, e^{j\omega t} \tag{3.3.5}$$

where $\{P(\omega)\}\, e^{j\omega t}$ is the load expressed as a complex vector.

Expressing the displacement as per 3.3.2, deriving it and substituting it into Equation (3.3.5), leads to:

$$\left[-\omega^2 M + j\omega B + K\right]\{x\} = \{P(\omega)\} \tag{3.3.6}$$

In the modal frequency response analysis (Nastran SOL 111), the mode shapes of the structure are used to uncouple the equations of motion. Tthe equations of motion are written in modal coordinates and uncoupled one from the other in order to obtain a set of uncoupled single degree of freedom equations.

Using modal coordinates, 3.3.5 can be written as:

$$-\omega^2 M\,[\phi]\{\xi(\omega)\} + j\omega B\,[\phi]\{\xi(\omega)\} + K\,[\phi]\{\xi(\omega)\} = \{P(\omega)\} \tag{3.3.7}$$

Finally, the orthogonality property of the mode shapes is used to formulate the structural problem in terms of the generalized mass and stiffness matrices, which are diagonal, and hence allow to uncouple the equations of motion. Equation (3.3.7) is premultiplied by $[\phi]^T$:

$$-\omega^2\,[\phi]^T M\,[\phi]\{\xi(\omega)\} + j\omega\,[\phi]^T B\,[\phi]\{\xi(\omega)\} + [\phi]^T K\,[\phi]\{\xi(\omega)\} = [\phi]^T\{P(\omega)\} \tag{3.3.8}$$

The terms in Equation 3.3.8 represent respectively:

- $[\phi]^T M [\phi]$: generalized mass matrix
- $[\phi]^T K [\phi]$: generalised stiffness matrix
- $[\phi]^T B [\phi]$: generalised damping matrix
- $[\phi]^T \{P\}$: modal force vector

Equation (3.3.8) represents a set of N uncoupled single degree of freedom equations, which solution is faster than the original coupled system. Once these equations are solved, the physical response can be obtained as the sum of the modal responses.

Linear Transient Response Analysis
Transient response analysis computes the behavior of a structure subjected to time-varying loads. The transient excitation is explicitly defined in the time domain and can be in the form of applied forces and/or enforced motions. The transient analysis typically determines displacements, velocities, and accelerations of the nodes, and forces and stresses in elements.

Two different methods of analysis can be implemented: direct and modal. The direct method (Nastran Sol 109) performs a numerical integration on the complete coupled equations of motion. The modal method utilizes the mode shapes of the structure to reduce and uncouple the equations of motion (when modal or no damping is used); the solution is then obtained through the summation of the individual modal responses.

The dynamic equation of motion is expressed as:

$$[M] \left\{ \ddot{x(t)} \right\} + [B] \left\{ \dot{x(t)} \right\} + [K] \{x\} = \{P(t)\} \tag{3.3.9}$$

The velocity $\left\{ \dot{x(t)} \right\}$ and acceleration $\left\{ \ddot{x(t)} \right\}$ can be represented using central finite differences as:

$$\{\dot{x}_n\} = \frac{1}{2\Delta t} \{x_{n+1} - x_{n-1}\} \tag{3.3.10}$$

$$\{\ddot{x}_n\} = \frac{1}{\Delta t^2} \{x_{n+1} - 2x_n + x_{n-1}\} \tag{3.3.11}$$

and by averaging the applied force over three adjacent time points, the equations of motion become:

$$\begin{aligned} \left[\frac{M}{\Delta t^2}\right] (x_{n+1} - 2x_n + x_{n-1}) + \left[\frac{B}{2\Delta t}\right] (x_{n+1} - x_{n-1}) + \\ + \left[\frac{K}{3}\right] (x_{n+1} + x_n + x_{n-1}) = \frac{1}{3} (P_{n+1} + P_n + P_{n-1}) \end{aligned} \tag{3.3.12}$$

Equation 3.3.12 can be rewritten as:

$$[A_1] \{x_{n+1}\} = [A_2] + [A_3] \{x_n\} + [A_4] \{x_{n-1}\} \tag{3.3.13}$$

where

$$[A_1] = \left[\frac{M}{\Delta t^2} + \frac{B}{2\Delta t} + \frac{K}{3}\right\}$$

$$[A_2] = \frac{1}{3}\left\{P_{n+1} + P_n + P_{n-1}\right\}$$

$$[A_2] = \left[\frac{2M}{\Delta t^2} - \frac{K}{3}\right]$$

$$[A_4] = \left[-\frac{M}{\Delta t^2} + \frac{B}{2\Delta t} - \frac{K}{3}\right\}$$

Equation (3.3.12) can be solved by decomposing matrix A_1, called the dynamic matrix, and applying it to the right end side. Matrix A_2, called the applied force matrix, is modified by the A_2 and A_3 terms at each time step. This approach gives a solution as a succession of static solutions where, at each time step, a forward-backward substitution of the load vector is performed.

The choice of a suitable integration time step is very important. The integration time step must be small enough to represent the load variation and to capture the maximum frequency of interest, called the cutoff frequency. If the integration time step Δt is constant, then matrix A_1 must only be decomposed once, leading to significant computational saving. Matrices $[M]$, $[B]$ and $[K]$ are assumed to be contant in time throughout the analysis. On the other hand if a variable time step is selected, then the dynamic matrix will be decomposed, with increases in the computational time.

3.4 Gust Loads

As described by Wright and Cooper in [75], air turbulence is the movement of the air through which the aircraft passes and is responsible for the in-flight loads on the aircraft known as gust loads. The effect of a gust is to suddenly change the wing incidence and consequently the lift, resulting in normal accelerations which affect the vibrational behaviour of the aircraft.

The two common approaches to gust analysis are the discrete gust and the continous air turbulence.

In the discrete gust approach it is assumed that the gust has a given profile, determined by a distribution of vertical air velocity over a finite length for a specific period of time. Different profiles have been employed in the calculations, the most common being the sharp-edged gust, the graded gust and the $1 - cos$ gust.

In the stochastic approach, no assumption is made on the gust shape and the gust is considered as a random distribution of velocity, constituted by a large number of different sinusoidal components. Such an approach adopts power spectral methods of analysis.

Discrete gusts

In the early stages of the study, the *sharp-edged* or *step gust* was considered. The basic assumption of this approach was that the aircraft velocity is undisturbed up to the moment the aircraft enters instantaneously into a uniform gust velocity field. This approach was, however, too reductive as it did not take into account that the gust velocity builds up in an interval of time. The step gust was then replaced by the graded gust, where it was supposed that the gust velocity increased linearly to its maximum value over a specified distance H. The modern representation of a gust is given by the $1 - cosine$ *gust*, where the description of the gust in the time domain is given by:

$$w_g(x_g) = \frac{w_{g0}}{2}(1 - cos\frac{2\pi V}{L_g}t) \quad 0 \leq x_g \leq L_g \tag{3.4.1}$$

where $V = \frac{x_g}{t}$ is the aircraft speed, x_g the aircraft position, w_{g0} the maximum gust velocity and L_g is the gust length.

The airworthiness requirements [147] set the value of the design maximum gust velocity depending on the gust length, altitude and speed of the aircraft.

An accurate representation of the gust response of the aircraft should consider also that the different parts of the aircraft (the wing and the tail, and for the case of swept wing also different sections of the same wing) encounter the gust at diferent times, leading to a *penetration effect*.

Initially, the simplified case of rigid aircraft and sharp-edged gust, with no penetration effect considered. If the aircraft is initially flying in a trimmed condition (lift=weight), the gust encounter will generate a vertical movement without pitching. The vertical gust velocity combined with the aircraft velocity would determine an instantaneous increase in the incidence $\Delta\alpha$ and a consequent lift increase ΔL. The maximum total load factor is given by:

$$n = 1 + \frac{\Delta L}{W} = 1 + \Delta n \tag{3.4.2}$$

As already explained, however, this approach would lead to incorrect estimation of the loads because it does not take into account the aircraft flexibility and the penetration effect and it assumes an instantaneous development of the gust velocity and of the lift force. A more realistic representation of a discrete gust is given by assuming a "gust alleviation factor" Kg. Remembering that the load factor n is a function of several parameters such as the air density ρ_0, the gust velocity w_g, the wing lift curve slope a, the aircraft weight W and the wing surface S_w, it is possible to rewrite equation 3.4.2 to explicitly include these parameters and the Kg factor. Pratt's equation is hence obtained:

$$n = 1 + \frac{\Delta L}{W} = 1 + \frac{\rho_0 w_g a K_g}{2W/S_w}V \tag{3.4.3}$$

The Pratt equation was used in the past to define the load factors at different flight conditions. A gust envelope, similar to a flight envelope, can be generated by plotting the gust load factor and the aircraft velocity. The envelope is used during the design stages to identify the worst loading cases.

This page is intentionally left blank.

CHAPTER 4

The Wing with Morphing High Lift Devices

This chapter presents the baseline reference data and the structural requirements for the design of a wing equipped with morphing high lift devices for a commercial aircraft. Section 4.1 presents the reference wing considered in this study. The traditional basic wing structure, consisting of a central wing box connected to moveable parts, is retained in order to have a favourable strength to weight ratio, and morphing high lift devices are included in the wing assembly instead of the conventional ones in order to significantly improve the aerodynamic performance of the wing.

The different parts of the reference wing, comprising the main wing box, the leading edge device and the trailing edge flap are presented. The geometric characteristics of the structure and the basic design parameters are given, including the skin materials and thicknesses, the number and position of the stringers, their size and layup.

The second part of the chapter presents the aerodynamic pressure load acting on the wing for different flight conditions. The deflection shape requirements for the morphing high lift devices based on the results of an aerodynamic optimisation process conducted by one of the SADE project Partners are illustrated in Section 4.2. The wing aerodynamic performance with the use of the morphing high lift devices was compared to the standard non morphed configuration to understand the potential benefits and to justify the design effort and the analysis presented in the following chapters.

4.1 The Reference Baseline Wing: Geometry and Materials

The reference baseline wing used in this current analysis belongs to a medium sized commercial aircraft. The wing geometry was provided by one of the Partners of the SADE Consortium and was determined using the A320 wing as a reference. The wing considered in this investigation had a wingspan of 39.65 m and an area of 172 m^2. The mean aerodynamic chord (MAC) was equal to 5.15 m. The preliminary structural and aerodynamic analysis was carried out at a reference section located outboard of the wing

kink, at 8.3 m from the root, where the total chord was 3.956 m, shown in Figure 4.1. Table 4.1 summarises the main wing geometrical parameters.

Area (m^2)	172
Aerodynamic Mean Chord (MAC) (m)	5.15
Span (m)	39.65
Aspect Ratio	9.14
Taper Ratio	0.2
Sweep Angle (°)	28

Table 4.1: Wing geometrical parameters

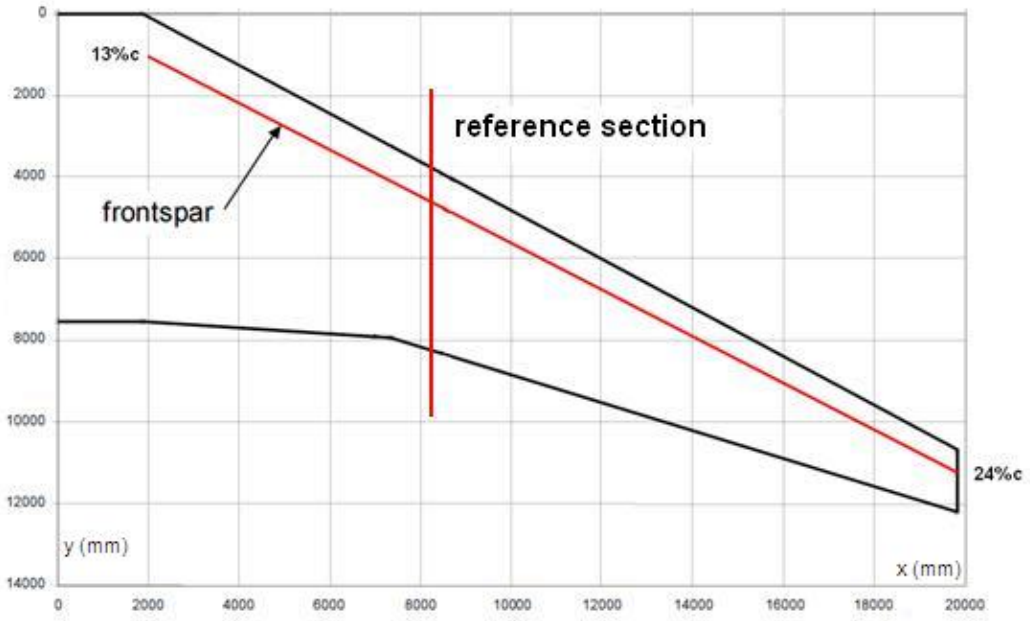

Figure 4.1: The reference baseline wing (dimensions in mm)

The wing structure was supported by two spars and thirty one ribs. The number of ribs, their pitch and the chordwise position of the spars were provided by one of the SADE project Partners. The front spar was located at 13% of the chord at the root and at 24% of the chord at the tip, running parallel to the leading edge. The rear spar, on the other hand, followed the trailing edge line, going from the 40% of the chord at the root section to 33% of the chord at the wing tip. The thirty one ribs were arranged with a pitch of 0.6 m from each other. Their orientation followed the direction of the airflow in the inboard section, before the engine mount, while in the outboard section they were arranged perpendicular to the front spar. The wing had a deformable leading edge, and was equipped with a single slotted Fowler flap with an actively deformable trailing edge.

4.1.1 The Wing Box and Leading Edge

The central wing box represents the main load carrying structural part of the SADE wing. At the reference section, the wing box had a chord of 1.855 m and an height of 0.438 m and 0.364 m at the front and rear spar respectively (see Figure 4.2). The leading edge device, mounted at the front spar, was 0.86 m chordwise and 0.44 m in height, as shown in Figure 4.3.

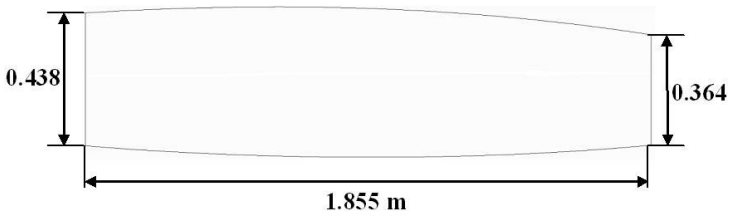

Figure 4.2: Wing box geometry at the reference section (m)

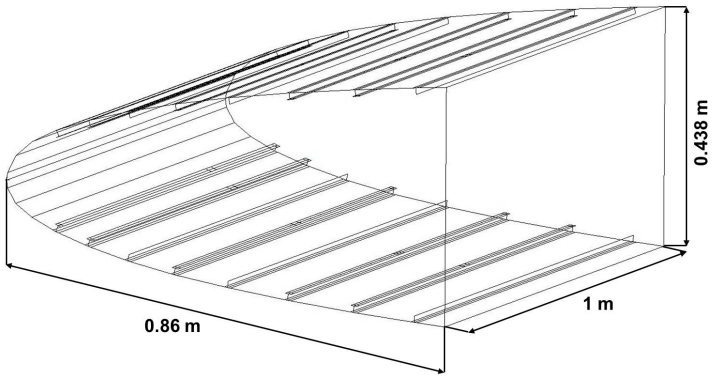

Figure 4.3: Leading edge device geometry at the reference section (m)

In the early stages of the Project, no detailed information about the skin panels, spars and ribs material properties was available. A preliminary design study, conducted by Morishima [108], set the materials and thicknesses for the wing box and leading edge.
The spars and ribs were made of a high strength carbon/epoxy composite laminate (M21/T800S), with 48 layers arranged in a symmetrical layup $[\pm 45/0/\pm 45/90/\pm 45/\pm 45/0/\pm 45/90/\pm 45/\pm 45/0/\pm 45/90/\pm 45]_s$ with a total thickness of 12 mm. The upper and lower skins were made of carbon fibre prepreg (HexTow IM7) and were reinforced by I-shaped stringers of the same material, but different laminate ply thicknesses (0.25 mm for the skins and 0.18 mm for the stringers). The leading edge skin was made of Aluminium 2024-T81 (Al), 2 mm in thickness. The leading edge skin was reinforced by eight metallic I-shaped stringers on both upper and lower skin panels, with flange and web 12 mm in length and 3 mm in thickness. Attention was paid to the correct selection of the layup for the composite parts to ensure that the structure did not exceed the stress limits and was not affected by buckling [108]. Table 4.2 summarises the material properties of the different wing box and leading edge components.

Material	E_1 (GPa)	E_2 (GPa)	G_{12} (GPa)	ν_{12}	X_t (MPa)	X_c (MPa)	Y_t (MPa)	Y_c (MPa)	S (MPa)
Al	72.4		28	0.33		450			295
IM7	164	10	5	0.3	2723	168	101	223	74
M21	172	10	5	0.3	3939	1669	50	250	79

Table 4.2: Wing material properties

4.1.2 The Trailing Edge Flap and Deployment Mechanism

The wing trailing edge was equipped with two single slotted Fowler flaps, for the inboard and outboard portions of the wing respectively. The present study considered only the inboard flap since geometry and aerodynamic data were only available in correspondence of the wing reference section.
Figure 4.4 presents the geometry of the inboard flap and of its rear morphing part.

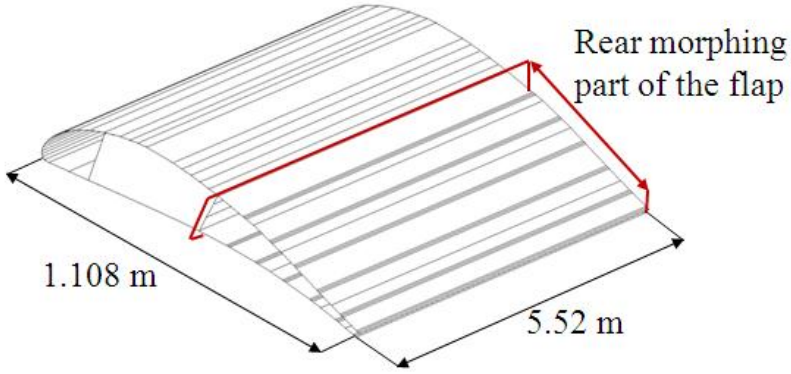

(a) Inboard flap geometry

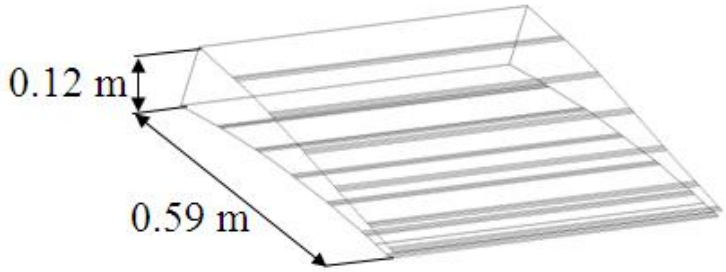

(b) Morphing trailing edge geometry

Figure 4.4: Inboard flap with active camber capabilites

The inboard flap had a constant chord of 1.108 m (28% of the wing chord) and a span of 5.52 m. The front part of the flap included the front spar, located at 30% of the chord, and twelve uniformly positioned flap ribs, while the flap rear spar was located at 47% of the flap chord.

The rear part of the flap structure, from the flap rear spar to its trailing edge, was designed to be flexible with active camber capabilities to further increase the lift during the take-off and landing phases. The chord of the morphing rear part was 0.59 m, corresponding to 53% of the flap chord, and had a maximum depth of 0.12 m measured at the rear spar.

No material properties were specified for the inboard flap, hence the materials selection was conducted as part of the preliminary analysis of the morphing flap structure in Chapters 5 and 6.

Both metallic and composite materials were considered for the skins and stringers. The skins and stringers thicknesses were set in the FE models presented in Section 5.2.1 following a preliminary analysis, similar to the one conducted by Morishima [108]. The metallic skin was made of aluminium 2024-T81 (Al) 2 mm in thickness, reinforced by 5 I-shaped aluminium stringers for each panel. The stringers had web and flanges of 12 mm and a thickness of 3 mm. Two composite skins were considered, made respectively of glass fibre reinforced plastics (GFRP) and carbon fibre reinforced plastics (CFRP). Both the composite skins were made of 12 layers having stacking sequence $[\pm 45/0_3/90]_s$. For the glass fibre skin, the ply thickness was equal to 0.25 mm and the skin panels were reinforced by 5 I-shaped stringers, made of aluminium, similar to the ones in the metallic skin. For the carbon fibre/epoxy skin, a high strength laminate (Hexply 8552/IM7) was considered. The ply thickness was equal to 0.184 mm and the skin was reinforced by 5 I-shaped carbon fibre/epoxy stringers. Table 4.3 summarises the material properties of the different materials adopted in this study.

Material	E_1 (GPa)	E_2 (GPa)	G_{12} (GPa)	ν_{12}	X_t (MPa)	X_c (MPa)	Y_t (MPa)	Y_c (MPa)	S (MPa)
Al	72.4		28	0.33		450			295
GFRP	39	8.6	4	0.25	1080	620	39	128	89
CFRP	164	10	5	0.3	2720	1690	111	250	80

Table 4.3: Inboard flap material properties

The flap structure was supported by a link-track flap deployment mechanism, similar to the one mounted on the Airbus 320 series. The deployment mechanism, shown in Figure 4.5, consisted of a forward link and a straight track.

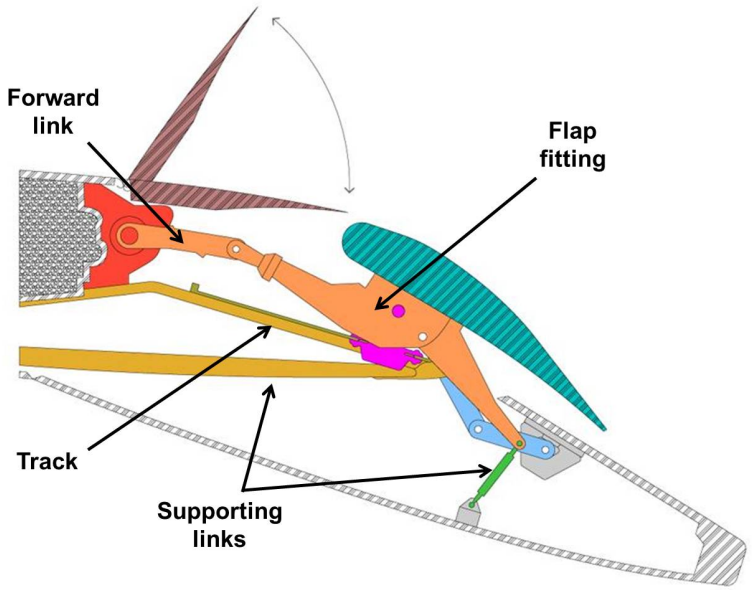

Figure 4.5: Parts composing the link-track deployment mechanism [109]

During the deployment, the trailing edge flap goes from the stowed position to the fully deployed configuration by means of a rotation plus a downward sliding. The forward link had the role of a drive link; a rotary actuator integrated at its pivot point provided the actuation load to move the flap. The lower end of this link was attached to a flap fitting below the flap. When the drive link rotated the flap and pushed it downwards, the flap was able to ride on the straight track thanks to a roller carriage attached at the same flap fitting with a pinned joint. As Rudolph points out in [11], the resultant of the aerodynamic forces for a single slotted flap is usually at around 32% of the flap chord. For this reason, the attachment point between the flap fitting and the roller carriage was located at about 30% of the flap chord in order to minimize the overturning moment caused by the air load. The straight track was also sloped downwards and supported by beams extending from the wing main structure.

The geometry of the flap deployment mechanism was obtained by scaling the dimensions of the A320 mechanism based on the flap chord [11]. The configuration considered corresponded to the fully deployed position of the flap, with 35° of rotation. All the parts constituting the mechanism were made of steel. A preliminary study ensured the mechanism was able to withstand the aerodynamic load from the flap.

4.2 The Aerodynamic Pressure Load

4.2.1 Deflection Shape Requirements for the Morphing High Lift Devices

The SADE wing with morphing high lift devices aims to achieve laminar flow, which is a highly desirable condition, because it generates less skin friction and leads to an improved lift over drag ratio compared to non laminar flows.

The ideal laminar wing would have a gapless leading edge and a smooth surface curvature, in order to reduce disturbances to the flow and to prevent its transition to turbulent flow. In conventional wings, however, the use of high lift devices and the typically high angles of attack induce strong suction peaks that destroy flow laminarity. A gapless morphing leading edge device would lead to a significant drag reduction and better lift over drag ratio at take-off, also helping to reduce airframe noise. Moreover, a continuous change of curvature for the upper wing surface would help to avoid the leading edge flow separation and the consequent reduction of performance. Similarly, a blunt nose would be preferable since a small nose radius could lead to strong suction peaks leading to turbulence. On the other hand, a gapless leading edge device offers a worse aerodynamic performance than a slotted device. For this reason, a smart trailing edge device is also designed to improve the overall wing performance.

Keeping in mind these design requirements, the desired deflected shape of the high lift devices was determined through an an aerodynamic force optimisation over the airfoil section conducted by two partners of the SADE Project, respectively the DLR and the CIRA research institutes for the leading [110] and trailing edge devices [111]. The optimisation was conducted assuming a two-element airfoil characterised by a main wing box with droop nose, and a single slotted Fowler flap. The objectives of the optimisation

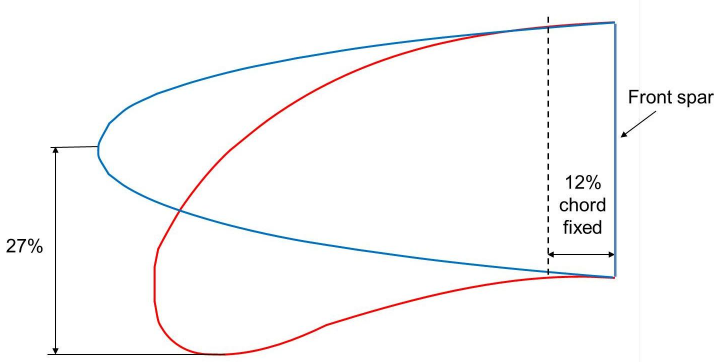

Figure 4.6: Leading edge deflection requirements

included the increase of the maximum lift coefficient C_{L_max} and of the maximum angle of attack α_{max} and an improvement of the lift over drag ratio L/D.

The desired deflected shape for the leading edge device of the SADE wing is represented by a rigid part, corresponding to the 12% of the leading edge chord, situated close to the front spar, and a displacement and change of curvature at the nose (see Figure 4.6). The maximum vertical displacement at the nose was set as 27% of the leading edge chord, corresponding to 21 cm, while the desired curvature (radius) of the nose was doubled with respect to the original shape.

A morphing trailing edge flap with a flexible rear end was considered to increase the wing camber in high lift configuration. The additional camber will determine a lift increase during take off and landing. Moreover, the smart trailing edge could be potentially employed also during cruise for minor shape adaptations, to reduce the off design effects, for load alleviation and roll augmentation. For the SADE trailing edge flap, the maximum vertical displacement required at the trailing edge was equal to 7% of the flap chord, corresponding to 7.89 cm, to be achieved together to the preliminary requirement of $\pm 25°$deflection at the trailing edge.

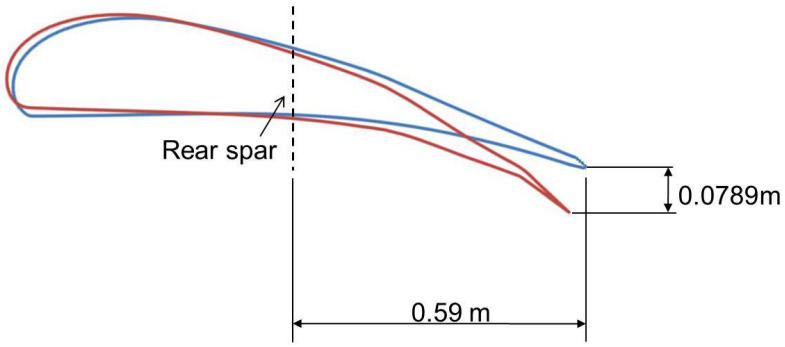

Figure 4.7: Trailing edge flap deflection requirements

4.2.2 Aerodynamic Pressure Load Calculation

The aerodynamic pressure load over the wing section was obtained from a computational fluid dynamics (CFD) simulation over a 2D airfoil section in different configurations.

Two different flight conditions were considered: cruise and landing. At cruise, in clean wing configuration, the aerodynamic pressure load was calculated at 31000 ft for a flow velocity of Mach 0.8. For the landing case, the conditions at the beginning of the descent phase were considered, characterised by an altitude of 20000 ft and an air temperature of 248.6 K. The wing angle of attack was set at 12°, with a Mach number of 0.15 and a Reynolds number of 7×10^6.

Figure 4.8: Airfoil in clean configuration during cruise (Model 1)

Different airfoil configurations were investigated: airfoil in cruise, having a clean configuration, with no high lift devices in operation (referred to as Model 1 and shown in Figure 4.8), and two high lift configurations, shown in Figure 4.9, of airfoil with flap deployed and leading edge in neutral position (Model 2) and airfoil with both leading edge and flap in operation (Model 3).

(a) Airfoil with flap deployed and neutral leading edge (Model 2)

(b) Airfoil with both leading edge and flap deployed (Model 3)

Figure 4.9: Airfoil in high lift configuration

The graph in Figure 4.10 shows the pressure distribution for the 2D airfoil in the three different configurations [112]. Although the pressure distribution in clean configuration will not be used for the analysis of the morphing flap, it has been reported for comparison purposes.

The blue continuous curve for Model 3 in Figure 4.10 represents a typical landing configuration with high lift devices fully deployed, where the selected leading edge device is the SADE droop nose following the deflection prescribed in Figure 4.6. In order to assess the effect of the morphing flap compared to a conventional deploying device, an additional configuration having the airfoil with leading edge deflected and flap not only deployed but also morphed was considered and is shown in Figure 4.11.

The graph in Figure 4.11 shows the combined effect of the morphing high lift devices on the pressure distribution along the airfoil, compared to the configuration with droop nose and flap only rigidly deployed. The use of a morphing leading edge stabilized the flow and led to a gentler pressure recovery, while the flap contributed to increase the lift generated. An overall lift increase of 121% was achieved for the case with droop nose and flap morphed.

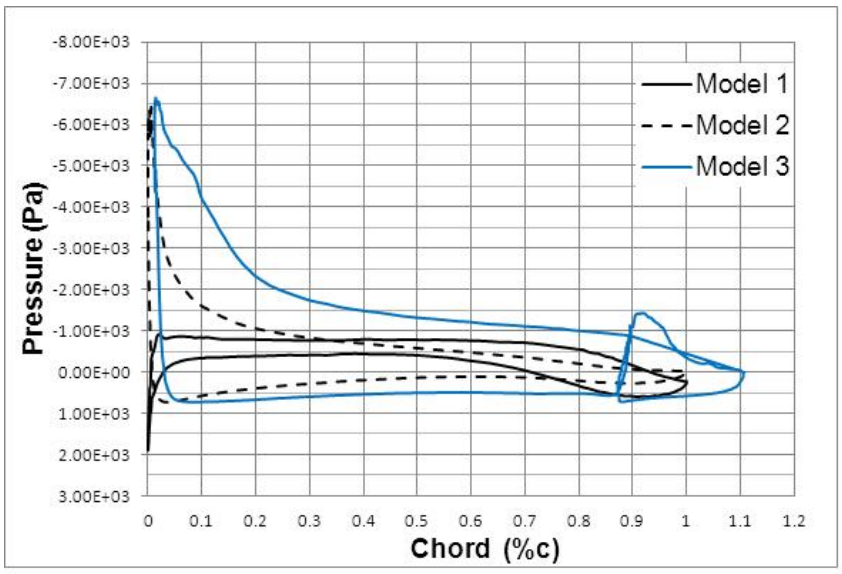

Figure 4.10: Pressure distribution over the 2D airfoil in different configurations (Pa) [112]

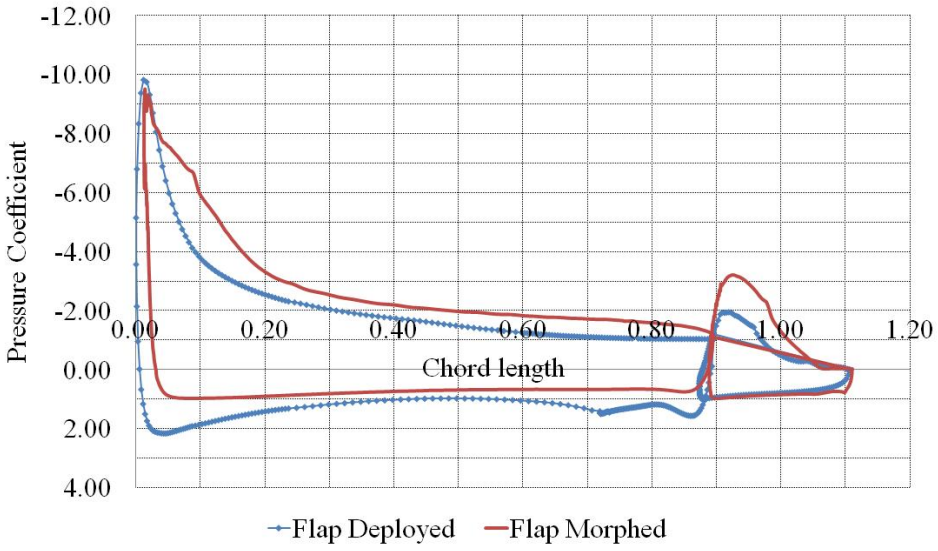

Figure 4.11: Aerodynamic pressure coefficient on the wing: comparison between the flap deployed and the flap deployed and morphed configurations

This page is intentionally left blank.

CHAPTER 5

Design and Modelling Approach for the Morphing Trailing Edge Flap

This chapter presents the novel design developed for the morphing flap with internal actuation mechanisms and illustrates the approach followed for the modelling of the morphing flap structure.

The innovative design proposed for the flap internal actuation mechanism is presented in Section 5.1. The actuation mechanism, based on the principle of eccentuation, was integrated in the flap device by bringing some significant design modifications to the trailing edge internal structure, as discussed in Section 5.1.2. These modifications included the replacement of the rib structure, the use of an open sliding trailing edge to ensure a uniform and smooth deflection and the inclusion of internal connections to preserve the airfoil shape while undergoing deflection.

The radical changes to the conventional flap structure required the set up of a specific modelling analysis approach in order to evaluate the structural behaviour of the morphing flap, as specified in Section 5.2. Special interest was given to the translation of the proposed design into a finite element model for detailed structural analysis.

In Section 5.3, the effect of the structural modifications introduced in Section 5.1.2 is discussed and the preliminary findings for a simplified flap model are presented. The benefits of the innovative open sliding trailing edge are shown and a novel procedure is proposed for the determination of the internal actuation loads required to deflect the structure and to conform to a desired target shape. An analysis is conducted on the internal connections to investigate their effect on the structural stiffness and to identify the most promising design solution.

Finally, Section 5.4 presents the details of a demonstrator model built to prove the feasibility of the design concept.

5.1 Design of the Morphing Flap with Internal Actuation Mechanism

5.1.1 The Eccentric Beam Actuation Mechanism

An eccentric beam actuation mechanism (EBAM) was specifically designed to deflect the morphing trailing edge. The principle of the eccentric actuation was initially developed in the 1970s within the DARPA project [27] to convert a rotational motion into a vertical displacement. In the original design, a bent beam called eccentuator was rotated by an electric servomotor at one of its ends. The other end, free to move, rode on a bearing surface, which was forced to move up or down depending on the beam rotation and consequently pushed the trailing edge skin downwards (or upwards, depending on the direction of rotation), as illustrated in Figure 5.1. A rotation of 90° allowed to achieve the maximum possible deflection of the surface. The eccentuator design was subsequently revisited by Muller [55] as part of the ADIF project.

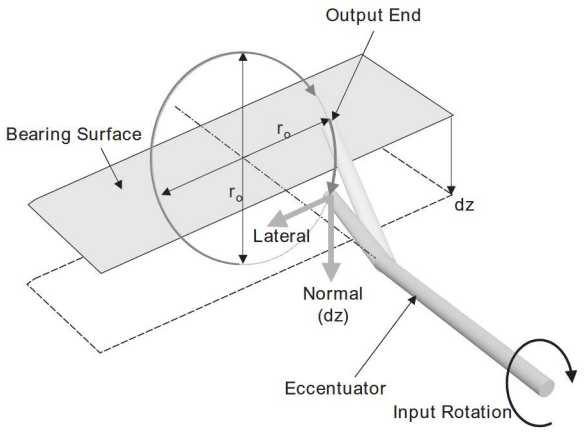

Figure 5.1: Eccentuator basic principle [27]

In this study, the DARPA/ADIF concept has been radically modified and adapted to the current morphing flap structure. In the proposed design, the eccentric beam actuation mechanism consists of a curved beam having discs of various size mounted along its length at different chordwise locations (see Figure 5.2). The presence of the discs (also known as cams) represents a significant improvement compared to the DARPA original concept, as the discs connect the beam to the flap skins and ensure the transfer of the actuation load from the actuation system to the structure in several points along the chord.

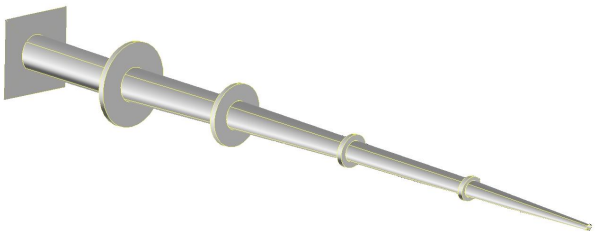

Figure 5.2: The eccentric beam actuation mechanism (EBAM): curved beam and discs

Both the eccentric curved beams and the discs were made of aluminium. The curved beam was a tube which diameter was gradually reduced from the rear spar of the flap to its trailing edge to fit into the smaller available space, varying from 0.034 m at the root to 0.008 m at the tip, while the beam thickness went from 4.5 mm to 2 mm.

The curved beam was mounted at the rear spar of the flap, where a rotary actuator provides the power necessary to set the beam into rotation and ensures that it remains in place once the desired shape has been achieved. When the beam is rotated, the discs push the skin downwards and force it to deform. Both the curved beam and the discs have been designed to ensure that the skin deformed following the desired deflected shape at any rotational angle and the discs have continuously varying radii to allow a smooth deflection. Each disc is located in correspondence of a couple of skin stringers, which provide a surface along which the disc can slide, acting as a rail track. Figure 5.3 shows the assembly of the eccentric beam mechanism and the trailing edge skin.

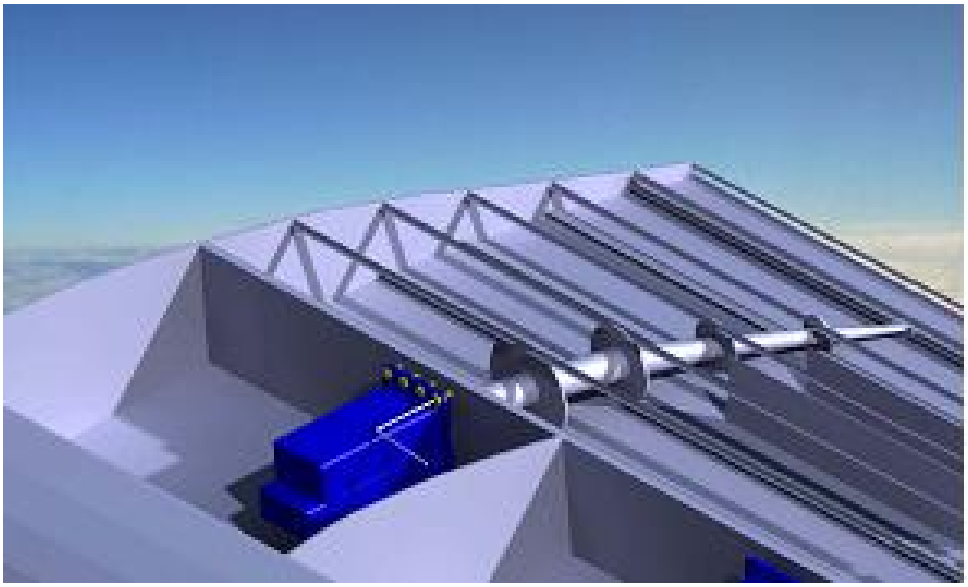

Figure 5.3: Eccentric beam actuation mechanism integrated in the flap structure

To ensure the continuity of the movement and the contact between discs and stringers, the discs have been arranged at an angle respect to the beam axis, as shown in Figure 5.4. As a result, when the beam rotates, the discs move in a direction parallel to the stringers (see Figure 5.5). The discs were not perfectly circular, but had a continuously varying radius to accomodate the small changes in the distance between beam and skin during deflection and to ensure that a smooth deflection shape was achieved. During the design phase, a linear curvature rate was assumed between the neutral and final deflected shape.

In order to meet the deflection targets specified in Section 4.2.1 along all the flap span, several eccentric beam actuation mechanisms have been arranged in the rear part of the flap with a pitch of 0.5 m one from each other.

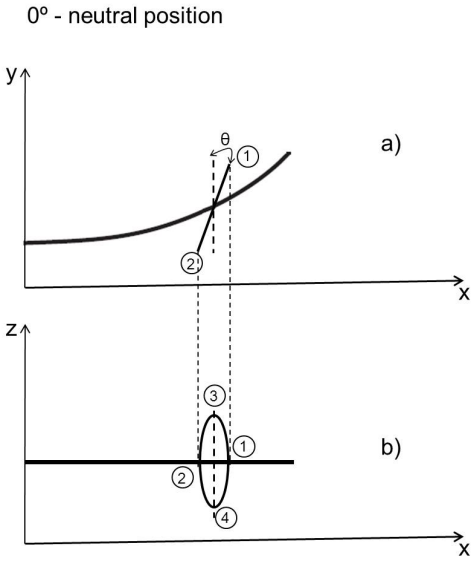

Figure 5.4: Beam in neutral position: a) view from top; b) view from side

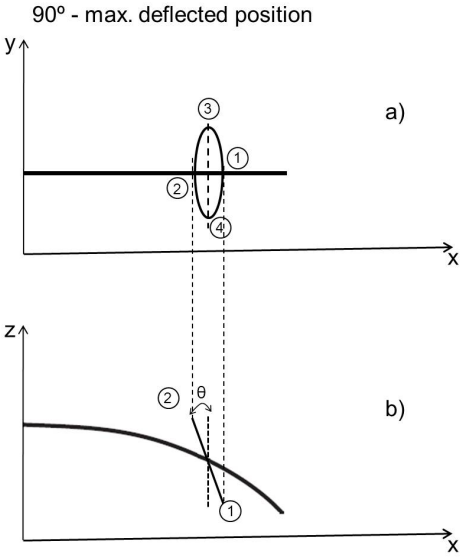

Figure 5.5: Beam in the 90° rotated position: a) view from top; b) view from side

5.1.2 The Modified Flap Internal Structure

A series of changes were made to the conventional internal structure of the flap in order to generate an effective and functional design for the morphing trailing edge with integrated eccentric beam actuation mechanisms. The design improvements implemented on the flap are listed below and will be addressed in detail in Section 5.3.

- **Use of the eccentric beam actuation mechanism as internal supporting structure**
  Firstly, no rib element was included in the rear part of the flap as they would make the flap structure too stiff and inadequate for morphing. The absence of the ribs was partially compensated by the discs connected to the eccentric beam, which contributed to maintain the flap trailing edge skins into the desired shape under the effect of the aerodynamic pressure load. The eccentric beam actuation mechanism has not only the role to provide the actuation load required for morphing, but also to offer support to the flap skin panels.

- **Open sliding trailing edge**
  Due to the different curvature of the upper and lower skins, trying to achieve a vertical deflection of the flap has the effect to generate a relative sliding of the skins. This effect becomes more evident when large vertical deflections are required and, due to the fact that the skins are connected at the trailing edge, it compromises the capability of the flap to achieve a uniform deflection shape. To eliminate this negative phenomenon, in this thesis an open sliding trailing edge is proposed, where the upper and lower skins instead of being rigidly connected are free to slide one over the other during the flap deflection. The unsuitability of the conventional closed trailing edge and the potential of the open sliding trailing edge are discussed in Section 5.3.1.

- **Additional internal connections**
  The proposed eccentric beam mechanism acts by pushing the lower skin of the flap into the desired deflection shape. However, in order to deflect the whole flap up to the required configuration, additional connections were required to force the upper skin to follow the lower one during the deflection. Moreover, since the areas between the discs of the actuation mechanism are no longer supported by the ribs, these connections contributed to prevent any undesired bubbling effect under the aerodynamic pressure load and to preserve the airfoil section during deflection. The additional internal connections contribute to transfer the actuation load from the eccentric beam to both skins. They also react the upwards pulling effect exterted by the aerodynamic pressure load to ensure the structural integrity of the morphing trailing edge and its functionality in the flap operative conditions.

5.2 Modelling and Analysis Methodology

The morphing flap considered in this study presents some unique features if compared to a conventional, non morphing high lift device. For this reason, the standard analysis approaches adopted for conventional structures are not always appropriate and able to

provide a comprehensive analysis of all the different aspects involved in the study of a morphing structure. The internal eccentric actuation mechanism and the changes implemented to the trailing edge internal structure to obtain a structure suitable for morphing resulted in the presence of parts not rigidly connected one to the other, such as the discs sliding over the stringers and the skins sliding over each other, and the morphing requirements led to changes to the structural stiffness and load distribution compared to a conventional flap design.

A preliminary analysis has been conducted on some peculiar aspects of the morphing flap, such as the effect of the open trailing edge on the flap deflection, the evaluation of the actuation loads required to deflect the structure up to the desired shape and the effect that the internal connections have on the structure as a whole. Subsequently, the structural behaviour of the flap has been investigated in detail using the finite element method: the deflection shape achieved and the level of stress and strain in the structure have been evaluated under the effect of the external aerodynamic load and the internal actuation. The interaction between the morphing flap and the airflow has been modelled to assess the effect of the aerodynamic load on the flap structure. Finally, the actuator design has been optimised to achieve the optimum deflected shape and the structural skin properties have been tailored to meet the shape requirements without violating the structural design constraints.

5.2.1 Finite Element Modelling of the Morphing Trailing Edge

The finite element method was the main method of analysis adopted in this study because it allows a detailed investigation of the complex interactions between the structural components and a comprehensive analysis of the morphing flap structure under the effect of aerodynamic and actuation loads. This section provides a description of the different models and modelling techniques adopted.

The modeling of the flap internal structure in a suitable way represents the first fundamental step of the FE analysis conducted in this research work. The main concern of the FE modelling process was to correctly represent the morphing flap structure to capture its structural behaviour without excessively increasing the complexity of the FE model. Three separate finite element models were built, each of them representing the flap structure with a different level of detail.

1. **Skin only trailing edge section**
   The first FE model considered a section of flap having a spanwise lenght of 1 m, extending from the rear spar to the trailing edge. Only the flap skin panels were modelled.

2. **Trailing edge flap section with EBAM mechanisms**
   The second FE model considered again a 1m span section of the flap trailing edge, with the addition of three eccentric beams with a pitch of 0.5m one from the other. The model included the curved beams, the discs and their connection to the upper and lower skins. Figure 5.6 shows the FE model of the 1 m span trailing edge section with EBAM devices. On one side of the flap model, since only a 1 m section of the flap was considered, the available space did not allow to fit a complete curved beam so a straight beam was included instead for analysis purposes.

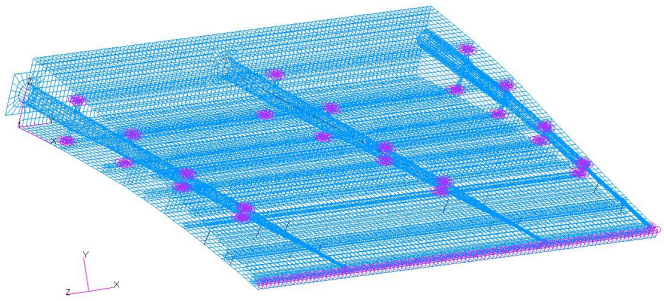

Figure 5.6: Finite element model of a 1 m span rear portion of the flap

3. **Inboard flap model with EBAM mechanisms**
   A model of the complete inboard flap, having a span of 5.52 m, was also built. The model included the front part of the flap, with the front spar and twelve uniformly positioned ribs, the rear spar and the trailing edge part with the integrated eccentric beam mechanisms to provide the actuation. The internal structure of the morphing portion was fully modeled including discs, open trailing edge and internal connections. The flap was supported by two link-track deployment mechanisms located at 30% and 70% of the flap span respectively. The link-track mechanisms were considered fixed in the fully deployed configuration at 35° of rotation of the flap.

4. **Inboard flap model with EBAM mechanisms in deflected configuration**
   A model of the inboard flap in deflected configuration was built to investigate the influence of the higher aerodynamic pressure on the morphed structure and the effect of the deflection on the overall structural stiffness.

The commercial software Patran/Nastran was chosen to generate the FE models of the structure and to investigate the structural behaviour of the flap in both static and dynamic conditions.

The flap skin panels, the rear spar, the stringers flanges and webs and the deployment mechanism were modelled as QUAD4 shell elements. At the trailing edge, the upper and lower skin panels were disconnected one from the other to allow sufficient sliding of the skins to achieve a uniform deflection along the flap. A different type of connection was hence required between the upper and lower skins to ensure the structural integrity of the flap under the effect of the aerodynamic load. Some possible practical ways to implement such connection are presented in Section 5.3.1. In the finite element model, the connections were represented by Multi Point Constraints (MPCs). The MPCs are non physical connections between two or more nodes which specify the relative motion of one node with respect to the others. For the trailing edge, the skins were allowed to slide one over the other along the chord and also to undergo small spanwise displacements during deflection; the nodes of the plates at the trailing edge were tied together with MPCs, so that every movement in the vertical plane was restrained and the distance between the skins remained unchanged.

For the models which included the internal actuation mechanism, the eccentric beams were modelled as QUAD4 shell elements, while the discs mounted on the eccentric beams

were modelled as 1D elements having beam properties, rigidly connected to the curved beam on one side and able to slide over the skin stringers on the other. Similarly to the open trailing edge, a sliding connection was set between the disc and the stringer flanges by using a set of MPCs between the corresponding elements on the disc and stringer. Two MPCs per disc were generated, to represent the connection to both the upper and lower skin, leading to a total of 10 MPCs per curved beam holding the skins in place and transferring the load during the deflection. In each of these MPCs, the direction orthogonal to the plane of the disc and stringer flanges was set as the direction of restrained motion, while the motion in the other two directions was unrestrained. For all the flap models, both the curved beams and the discs were made of aluminium.

Additional connections between the upper and lower skin were introduced. Sections 5.3.3 and 5.3.4 present the study conducted to select the most suitable connection and specify how they were represented in the finite element model.

5.2.2 Morphing Trailing Edge Experimental Model

A demonstrator model was built to prove the effectiveness of the design concept and to investigate from an experimental point of view the issues related to the innovative flap structure considered. The main focus of the experimental investigation was the assessment of the load-deflection relation for the trailing edge flap and the influence of the internal connections on the flap stiffness. The details of the model and an overview of the main findings are given in Section 5.4.

5.2.3 Aeroelastic Analysis

The fluid-structure interaction between the flap with morphing trailing edge and the airflow has been investigated to asses the effect of the air pressure on the flap deflection. Different approaches to the calculation of the aerodynamic load have been considered, including ESDU methods, panel method and CFD analysis. The interaction between the flap structure and the airflow has been investigated by setting up an iterative analysis involving the finite element method and the Xfoil software based on panel method. The aeroelastic analysis of the flap is discussed in Chapter 7.

5.2.4 Optimisation Analysis

The optimisation approaches found in literature and conventionally adopted for aircraft structures are not suitable for the optimisation of the morphing flap with internal actuation mechanism. In fact, the additional deflection shape requirements have to be considered in the analysis and the internal actuation mechanism itself needs to be included in the optimisation process. Within this research work, a new procedure has been developed for the optimisation of the morphing structure. Firstly, a study has been conducted to determine the optimal location of the discs on the eccentric beam, i.e. the optimal loading positions chordwise for the flap. An analytical approach based on beam theory has been implemented for the optimisation of the internal actuation mechanism

and has been compared to the results from finite element analysis. Subsequently, the material properties of the flap structure have been optimised by implementing an iterative approach which combines the results of the finite element analysis with a gradient based optimiser. The optimisation of the morphing flap is detailed in Chapter 8.

5.3 Preliminary Analysis of the Morphing Flap

A preliminary investigation was conducted on the innovative morphing flap structure described in the previous sections. The main objectives of this analysis were the assessment of the impact that the design improvements such as the open trailing edge and the additional connections have on the structural behaviour of the flap and the evaluation of the actuation load required for deflection. The analysis was conducted on the FE model of the flap skins only.

5.3.1 The Open Sliding Trailing Edge

A preliminary study showed that when large vertical deflections were imposed to the trailing edge of the morphing flap, an undesirable shape was achieved. The skins exhibited a change in their curvature along the chord and a series of bubbles appeared on the lower skin surface.

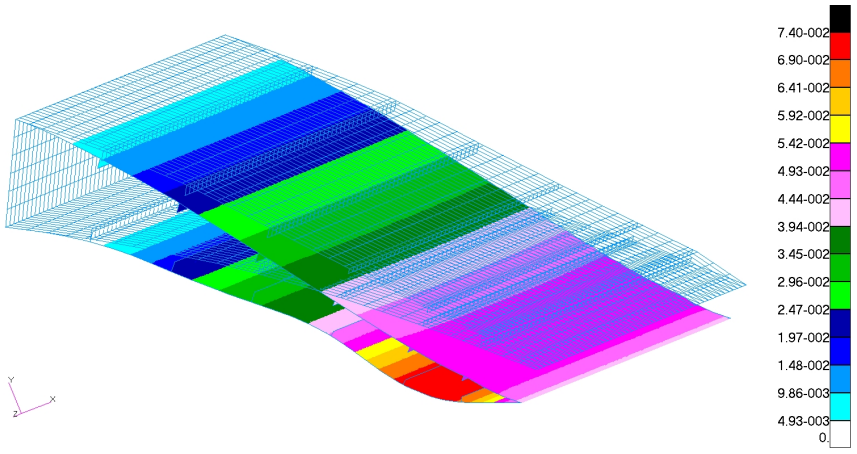

Figure 5.7: Closed trailing edge

Figure 5.7 shows the deflected shape of the flap with closed TE obtained from the FE analysis when the aerodynamic load is applied. It can be observed that at a certain location along the chord the skins went from a convex to a concave curvature. Moreover, a series of bubbles appeared on the lower skin surface, indicating that the constraints in terms of displacement applied to the structure were too rigid to allow it to meet the required shape in some of its points. Another negative effect of the large bending that can be noted from Figure 5.7 is the change in the cross section of the TE flap, with the upper and lower skins becoming closer after the deflection.

When a bending moment is applied to a thin-walled, cambered, long structure such as the current flap model, undesired crushing components will arise in it together with the

expected compressive/tensile components of the force due to bending. This negative phenomenon, called "Brazier effect" [113], is a consequence of the nonlinearity in the bending response of the structure. As a result, the upper and lower skins of the flap become closer and eventually crush as the imposed load and deflection are increased, similarly to what happens in a circular cylindrical tube subject to large bending. As pointed out by Cecchini and Weaver [114], although the Brazier effect is unlikely to occur as a failure mode, it has a strong influence on the local buckling of the skins and material failure, as well as an effect on the dynamic behaviour because of the nonlinearity in the bending response [114].

The limited sliding between the upper and lower skins at the trailing edge played an important role in the development of the double curved shape. A new design was hence adopted: the upper and lower skins of the flap were separated one from the other, creating an open trailing edge. The flap with the new open sliding trailing edge, however, requires additional connections between the upper and lower skins in order to maintain its structural integrity under the aerodynamic and actuation loads and to compensate for the stiffness reduction caused by the open trailing edge. The flap skins were constrained to have no relative vertical displacements, but were left free to slide one over the other in chordwise direction during the deflection.

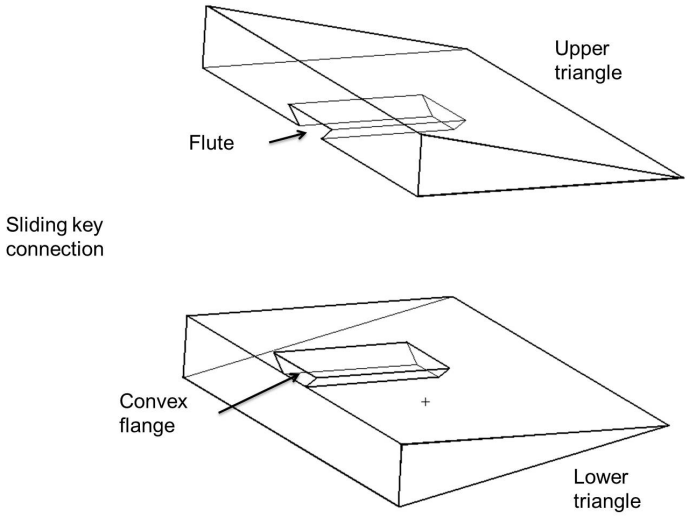

Figure 5.8: Connection between upper and lower skins at the trailing edge

Figure 5.8 illustrates a possible way to implement the sliding connection at the flap trailing edge. The upper and lower skins end with a solid part having a triangular shape. The two solid parts are kept together with a sliding key connection: a flute is obtained in one of the two solid triangles and the other solid part is equipped with a convex flange having a shape matching that of the flute. This connection allows the relative sliding of the skins and, at the same time, ensures that the skins remain connected at the trailing edge.

Other possible ways to connect the two skins, not investigated in this thesis, could involve the use of a rubber insert at the trailing edge.

5.3.2 A New Procedure for the Actuation Loads Estimation

The analysis of the morphing trailing edge flap presented the problem of finding the loads required to achieve a prescribed deflection shape. While the determination of the structural displacements under a certain imposed load is a relatively easy procedure which can be implemented in a specific nonlinear static solver, the inverse problem arising for the case of a morphing structure requires a different approach. First of all, an analytical prediction of the required loads could be obtained only for a restricted number of simplified problems, where the structural properties are all known and the structure can be treated, for instance, as a beam. The trailing edge flap considered in this study, however, has a complicated internal structure and undergoes a variety of loads, such as distributed air pressures and actuation forces. For these reasons, the finite element analysis was considered the most convenient approach to the problem. The presence of sliding between the components and the use of connections that affect the structural stiffness led to the choice of a non-linear type of analysis in order to correctly capture the structural behaviour. No standard procedure is currently available to determine the loads required to achieve a certain deflection shape. A new, two-step approach was implemented.

The approach represents an application of the virtual work principle and is based on the notion that the reaction force exhibited by the structure following the application of an imposed displacements represents the actuation force required to achieve that specific deflection. For the flap, the reactions to the application of the desired morphed configuration would hence represent the actuation load required.

In the first step, once the target deflected configuration specified in Chapter 4 had been provided, the desired vertical displacement in selected points along the chord was applied as an imposed displacement to the structure in those same locations. For the flap, the selected positions were the five disc-skin contact points, uniformly distributed along the chord. (This hypothesis will subsequently be relaxed in Chapter 8). A nonlinear Nastran run using Sol 600 was then performed to evaluate the reaction forces generated in these points following the forced displacement of the structure.

In the second step of the analysis, the reaction forces from FE analysis were applied as concentrated forces acting in the disc to skin contact points and the deflection of the flap under these loads was evaluated by using a geometrically nonlinear Nastran Sol 106 analysis. The results showed that the actuation loads determined following the proposed two-step approach were effectively able to morph the flap into the desired configuration.

The procedure described above for the determination of the actuation loads of the morphing flap is clearly related to the stiffness of the structure which, in turn, is influenced by the design selected for the internal structure. Hence, in order to assess the actuation load required to deflect the flap trailing edge, it is necessary to define the selected design in detail.

5.3.3 The Skin Connections

The flap with open trailing edge adopted to achieve a uniform deflected shape required some additional connections between the upper and lower skins to ensure its structural integrity was maintained under the effect of the actuation and aerodynamic loads and

to ensure the functionality of its actuation system. Without any connection, the upper and lower skins would not keep their relative distance during deflection; moreover, the aerodynamic pressure load acting on the skins would pull them apart. In addition, the skin connections would help to transfer the actuation force exerted through the discs on the lower skin to the upper skin.

An accurate design of the connections was required. In fact, an excessively rigid connection would limit the overall flexibility of the morphing TE flap, leading to a considerable increase of the actuation power or even preventing the flap from achieving the required deflection. On the other hand, a connection without adequate stiffness would not provide adequate flap structural stiffness to carry the external load and transfer the internal force between the skins. Any type of connection has a negative influence on the relative sliding between the upper and the lower skin, which is inevitably limited compared to the sliding in the case of no connections. The limitation introduced depends on two factors: the length of the connection itself and its capability to rotate with respect to its attachment points on the skin while the flap is deflected.
Different types of connection were considered, characterised by different structural properties. A simple way to connect the skins could be by using rods or beams positioned along the flap chord. The rod, pin jointed to the skin surfaces, would allow a certain sliding thanks to the rotation at the skin-connection attachment points during the deflection of the flap. The maximum achievable sliding between the skins in this case would be equal to the length of the shortest connection used. As a drawback, rods would allow the skin distance to change. Conversely, beam connections, clamped at the skin, would maintain the skin distance but substantially limit the achievable sliding and introduce additional stiffness into the structure. Both rods and beams have the disadvantage to cause a high stress concentration in the points of connection to the skins. As the connections are subject mainly to a tensile load, a thin layer of fabric material connected to the skins in spanwise direction could be used instead of point connections. This would prevent the skins from being pulled apart and would allow their sliding and a uniform deflection of the flap.

A study was carried out to assess the different types of skin connections in terms of actuation force demand. The types of connection discussed above were modelled and added to the structural FE model representing the flap skins to determine which of them provided the best compromise in terms of flexibility, effective load transfer, low actuation load and effectiveness in maintaining the structural integrity. In the FE model, it was also possible to simulate a connection that respects the ideal condition of unrestrained sliding by using a Multi Point Constraint. The MPC imposes a fixed distance between the skins by tiying together the displacement of the skin nodes in the vertical direction and does not constrain the displacement in the chordwise and spanwise directions. It must be noted, however, that this is a fictitious constraint, which does not fully represent a practical connection. Hence, it can be useful for comparison purposes but it does not represent one of the design alternatives.

The analysis was conducted considering one connection located at 2/3 of the flap chord distance from the rear spar, as shown in Figure 5.9.

The connections were assessed based on the actuation load required to achieve a fixed deflection of 0.08 m at the flap trailing edge. The reference data was represented by the actuation load required to deflect up to 0.08 m the lower skin of the flap, which

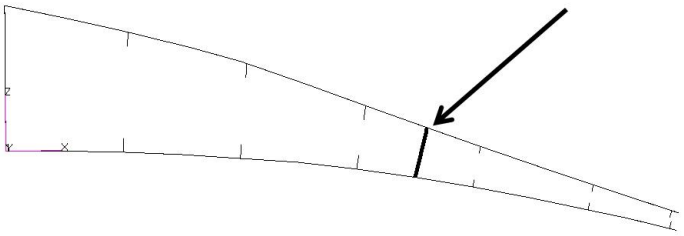

Figure 5.9: Position of the skin connection

was considered as a simple plate, clamped at one side in correspondence of the flap rear spar and not connected to the upper skin. The procedure described in Section 5.3.2 was used for the evaluation of the actuation loads. Table 5.1 summarises the actuation load required to achieve a vertical displacement of 0.08 m for different types of skin connection, when no aerodynamic load is applied to the flap model.

Type of connection	Actuation load required $[N]$
Single skin (no connection)	42.6
MPC	44.2
GFRP layer close to spar	95
Rod	97
GFRP layer close to TE	277
Beam	291
Two GFRP layers	545
Two GFRP layers + trailing edge sliding connection	861

Table 5.1: Actuation forces for different skin connections

Firstly, a numerical RBE2 type MPC was used to keep the skins together. RBE2 MPCs are clusters of rigid elements characterised by one independent node and several dependent nodes which are constrained to follow the displacements of the independent one. The actuation load required was very similar to the one for the single skin. However this constraint did not represent a realistic connection and for this reason it was replaced with a rod having a cross sectional area of 28 mm^2. The actuation load obtained for this case was more than twice the single skin actuation load. Similarly, a beam connection having the same cross sectional area and location of the rod was analysed, resulting in a much higher load. Both the rod and the beam solutions led to high local stresses arising in the skins. Moreover, the deflection shape achieved by the flap trailing edge was not uniform due to the presence of point to point connections and, for these reasons, these two types of connection were discarded.

Subsequently, thin layers of glass fibre/epoxy resin, 0.5 mm in thickness, were considered. These connections mainly presented a membrane behaviour and for this reason were modelled as QUAD4 elements having their bending degrees of freedom restrained. The GFRP layer provided a very promising uniform spanwise deflection of the flap, however, a single layer close to the trailing edge did not offer enough support for the skins at mid-chord. A second arrangement was hence considered, represented by two thin GFRP layers located at 1/3 and 2/3 of the chord. The actuation load obtained for this case

was considerably higher than all the others, however it offered a very good flap deflection shape. Finally, the two glass fibre/epoxy layers were coupled with a sliding constraint at the trailing edge, representing the open sliding trailing edge, to ensure that the initial flap shape and the vertical distance between the upper and lower skin were preserved during the deflection. This final arrangement presented the highest actuation force requirements, however it was able to meet the deflection shape requirements, as shown in Figure 5.10 and was hence selected for the flap design.

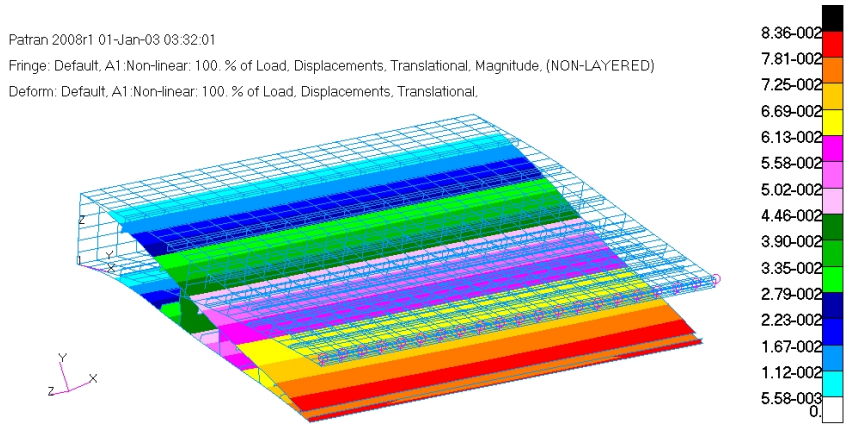

Figure 5.10: Model with glass fibre/epoxy layers and sliding connection at the trailing edge

5.3.4 Influence of the Aerodynamic Pressure on the Flap Structure

If the aerodynamic pressure load is applied on the flap trailing edge structure, the actuation load required to achieve the deflected shape was expected to increase. In fact, part of the actuation load would be needed to overcome the elastic reaction of the structure, while an add1itional contribution would be required to balance the adverse aerodynamic load. Table 5.2 compares the actuation load required to deflect the flap structure up to 0.08 m for the different skin connections previously considered, when the aerodynamic loads were applied to the model.

The percentage of the actuation load required to overcome the elastic reaction of the skins changed depending on the type of connection adopted, becoming gradually higher in correspondence of stiffer connection designs and peaking at 83.59% of the total actuation load for the arrangement with two GFRP layers and the sliding constraint at the trailing edge. Despite the increase in the actuation force, the application of the aerodynamic pressure to the structure gave a positive contribution to a uniform and smooth deflected shape. In fact, the aerodynamic pressure load and its upwards pulling action helped to reduce the undesired components of stress acting on the skins. From the analysis it was found that the connections close to the clamped section were in compression, while the ones close to the trailing edge were in tension. The undesired compressive stresses were the result of the skins being pushed closer to each other and their intensity was found to be lower when the aerodynamic pressure load was applied to the model. Hence, despite the actuation increase, the aerodynamic load had the beneficial effect to alleviate

Type of connection	Total actuation load required [N]	Load to overcome the elastic reaction of the skins(%)
Single skin (no connection)	121	35.21
MPC	199	22.21
GFRP Layer close to spar	135	70.37
Rod	518	18.72
GFRP layer close to TE	527	52.56
Beam	575	50.61
Two GFRP layers	668	81.59
Two GFRP layers + TE sliding connection	1030	83.59

Table 5.2: Actuation force requirement for different skin connections when the aerodynamic pressure load is applied

the compressive stress components arising in some of the connections between the skins while undergoing deflection.

5.3.5 The Connections between Skin and Discs

As shown in Figures 5.4 and 5.5, during the rotation, the discs experience small chordwise movements. A disc-skin connection should be able to allow these chordwise movements as well as to ensure the necessary sliding of the disc in spanwise direction during the rotation of the eccentric beam. Figure 5.11 shows a possible type of connection allowing both the chordwise and spanwise sliding. The discs were designed with a flange and were hence able to slide on the surface provided by the skin I-shaped stringers upper flange during the beam rotation. A small roller connected the disc and stringer flanges, which acted as a track.

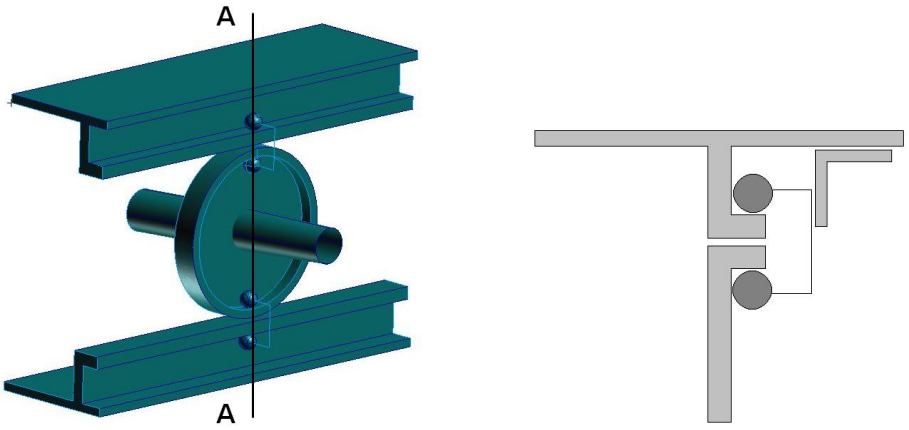

(a) Schematic representation (b) Side view - Section AA

Figure 5.11: Connection between skin and discs

In the flap structure, the design of a suitable disc-skin connection was complicated by

the small vertical space available between the skins. For this reason, the disc flanges were considered to be in contact with the I-shaped skin stringers with no other physical connection. The skin connections described in the previous Section 5.3.3 ensured that the disc-skin contact was mantained under the vertical pulling action of the aerodynamic load. The discs, on the other hand, were able to react the compressive loads and the crushing forces between the skins. The combined effect of the discs and the skin connections ensured that a constant distance between the upper and lower skins was mantained and that the discs were always in contact with the skins.

5.3.6 Actuation Loads on the Flap

The analyses presented in the previous sections have contributed to define the final design of the morphing flap and to specify the details of the structural assembly. The need to satisfy the deflection shape requirements and to achieve a smooth and uniformly deflected configuration have led to the choice of the open sliding trailing edge, while thin layers of glass fibre/epoxy have been chosen as the skin connections to preserve the shape of the airfoil section.

This section presents the evaluation of the actuation loads for the morphing flap with open trailing edge and thin layer connections. The analysis followed the procedure presented in Section 5.3.2. The use of a finite element model offered great flexibility and the possibility to investigate different skin materials and loading conditions on the flap. Three different skin materials were considered: aluminium, glass fibre/epoxy (GFRP) and carbon fibre/epoxy (CFRP). The aluminium skin panels offer good strength capabilities and low weight. Moreover, aluminium is easily machinable in the required geometry and allows to avoid all the complications connected to the use of composites. To evaluate the potential offered by composite materials in the field of morphing wing structures, the metallic skin was compared to a glass fibre/epoxy and a carbon fibre epoxy skins respectively. The carbon fibre/epoxy material was selected for its high specific strength properties. The glass fibre/epoxy material was chosen because it offers a elongation value of 4%, higher than carbon fibre/epoxy (1-2%). The high elongation capability could prove beneficial during the morphing of the trailing edge skins in order to achieve low strains in the skins.

The total actuation force required to deflect the flap structure in operative conditions will be obtained as the sum of two contributions: the actuation force needed to elastically force the skins into the desired shape and the actuation force required to overcome the aerodynamic pressure load. Initially, the displacements were imposed to the flap skins in absence of any other loading in order to assess the actuation force required to elastically deflect the structure. Subsequently, the process was repeated when the aerodynamic pressure load was applied to the flap to evaluate the impact of the air pressure on the actuation load required.

Figure 5.12 illustrates the five loading positions considered along the flap chord. Table 5.3 presents the loads required to deflect the trailing edge flap structure up to the target shape for the three skin materials. Both cases of structural deflection only and structural deflection plus aerodynamic load were assessed.

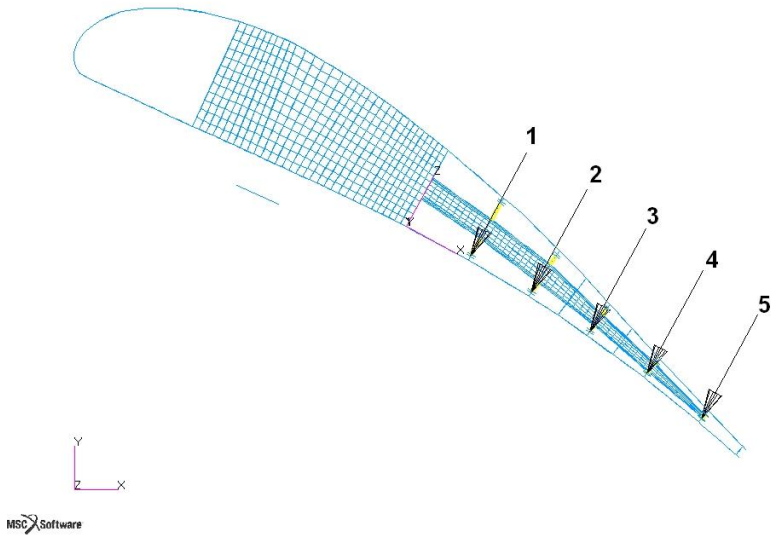

Figure 5.12: Loading positions along the flap chord

	Actuation Load Results $[N]$					
	Aluminium		GFRP		CFRP	
Loading Position	Structure	Structure +Airload	Structure	Structure +Airload	Structure	Structure +Airload
1	292	320	239	263	333	324
2	885	746	929	838	1210	1120
3	214	1220	222	1040	299	1270
4	891	1030	805	909	924	1030
5	551	707	547	679	680	883
	2883	4023	2742	3729	3446	4627

Table 5.3: Forces required to deflect the flap $[N]$

The graph in Figure 5.13 shows a comparison between the total actuation load requirements with and without aerodynamic loads included in the analysis. As expected, the inclusion of the air pressure determined an increase in the actuation load required. The fraction of actuation load required to elastically deflect the flap skins amounted to 71% of the total actuation for the aluminium skin, 73.5% for the glass fibre/epoxy skin and 74.5% for the carbon fibre/epoxy skin respectively.

Once the load required to deflect the morphing trailing edge was found, the corresponding torque needed at the curved beam root of the EBAM mechanism was calculated. The intermediate deflected shape between the neutral and the final configuration was assumed to be linearly varying with the rotation angle of the curved beam. For each angle of rotation, the torque was obtained by multiplying the estimated force by the moment arm, given by the distance between the centre of the disc and the centre of rotation of the beam.

Figure 5.14 shows the torque required to elastically deflect the flap skins with and without

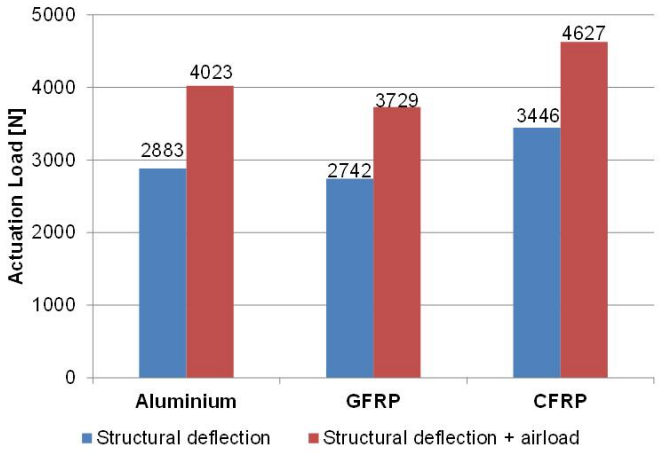

Figure 5.13: Actuation load required to deflect the structure with and without aerodynamic load $[N]$

aerodynamic pressure load on the flap and the total torque resulting from the sum of these two contributions for the cases of aluminium (a), carbon fibre/epoxy (b) and glass fibre/epoxy (c) skin materials. In all cases, the maximum torque requirement was reached in correspondence of approximately 45° rotation of the eccentric beam. The maximum total torque was equal to 58.2 Nm per beam for the aluminium skin and to 53.8 Nm per beam for the glass fibre/epoxy skin, while the carbon fibre/epoxy skin exhibited slightly higher requirements of 64.7 Nm.

The demanding design requirements specify that the full deflection of the flap must be achieved at a speed of $40°/s$, hence the eccentric beams must be able to go from their neutral position to the fully morphed rotation of 90° and back in 4.5 s. Consequently, the maximum power demand to deflect the skins at the prescribed deflection speed was equal to 40.6 W for the aluminium skin, 37.5 W for the glass fibre/epoxy skin and 45.1 W for the carbon fibre/epoxy skin. These data refer to a single EBAM mechanism. The total power consumption to deflect the inboard flap was obtained considering that 11 beams were distributed in the 5.52 m span flap structure. The total power consumption was estimated as equal to 446.6 W, 412.5 W and 496.1 W respectively.

5.4 Demonstration Model

A 1:1 scale demonstrator model was built to prove the effectiveness of the design concept. The demonstrator represented a section of the morphing trailing edge flap having 0.5 m span. Its main components included the rear spar, modelled as a C-section beam, the upper and lower skin panels and the internal actuation mechanism. All the structural parts were made of aluminium and were assembled using fasteners. The skins, 2 mm in thickness, were reinforced by 5 stringers; the eccentric beam actuation mechanism was manufactured by using a bent aluminium tube having 5 uniformly spaced discs welded to it.

The skin panels conformed to the airfoil shape prescribed by the SADE project. As

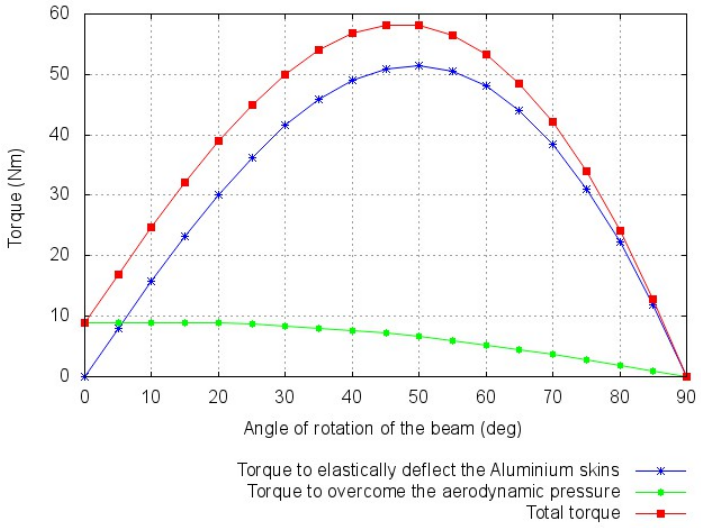

(a) Aluminium skin

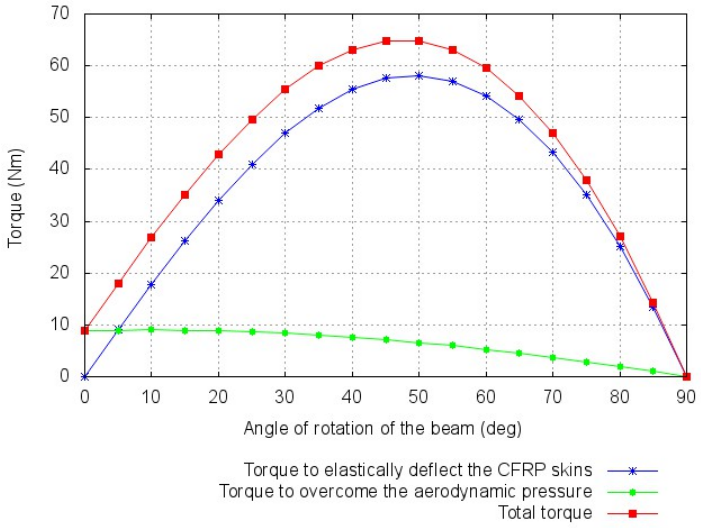

(b) Carbon fibre/epoxy skin

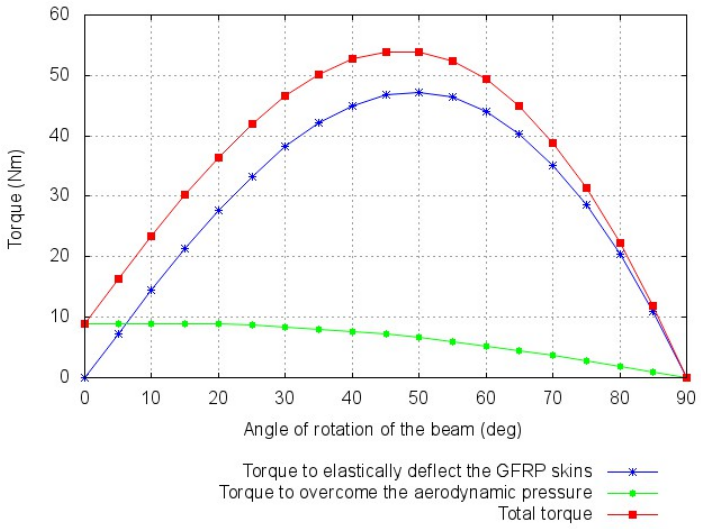

(c) Glass fibre/epoxy skin

Figure 5.14: Torque estimation for different skin materials: (a) aluminium; (b) carbon fibre/epoxy; (c) glass fibre/epoxy ($[Nm]$)

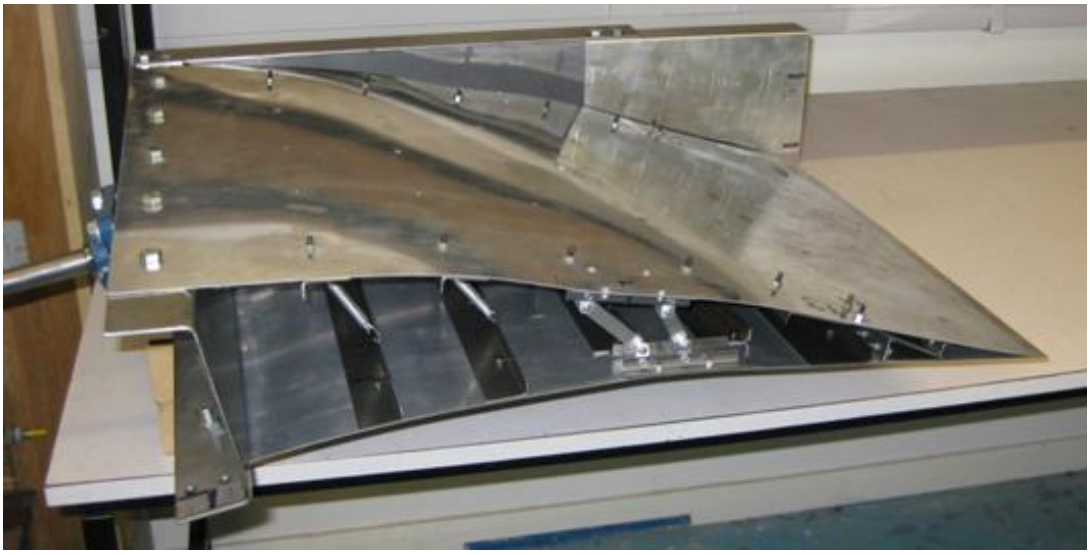

Figure 5.15: Flap demonstrator

specified in Section 5.3.1, the upper and lower skins were left open at the trailing edge and the final portion of the skin panels was shaped as two empty triangles able to slide over each other during the deflection, as shown in Figure 5.16.

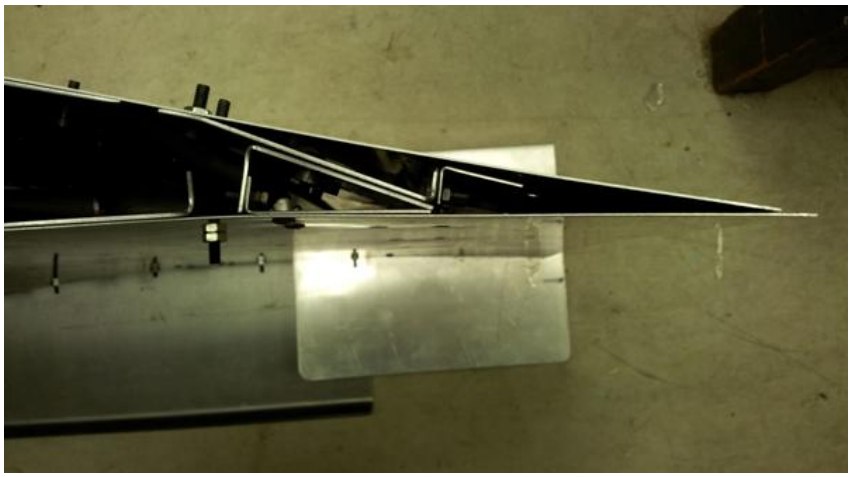

Figure 5.16: The sliding trailing edge of the demonstrator model

Spring connections between the skins were set as well as removable pin jointed connections on the two sides of the flap, presented in Figures 5.17 and 5.18, to preserve the flap shape during the deflection and to ensure the disc to skin contact.

The actuation mechanism was positioned at the mid-span of the trailing edge section. The curved beam extended from the flap trailing edge through the rear spar and ended with a handle to provide manual actuation, shown in Figure 5.19. A 90° rotation of the handle from horizontal to vertical position allowed the curved beam to go from the initial neutral configuration to the fully deflected one. A bearing was mounted at the rear spar to connect the handle to the curved beam and to ensure the transmission of the rotary motion.

The deflection study conducted on the demonstrator model consisted in applying a progressively increasing weight to the handle in order to generate a rotation of the curved

Figure 5.17: Internal structure of the flap

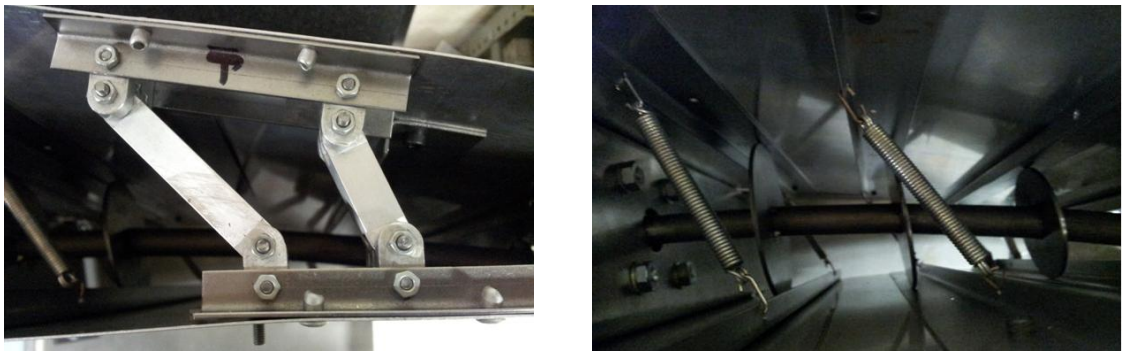

(a) Links between upper and lower skins

(b) Spring connection

Figure 5.18: Internal connections

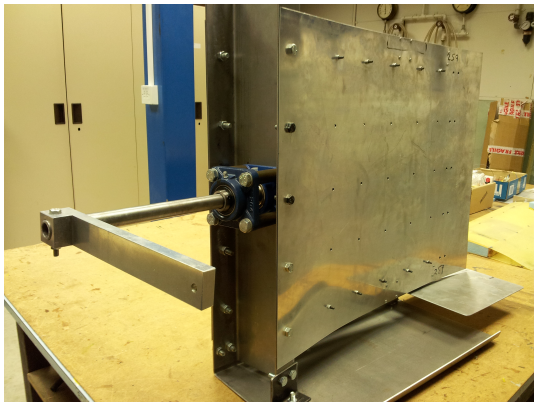

Figure 5.19: Handle and bearing connection to the curved beam for the application of loads

beam and, hence, a deflection of the flap skins. Due to time and budget constraints, the study considered a limited number of weight increases.

The demonstrator model was analysed for the two cases of pin jointed connections active and released. In the first step of the analysis, the flap demonstrator with all the skin connections in place was considered and a gradually increasing weight was applied to the handle until the desired deflection was reached at the flap trailing edge. Table 5.4 presents the weights applied and the corresponding deflection they generated. The desired deflection of approximately 0.075 m was achieved in correspondence of an applied weight of 4.036 kg.

Mass (kg)	Deflection (m)
0	0
1.371	0.028
2.433	0.046
3.340	0.061
4.036	0.075

Table 5.4: Mass-deflection data for the flap with internal connections

Subsequently, one of the internal connections pin jointed to the flap skins was released and the same weights presented in Table 5.4 were reapplied to the flap structure to assess the effect of the skin connection on the structural deflection. Table 5.5 presents the new deflection values. It can be noted how the maximum deflection was achieved for a weight of 3.34 Kg, 17% lower than the maximum load with connections in place.

Mass (kg)	Deflection (m)
0	0
1.371	0.039
2.433	0.0655
3.340	0.078

Table 5.5: Mass-deflection data for the flap with internal connections released

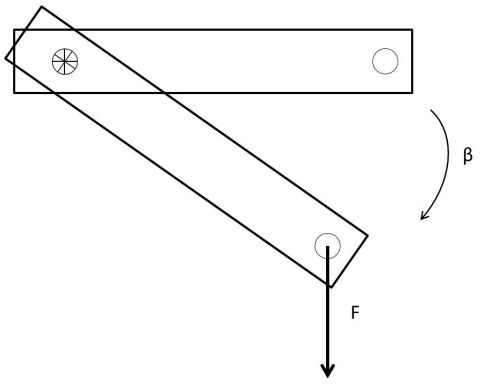

Figure 5.20: Handle with applied load

Let β be the angle of deflection of the handle measured from the initial horizontal position at each weight increase step, as illustrated in Figure 5.20 and R be the length of the

handle. For a generic position of the handle, defined by the angle β, the force F, due to the weights and directed vertically, generates a torque equal to:

$$T = FRcos\beta \tag{5.4.1}$$

For large angles of rotation, the torque T does not vary linearly with the displacement. Figure 5.21 shows the plot of the applied force to deflection relation exhibited by the flap model, nonlinear for large deflections.

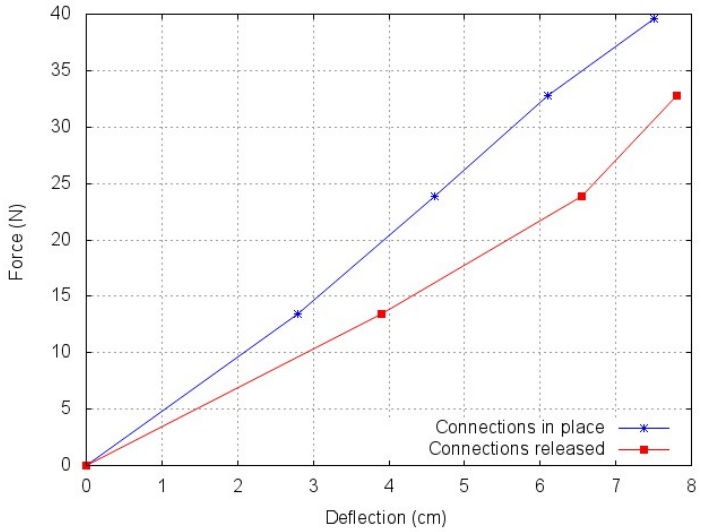

Figure 5.21: Force-displacement relation for the demonstrator with and without skin connections in place

The presence of the pin jointed connections between the skins affected the overall flap stiffness and, consequently, the maximum deflection achieved at the trailing edge of the flap model under the same actuation. Moreover, the connections influenced the shape of the flap section and the relative distance between upper and lower skins during the deflection. The distance between the upper and the lower skins was measured in different points along the flap chord for the two cases and differences between 1 and 3 mm were obtained.

Figure 5.22 presents the applied force to deflection relation exhibited by the flap FE model and the impact of the FE model connections release on the flap stiffness. Small differences between the flap demonstrator and the FE model, introduced with the objective to keep the manufacturing process fast and easy, led to some discrepancies in the actuation load values required for deflection. In particular, the use of thin layers of glass fibre/epoxy as the internal connections in the FE model, as opposed to pin jointed connections in the demonstrator, had a large impact on the actuation values.

The flap model proved that the eccentric beam concept was able to deflect the structure into the desired target shape. The actuation required to achieve the desired shape with and without pin jointed connections was measured to evaluate the stiffness increase generated by such connections. Figure 5.23 presents the outline of the deflected shape obtained for the cases of skin connections in place and released respectively.

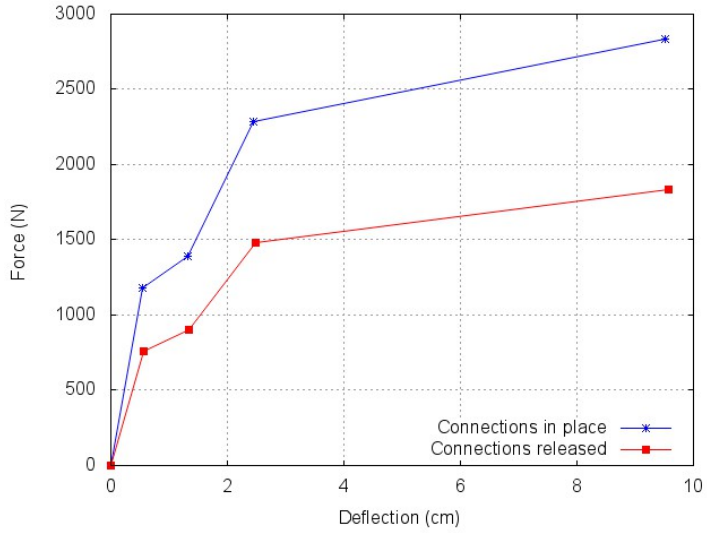

Figure 5.22: Force-displacement relation for the FE model with and without skin connections in place

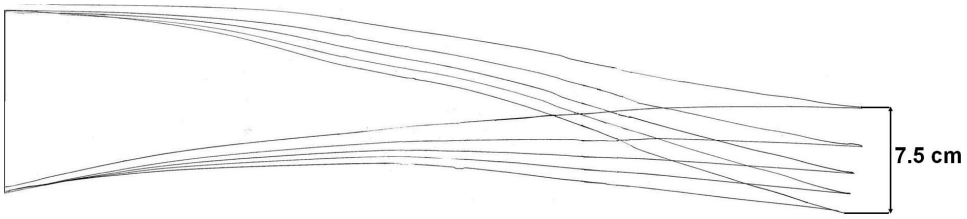

(a) Model with skin connections in place

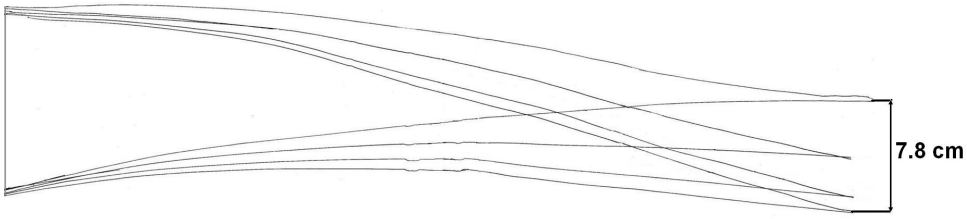

(b) Model with skin connections released

Figure 5.23: Deflection of the flap demonstrator model

CHAPTER 6

Nonlinear Static and Dynamic Analysis of the Morphing Trailing Edge Flap

This chapter presents the results of the structural analysis conducted on the morphing trailing edge flap. The feasibility of the EBAM design concept as an internal actuation mechanism for the flap is proved and the flap structural behaviour and strength capabilities are illustrated in a variety of configurations and loading conditions.

The structure has been analysed using the finite element method. The different finite element models of the trailing edge flap presented in Chapter 5 have been used to represent the flap with different degrees of accuracy.

Section 6.1 presents the analysis of a 1 m span section of the morphing trailing edge with integrated actuation mechanism. Firstly, the effect of the aerodynamic load on the structure was assessed. A geometric nonlinear analysis was then conducted in order to account for the deflection of the trailing edge under the internal actuation load. Different skin materials have been considered and their effect on the structural strength of the flap have been investigated by evaluating the stress and strain distribution due to the internal and external loads. In Section 6.2, the analysis has been extended to the full scale inboard flap. A complete finite element model of the flap with integrated actuation mechanisms distributed along the span was built. The flap was supported by its deployment mechanism and two material options were considered for the flap skin panels, aluminium and carbon fibre/epoxy composite. Both the neutral and fully morphed configuration were evaluated and the influence of the internal actuation mechanism on the structural stiffness was investigated. Finally, in Section 6.4, the dynamic behaviour of the flap was investigated. The natural frequencies of the flap were identified and the transient response to a time-varying sinusoidal input load was investigated to show that the structure was able to sustain transient air pressure loads.

6.1 Nonlinear Static Analysis of a Morphing Trailing Edge Section

6.1.1 Analysis under Static Aerodynamic Load

In the first stages of the analysis, the trailing edge flap structure was analysed under the effect of the air pressure loads to prove that the proposed design of a flap with integrated eccentric beam mechanism was able to withstand the external loads. The aerodynamic pressure loads presented in Section 4.2.2 was applied to the flap skin surfaces. The trailing edge flap model was considered clamped at the rear spar with the beams set in neutral undeflected position.The aerodynamic pressure was considered positive if it deflected the flap skins outwards, while it was negative if the skins tended to collapse inwards. Three different materials, aluminium, carbon fibre/epoxy and glass fibre/epoxy, were considered for the skin panels.
Table 6.1 summarizes the deflection, stress and strain results for the three flap models. The maximum deflection achieved under the effect of aerodynamic load was 1.12 mm for the model with aluminium skin, 1.15 mm for the model with carbon fibre/epoxy and 1.68 mm for the glass fibre skin material. The stresses σ_1 and σ_2 were taken in chordwise and spanwise direction for the aluminium skin and in fibre and off-fibre directions for the carbon fibre/epoxy and for the glass fibre/epoxy skins. The strains ϵ_1 and ϵ_2 were measured in the global coordinate system. The stress and strain values measured in the structure were considerably lower than the maximum allowable for the materials, with the maximum stresses located at the curved beam root.

Skin Material	Aluminium	CFRP	GFRP
Max deflection (mm)	1.12	1.15	1.68
σ_1 (MPa)	10.5	11.3	38.9
σ_2 (MPa)	3.79	3.85	10.6
ϵ_1 $(\mu\epsilon)$	129	129	155
ϵ_2 $(\mu\epsilon)$	37.5	93.5	239

Table 6.1: Flap under aerodynamic load

Figure 6.1 shows the distribution of vertical displacement along the flap trailing edge section for the different skin materals considered. The maximum displacement was achieved for all the models at the trailing edge, in the region between the two curved beams. The glass fibre/epoxy skin presented a larger and uneven deflection compared to the aluminium and carbon fibre/epoxy skins due to its lower material stiffness. For all the skin materials investigated, the displacement achieved was smaller than the skin thickness, indicating that the flap with EBAM internal actuation mechanisms and additional skin connections was able to retain its original configuration under the effect of the aerodynamic pressure.

The preliminary assessment of the structural behaviour under aerodynamic pressure loads showed that the eccentric beam mechanism was able to support the flap skin panels in

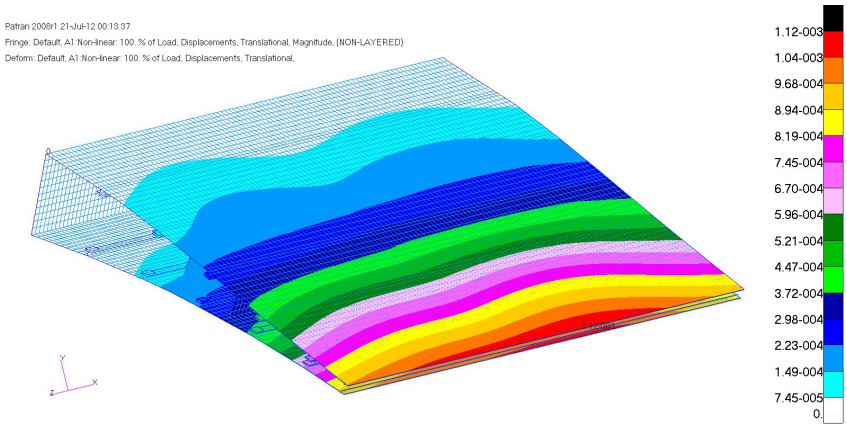

(a) Flap with aluminium skin

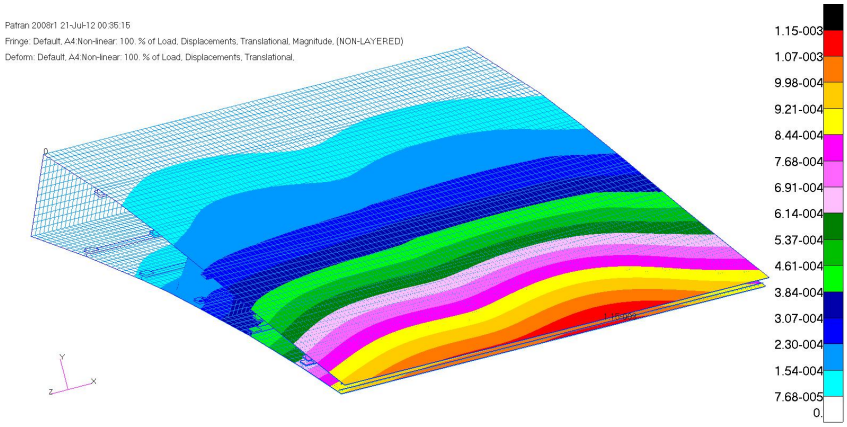

(b) Flap with carbon fibre/epoxy skin

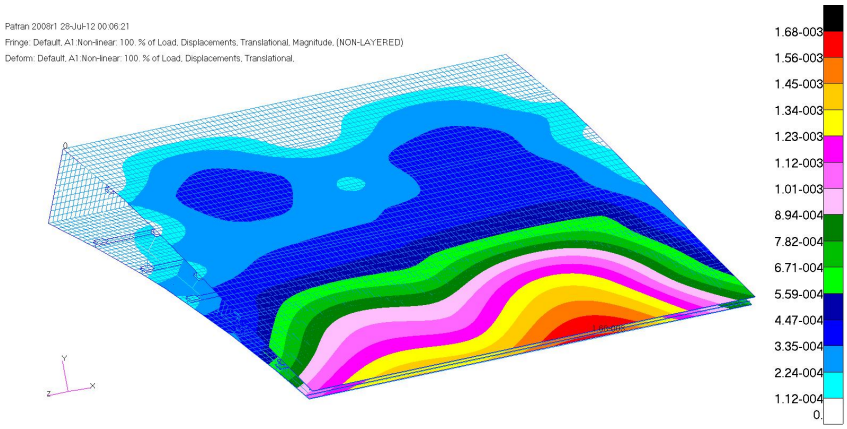

(c) Flap with glass fibre/epoxy skin

Figure 6.1: Trailing edge flap section under aerodynamic pressure load: deflection (m)

the usual operative conditions. The discs and the additional connections between upper and lower skins effectively contributed to preserve the structural integrity of the flap.

6.1.2 Nonlinear Static Analysis of the Morphing Trailing Edge Section

Once the effect of the air pressure on the morphing trailing edge flap was evaluated, the internal actuation loads previously estimated in Section 5.3.6 were included in the analysis. The morphing capabilities of the flap were investigated to prove that the proposed design with EBAM actuators was able to achieve the desired vertical displacement. Moreover, the performance of the materials selected for the flap skins was assessed.

In order to allow the flap trailing edge to deflect under the actuation load, the flap model was considered fully clamped along the rear spar, but the curved beams were set free to rotate and the actuation loads were applied to the model as concentrated forces on the lower skin stringers in correspondence of the disc-stringer sliding contact.

Figure 6.2 shows the loading distribution over the flap trailing edge section. On the left hand side of the FE model the 1 m span did not offer enough space to fit a curved beam and, in order to provide support to the skin and actuation loads for the deflection, a straight beam was included in the model. The presence of the straight beam, in turn, slighlty altered the distribution of the applied forces and led to the maximum vertical deflection to be achieved on the left hand side of the FE model for all the three material skin options considered, rather than uniformly along the flap. The issues connected to the reduced span of the FE model will be addressed and solved in the next sections, where the full span inboard flap will be analysed.

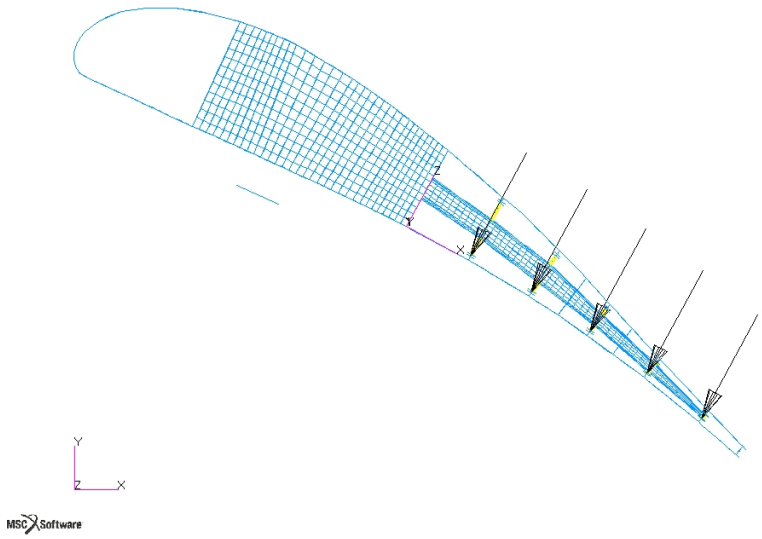

Figure 6.2: Load distribution along the flap chord

As large displacements were expected along the structure, a geometrically nonlinear static analysis was conducted and Nastran Sol 106 was adopted. The analysis was conducted for the three different skin materials considered in the Section 5.3.6: aluminium, carbon

fibre/epoxy and glass fibre/epoxy. The choice of the skin material affected the magnitude of the actuation load required and, conversely, the stress levels in the skins. The performance of the three different materials was compared in terms of actuation load required to deflect the flap, capability of achieving a satisfactory deflected shape and of the resulting stresses and strains in the structure. In some cases, high stress and strain concentrations were obtained in correspondence of the nodes where the actuation loads were applied. These high values did not represent the true level of stress or strain in the structure as they were the result of the application of the actuation load in the node, leading to a singularity in the FE results. For this reason, the slightly lower stress values, obtained from a nearby node away from the region of influence of the singularity, were considered to be more accurate.

6.1.2.1 Flap with aluminium skin

The trailing edge flap section with aluminium skin achieved a maximum deflection of 8.61 cm under the effect of a total actuation load of 4.02 kN, as shown in Figure 6.3.

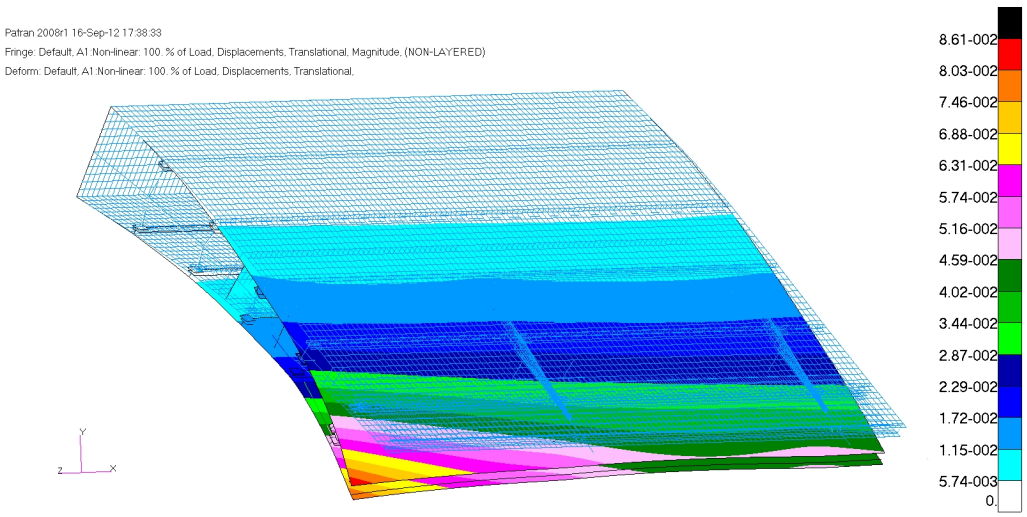

Figure 6.3: Trailing edge flap section with aluminium skin: deflection under aerodynamic and actuation loads (m)

Figures 6.4 and 6.5 show the stress distribution in the aluminium skin in chordwise and spanwise directions. The maximum stress was equal to 370 MPa in chordwise direction and to 200 MPa in spanwise direction, both within the material allowable of 450 MPa. Also the shear stress, equal to 104 MPa, was safely lower than the maximum strength allowable of 295 MPa.

The strain results were also below the design allowable of 4000 $\mu\epsilon$, with a value of 1190 $\mu\epsilon$ in chordwise direction, 2220 $\mu\epsilon$ in spanwise direction and a shear strain of 325 $\mu\epsilon$.

6.1.2.2 Flap with glass fibre/epoxy skin

The trailing edge flap model with glass fibre/epoxy skin managed to achieve a maximum vertical displacement of 8.37 cm under the effect of a total actuation load of 3.73 kN. Figure 6.6 presents the deflected shape obtained.

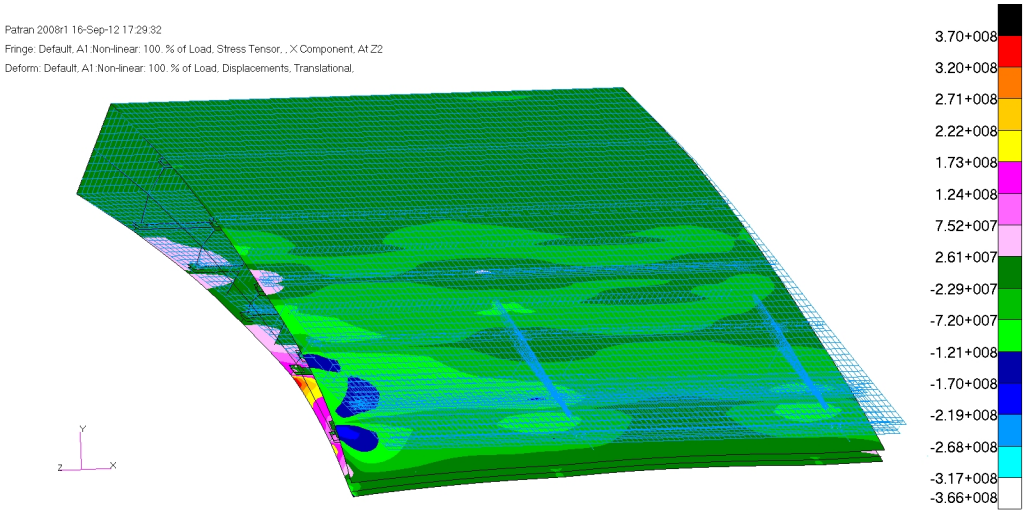

Figure 6.4: Trailing edge flap section with aluminium skin: stress in chordwise direction (Pa)

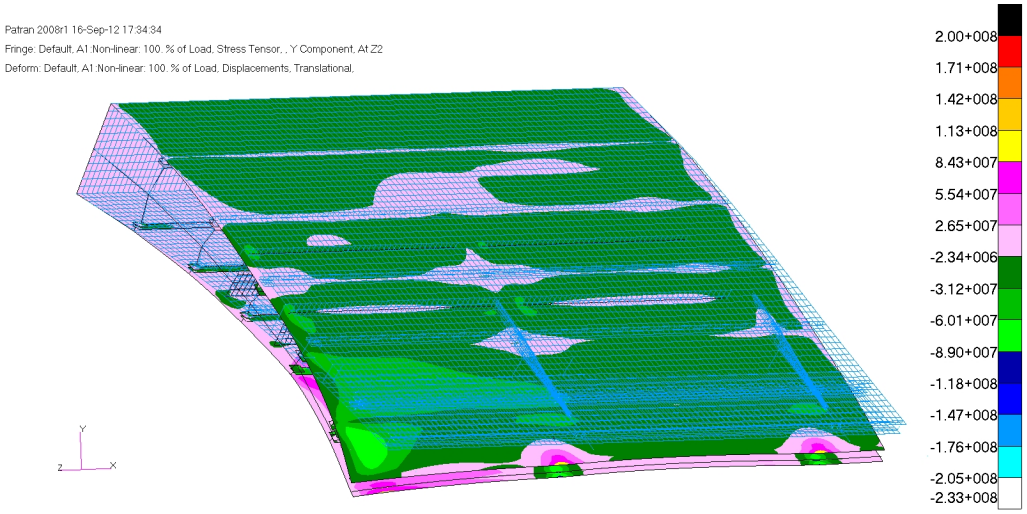

Figure 6.5: Trailing edge flap section with aluminium skin: stress in spanwise direction (Pa)

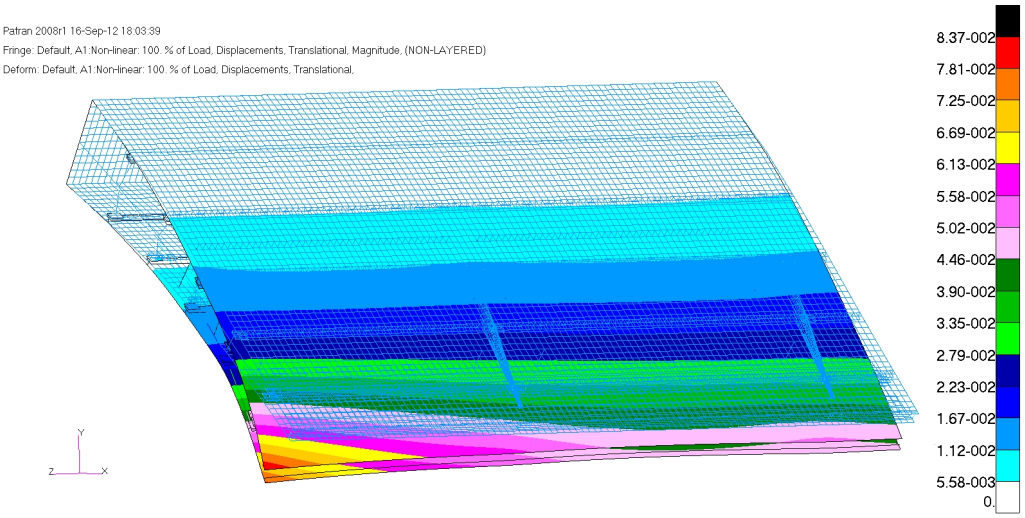

Figure 6.6: Trailing edge flap section with glass fibre/epoxy skin: deflection under aerodynamic and actuation loads (m)

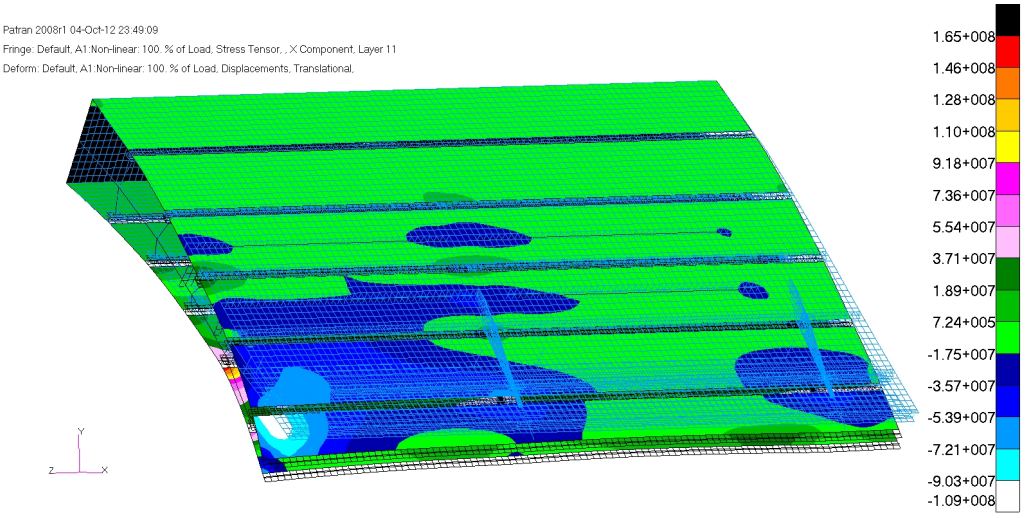

(a) Stress in fibre direction in layer 11 at $-45°$

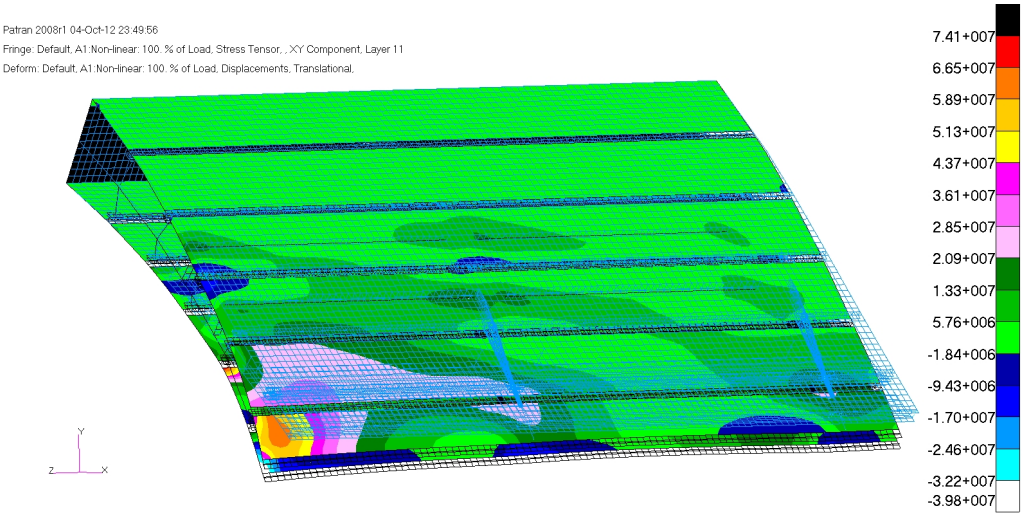

(b) Shear stress in in layer 11 at $-45°$

Figure 6.7: Trailing edge flap section with glass fibre/epoxy skin: stress results (Pa)

Figure 6.7 shows the highest stress distribution in the glass fibre/epoxy skin. The structural behaviour of the composite skin was assessed by considering the ply stresses and strains and discarding the peak stress value due to FE singularity.

The bar chart in Figure 6.8 shows the maximum ply stresses for the flap with glass fibre/epoxy skin having a layup $[\pm 45/0_3/90]_s$ with the 0° layers orientated in the chordwise direction. The higher stress value for the skin was the stress in the fibre direction for the ±45° layers, equal to 165 MPa for ply 11 and lower than the maximum allowable of 1080 MPa for the glass fibre/epoxy composite. The shear stresses in all the layers were lower than the maximum allowable of 89 MPa, with a maximum of 74.1 MPa in the ±45° layers. While the stresses in fibre direction and the shear stresses were acceptable for all the skin layers, the stress in the off fibre direction exceeded the material strength allowable of 39 MPa, leading to the stress failure of the skin. In particular, the maximum off fibre tensile stress of 104 MPa occurred in layer 11 of the composite skin, oriented at −45°. The layers having 0° orientation also presented high off fibre stresses, with a maximum of 41.9 MPa in layer 10.

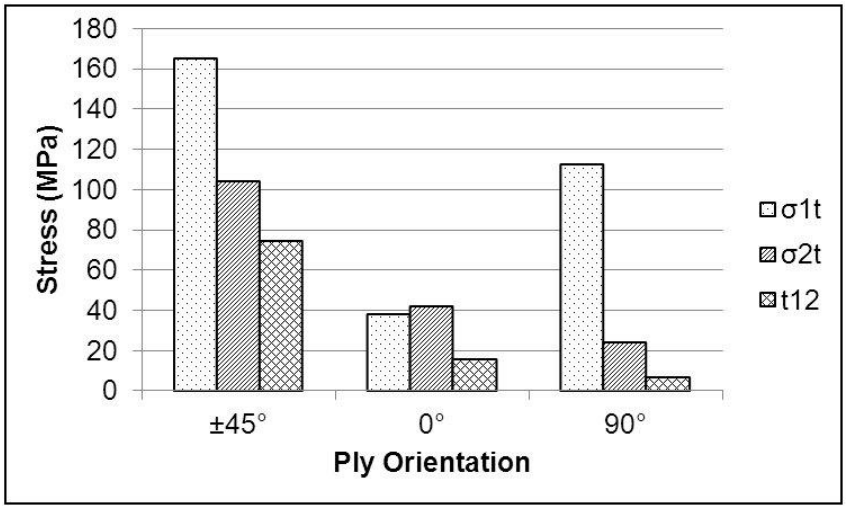

Figure 6.8: Ply by ply stresses in the glass fibre skin of the flap section (Pa)

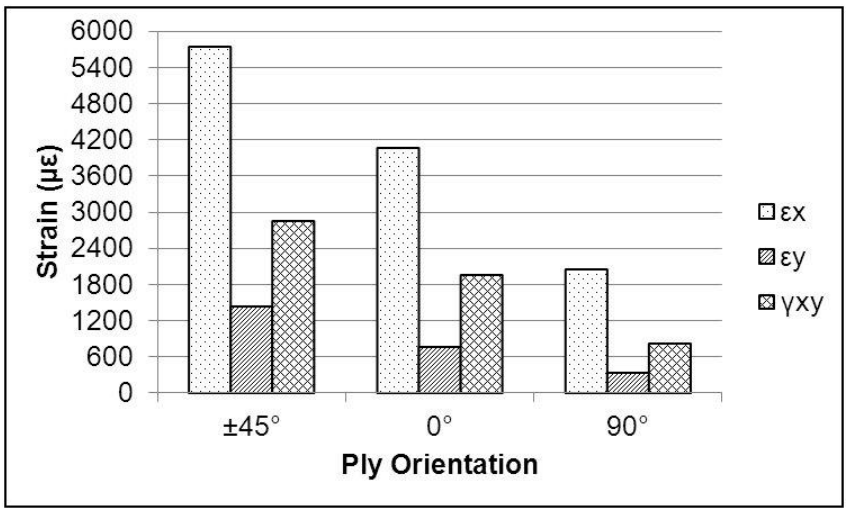

Figure 6.9: Ply by ply strains in the glass fibre skin of the flap section ($\mu\epsilon$)

Figure 6.9 presents the ply by ply strain in the glass fibre/epoxy skin. The ±45° layers presented a peak strain value in the fibre direction of 7200 $\mu\epsilon$, due to a FE singularity in the point of application of the load and exceeding the design allowable of 4000 $\mu\epsilon$; even discarding this high value, high strains of 5740 $\mu\epsilon$ were obtained. The 90° layers exhibited lower strain values, while a high strain concentration of 4050 $\mu\epsilon$ occurred in the plies at 0°, in proximity of one of the actuation load application points.

6.1.2.3 Flap with carbon fibre/epoxy skin

The third skin material to be considered was a carbon fibre/epoxy composite with layup $[\pm 45/0/90]_s$. Figure 6.10 shows the vertical deflection achieved under an actuation load of 4.63 kN. An average deflection of 8.06 cm was obtained along the trailing edge, with a maximum displacement of 10.1 cm at the left corner of the flap.

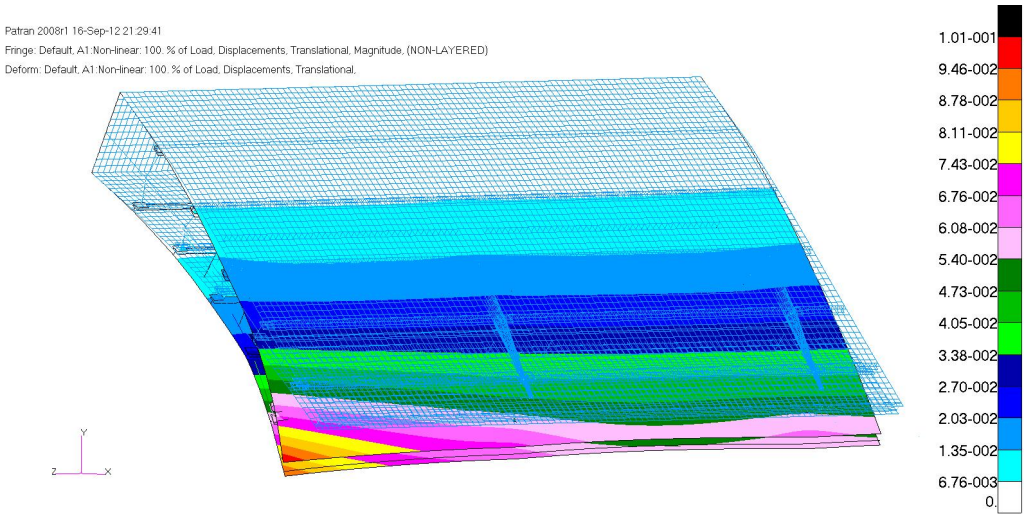

Figure 6.10: Flap trailing edge section with carbon fibre/epoxy skin: deflection under aerodynamic and actuation loads (m)

The chart in Figure 6.11 presents the stress results obtained in each group of plies for the composite skin. The maximum tensile stress in fibre direction was obtained for layer 10, oriented at 0° and, discarding the stress singularities, was equal to 440 MPa, lower than the maximum allowable of 2720 MPa. The maximum off fibre tensile stress of 30 MPa was obtained for the layers at ±45°, in the 12-th layer and the maximum shear stress of 31.9 MPa was recorded in the ±45° layers, in layer 11. Both values were below their respective allowables of 111 MPa and 80 MPa.

The strain results for the carbon fibre/epoxy skin, shown in Figure 6.12, did not exceed the maximum design allowable of 4000 $\mu\epsilon$. Layer 12 at 45° exhibited the maximum strain in fibre direction and in plane shear strain, equal to 3900 $\mu\epsilon$ and 2690 $\mu\epsilon$ respectively, while the maximum off fibre strain of 3430 was obtained for layer 1 at ±45°.

Figure 6.13 shows the maximum stress distribution in the carbon fibre/epoxy skin.

The nonlinear static analysis conducted on a 1 m section of the morphing trailing flap provided an useful insight into the behaviour of the flap with internal actuation system. The EBAM mechanism integrated in the flap structure has ensured high flexibility in the

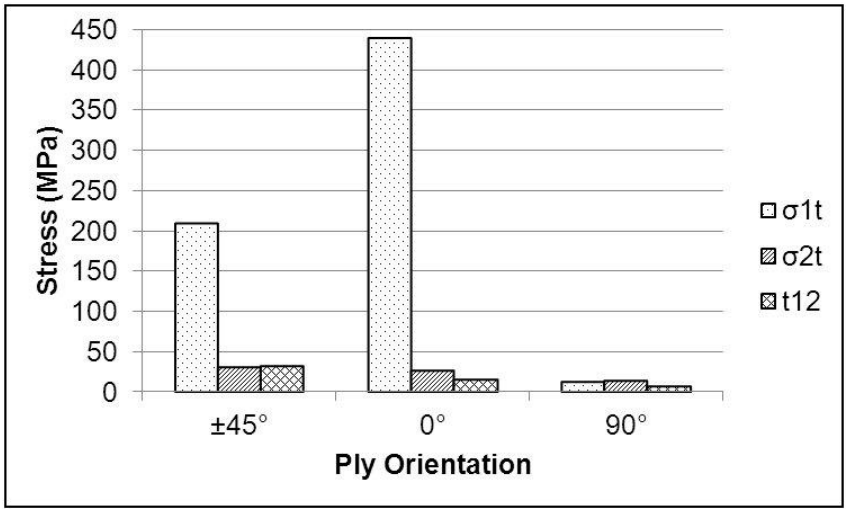

Figure 6.11: Ply by ply stresses in the carbon fibre skin of the flap section (Pa)

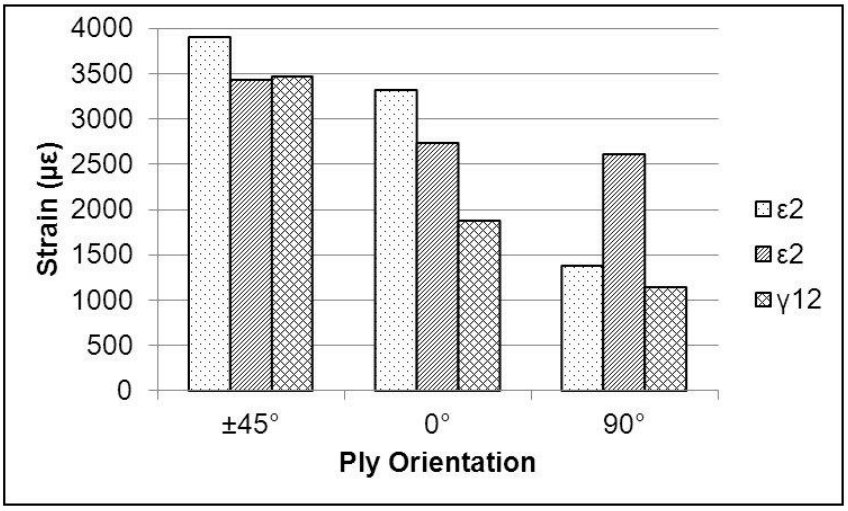

Figure 6.12: Ply by ply strains in the carbon fibre skin of the flap section ($\mu\epsilon$)

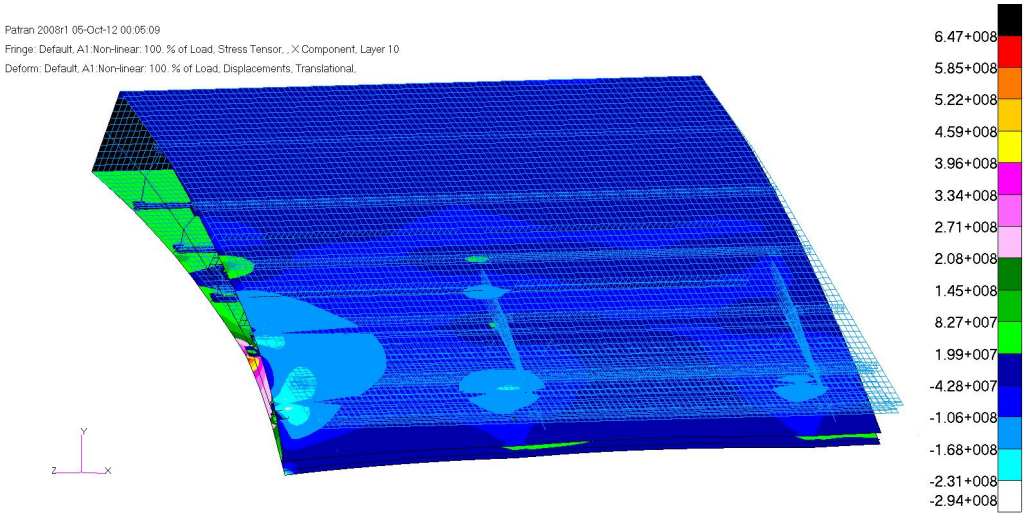

(a) Tensile stress in fibre direction in layer 10 at 0° (discard peak stress at singularity where point load was applied)

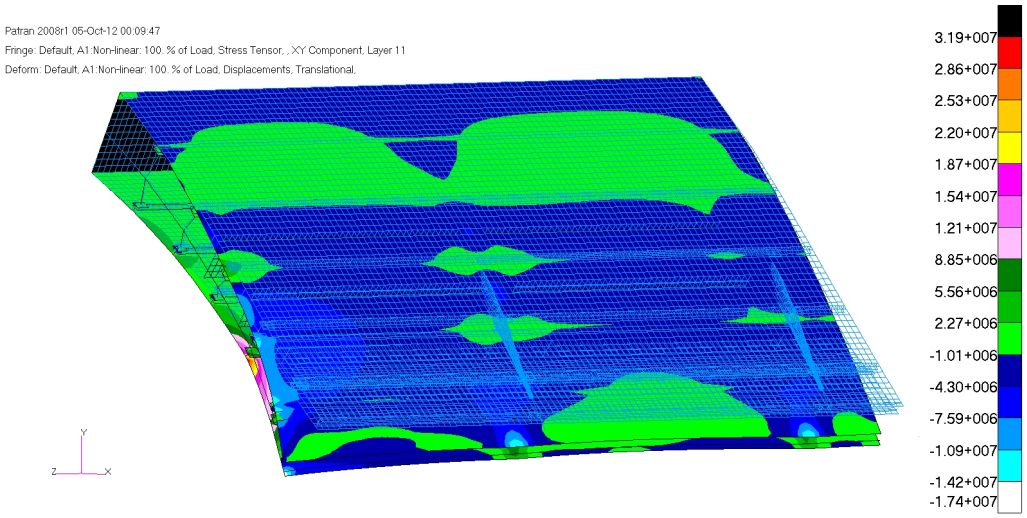

(b) Shear stress in layer 11 at −45°

Figure 6.13: Trailing edge flap section with carbon fibre/epoxy skin: stress results (Pa)

chordwise direction while preserving the structural stiffness required for the functionality and reliability of the flap. The structure subject to aerodynamic and actuation loads has been able to achieve the desired deflection shape regardless of the skin material considered. The EBAM device has proved to be suitable to replace the flap internal structure, and able to offer enough support to the skins under the external air pressure. Moreover, the EBAM device has been able to transfer the actuation load for morphing to the skins. The use of an open trailing edge and the sliding constraint imposed between the top and bottom skins have ensured a uniform deflection shape. The additional skin connections distributed along the span have successfully reacted the upwards pulling load of the aerodynamic pressure.

Both the aluminium and carbon fibre/epoxy skin panels have shown acceptable levels of stress and have met the design requirement of a maximum strain not higher than 4000 $\mu\epsilon$. On the other hand, the glass fibre/epoxy skin exhibited higher stresses in the layers at $\pm 45°$ and $0°$ as well as strain values beyond the maximum design allowable and, for this reason, it will no longer be considered in the analysis.

6.2 Nonlinear Static Analysis of the Inboard Morphing Flap

The study conducted for a 1 m span portion of the trailing edge flap, presented in the previous paragraphs, was extended to the inboard flap to prove the effectiveness of the design on a real scale flap model and to ensure the strength limits were not violated for the full scale structure.

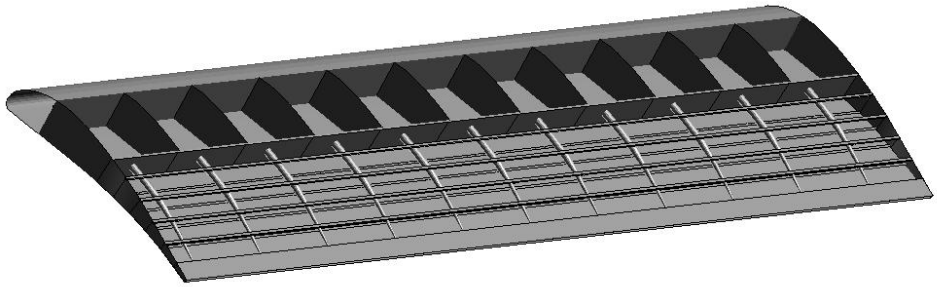

Figure 6.14: Inboard flap integrated with distributed EBAM along the span

The inboard flap structure had a total span of 5.52 m and a total of 11 EBAM mechanisms were fitted in its rear morphing part. Following the preliminary results of Section 6.1.2, two possible choices of skin materials were considered, aluminium and carbon fibre/epoxy. The flap was supported by two link-track deployment mechanisms, presented in Chapter 4, which were considered fixed in the fully deployed configuration at 35° of rotation of the flap. The link and the track were clamped to represent the connection to the main wing box structure. On the other side of the mechanism, the flap fittings were attached to the lower surface of the flap at 25% and 75% of the span. The finite element model of the inboard flap followed the modelling approach described in Section 5.2.1. The deployment mechanism was modelled using QUAD4 elements and RBE2 Multi Point Constraints (MPCs) were applied between the nodes to model the joints between the links and the

roller riding on the track. The inboard flap was analysed under the effect of the air pressure loads and internal actuation forces from the EBAM mechanism.

6.2.1 Inboard Flap under Aerodynamic Pressure Loads

Firstly, the effect of the aerodynamic pressure load on the inboard flap was investigated. Table 6.2 shows the deflection and the overall stresses and strains generated by the air pressure load. Similarly to the trailing edge flap section, the magnitude of the vertical displacement was small and comparable to the skin thickness and the effect of the aerodynamic load on the structure did not raise any concern as the corresponding stresses and strains in the structure were extremely low.

Skin Material	Aluminium	Carbon fibre/epoxy
Max deflection (mm)	3.69	3.58
σ_1 (MPa)	43.8	24.9
σ_2 (MPa)	11.4	15.4
τ_{12} (MPa)	30.3	8.33
ϵ_1 $(\mu\epsilon)$	337	353
ϵ_2 $(\mu\epsilon)$	376	376
γ_{12} $(\mu\epsilon)$	104	93.8

Table 6.2: Inboard flap under aerodynamic load

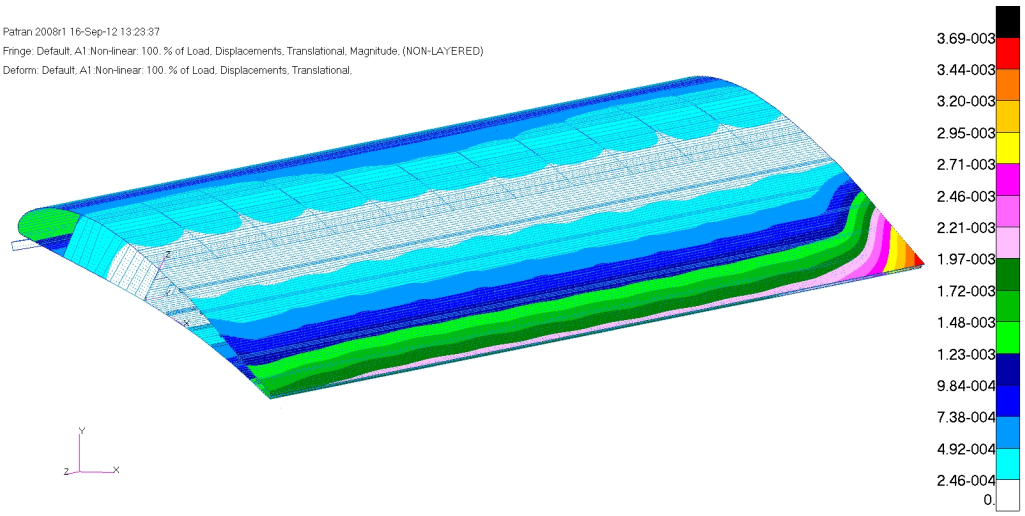

Figure 6.15: Inboard flap with aluminium skin under aerodynamic load: total deflection (m)

Figures 6.15 and 6.16 showh the maximum vertical deflection of 3.69 mm and 3.58 mm obtained for the flap with aluminium skin and CFRP skin respectively. In both cases the maximum vertical deflection was achieved at the flap trailing edge, on the side opposite to the eccentric beam curvature. The analysis of the deflection under the aerodynamic load allowed also to evaluate the effect of the support offered by the flap deployment mechanism to the structure. The flap, supported at 30% and 70% of its span, exhibited

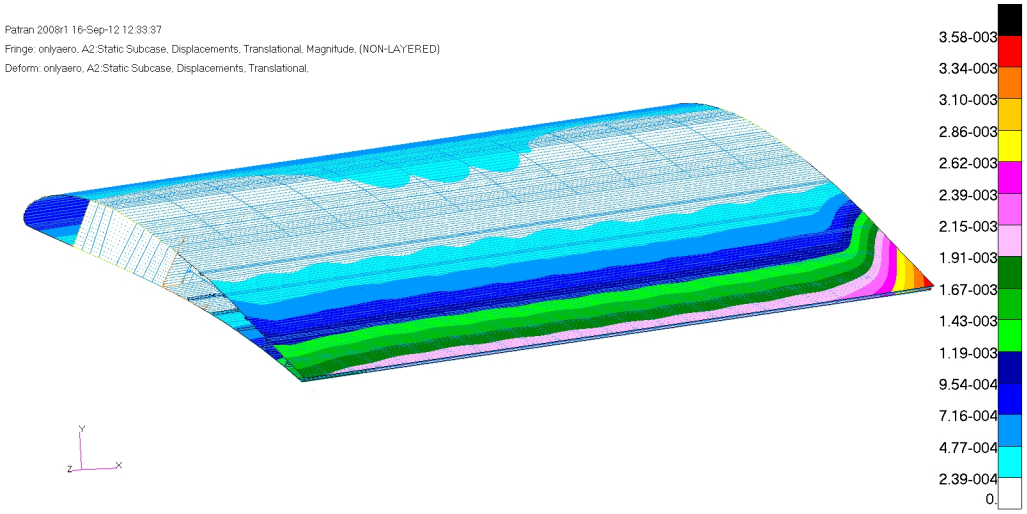

Figure 6.16: Inboard flap with carbon fibre/epoxy skin under aerodynamic load: total deflection (m)

a vertical deflection slightly higher in the flap central section than at its sides, as it can be noted from Figure 6.16. The deflection, due to the bending under the aerodynamic load, was however very small, lower than 0.1 mm. Moreover, the attachment of the flap to the wing rear spar in a commercial aircraft usually includes also a mid-cruise roller, located around the flap mid-span, which will provide further guidance to the flap during the deployment and will mitigate the effect of the spanwise bending on the flap structure. For these reasons, in this current analysis the flap spanwise vertical deflection was neglected.

6.2.2 Inboard flap under Actuation and Aerodynamic Loads

The inboard flap with integrated EBAM actuation mechanism was subsequently analysed under the effect of both the aerodynamic pressure and the actuation loads. A nonlinear analysis was conducted to account for the large deflections expected in the structure and the Nastran Sol 106 was chosen to ensure a detailed evaluation of the deflections, stresses and strains arising in the flap with morphing trailing edge.

The desired deflected shape was consistently achieved along the flap span thanks to the 11 eccentric beams uniformly distributed in the flap trailing edge with a constant pitch of 0.5 m. The curved beams ensured a more uniform spanwise distribution of vertical load if compared to the trailing edge section. In particular, Figure 6.17 shows that the inboard flap with aluminium skin achieved a deflected shape of 8.35 cm and met the morphing requirements prescribed in Section 4.2.1 for the SADE flap. Similarly, the inboard flap with carbon fibre/epoxy skin was also able to achieve the target deflection, with a displacement of 7.94 cm at the trailing edge, as shown in Figure 6.18. In both cases, the eccentric beam actuation mechanism proved to effectively deflect the trailing edge flap into the desired configuration. Moreover, the use of the open sliding trailing edge and internal connections provided by the glass fibre layers ensured a uniform and smooth deflection along the whole flap.

The stresses and strains arising in the flap structure with EBAM actuation system were

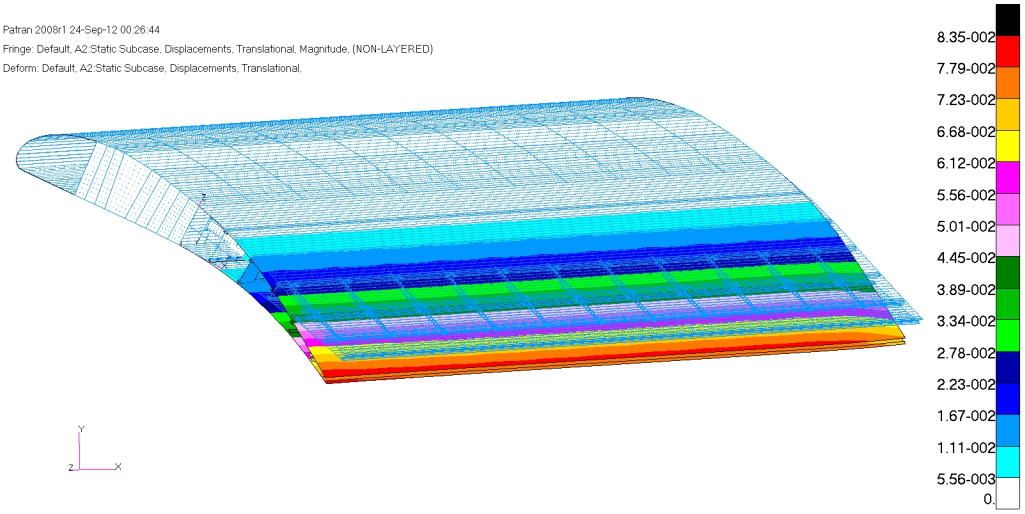

Figure 6.17: Inboard flap with aluminium skin under aerodynamic and actuation loads: deflected shape (m)

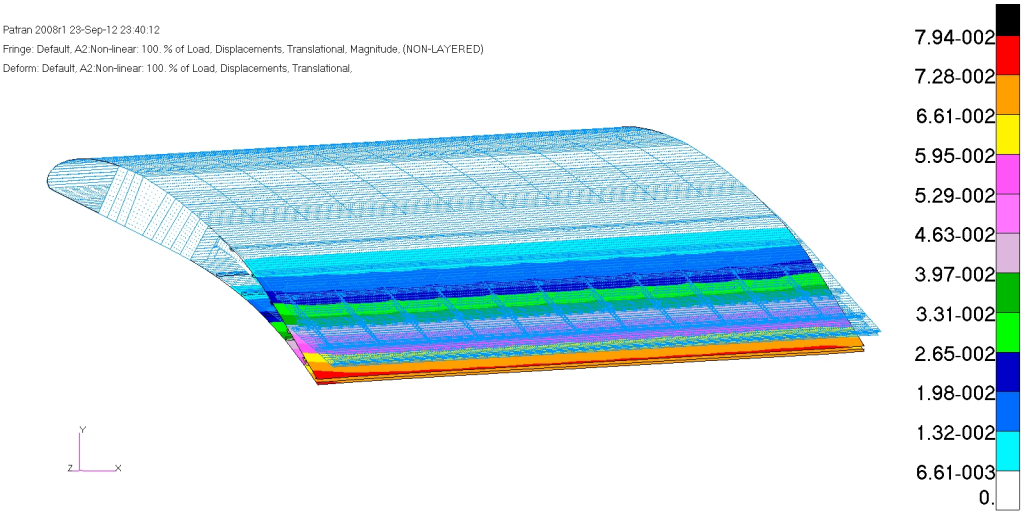

Figure 6.18: Inboard flap with carbon fibre/epoxy skin under aerodynamic and actuation loads: deflected shape (m)

subsequently evaluated. Figure 6.19 presents the chordwise stress distribution in the inboard flap with aluminium skin. Discarding the stress concentrations, a maximum chordwise tensile stress of 238 MPa was achieved, while a tensile stress of 182 MPa was obtained spanwise. The stresses in both chordwise and spanwise directions did not exceed the maximum stress allowable of 450 MPa. A shear stress value of 50.8 MPa was obtained, as shown in Figure 6.20, safely below the aluminium allowable of 295 MPa.

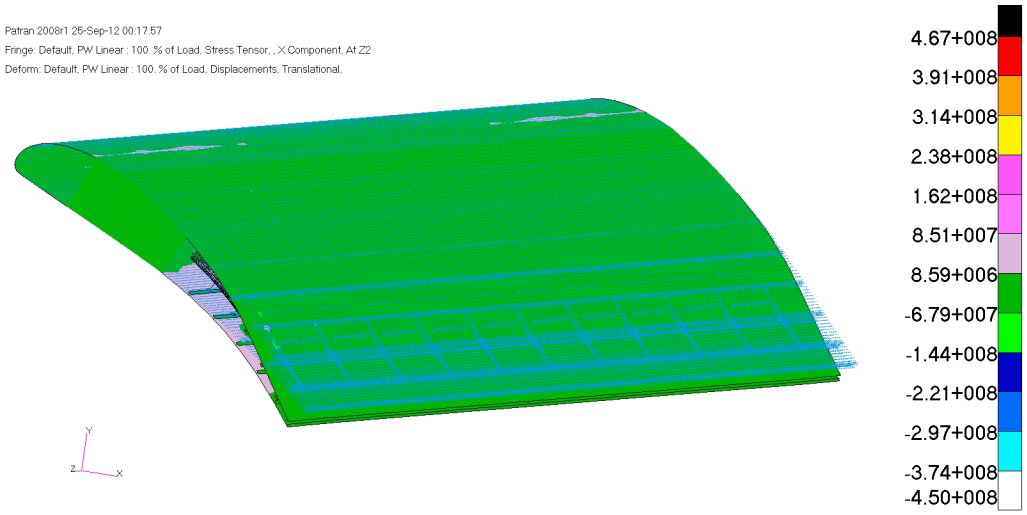

Figure 6.19: Inboard flap with aluminium skin: chordwise stress distribution (MPa)

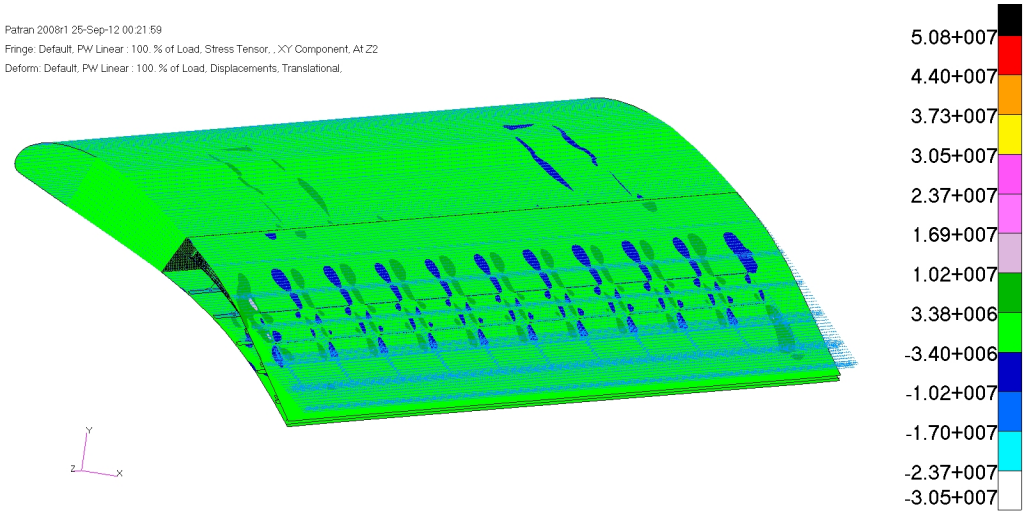

Figure 6.20: Inboard flap with aluminium skin: shear stress distribution (MPa)

The structural behaviour of the composite skin was assessed by considering the ply stresses and strains and discarding the local stress concentrations. Figure 6.21 shows the ply by ply fibre, off fibre and shear stresses for the flap with carbon fibre/epoxy skins, where 0° indicates the plies with fibres in chordwise direction. The maximum tensile stress of 187 MPa in fibre direction was reached in layer 11 at $-45°$. The off fibre maximum stress and the shear stress in the CFRP skin were equal to 74.6 MPa and 53.7 MPa respectively, in layers 12 and 11.

The stress distribution in layer 11 of the carbon fibre/epoxy skin is presented in Figures 6.22 and 6.23.

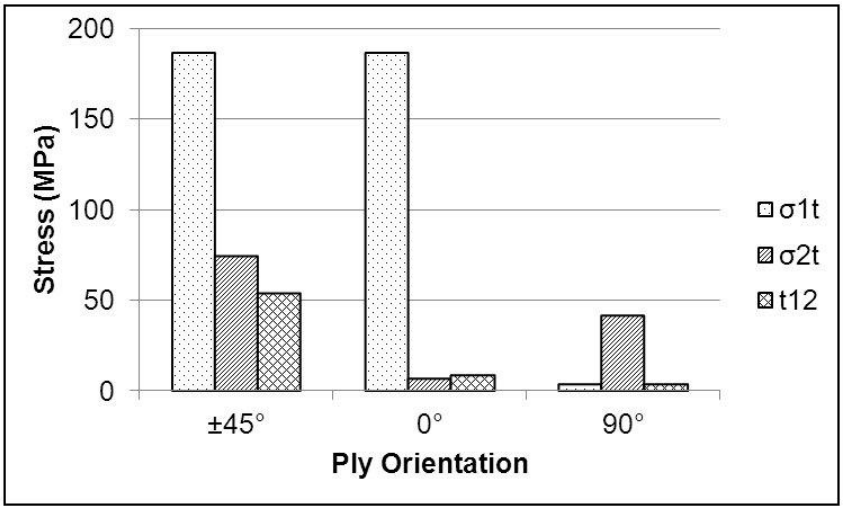

Figure 6.21: Ply by ply stresses in the carbon fibre/epoxy skin of the inboard flap (MPa)

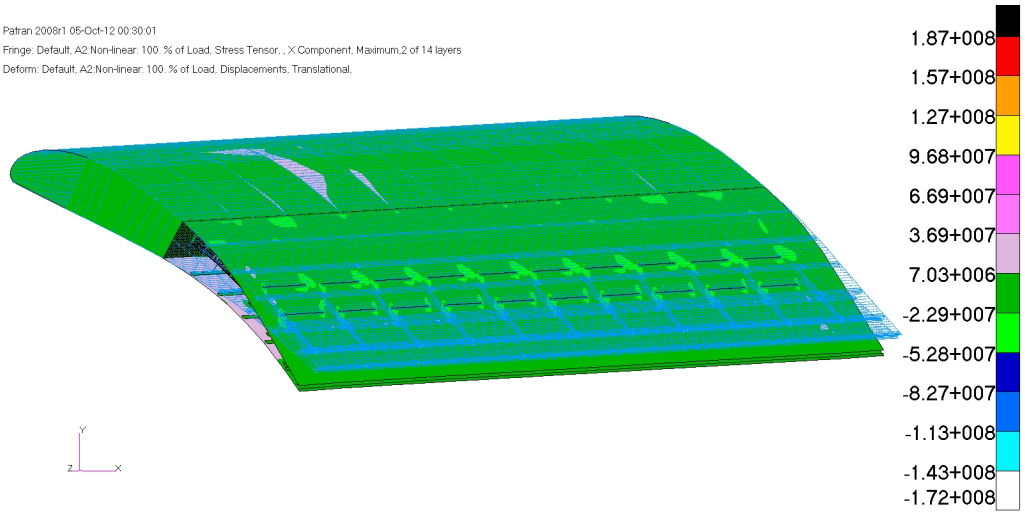

Figure 6.22: Inboard flap with carbon fibre/epoxy skin: stress distribution in fibre direction, layer 11 at $-45°$(MPa)

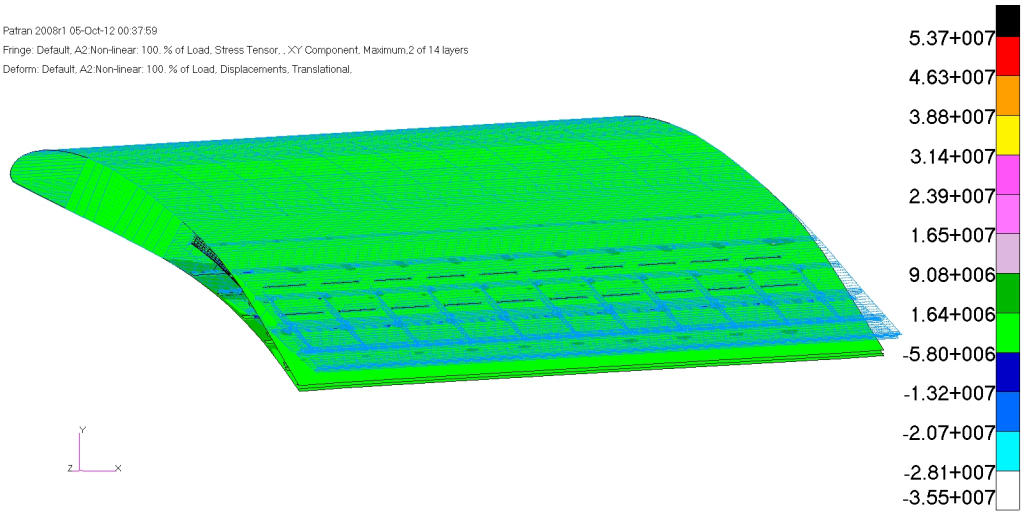

Figure 6.23: Inboard flap with carbon fibre/epoxy skin: shear stress distribution, layer 11 at $-45°$(MPa)

To verify that the inboard flap with composite skin exhibited safe stress levels, the Tsai-Wu stress criterion was applied to the structure. Figure 6.24 presents the results obtained using the Laminate Modeler tool in the Patran software. A maximum failure index of 0.54 was obtained for the 12-th skin layer, oriented at 45°.

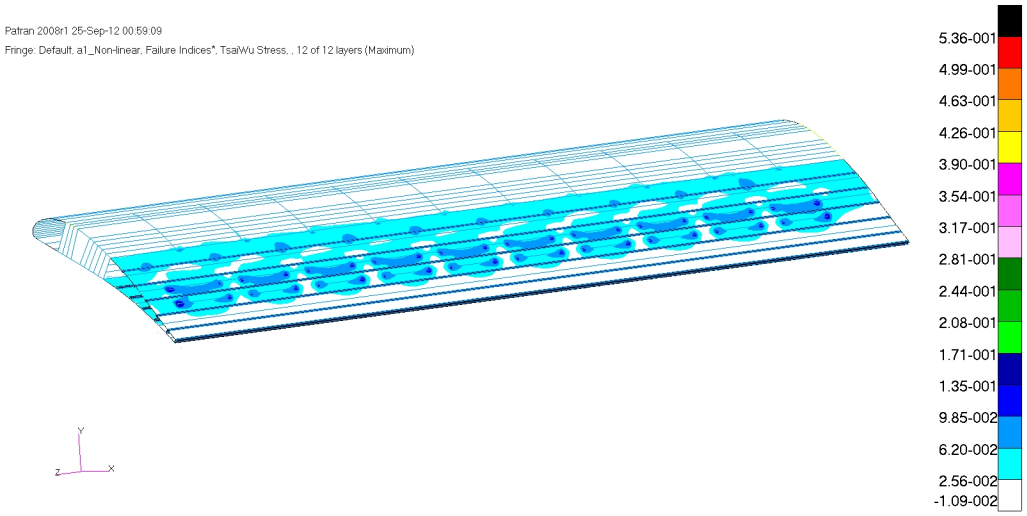

Figure 6.24: Tsai-Wu failure indices in the composite inboard flap

Both the models with aluminum and carbon fibre/epoxy skins maintained acceptable stress levels under the aerodynamic and actuation load, however the carbon fibre/epoxy skin exhibited lower stress values in the directions critical for the chordwise morphing.

Subsequently, the strain values in the flap skin were analysed. The inboard flap with aluminium skin exhibited strains safely lower than the maximum design allowable of 4000 $\mu\epsilon$. In particular, a maximum chordwise strain of 2580 $\mu\epsilon$ was obtained, while the spanwise and shear strains were equal to 1050 $\mu\epsilon$ and 1760 $\mu\epsilon$ respectively.

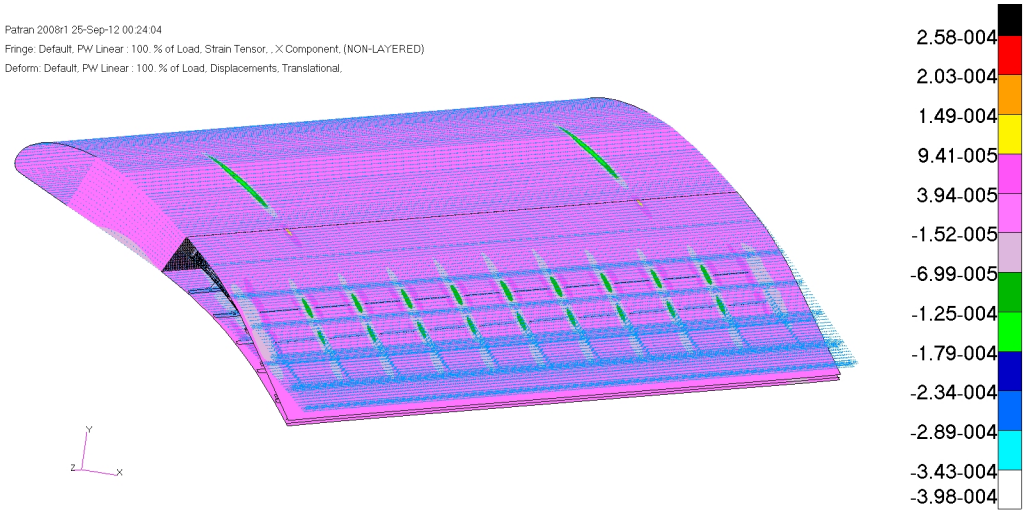

Figure 6.25: Inboard flap with aluminium skin: chordwise strain distribution (ϵ)

Figure 6.27 presents the strain distribution in the carbon fibre/epoxy skin. The maximum strain of 1790 $\mu\epsilon$ was reached in the plies at $\pm 45°$. Figure 6.28 shows that the strain in all the fibres of the composite skin remained well below the design allowable of 4000 $\mu\epsilon$.

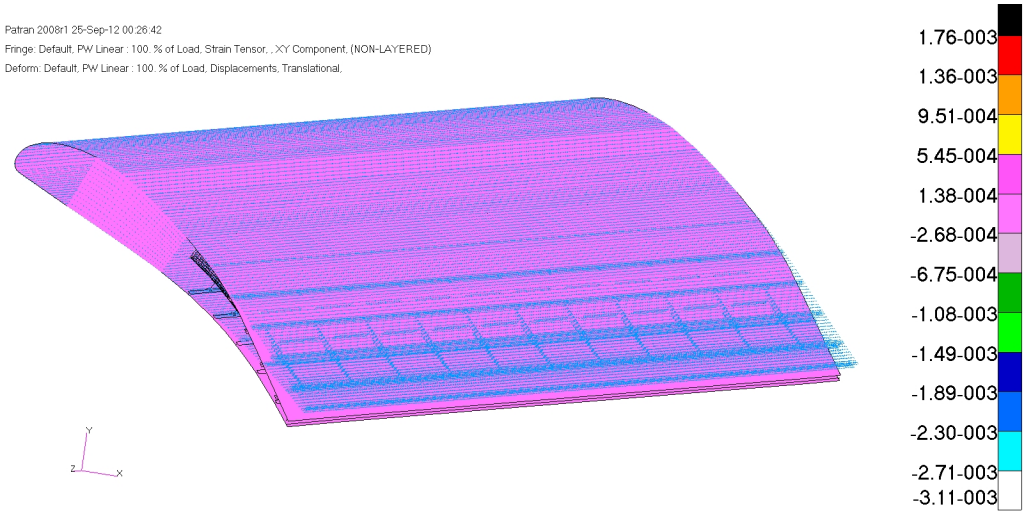

Figure 6.26: Inboard flap with aluminium skin: shear strain distribution (ϵ)

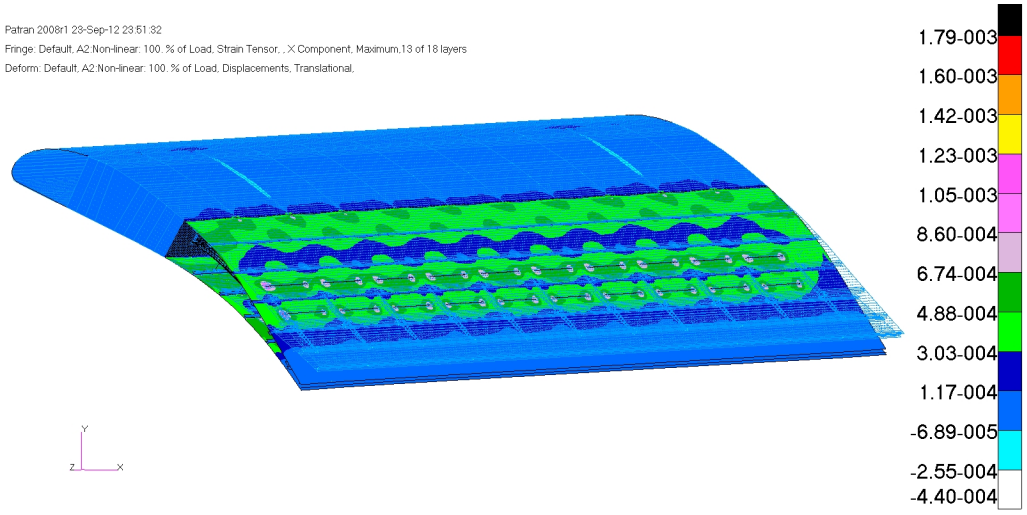

Figure 6.27: Inboard flap with carbon fibre/epoxy skin: strain distribution in the layers at $\pm 45°$ (ϵ)

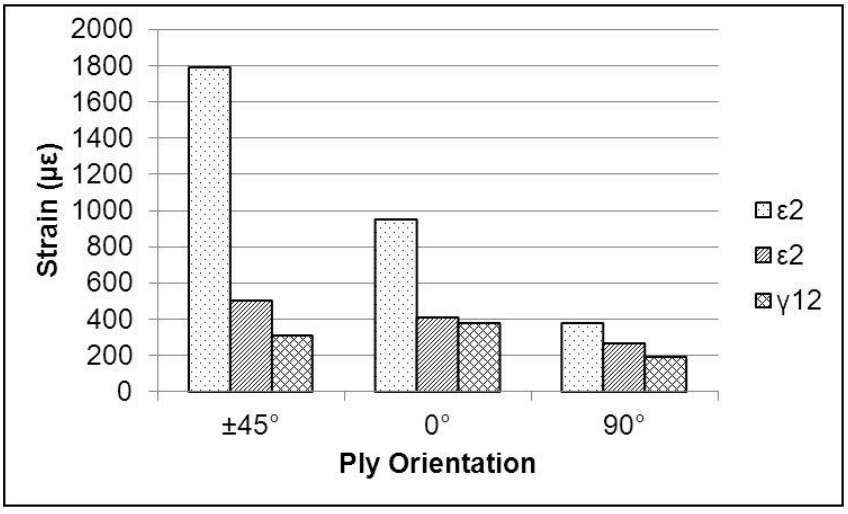

Figure 6.28: Ply by ply strains in the carbon fibre/epoxy skin of the inboard flap ($\mu\epsilon$)

The current analysis has shown that the inboard flap with EBAM actuation mechanisms is able to achieve a uniform morphed shape along its span and to reach the desired vertical deflection at the trailing edge. Both the materials selected for the skin panels satisfied the structural strength requirements. The model with aluminium skin required a slightly lower actuation load of 4.02 kN opposed to 4.63 kN of the carbon fibre/epoxy skin, the latter offered the advantage of lower stress and strain levels.

A buckling analysis was also conducted as part of the static study of the inboard flap. Table 6.3 presents the results obtained for the first three modes. The buckling load factor was safely above 1 for both the models with aluminium and carbon fibre/epoxy skin. As shown in Figure 6.29, the critical area was represented by the internal connections between the upper and lower skins, indicating that the flap main structure is adequately reinforced against panel buckling.

Mode No.	Aluminium	Carbon fibre/epoxy
1	2.11	1.59
2	2.16	1.69
3	2.62	1.91

Table 6.3: Inboard flap buckling load factors

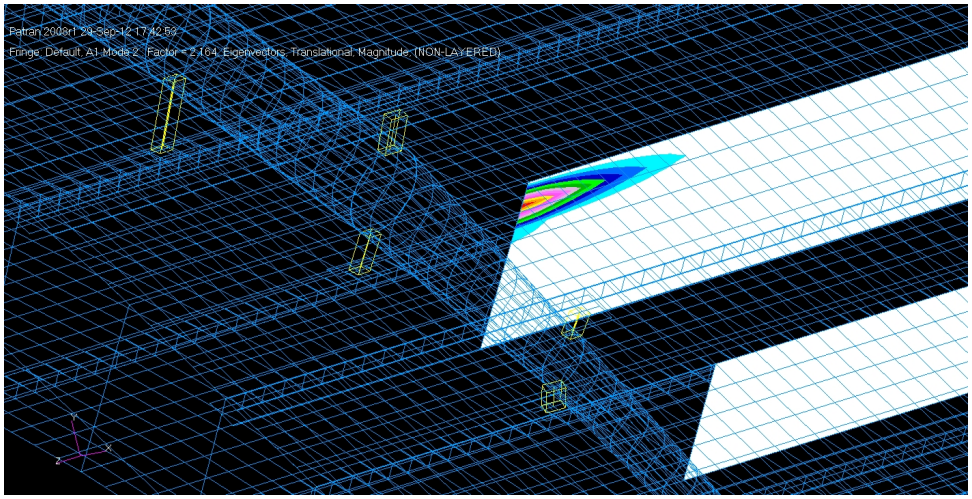

Figure 6.29: Inboard flap first buckling mode

6.2.3 Effect of the Deployment Mechanism

As described in Chapter 4, the inboard flap was supported by two link-track deployment mechanisms, located at 30% and 70% of its span. The mechanism consists of a link arm, moved by an actuator, plus a track to allow the flap to move back and forth. Both these parts are connected to the rear spar. Moreover, the flap is attached to the deployment mechanisms by a small fitting located at 32% of the flap chord, arranged roughy in correspondence of the aerodynamic resultant on the flap and positioned so to not interfere with the flap deployment and, hence, with the morphing of its rear part.

A finite element model of the link-track mechanism was generated in order to capture the behaviour of its components under the aerodynamic pressure load and to assess their capability to support the flap structure.

Figure 6.30 shows the vertical deflection of the link-track mechanism under aerodynamic load: a deflection of 0.58 mm was obtained, proving that the flap deployment mechanism is stiff enough to withstand the aerodynamic pressure with minimal vertical deflection. The stress applied to the deployment mechanism was also low and equal to 125 MPa in chordwise direction, as shown in Figure 6.31.

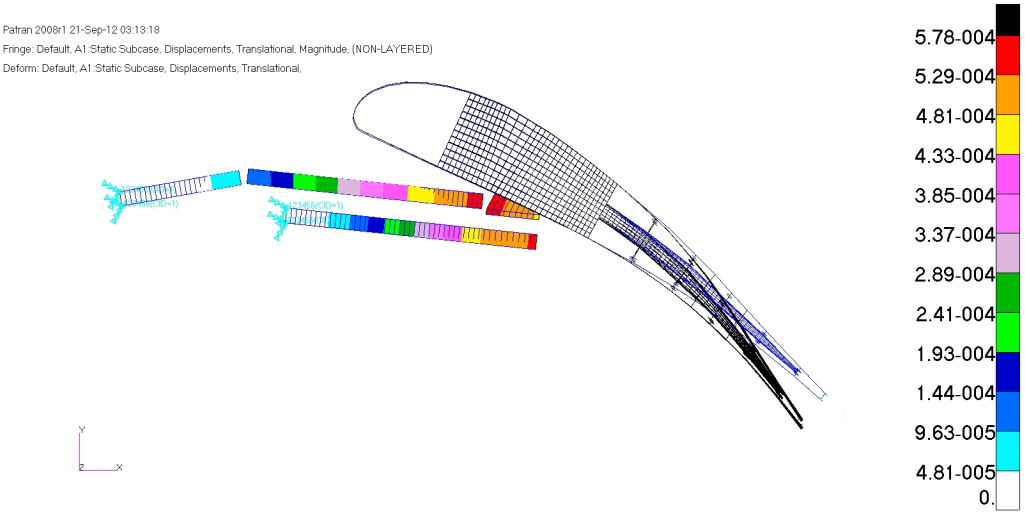

Figure 6.30: Deflection of the deployment mechanism under aerodynamic loads (m)

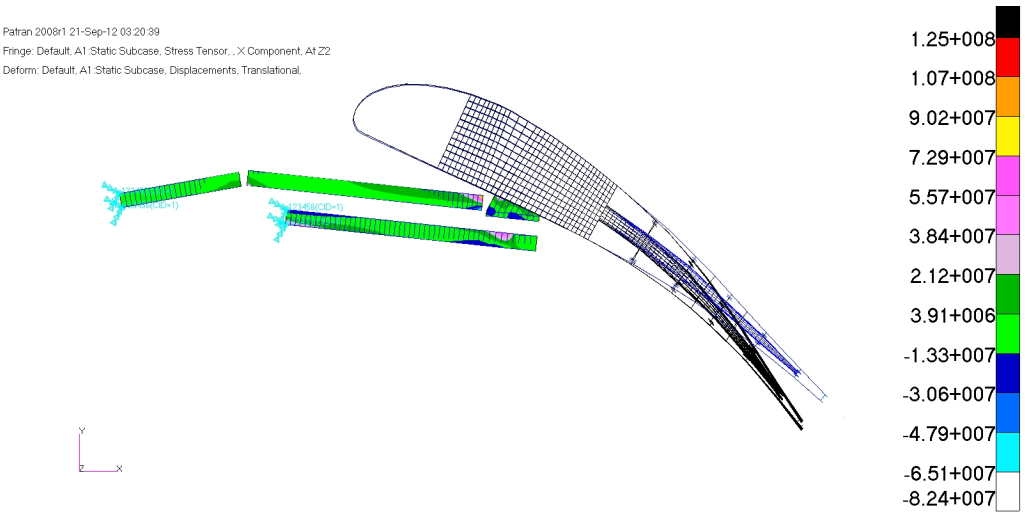

Figure 6.31: Chordwise stress distribution in the deployment mechanism (MPa)

6.3 Model in Deflected Position

As shown in the previous section, the model is able to deflect into the desired morphed configuration subject to the application of the actuation loads. Once the flap has reached its morphed configuration, the eccentric beams in the morphed trailing edge will have

rotated by 90° downwards compared to their neutral position and the skin panels will follow the prescribed deflection of the trailing edge. As shown in Section 5.3.6, in this configuration the EBAM actuation mechanism does not provide any actuation load and the actuators located at the rear spar have only the role to keep the eccentric beams in the fully deflected position to allow the flap to retain the morphed shape under the effect of the aerodynamic pressure load. Since the flap is more cambered and it is assumed that for the flight condition of flap deflected also the morphing leading edge device will be in use, the aerodynamic load on the airfoil with morphed high lift devices is higher than the one in neutral configuration, as presented in Section 4.2. On the other hand, the morphed flap presents a smaller effective chord due to the deflection, which partially counteracts the increase of aerodynamic load on the structure.

A finite element model of the morphed flap was created and a geometrically nonlinear analysis was run to assess the effect of the increased aerodynamic load on the deflected flap. The internal structure of the flap was modeled exactly in the same way as the non deflected models, as detailed in Section 5.2.1, only with eccentric beams rotated by 90°. As shown in Figures 6.32 and 6.33, the vertical deflection achieved by the flap in morphed configuration at the trailing edge was equal to 3.59 mm and 2.76 mm for the flap made of aluminium and carbon fibre/epoxy respectively. Interestingly, the area of maximum vertical deflection under the increased aerodynamic load was located at the flap leading edge due to the higher pressure peak in this area. The results show that the morphed trailing edge was able to retain its morphed configuration with reasonably small deflection under the effect of the external aerodynamic pressure.

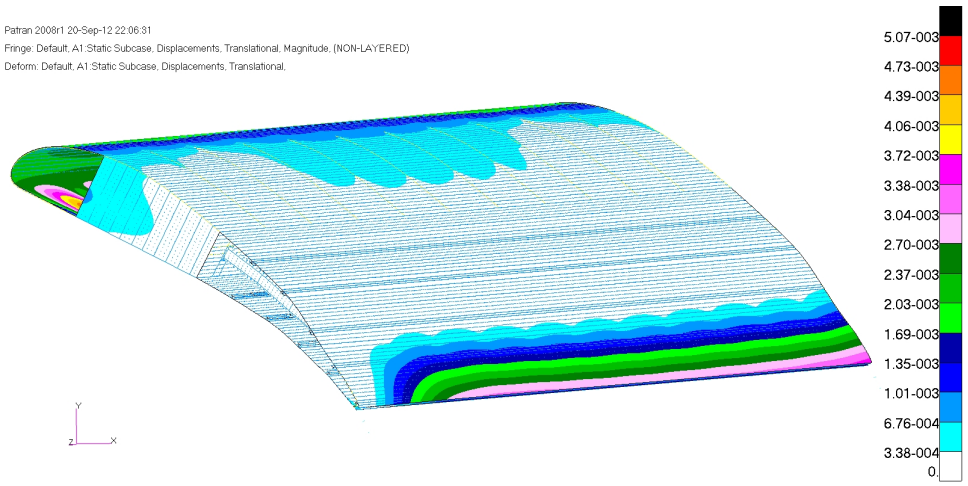

Figure 6.32: Inboard flap with aluminium skin in morphed configuration: deflection under aerodynamic load (m)

6.3.1 Stiffness Variation of the Root

A study was conducted on the flap in both the undeformed and fully morphed configurations in order to assess the impact of the actuator stiffness on the overall structural stiffness and its influence on the capability of the morphing trailing edge to resist the effect of the air pressure loads. The effective stiffness of the actuator was represented by considering a small portion of the eccentric beam, located at its root, and varying its

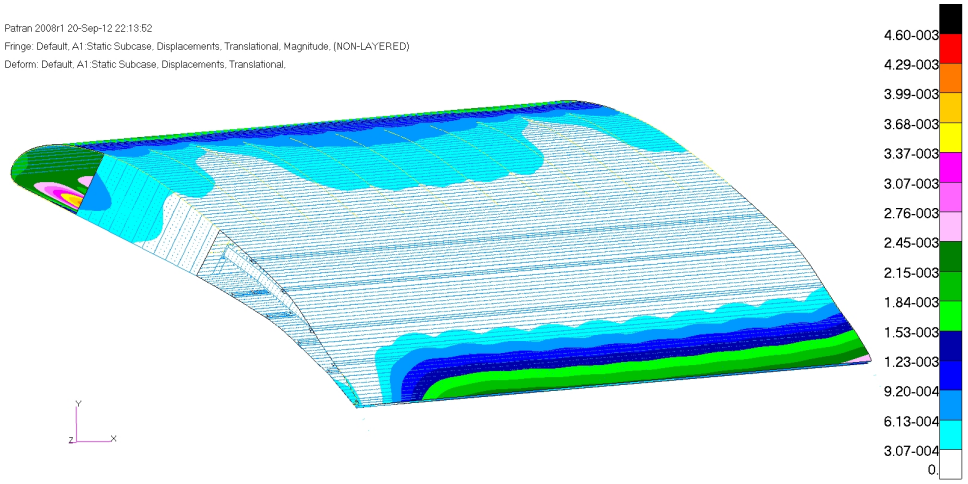

Figure 6.33: Inboard flap with carbon fibre/epoxy skin in morphed configuration: deflection under aerodynamic load (m)

stiffness from 100% to 10% of its original value by acting on the material properties of the area.

The structural behaviour of the flap under the aerodynamic pressure load was evaluated for the "softer" beam roots and the results were compared to the case of flap with curved beams having full stiffness, in order to estimate the capability of the eccentric beam actuation mechanisms to act as an internal support structure for the skin panels even in the case of smaller actuator stiffness. Tables 6.4 and 6.5 offer a comparison of the results obtained.

As expected, the softer actuators led to an increased trailing edge deflection. For the flap in neutral configuration, the deflection went from 3.69 mm to 4.45 mm and from 3.58 mm to 4.30 mm for aluminiun and carbon fibre/epox skin respectively. For the flap in deformed configuration, the deflection increased from 3.59 mm to 3.74 mm for the aluminium skin, and from 2.76 mm to 2.80 mm for the carbon fibre epoxy skin. The elastic deformation of the trailing edge flap due to the applied aerodynamic pressure remained small and negligible if compared to the desired deflected shape in all the cases investigated. This result proved that the EBAM device was able to keep the trailing edge flap in the desired configuration under the external aerodynamic load.

The change in the actuator stiffness had negligible effects on the stress values in the structure when the flap was in neutral position. Table 6.4 shows the maximum normal stress in chordwise direction and the in plane shear stress due to the aerodynamic load for the two configurations of flap neutral and morphed. On the other hand, the reduction of the root stiffness strongly affected the strain in chordwise and in shear. As presented in Table 6.5, the higher strain values were obtained when the root stiffness was reduced to 10% of that of the original case. The strain values, however, remained lower than the design allowable of 4000 $\mu\epsilon$.

Flap Configuration	100% root stiffness				10% root stiffness			
	σ_x (MPa)		τ_{xy} (MPa)		σ_x (MPa)		τ_{xy} (MPa)	
	Skin	Beam	Skin	Beam	Skin	Beam	Skin	Beam
Neutral	18.6	23.1	8.40	29.5	17.4	19.4	10.9	30.8
Deployed	51.2	34.2	51.9	12.3	53.6	36.4	46.1	14.4

Table 6.4: Effect of the beam root stiffness on the stresses: carbon fibre/epoxy skin

Flap Configuration	100% root stiffness				10% root stiffness			
	ϵ_x (MPa)		γ_{xy} (MPa)		ϵ_x (MPa)		γ_{xy} (MPa)	
	Skin	Beam	Skin	Beam	Skin	Beam	Skin	Beam
Neutral	141	323	92.9	43.6	138	2590	398	252
Deployed	519	187	232	59.4	578	197	230	59.7

Table 6.5: Effect of the beam root stiffness on the strains: carbon fibre/epoxy skin

6.4 Dynamic Response Analysis of the Morphing Trailing Edge Flap

The dynamic behaviour of the morphing flap was analysed. Table 6.6 presents the mass properties of the trailing edge flap materials considered in the dynamic analysis.

Material	ρ (kg/m^3)
Al	2700
CFRP	1850
GFRP	2100
Steel	7849

Table 6.6: Trailing edge flap materials mass properties

A modal analysis was firstly conducted to evaluate the natural frequency and mode shapes with the flap with internal EBAM actuation mechanism. Subsequently, a frequency response study was carried out. Finally, the dynamic response of the flap to a transient input load representing a time varying aerodynamic pressure load was analysed for both the aluminium and carbon fibre/epoxy skin materials. The influence of the actuator stiffness at the root of the eccentric beam and the support offered by the flap deploying mechanism were also taken into account.

6.4.1 Natural Vibration Analysis

A preliminary modal analysis was carried out on the inboard flap to obtain the natural frequencies and mode shapes of the structure. The analysis considered both neutral and

deployed flap configurations.

Table 6.7 summarizes the first five modes of the structure in neutral configuration, with eccentric beams having full stiffness. The flap with carbon fibre/epoxy skin was stiffer than the aluminium one, which exhibited slightly lower natural frequencies. The first natural frequency of the flap structure was equal to 20.20 Hz and 24.25 Hz for the models with Aluminum and carbon fibre/epoxy skin respectively, corresponding to the first structural bending mode.

Flap in neutral configuration		
Mode No.	Aluminium [Hz]	Carbon fibre/epoxy [Hz]
1	20.20	24.25
2	23.13	26.22
3	24.78	28.02
4	27.60	31.20
5	31.18	35.27

Table 6.7: Natural frequencies of the inboard flap with EBAM actuation mechanism: neutral configuration, 100% beam root stiffness

Flap in deflected configuration		
Mode No.	Aluminium [Hz]	Carbon fibre/epoxy [Hz]
1	24.00	29.95
2	24.85	31.14
3	26.55	33.09
4	29.46	36.19
5	33.99	40.84

Table 6.8: Natural frequencies of the inboard flap with EBAM actuation mechanism: deployed configuration, 100% beam root stiffness

When the flap was morphed into the final deflected configuration, its natural frequencies increased, as shown in Table 6.8. This reduction can be explained considering the smaller effective chord of the morphed flap. The first natural frequency increased to 24 Hz for the aluminium flap and to 29.95 Hz for the carbon fibre/epoxy one. Similarly to the case of neutral configuration, the composite skin flap was stiffer than the metallic skin one.

The natural modes analysis was repeatd to asses the effect of the actuator stiffness on the vibrational characteristics of the structure. The stiffness of the eccentric beams root was reduced to 10% of its original value. The natural frequencies obtained are shown in Tables 6.9 and 6.10 for the flap in neutral and deflected configuration respectively. A 15% reduction in the first natural frequency was noted for the flap in neutral configuration, regardless of the skin material. Similarly to the previous cases, the flap in deformed configuration exhibited higher frequencies compared to the neutral configuration even in the case of smaller actuator stiffness. Moreover, the first natural frequency values reduced

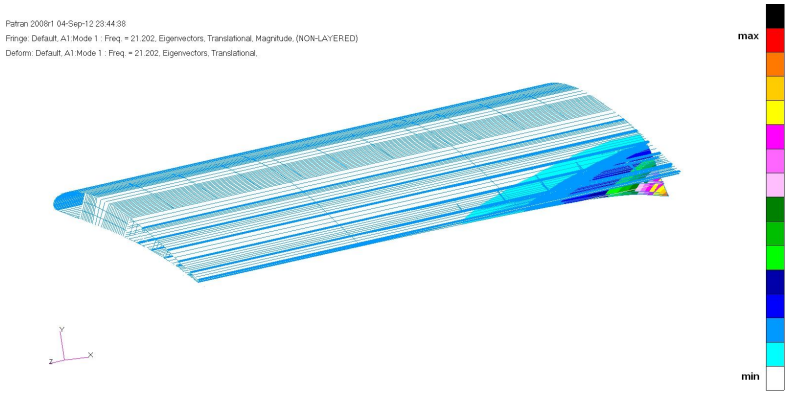

(a) Mode 1

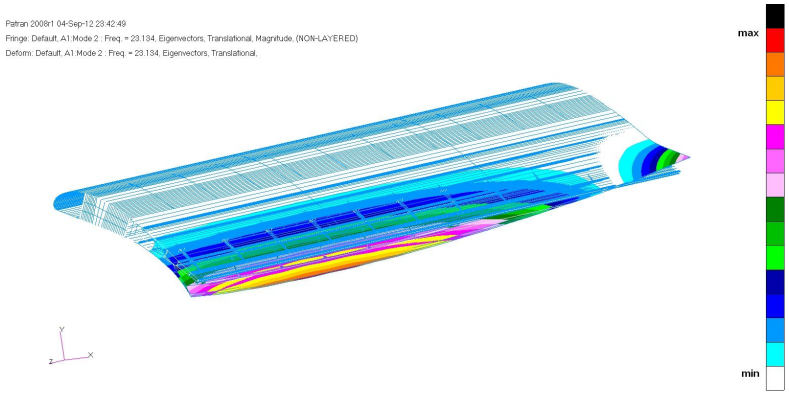

(b) Mode 2

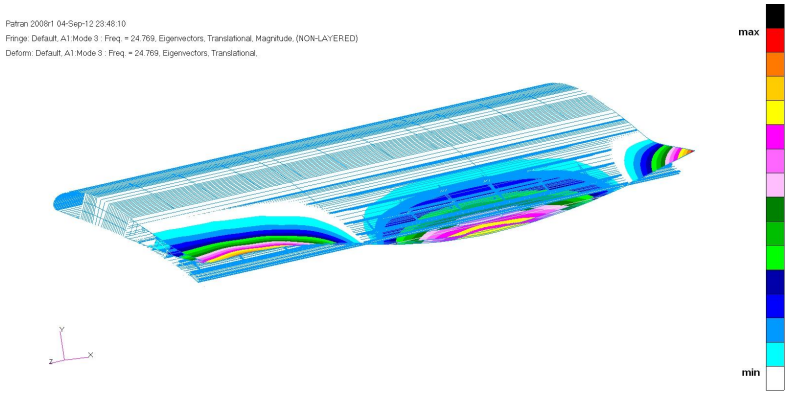

(c) Mode 3

Figure 6.34: Modes 1, 2 and 3 of vibration for the inboard flap with aluminium skin

only by 2% and 3% for the metallic and composite flaps respect to the full stiffness case. This result confirmed that the structure in its morphed configuration has an improved vibrational behaviour.

Mode No.	Flap in neutral configuration	
	aluminium [Hz]	CFRP [Hz]
1	17.87	20.32
2	19.24	21.76
3	22.23	24.96
4	26.33	29.63
5	30.61	34.58

Table 6.9: Natural frequencies of the inboard flap with EBAM actuation mechanism: neutral configuration, 10% beam root stiffness

Mode No.	Flap in deflected configuration	
	aluminium [Hz]	CFRP [Hz]
1	23.49	29.02
2	24.56	30.64
3	26.42	32.85
4	29.39	36.08
5	33.90	40.76

Table 6.10: Natural frequencies of the inboard flap with EBAM actuation mechanism: deployed configuration, 10% beam root stiffness

A separate modal analysis was carried out on the flap deployment mechanism to investigate its contribution to the flap dynamic behavior. The mechanism was dimensioned to have a very low deflection and high stability under the aerodynamic load; hence, it was much stiffer than the flap structure, which, on the contrary, had to be flexible enough to achieve morphing. As expected, the natural frequencies of the mechanism were higher than those of the flap structure, with the first mode having a frequency of 76.2 Hz. For this reason, the deployment mechanism did not represent a critical component of the structure.

6.4.2 Frequency Response

A frequency response analysis was carried out to compute the structural response to steady-state oscillatory excitation. This study allowed to predict the most excitable frequencies of the structures, which were compared with the natural frequencies obtained from the modal analysis conducted in Section 6.4.1, to validate the results and to ensure that the finite element model was correctly capturing the structural dynamic behaviour of the structure. A direct frequency response analysis was adopted to solve the coupled

equations of motion in terms of forcing frequency and the structural response was computed at discrete frequency steps by using Nastran Sol 108. A unit force was defined as a function of frequency and was applied as a point load at the trailing edge corner. A suitable interval of frequencies was analysed for each case.

Firstly, the analysis was conducted on the flap in neutral configuration. Figure 6.35 shows the graph of the frequency response function for the inboard flap with aluminium skin in the range 0-30 Hz. It can be noticed that a peak in the response occurred in correspondence to the first natural frequency of the structure at 20 Hz. Secondary peaks also occurred in correspondence to the other natural frequencies.
Similarly, Figure 6.36 shows the frequency response of the inboard flap with carbon fibre/epoxy skin in the range 0-30 Hz, with a peak at approximately 24 Hz.

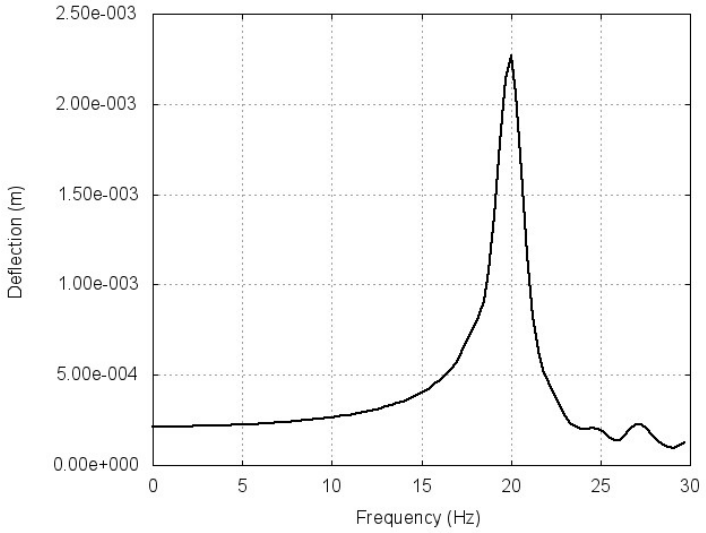

Figure 6.35: Inboard flap aluminium skin frequency response: 100% beam root stiffness in neutral configuration

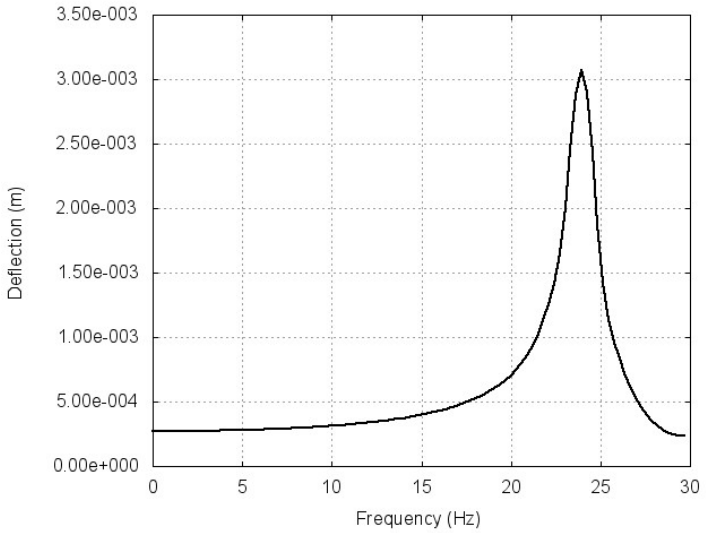

Figure 6.36: Inboard flap carbon fibre/skin frequency response: 100% beam root stiffness in neutral configuration

The analysis was then repeated for the flap in morphed configuration. The results are presented in Figures 6.37 and 6.38. Figure 6.38 shows additional modes as the frequency range of analysis for the flap with carbon fibre/epoxy skin was extended from 0-30 Hz to 0-45 Hz to account for the higher natural frequencies obtained from the modal analysis (see Tables 6.7 and 6.8).

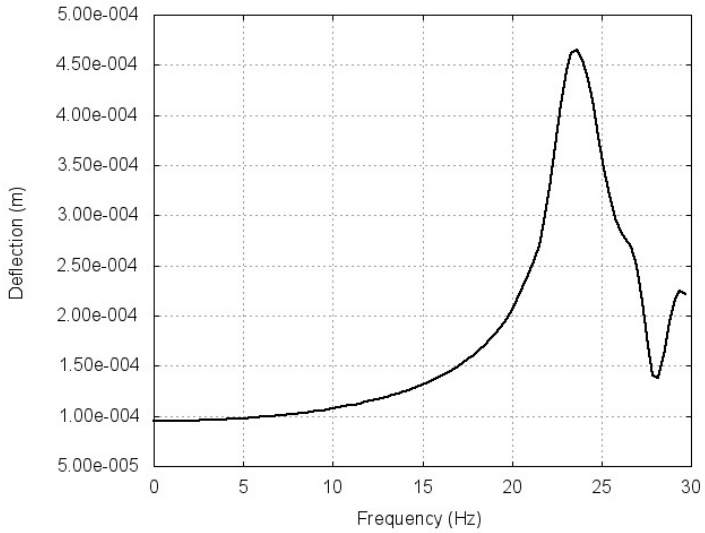

Figure 6.37: Inboard flap aluminium skin frequency response: 100% beam root stiffness in morphed configuration

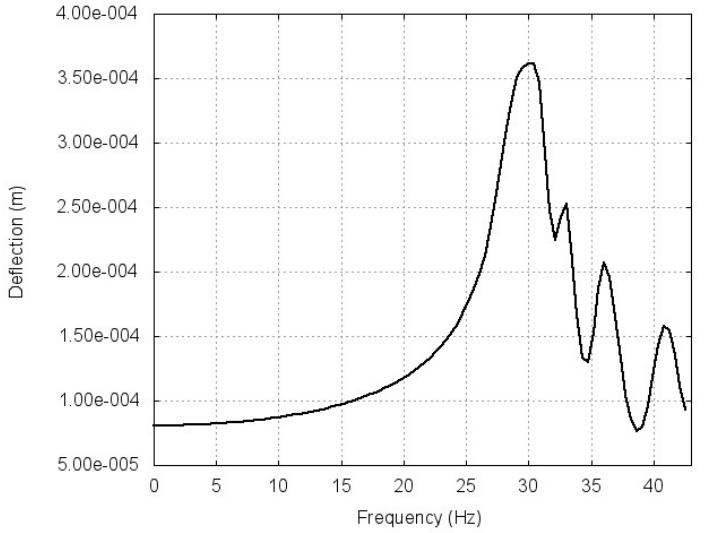

Figure 6.38: Inboard flap carbon fibre/epoxy skin frequency response: 100% beam root stiffness in morphed configuration

Finally, Figure 6.39 shows the link-track deployment mechanism frequency response, exhibiting a peak in correspondence of the first natural frequency, at around 76 Hz.

Based on the frequency response obtained for the structure, some predictions can be made on the response of the structure to input loads at different frequencies. When an input load with low frequency is applied to the flap, it is expected that the inertia terms will be negligible, leading to few oscillations that quickly damp out. On the other hand, input

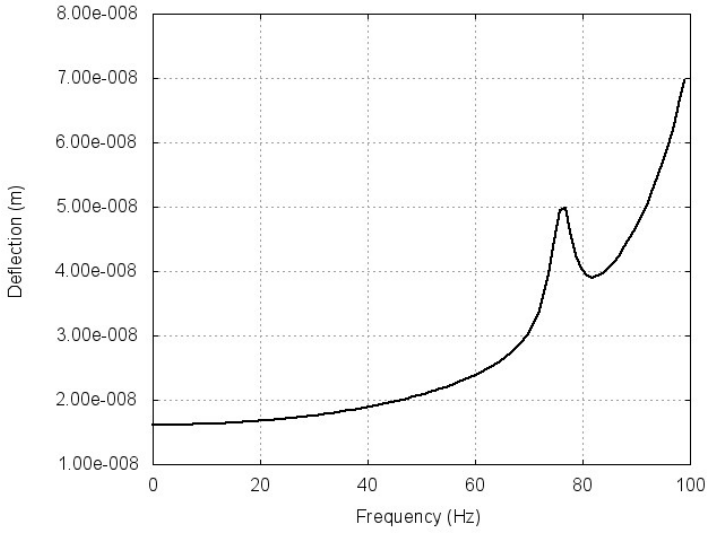

Figure 6.39: Link-track deployment mechanism frequency response

loads of higher frequency will be characterised by more evident oscillations, due to the increasing importance of the inertial contribution. When the input frequency approaches the natural frequencies of the structure, a peak of the response is expected, as predicted by theory [54].

6.4.3 Gust Response Analysis

A transient response analysis was conducted on the flap model to evaluate its behaviour under time varying aerodynamic loads. These loads can be used to approximate the effect of a gust on the flap structure.

The analysis was carried out for the landing case, when the flap was fully deployed, as this represents the most onerous condition. An input load with a 1-cos shape was considered for this study to represent a discrete gust. The CS-25 Regulations [147] specify the design criteria for the determination of the limit gust loads on a high lift device. The shape of the gust acting on the flap was described using the same expression presented for the whole airplane in CS 25.341:

$$U = \frac{U_{ds}}{2}\left[1 - cos\left(\frac{\pi s}{H}\right)\right] \tag{6.4.1}$$

and

$$U = 0 \qquad s > 2H \tag{6.4.2}$$

where s in the distance penetrated into the gust, U_{sd} is the design gust velocity expressed in equivalent airspeed and H is the gust gradient, which is the distance parallel to the airplane's flight path for the gust to reach its peak velocity. Based on the information provided in the CS 25.345, specific for high lift devices, the gust velocity and the gust load factor were calculated. For a high lift device, the design gust velocity was set equal to $7.62m/s$ Equivalent Air Speed, while H is equal to 12.5 times the mean geometric chord of the wing.

According to the data provided by the SADE Partners, the airspeed at the beginning of the descent phase was equal to 124.5 m/s. A gust load factor of 1.33 was obtained (i.e. the magnitude of the gust load was 1.33 times the static aerodynamic pressure). From CS-25 it was also possible to evaluate the frequency of the gust, which resulted to be 3.45 Hz. The transient gust load was applied to the structure as an additional time dependent pressure. At time 0 s the static pressure load was applied and once the structure was stable the gust load was applied for two cycles.

The structural damping was included in the transient response analysis by expressing it as an equivalent viscous damping.

Figures 6.40 and 6.41 show the gust response of a point of the flap skin along the trailing edge for the models with aluminum and carbon fibre/epoxy skin respectively. The sudden gust force had the effect to increase vertical deflection of the trailing edge compared to the static air pressure load and led to a maximum vertical displacement of 1.36 cm and 1.30 cm respectively. However, the structure returned to its original position as soon as the dynamic load was released.

An additional study was conducted to investigate the effect of an higher load frequency on the structure. Figures 6.42 and 6.43 show the response of the flap structure to a 1-cos type input for an additional value of the input load frequency equal to 15 Hz. As expected, as the load frequency approached the first natural frequency, the structure exhibited larger oscillations.

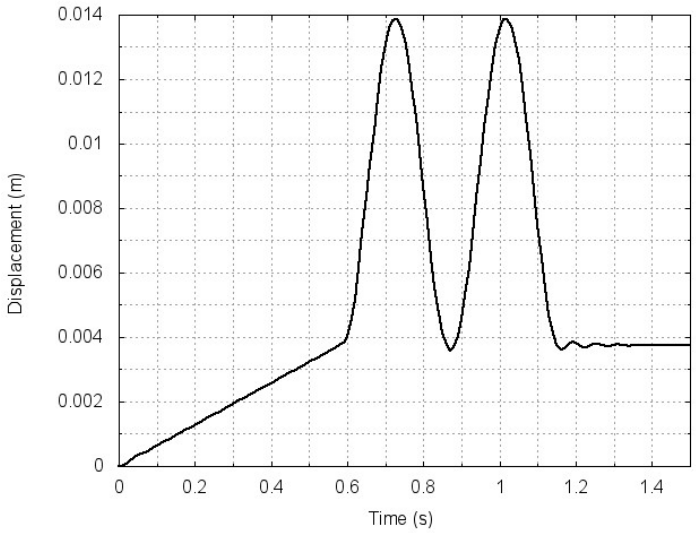

Figure 6.40: Gust response for the flap with aluminium skin with gust frequency 3.45 Hz and gust load factor 1.33

As any metallic structure the aluminium flap was subject to fatigue concerns. From the material S-N curve [115] it was estimated that the skin would withstand up to 3.5×10^5 load cycles when subject to the estimated high stresses during deployment. This number of cycles was higher than the number of flights required and therefore the structure met the fatigue design specifications.

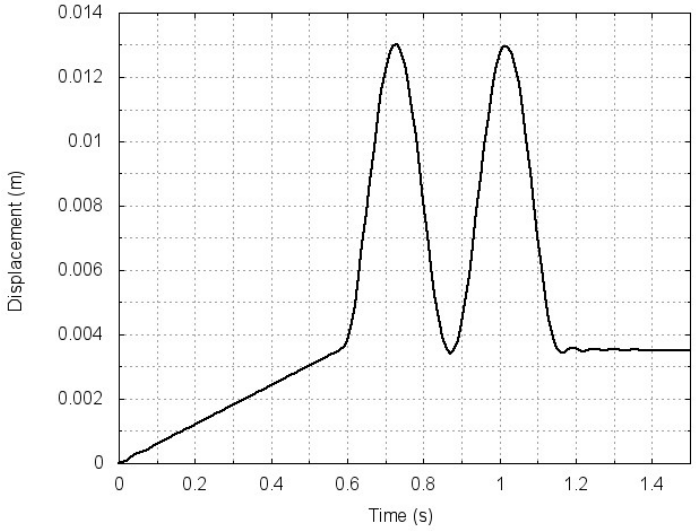

Figure 6.41: Gust response for the flap with carbon fibre/epoxy skin with gust frequency 3.45 Hz and gust load factor 1.33

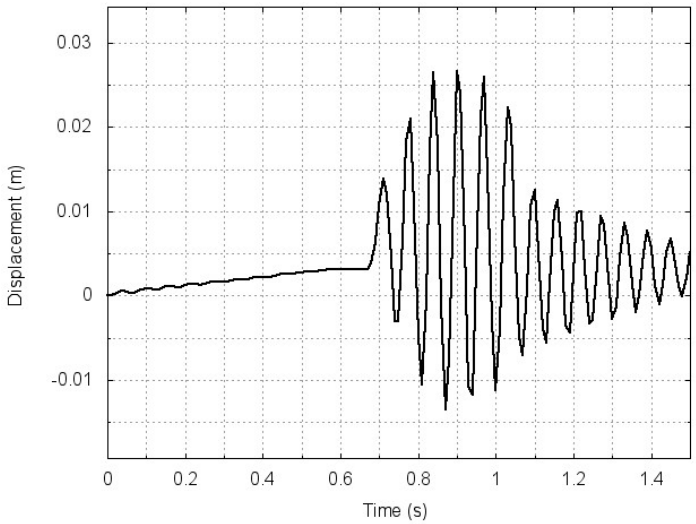

Figure 6.42: Gust response for the flap with aluminium skin with frequency 15 Hz and gust load factor 1.33

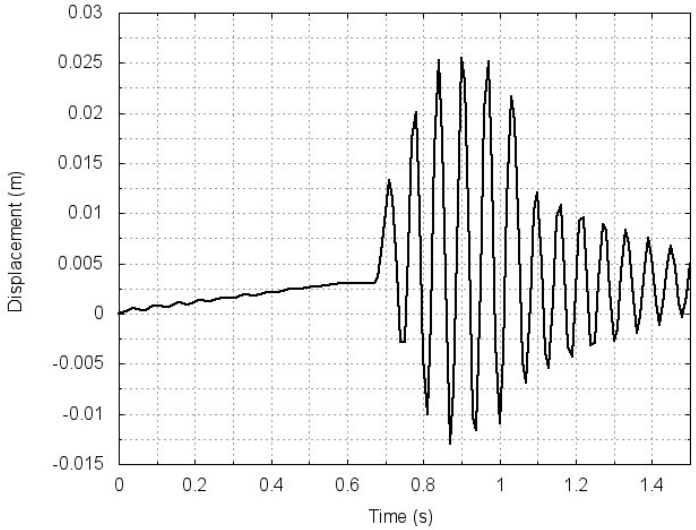

Figure 6.43: Gust response for the flap with carbon fibre/epoxy skin with frequency 15 Hz and gust load factor 1.33

This page is intentionally left blank.

CHAPTER 7

Aeroelastic Analysis of the Morphing Trailing Edge Flap

In this chapter the interaction between the aerodynamic pressure loads and the trailing edge flap structure is investigated and its effect on the flap shape is assessed. Section 7.1 presents an overview of the methods to calculate the aerodynamic pressure distribution over the slotted flap, from approximated methods to sophisticated computational analyses. Section 7.2.2 presents the code developed in this study to interface the commercial softwares Xfoil and Nastran, to conduct a preliminary aeroelastic analysis of the morphing trailing edge flap. Some simplificative assumptions were made on the pressure load distribution on the flap and on the mechanism of interaction between the structure and the aerodynamic pressure. The results of such investigation are shown in Section 7.2.4.

7.1 Aerodynamic Pressure Loads

An accurate evaluation of the aerodynamic loads resulting from the deployment of the flap and acting on the flap itself can be obtained only by using sophisticate CFD tools. In fact, for a single slotted Fowler flap, the overall increase in lift is the result of three different contributions:

- the increase in the chord of the airfoil due to the Fowler motion
- the increase in camber due to deployment
- the presence of the slot

and the relative influence on the total lift increment of each of these elements cannot be easily determined.

7.1.1 Howe's Approximate Method

In order to conduct a preliminary estimation of the chordwise load distribution, some simplified assumptions were adopted, following the method proposed in Howe [116] and here recalled. The total chordwise load can be derived by superposition of two different load distributions, one due to the angle of attack and the other to the flap deflection. For the sake of simplicity the flap is supposed to be a plain flap (without Fowler motion and without slot) whose chord is c_f. Firstly, only the effect of the angle of attack on the chordwise pressure distribution over a section of the wing in the clean configuration is considered. It is assumed in [116] that the pressure p can be represented by a second-order polynomial as:

$$p = ax^2 + bx + c \tag{7.1.1}$$

the coefficients a, b, c depending only on the position of the centre of pressure on the chord. These coefficients have been obtained by Howe [116] by imposing that the pressure at the trailing edge of the wing is zero, that the area under the curve representing p is unity for a unit chord and that the moment of the area about the leading edge for unit area is equal to the position of the centre of pressure. With these assumptions we have:

$$p_\alpha = 6\left[1 - 2\overline{x} + (8\overline{x} - 3)\,x + 2\,(1 - 3\overline{x})\,x^2\right] \tag{7.1.2}$$

Subsequently, it is possible to evaluate the pressure distribution consequent to the deflection of a flap. As already stated the flap is simply a plain one and its only degree of freedom is represented by the deflection angle β. It is assumed in [116] that forward of the hinge-line a parabolic pressure distribution applies (exactly as in the case of the clean wing configuration), and that afterwards of the hinge-line the pressure distribution becomes triangular in shape. The coefficients a_f, b_f and c_f needed to define the parabolic distribution from the leading edge of the wing to the hinge-line of the flap are necessarily different from the ones estimated for the clean wing case because they are affected by the presence of the flap. Previous studies, which are now summarised in the ESDU reports [116], [117], [118],[119] and [120], have shown that the coefficients a_f, b_f and c_f depend on the following parameters:

- the ratio $R = -b_2/a_2$ of the hinge moment coefficient b_2 of a round nose flap and the lift curve slope a_2 due to the deflection of the plain flap;
- the ratio $r = c_f/c$ of the flap chord c_f aft of the hinge-line and the total chord c
- the position $\overline{x_w}$ of the centre of pressure of load forward of the hinge-line.

These coefficients can be written as:

$$a_f = 6\left[R - 2\,(1 - 2Rr)\,[x_w - (1 - r)\,/2]\,/\,(1 - r)^2\right] \tag{7.1.3}$$

$$b_f = 36\left[2\,(1 - 3Rr)\,[2x_w/3 - 4]\,/\,(1 - r)^2 - R\right]/\,(1 - r) \tag{7.1.4}$$

$$c_f = 12\left[3R - (1 - 3Rr)\,[3x_w - (1 - r)]\,/\,(1 - r)^2\right]/\,(1 - r) \tag{7.1.5}$$

The pressure distribution due to flap deflection will be calculated as:

$$p_f = c_f x^2 + b_f x + a_f \tag{7.1.6}$$

The total chordwise pressure distribution due to both the angle of attack and the deflection of the flap is obtained by simply adding together the two contributions.

$$p = p_\alpha + p_f \tag{7.1.7}$$

These very simple expressions for chordwise pressure distribution provide an estimation of aerodynamic loads which is accurate enough to be used during the initial design and the preliminary structural analysis of a wing. However, as Howe points out [116], for flap deflections over 20° these formulae become less accurate.

7.1.2 ESDU Datasheet

The method to estimate the aerodynamic pressure presented in the previous section has a high degree of approximation. Moreover, it should be noted that the coefficients a_2 and b_2, which are respectively the slope of the lift curve and the slope of the hinge moment curve due to the deflection of the flap, are usually calculated by means of some empirical relations provided in the ESDU databases [117] and [118] and built using experimental data, rather than evaluated using an analytical expression. The coefficients a_2 and b_2 are strongly dependent on the geometry of the airfoil (i.e chord c, relative thickness t/c and trailing edge angle τ) and of the flap (i.e. its chord c_f), but also on the characteristics of the flow (Reynolds number). With the hypothesis of a standard airfoil, the trailing edge angle τ is known once it is known the relative thickness t/c of the airfoil. In fact, $tan\tau/2 = t/c$.

The parameters a_2 and b_2 have been calculated for the SADE wing by assuming as the reference airfoil a standard NACA 4412. For the SADE wing the following data are also known:

Table 7.1: Geometric and aerodynamic parameters for the SADE wing

$r = c_f/c$	0.2
t/c	0.12
Reynolds number	710^6

The reference airfoil is a standard NACA 4412. Based on the knowledge of the Reynolds number and of the geometry of the airfoil, from the ESDU Wings 01.01.05 documentation [119] it is possible to obtain the coefficient $(a_1)_0/(a_1)_{0T}$, which represents the ratio of the real and theoretical slope of the lift coefficient.

$$\frac{(a_1)_0}{(a_1)_{0T}} = 0.872$$

From the ESDU Controls 01.01.03 [120] it is possible to find out the $(a_2)_0/(a_2)_{0T}$, which is the same ratio evaluated in presence of a control surface deflection, and also the $(a_2)_{0T}$,

which is the theoretical slope of the lift coefficient curve in presence of a control surface deflection.

$$\frac{(a_2)_0}{(a_2)_{0T}} = 0.81 \qquad (a_2)_{0T} = 4.55\ rad^{-1}$$

Hence:

$$(a_2)_0 = \frac{(a_2)_0}{(a_2)_{0T}}\,(a_2)_{0T} = 3.69\ rad^{-1}$$

In the same way using the ESDU Controls 04.01.02 documentation [121] it is possible to calculate the parameters related to the hinge moment coefficient $(b_2)_0$ based on the $\frac{(b_2)_0}{(b_2)_{0T}}$ and the $(b_2)_{0T}$.

$$\frac{(b_1)_0}{(b_1)_{0T}} = 0.84 \qquad (a_2)_{0T} = 0.865$$

Hence:

$$(b_2)_0 = \frac{(b_2)_0}{(b_2)_{0T}}\,(b_2)_{0T} = -0.73$$

In the end the ratio R can be evaluated as:

$$R = -\frac{b_2}{a_2} = 0.197$$

Furthermore, Howe [116] provides a list of empirical equations to determine the position of the centre of pressure $\overline{x}$, which depends on the angle of attack α, for the airfoil with and without flap surface deflected.

The values obtained can be substituted in the Equations 7.1.3 to 7.1.5 to evaluate the pressure distributions p_α and p_f. Considering an angle of attack $\alpha = 12°$, the value $\overline{x} = 0.33$ is obtained for the centre of pressure and the corresponding p_α is presented in Figure 7.1.

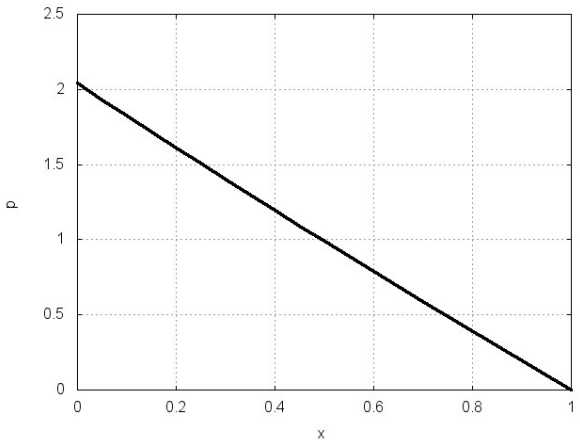

Figure 7.1: Estimated pressure distribution due to angle of attack

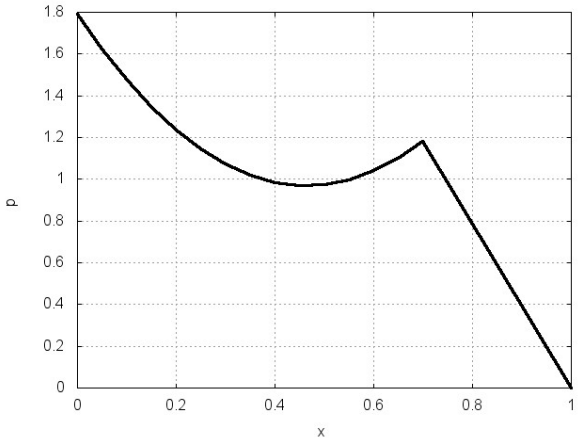

Figure 7.2: Estimated pressure distribution due to the deployment of the flap

When considering the deflected flap, the pressure distribution initially follows the equation of p_f from the leading edge of the wing to the hinge line of the flap, becoming triangular shaped after the hinge line, as shown in Figure 7.2.

The overall pressure distribution then is given by the sum of these two contributions, as shown in Figure 7.3.

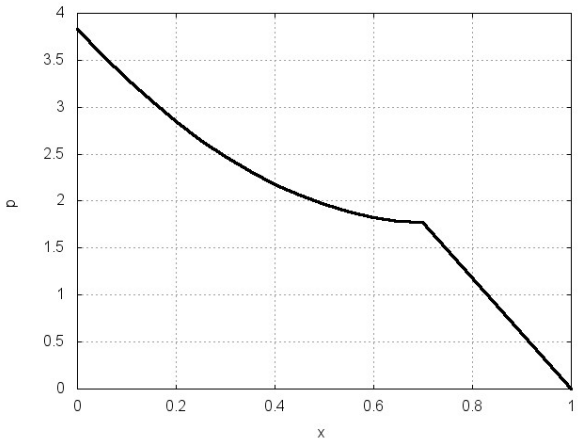

Figure 7.3: Estimated pressure distribution due to both angle of attack and flap deployed

7.1.3 CFD Methods

In the initial phases of the analysis, the aerodynamic loads on the inboard flap of the SADE wing were estimated by using Howe's and ESDU procedures described in Section 7.1.1 and 7.1.2. Subsequently, these aerodynamic loads were replaced with a more accurate evaluation conducted using the the commercial CFD software CFX [112]. The aerodynamic pressure over the wing with flap deployed was calculated by one of the partners of the SADE project [112] and then manually applied to the finite element model of the structure.

7.1.4 The Xfoil Software for Panel Method Applications

ESDU and Howe's method of analysis and the CFD approach represent the two extreme ways to evaluate the aerodynamic pressure load around a body. A solution offering an intermediate degree of approximation between these two approaches is represented by panel methods.

Panel methods are techniques to solve incompressible potential flows, based on three main simplificative assumptions on the characteristics of the air flow: the compressibility of air is neglected, the curl of the velocity field is assumed to be zero, the viscosity of air in the flow field is also neglected. Under these assumptions, the velocity in the flow field can be represented as the gradient of a scalar velocity potential ϕ and the flow is governed by Laplace's equation $\nabla^2\phi = 0$ (see Anderson [124] for a complete discussion on potential flows).

Panel methods can be applied to both 2D and 3D problems. The first step of the solution procedure consists in discretising the body immersed in the flow by dividing its surface in a certain number of panels. Considering the case of an airfoil, its contour can be discretised and divided into segments, also called panels because they represent the section of an infinitely long panel surface. Each panel is defined by its two end points, called panel joints, and by a control point, located at the panel centre. The use of a higher number of panels leads to a more accurate solution, since it offers a better representation of the airfoil shape. Subsequently, vortex sheets of unknown strength γ are placed on each panel to mimic the effect of the airflow around the airfoil. Each vortex sheet will determine a certain amount of circulation and hence lift around the airfoil. The core of the method consist in determining the strength γ of the vortex distribution by solving Laplace's equation in some specific point along the airfoil, where specific flow conditions, such as the tangent-flow boundary condition, have to be satisfied. This process leads to a system of linear algebraic equations in the unknown vortex strengths.

Panel methods offer a fast and reasonably good approximation of the airflow around a body, when more complex solutions like CFD results are not available or too expensive to obtain. These methods are able to predict very well the lift generated but, unfortunately, they do not offer any drag results.

In this chapter, the software Xfoil [122] was chosen as the panel method solver for the analysis of the inboard flap. Xfoil was written by Mark Drela in 1986 using the Fortran 77 programming language and was developed as an interactive program for the design and analysis of subsonic isolated airfoils [123]. As specified by Drela in his paper [123], the inviscid formulation adopted is a simple linear-vorticity stream function panel method. The equations are closed with an explicit Kutta condition applied at the trailing edge. A viscous correction was included in the analysis to allow the user to consider the effect of the boundary layer and wake along the airfoil. Moreover, a compressibility correction is incorporated, allowing good compressible predictions even when the velocity reaches high subsonic Mach numbers (higher than 0.3). All the source codes have been made public by the Author and this has allowed various upgrades and enhancements. The program was developed with an interactive interface, however the traditional batch-type execution is also possible. In the current research, the Xfoil source code has been modified to include an interface with the Nastran structural solver to conduct a coupled analysis and to

evaluate the effect of the fluid-structure interaction on the inboard flap with morphing trailing edge.

7.2 The Fluid-Structure Interface

7.2.1 Computational Aeroelasticity

The behaviour of a generic structure can be analysed by considering the generalised equations of motion, which can be written as:

$$[M]q''(t) + [C]q'(t) + [K]q(t) = F(t) \tag{7.2.1}$$

where $q(t)$ is the generalized displacement vector, linked to the structural displacement $w(x, y, z, t)$ with the relation $w(x, y, z, t) = \sum \{q_i(t)\Phi_i(x, y, z)\}$. $\Phi_i(x, y, z)$ indicates the normal modes of the structure, $[M]$, $[C]$ and $[K]$ are the generalised mass, damping and stiffness matrices and the term $F(t)$ on the right hand side is the generalised force vector, which represents the link between the unsteady aerodynamic and inertial loads and the structural dynamics.

As it can be observed from the above equations, the terms representing the structures, the aerodynamics and the dynamics are distinct from each other and this allows to choose different methods for any particular system. On the other hand, however, it is necessary to develop an interface between the fluid domain and the structure in order to ensure that the interaction of the two is correctly assessed.

Guruswamy [125] offers an extensive review of computational aeroelasticity methods. As shown in Figure 7.4, several different approaches for fluid-structure analysis are available, with different levels of fidelity. Depending on the methods of analysis and interface chosen, three main categories of computational aeroelastic models can be identified: fully coupled, closely coupled and loosely coupled models.

In the fully coupled models, the structural and aerodynamic equations are combined, then solved and integrated in time simultaneously. This approach has the disadvantage to be computationally expensive and has limitations on the complexity of the models and on the grid size.

Loosely coupled models, on the other hand, are based on the separate solution of the structural and fluid equations, using different computational grids for the two subsystems. This leads to a great flexibility in the choice of the solvers. An interface technique has to be developed to ensure the exchange of information between the two modules. However, this exchange of information is set only after partial or complete convergence, hence loosely coupled models generally suffer from low accuracy and their use is limited to small perturbations and models with moderate nonlinearities.

Finally, closely coupled models are widely used in computational aeroelasticity because they offer a good compromise between accuracy and complexity. Different solvers are used for fluid and structure, however these solvers are tightly coupled into one single module by using a suitable interface. The interface ensures that the surface loads obtained

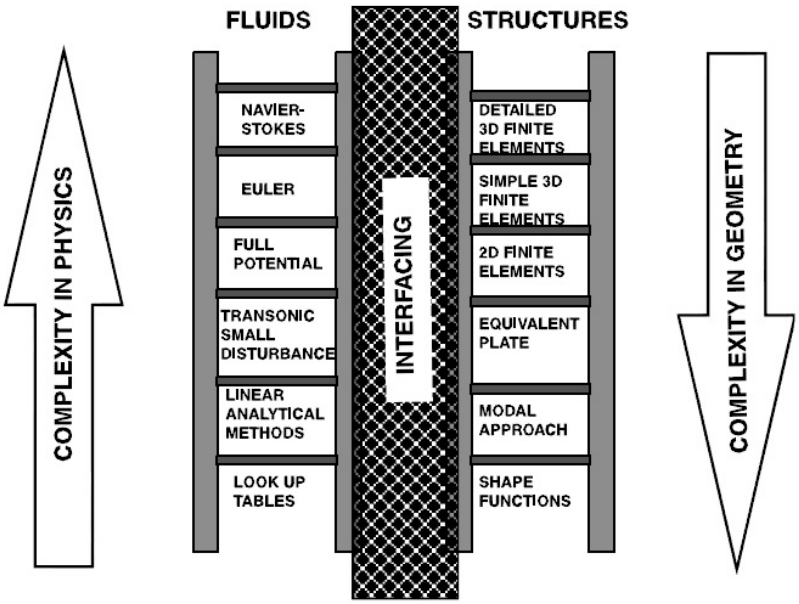

Figure 7.4: Models with different levels of fidelity for flow and structure [125]

from the fluid solver are transferred and correctly applied to the structure and, vice versa, the structural displacements are correctly mapped from the structural model to the aerodynamic grid.

In general, if a CFD solver is used to determine the aerodynamic load, once the displacements are transferred to the fluid model, it is necessary to re-mesh the fluid domain as the aeroelastic analysis marches in time. Various moving boundary techniques have been developed to address this aspect of the aeroelastic analysis, and a vast literature can be found about this topic (see [125] and [126]). Cavagna et al. [127] have also investigated the possibility to conduct a high fidelity aeroelastic analysis using existing commercial software rather than specifically written codes, in order to satisfy the need of the industry for fast and relatively cheap solutions.

In the first phase of this investigation, the Xfoil code, based on high order panel method, has been chosen as the fluid solver instead of a CFD one to have a first and quick approximated evaluation of the aerodynamic pressure load on the airfoil. As shown by Lafountain [128], the results of this approach are very accurate and represent a good starting point to develop further analyses. Xfoil automatically tailors the panelling characteristics depending on the airfoil geometry. For this reason, the re-meshing of the fluid domain will not be addressed.

7.2.2 The Xfoil-Nastran Interface for the Analysis of the Morphing Flap

The aerodynamic pressure load on the inboard flap structure was evaluated using the Xfoil software described in the previous sections (see also [122], [123]). Figure 7.5 shows the typical data flow followed by Xfoil for the resolution of the flow over an airfoil. An interactive interface allows the user to load one of the standard NACA airfoils or

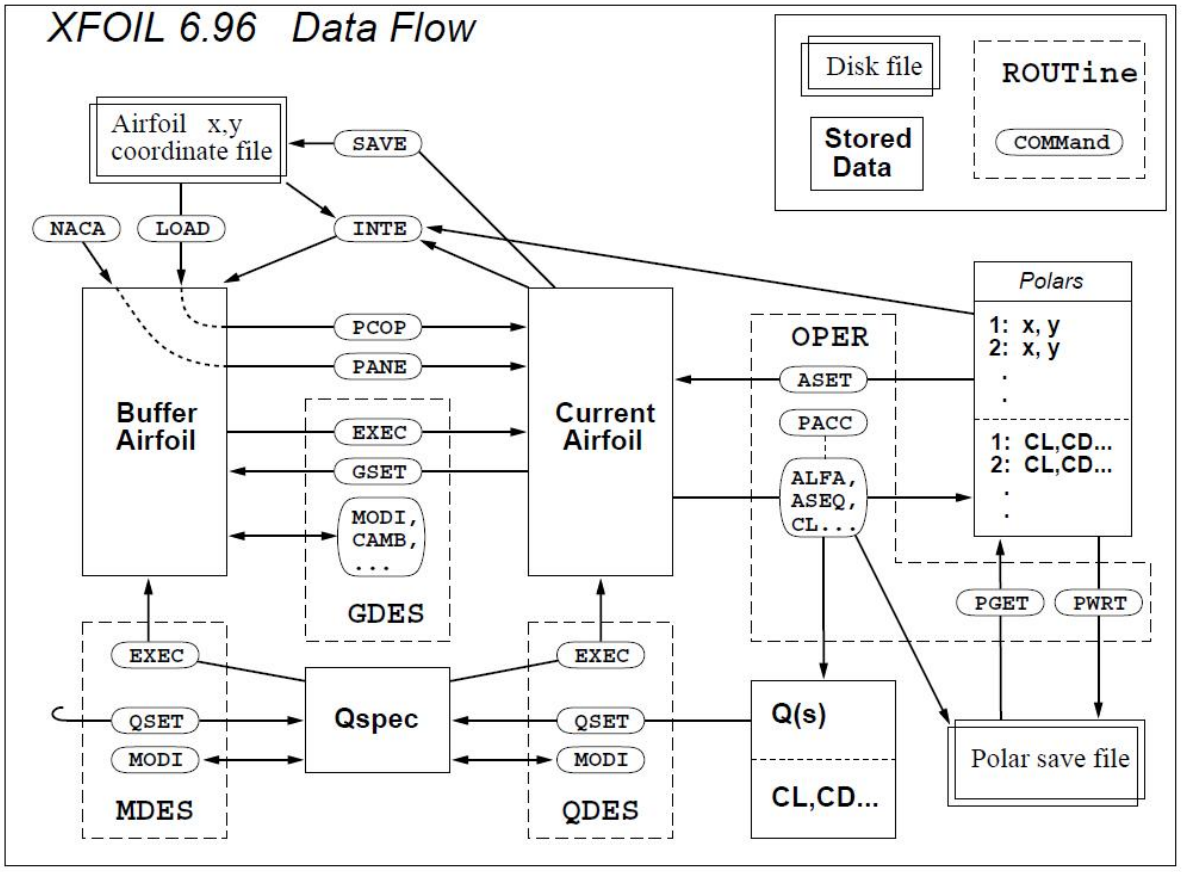

Figure 7.5: Xfoil Data Flow ([122], [123])

a personalised set of airfoil coordinates, to specify the Reynolds number, the angle of attack and the density of panels required in the analysis. Xfoil then provides the C_P distribution, the polars, the $C_L - \alpha$ diagram and other relevant aerodynamic quantities.

In the interface program developed for this research study, this fully interactive interface approach has been replaced with a batch-type execution, which can be more conveniently included in an automatic iterative procedure for the aeroelastic calculations. Once the Xfoil application is executed within the aeroelastic interface program, the buffer airfoil coordinates are read from file via the LOAD command and its coordinates are normalized. Other inputs such as the Reynolds number and the angle of attack are also specified directly in the file. The pressure coefficient C_p on the airfoil is then evaluated. For the current analysis of the SADE inboard flap, a Reynolds number Re of 7000000 and an angle of attack of 0° were assumed. It was decided to have the same Re and α values throughout all the iterations.

The structural model of the trailing edge flap was created using the commercial software MSC Patran. The skin-only model presented in Chapter 5 was considered for this preliminary analysis. The structural results were obtained by running a Nastran nonlinear static analysis (Sol 106).

7.2.3 Structure of the interface

The interface main program is able to call different subroutines and at the same time to launch the Nastran and Xfoil runs from shell. Three files must be provided for the analysis:

- The structural .bdf file created using Patran
- The Xfoil input file containing the coordinates of the point of the aerodynamic section
- The list of the nodes corresponding to the point of the aerodynamic section, to interface the two domains

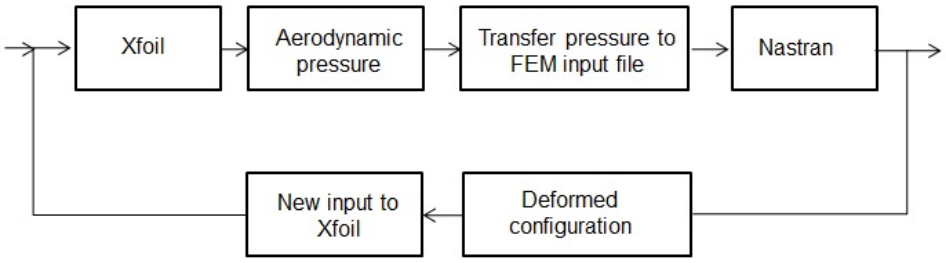

Figure 7.6: Fluid-structure interaction in the Nastran/Xfoil interface

The interface program implements an iterative structural and aerodynamic analysis illustrated in Figure 7.6. Initially, the structural data were used to generate a deformed aerodynamic section for the aerodynamic solver. The Xfoil is then run to obtain the

pressure coefficients distribution over the flap structure. The pressure coefficients were converted into a pressure distribution and re-applied to the flap structure. A final structural run is then performed to generate the new flap deformed configuration under the new aerodynamic load. All these steps were repeated until the shape converged to its final equilibrium value.

Attention was paid to ensure the necessary accuracy in all the steps of the iterative analysis. The number and location of the points defining the aerodynamic section was carefully selected in order to achieve a smooth aerodynamic surface. Moreover, the number of points considered in the aerodynamic and structural analysis was different and an interpolation was required in order to transfer the data from the aerodynamic to the structural solver.

In order to interface the Xfoil and Nastran software, it was fundamental to know the characteristics of the input and output files for both solvers. The Xfoil input and output files were simple text files containing the coordinates of the airfoil and the corresponding values of the pressure coefficient respectively. On the other hand, the input and output files for the structural analysis were much more complex since they had to provide to the analysis all the characteristics of the structure. In particular:

- Nastran input file
  The MSC Nastran input file for the structural analysis (.bdf file) consists of different sections: the Nastran statement, the file management section, the executive control section, the case control section and the bulk data section. The first three sections contain statements to specify system parameters that control internal solution processing, assign files and manipulate the database, select the solution sequence to be run. The case control section is used to define the case loads and to specify the output requests. The bulk data section contains all the information needed to describe the structural model and to define the analysis such as the grid points, elements, constraints and loads. The interface program acted mainly on the bulk data section, by reading the input file to obtain the initial configuration and, more importantly, by rewriting the parts connected to the definition of the aerodynamic pressure load on the model. Since the .bdf file is written in a special ten-field format, an extensive use of the Nastran and Patran Guides ([105], [106], [107]) was made to understand the main characteristics of the bulk data entries.

- Nastran output file
  Once a Nastran run is submitted, several output files can be generated, depending on the input file requests. The main output file is the .f06, an ASCII file that can be opened with any text editor, containing the printed output such as displacements, element forces, stresses... Similarly to the .bdf file, the .f06 file has a standard format and the data are organised into separate fields. The part relevant to the aeroelastic interface is the section containing the displacements of the model for each node.

7.2.4 Results of the Aeroelastic Analysis of the Morphing Flap

7.2.4.1 Aerodynamic Load on the Flap

As already mentioned in Section 7.1, the use of Xfoil to evaluate the aerodynamic pressure load on the flap represents an approximation and CFD methods would offer a more accurate prediction of the C_P distribution.

One of the biggest limitation of Xfoil is the impossibility to consider the presence of the flap slot. To overcome this issue, it was assumed to consider the flap as a wing, the C_P distribution was evaluated on the airfoil normalized with respect to the chord and the resulting C_p was then scaled with respect to the max C_p value obtained from the CFD calculations.

7.2.4.2 Full scale inboard flap

The interface program was used to study the deflection of the trailing edge structure under the effect of the aerodynamic load and, simultaneously, the effect that such deflection has on the pressure distribution. The inboard flap was considered for the iterative analysis. The flap was supported by its deployment mechanism at two spanwise locations at 30% and 70% of the flap span. The interface study allowed to identify for each step of the iteration:

- The pressure coefficient c_p on the flap section (and hence the aerodynamic pressure distribution on the flap)
- The structural deflection achieved under the effect of the aerodynamic pressure
- The effect of the structural deformation on the aerodynamic pressure distribution

In the first step of the iterative analysis, the Xfoil evaluated the aerodynamic loads on the flap in neutral configuration. Figure 7.7 shows the distribution of panels along the flap section. The default number of panels chosen by Xfoil, equal to 160, was increased to 200 to ensure a good numerical accuracy, and the panel density was set higher in the areas of high curvature, such as the leading edge, and at the trailing edge.

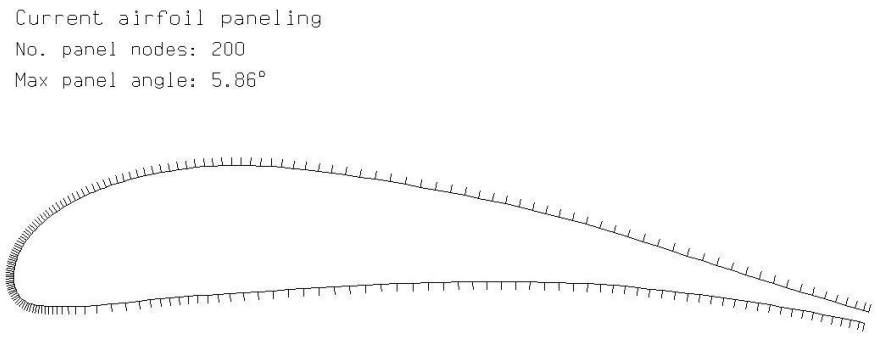

Figure 7.7: Flap section for aerodynamic analysis: panels

The pressure module of the interface program then provided to convert the $c_p$into pressures by considering a density ρ of $0.69Kg/m^3$ and a flight speed of 124.5 m/s and the resultant pressure distribution was applied as a distributed load over the flap structure. A Nastran run was then performed to obtain the deformed configuration of the structure. The upwards aerodynamic load had the effect to generate a vertical deflection and, consequently, a change to the aerodynamic section of the flap. The structural module of the interface program was able to extract the coordinates of the flap mid-section and to generate a modified airfoil section for the Xfoil aerodynamic solver. The steps above were repeated until convergence was reached, hence until the aerodynamic pressure distribution and the vertical deflection of the flap became constant between two consecutive iterations.

Figure 7.8 presents the c_p distribution over the flap structure for the first iteration. The results obtained in the intermediate iterations showed an oscillating trend in the aerodynamic pressure load developed over the flap structure before convergence. A 29% difference in the maximum c_p was obtained between the initial and the converged pressure distributions, as presented in Figure 7.9.

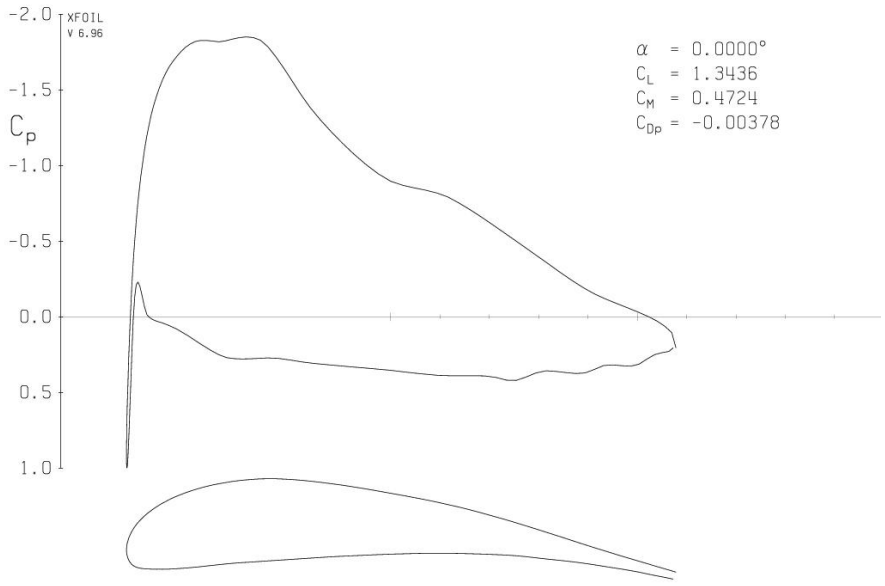

Figure 7.8: c_p distribution over the flap: initial iteration

The first iteration generated a total vertical displacement of 3.40 mm, as illustrated in Figure 7.10. Despite the approximation involved in the use of the Xfoil and the higher order panel method, it can be noted that the vertical deflection achieved in the first step of the iterative analysis is similar to the static flap deflection of 3.75 mm presented in Chapter 6, where air pressures derived by CFD method were used.

The results obtained in the subsequent iterations showed an oscillating trend in the aerodynamic pressure load developed over the flap structure and, consequently, in the flap displacement. When the interaction between the structure and the airflow is considered, the flap displacement under the effect of the final aerodynamic load is expected to be lower than the initial uncoupled value. In fact, the upwards aerodynamic pressure load

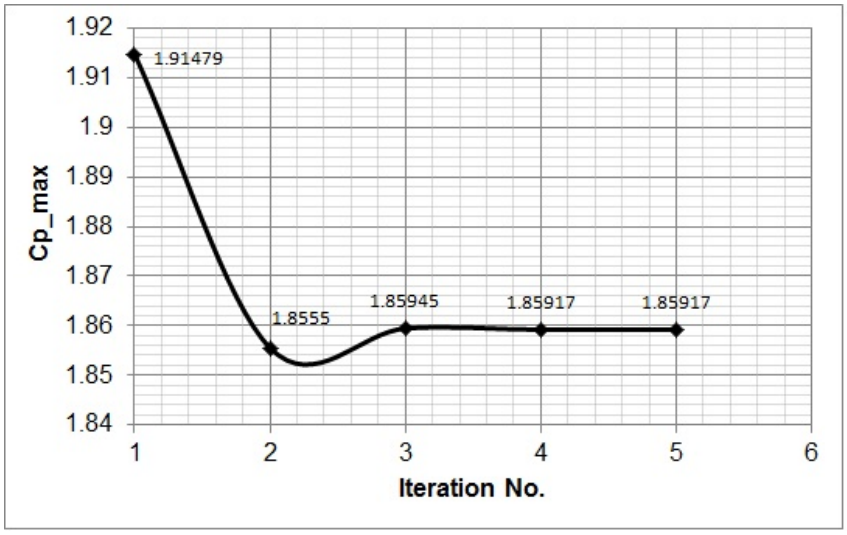

Figure 7.9: Max c_p variation between the iterations

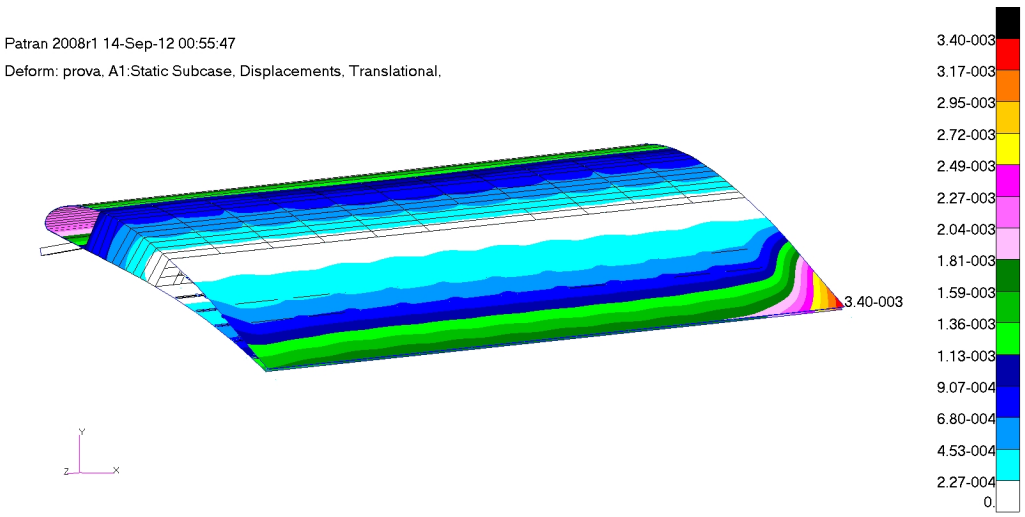

Figure 7.10: Flap displacement under air pressure load: initial iteration

has the effect to reduce the flap camber, leading to a reduction of the overall c_p. However, once the c_p and consequently the air pressure loads on the flap has reduced, the flap could go back to a more cambered configuration, with a consequent increase in the c_p. In the current analysis of the flap with morphing trailing edge, the alternate trends in the c_p distribution and flap camber led to a flap displacement, measured at the trailing edge extreme point, oscillating towards a constant final value, as shown in Figure 7.9. Convergence was achieved after 5 iterations. Figure 7.11 presents the final deflection of the flap, equal to 1.66 mm.

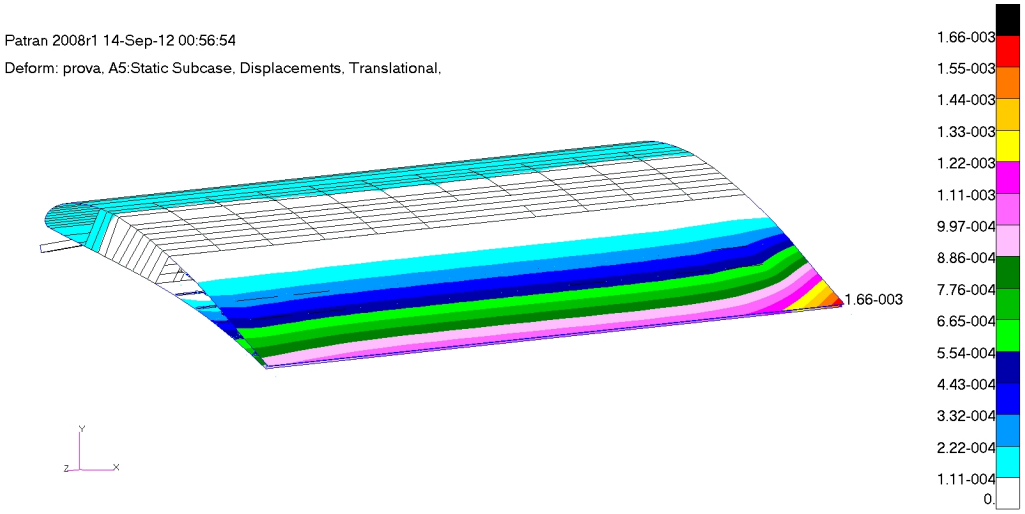

Figure 7.11: Flap displacement under air pressure load: final iteration

As known from the structural static analysis, the aerodynamic pressure load and the actuation load required to morph the flap act in opposite directions. Hence, the presence of the airflow has the effect to increase the actuation load required to morph the flap into the desired deflected shape. On the other hand, the iterative analysis of the flap has shown that the flap under the effect of the aerodynamic load is statically stable since the interaction between the aerodynamic load and the structural deflection tends to bring the flap into an equilibrium configuration. From a global point of view, the presence of the flap positively contributes to the structural stability of the wing with morphing high lift devices. In fact, considering only the morphing leading edge, an increase in the aerodynamic load generates an upwards structural deflection which, in turns, would determine an increase in the local angle of attack and a further increase in the aerodynamic load. This unstable behaviour is partially counteracted by the presence of the flap, which helps to preserve a desirable aerodynamic configuration while contributing to the overall lifting capabilities of the wing.

This page is intentionally left blank.

CHAPTER 8

Optimisation of an Actuated Morphing Structure

In the previous chapters it has been often stressed that the traditional design and analysis methods applied to conventional aircraft no longer hold in the case of morphing structures and innovative analysis approaches are hence required. The optimisation of the design and structural characteristics of a morphing structure presents similar challenges. In fact, a morphing structure has additional requirements to satisfy, such as the achievement of a prescribed deflection shape, and the combined effect of the different design parameters is not always easy to evaluate.

This chapter presents a procedure for the design optimisation of a morphing structure and its application to the flap with morphing trailing edge presented in the previous chapters. In Section 8.1, the general optimisation problem is defined and a rapid overview of the steps followed during the optimisation process is given. The analysis was limited to the morphing flap with aluminium skin. Section 8.2 presents a study conducted to determine the characteristics of the EBAM actuation mechanism by specifying the number and position of the actuation loads. The target deflection based on the aerodynamic performance of the airfoil is considered and different approaches were used to identify and achieve the closest approximation of the desired deformed shape. An analytical approach based on the standard beam theory was developed and applied to the morphing trailing edge of the flap to obtain the right combination of deflection and actuation load in each point. The beam model results were compared with a finite element based study of the effectiveness of the various loading points combinations. Once the details of the actuation were determined, the optimisation was extended to consider the material properties of the skin panels. An optimization procedure was implemented by coupling the Fortran-based optimization subroutine ADS, developed by NASA in the 1980s, with the Nastran structural solver. The details of the interface analysis between ADS and Nastran and the results of the optimisation are presented in Section 8.3. The skin thickness was tailored in order to achieve a desired deflected shape under specified stress constraints. The stress and strain results for the morphing trailing edge flap, presented in Section 8.5, showed the potential to achieve significant weight reduction while maintaining good load carrying capabilities and meeting the shape requirements.

8.1 The general optimisation problem

The general optimisation problem consists in determining the values of the design variables $\underline{x} = (x_1, \ldots, x_n)$ that minimise a function $F(\underline{x})$ subject to some specific conditions:

$$\begin{aligned} &min \quad F(\underline{x}) \\ &g_j(x) \leq 0, \qquad j = 1, \ldots, m \\ &H_k(x) = 0, \qquad k = 1, \ldots, l \\ &L_i \leq x_i \leq U_i, \qquad i = 1, \ldots n \end{aligned} \tag{8.1.1}$$

$F(\underline{x})$ is called the objective function and its value depends on the design variables. In structural optimisation problems, the design variables typically represent physical characteristics of the structure, dimensions or skin thicknesses for example, and the objective function is often the weight of the structure. The $g_j(x)$ represent m inequality constraints while the $H_k(x)$ represent l equality constraints. The last n conditions are the side constraints, used to define and limit the region where to search for the optimum.
The constraints $g_j(x)$ and $H_k(x)$ express bounds and conditions for some meaningful quantities of the problem. For instance, the $g_j(x)$ constraints could refer to the stresses in the structure and could be used to impose a maximum stress limit, by expressing them in the form $\sigma/\sigma_{max} - 1 \leq 0$, where σ_{max} is the maximum allowable stress and σ is the current calculated stress.

A simple yet meaningful formulation of the problem to solve is the first step for an efficient optimisation process. Depending on the objective function and constraints, the optimisation problems can be classified as linear on nonlinear and different solution techniques can be implemented. The solution of a generic optimisation problem can be divided into three different levels:

- Strategy: technique to adopt for the solution of a specified problem, for example, unconstrained minimisation or linear programming
- Optimiser: algorithm or method to use for the solution of the optimisation problem
- One-dimensional search: technique to determine the iteration points

Several choices of strategies, optimisers and one-dimensional search methods have been developed to solve a wide range of problems. Gradient-based optimisation methods are often used for many types of problems. In these methods, after a preliminary analysis of the problem, an initial point in the design space is selected and the objective function, the constraints and their gradients with respect to the design variables are evaluated. The gradients are used to identify a descent direction, which minimizes the objective function. The design point is hence modified by following this descent direction and by changing the current values of the design variables accordingly. The objective function and constraints are then re-evaluated for the new design point and this process is repeated until final convergence is reached. Nonlinear optimisation problems are often solved using a group of gradient based methods called methods of feasible directions (MFDs) [129]. From a mathematical point of view, $h \neq 0$ is a feasible direction of descent if there exists an $\overline{\alpha}$ such that $\forall \alpha \in (0, \overline{\alpha}]$ the following two properties hold:

$$x + \alpha h \quad \in \Gamma \tag{8.1.2}$$

$$f^0(x + \alpha h) \leq f^0(x) \tag{8.1.3}$$

where Γ is the portion of the design space satisfying the conditions $g_j(x) \leq 0, j = 1, \ldots, m$. In order to find a feasible direction, the evaluation of the function and its gradient is required at each iteration; the step length along the feasible direction is then found by performing a constrained one dimensional search. These steps are repeated until convergence. Although other algorithms are more interesting from a mathematical point of view, the MFDs are used in structural design optimisation because they offer a series of advantages. Firstly, all the subsequent designs generated during the process are feasible, they improve at each iteration and could be used as intermediate design steps. Moreover, the algorithm only employs first order derivatives, resulting in reasonable computational costs if compared to other more sophisticated methods.

8.1.1 Optimisation Problems for Morphing Structures

Structural optimisation methods have traditionally had the primary objective to minimize the structural weight without compromising the load carrying capability of the structure and the techniques described in Section 8.1 above have been widely applied over the years.

The optimisation of a morphing wing structure, on the other hand, requires a different approach to the problem. As discussed by Moorhouse, Sanders et al. in [33], in fact, it is expected that morphing structures will exhibit some weight penalty compared to the non-morphing designs. Hence, the primary objective of the optimisation procedure is not the minimisation of the structural weight but the achievement of the prescribed deflection, in order to improve the wing performance and to overcome the inevitable weight penalty due to the presence of the actuators. Other key parameters to consider in the optimisation problem are the stress levels in the structure, which must meet the material strength requirements, and the total actuation load required for morphing, which should be as low as possible.

In this chapter, an optimisation process is presented to improve the design of the flap with morphing trailing edge. The optimisation was divided in two steps and focused initially on the eccentric beam actuation mechanism, and later on the thickness of the skin panels.

In the first stage of the analysis, the objective was to determine the best loading positions along the flap chord in order to achieve a deflected shape which was the closest possible to the specified requirements.

In the second phase of the optimisation, the skin panels were considered and the possibility of achieving some weight saving by reducing the skin thickness was investigated. The morphing flap structure presented conflicting requirements: on one hand, a thin skin is beneficial because it facilitates the morphing of the structure, leading to smaller actuation loads, on the other hand, the presence of the additional actuation loads to achieve the morphing of the structure requires enough structural stiffness to withstand the increased level of sollecitation.

8.2 Shape Studies for the Trailing Edge Flap

8.2.1 The Target Deflected Shape

The desired deflected shape for a wing structure with morphing capabilities is usually determined based on aerodynamic considerations, in order to achieve a configuration able to improve the aerodynamic performance of the wing. With reference to the wing in this current analysis, as already specified in Chapter 4, the deflection requirements for the SADE wing were determined through an aerodynamic optimisation conducted by other Partners of the project. The wing was considered as a two-component airfoil plus droop nose and the specific objective of the aerodynamic optimisation was to achieve a higher maximum lift coefficient.

The specific shape deflection requirements are presented in Section 4.2.1. Figure 8.1 shows a schematic representation of the flap lower skin from the rear spar to the trailing edge.

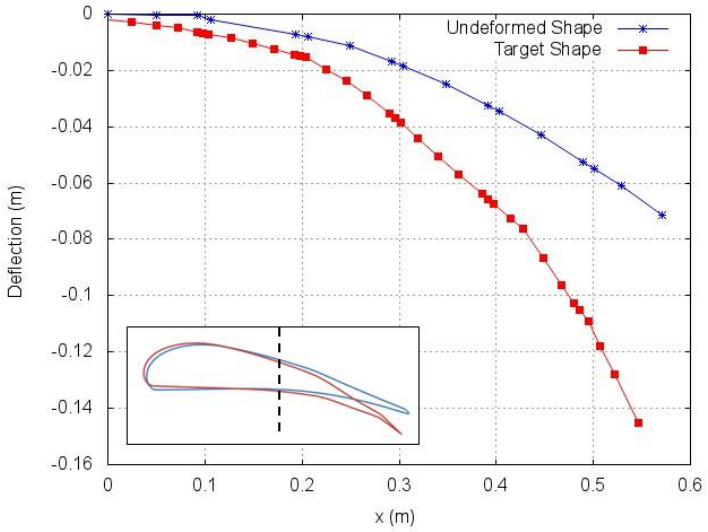

Figure 8.1: Flap trailing edge deflection requirements

During the initial stages of the design, presented in Chapter 5, the curvature of the eccentric beam in the EBAM mechanism and the actuation load applied were specifically selected in order to meet the shape requirements. However, despite the careful design of the curved beam, a closer look at the deflection achieved point by point along the flap chord has shown that some small differences may arise between the deflected shape achieved by the structure and the desired shape prescribed by the aerodynamics. These discrepancies could be related to very demanding shape requirements in some of the points or to the presence of highly cambered regions and sharp bends. The objective of the optimization study conducted in this chapter is to minimize such shape difference by acting on the characteristics of the actuation mechanism and on the material properties of the flap skins. The design presented in Chapter 5 for the morphing flap with EBAM actuation mechanism considered five uniformly distributed loads. The analysis presented in this section aims to improve the morphed shape achieved by acting on the number and chordwise position of the actuation loads.

8.2.2 Mathematical Approximation

It can be observed that the problem of finding the best locations where to apply the actuation loads shares some similarities with the problem of the best polynomial approximation of a given function. In the polynomial approximation, a given target function is approximated with a polynomial of order n over $n+1$ points in a selected interval. Transposing this to the case of the trailing edge flap, the target deflected shape could be approximated with a n-th order polynomial over $n+1$ specified loading points of the airfoil section. It could be assumed that imposed displacements are applied to these $n+1$ points, to force them in the desired position after deflection, while the rest of the structure will follow the prescribed shape more or less accurately depending on which points have been selected. This approach shares some similarities with the analysis conducted by Rhodes and Santer in [130], where special splines were used to assess the effectiveness of each loading point to fulfill the morphing requirements.

The polinomial interpolation was carried out on the interval $[0, c]$ representing the lenght of the rear morphing part of the flap, from the rear spar to the trailing edge. The best polynomial $p_n(x)$ that approximates the target shape $f(x)$ over $[0, c]$ can be defined as the polynomial that minimises the distance between these two functions:

$$d(f, p) = \int_0^c |f(x) - p_n(x)|\, dx \tag{8.2.1}$$

Three cases were considered, corresponding to a number of actuation loads equal to 3, 4 or 5. Assuming $n+1 = 3$, 4 and 5, a n-th order polynomial $p_n(x)$ can be written for the interpolation:

$$p_n(x) = \sum_{n=0}^{n} C_i x^n \tag{8.2.2}$$

where the C_i are n unknown coefficients. The value of the polynomial in the point x_i is set equal to the target deflection $f(x_i)$ for each of the $n+1$ points:

$$p_n(x_i) = f(x_i) \qquad i = 1, \ldots n+1 \tag{8.2.3}$$

By developing these equations, a $(n+1) \times (n+1)$ system of equations is obtained, which allows the determination of the coefficients C_i of the interpolating polynomial and the evaluation of the deflection shape achieved.

The desired deflected shape of the flap trailing edge presented in Figure 8.1 was defined at several specific points along the flap chord. The best fitting polynomial was determined by settinng the number of points considered equal to 3, 4 or 5 and by analysing all the possible combinations of loading positions to choose the one providing the minimum error. The loading positions determined using this approach are summarised in Table 8.1, where x_i represents the distance from the rear spar of the $i-th$ interpolating point.

Figures 8.2 to 8.4 show the trailing edge deflected shape achieved by considering 3, 4 and 5 actuation points respectively. The use of 3 interpolating points led to inaccurate

No. of Points	x_1	x_2	x_3	x_4	x_5
3	9.78e-2	0.198	0.246	-	-
4	4.99e-2	0.127	0.267	0.392	-
5	2.49e-2	0.127	0.204	0.392	0.54

Table 8.1: Best interpolating positions for 3, 4 and 5 points

results, with the curve unable to follow the flap desired deflection in large regions close to the origin (the rear spar) and to the trailing edge. Increasing the number of points to 4 and 5 led to significant improvement in the curve achieved.

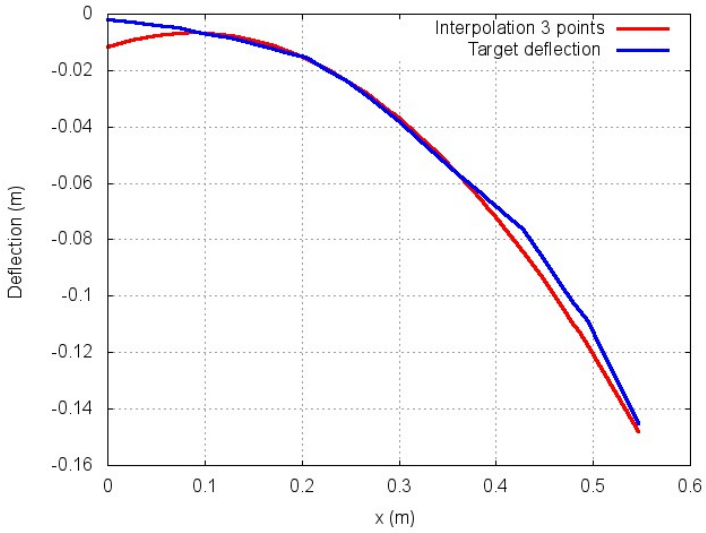

Figure 8.2: Shape interpolation with 3 interpolating points

From a purely mathematical point of view, once chosen the order n of the approximated polynomial, if the $f(x)$ is differentiable up to $n+1$, the best approximated polynomial $p_n(x)$ can be found using the Chebyshev theorem. This theorem states that the n-th order polynomial $p_n(x)$ that gives the best approximation of $f(x)$ over $[a,b]$ is the polynomial that interpolates $f(x)$ in the $n+1$ points:

$$x_k = \frac{a+b}{2} + \frac{b-a}{2} cos\left(k\frac{\pi}{n+2}\right) \qquad k = 1, 2, ..., n+1 \tag{8.2.4}$$

As an example, a third order polynomial $p_3(x) = C_1x^3 + C_2x^2 + C_3x + C_4$ was chosen for the interpolation and the four nodes over the interval $[0, 0.54]$ were calculated following Equation 8.2.4 as:

$$x_1 = 0.47939 \qquad x_2 = 0.34689 \qquad x_3 = 0.18311 \qquad x_4 = 0.05061 \tag{8.2.5}$$

The target shape function was approximated with a polynomial of the fifth order as:

$$f(x) = -30.88x^5 + 39.362x^4 - 18.185x^3 + 3.1722x^2 - 0.2767x - 0.0005 \tag{8.2.6}$$

over the interval $[0, 0.54]$. The function $f(x)$ was evaluated in the specified 4 points, leading to a 4×4 system of equations in the form:

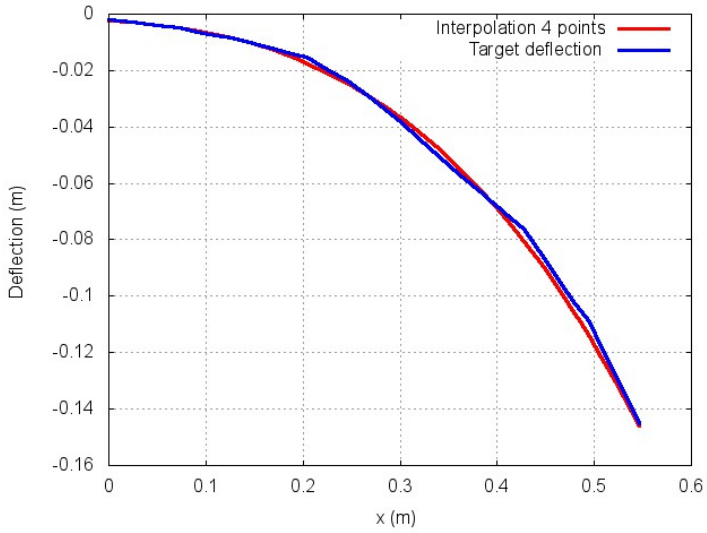

Figure 8.3: Shape interpolation with 4 interpolating points

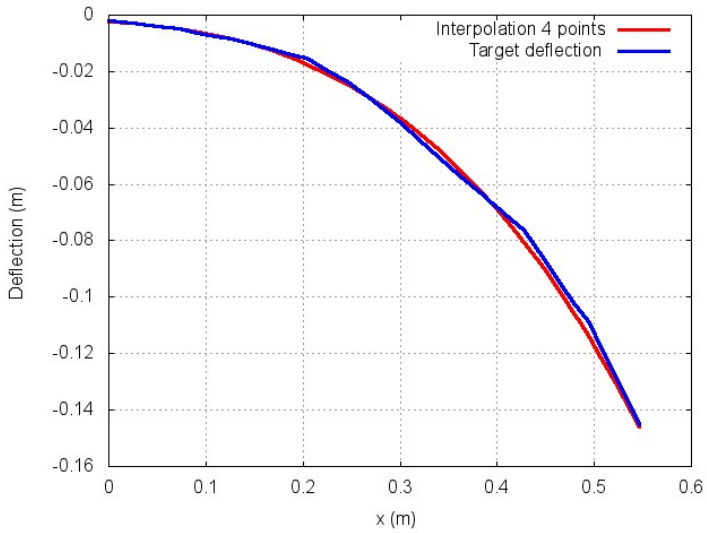

Figure 8.4: Shape interpolation with 5 interpolating points

$$C_1 x_i^3 + C_2 x_i^2 + C_3 x_i + C_4 = f(x_i) \qquad i = 1, 4 \tag{8.2.7}$$

which allowed the determination of the coefficients C_i of the interpolating polynomial and the evaluation of the deflection shape achieved, shown in Figure 8.5.

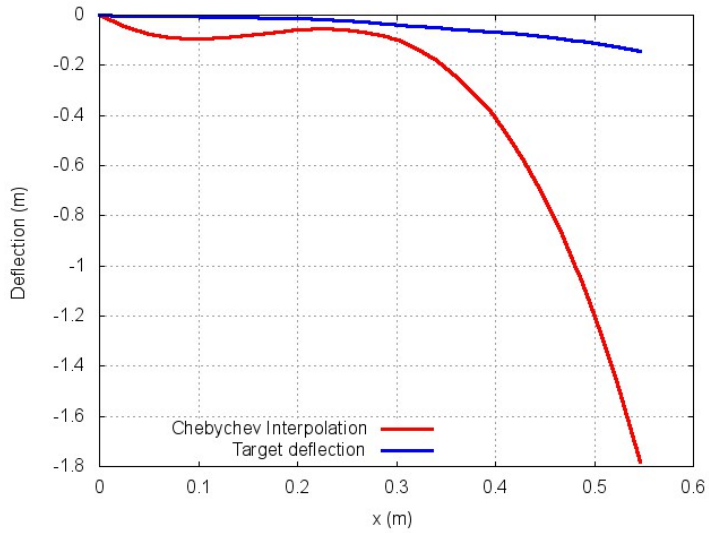

Figure 8.5: Shape interpolation using Chebyshev polinomial

This approach allowed a mathematical choice of the locations were the actuation loads are applied. These locations, represented by the Chebyshev nodes, are fixed once the interval $[a, b]$ and the order n of the approximation have been selected. Although this approach ensured the minimum distance between the target shape and the approximated polynomial over the interval of interest, the results obtained lacked of a proper physical meaning. In fact, neither the use of the Chebyshev nodes nor the approximated polynomial included in the analysis any physical property of the structure or any boundary condition at the ends of the flap. As a consequence, while in the interpolating nodes the deflected shape described by the approximated polynomial meets the target deflection, there is no guarantee that the deflection of the structure in the other points would follow the desired shape, expecially at the clamped and at the free ends of the structure.
Adding points to the interpolation would lead to a higher order approximating function and, as expected, to a better approximation of the target shape. However, the lack of connection to the physical structural problem led to unsatisfactory results and this approach was abandoned.

8.2.3 Beam Model

In order to determine a better approximation of the morphing flap deflected shape, the trailing edge structure was represented as a cantilever beam deflected by transverse loads applied at various locations along the chord.

The general equation of the deflection curve of the beam is:

$$EI\frac{d^2y}{dx^2} = -M \tag{8.2.8}$$

where M is the bending moment applied to the structure, which is a function of x only if transverse loads are considered.

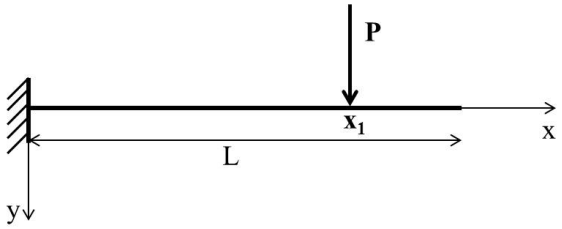

Figure 8.6: Cantilever beam under transverse concentrated load

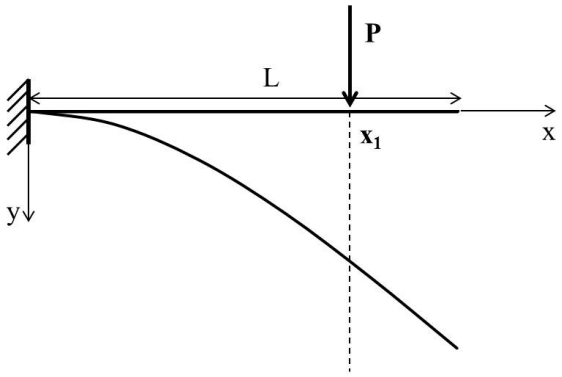

Figure 8.7: Deflection of a cantilever beam under transverse concentrated load

The deflection of a cantilever beam with a single transverse load P applied is:

$$EI\frac{d^2y}{dx^2} = P(L-x) \tag{8.2.9}$$

By integration, the equation becomes

$$EI\frac{dy}{dx} = Px(L-\frac{x}{2}) + C_1 \tag{8.2.10}$$

$$EIy = Px^2(\frac{L}{2}-\frac{x}{6}) + C_1x + C_2 \tag{8.2.11}$$

The constants C_1 and C_2 can be calculated by imposing the boundary condition of beam clamped at its left hand. Hence, the deflection and the slope in $x = 0$ are 0 and $C_1 = C_2 = 0$.

$$y = \frac{PL}{2EI}x^2 - \frac{P}{6EI}x^3 \tag{8.2.12}$$

Considering a cantilever beam, having length L, with a load P applied in x_1, its deflection will follow Equation (8.2.12) for $0 \leq x \leq x_1$ and it will become linear for $x_1 \leq x \leq L$:

$$y = \frac{PL}{2EI}x^2 - \frac{P}{6EI}x^3 \qquad 0 \leq x \leq x_1 \tag{8.2.13}$$

$$y = \left[\frac{PL}{2EI}x_1^2 - \frac{P}{6EI}x_1^3\right] + \left[\frac{PL}{2EI}x_1 - \frac{P}{6EI}x_1^2\right](x - x_1) \qquad x_1 \leq x \leq L \qquad (8.2.14)$$

If more than one transverse load is applied, then the total deflection in each point of the beam can be obtained by applying the superposition principle and superimposing the deflections produced by each of the single loads in that point.

The application of the beam theory is straightforward in the case the transverse loads on the structure are known. In the case of a morphing flap that needs to conform to a given shape, however, the problem to be analysed is slightly different. The loads applied to the structure to get the desired shape are unknown since they depend on the position where they are applied. However, they can be determined based on the values assumed by each couple of points (x, y), where x is the chordwise coordinate and y is the corresponding desired vertical deflection in that point.
In this study, an inverse approach is proposed to determine the loads required in specific locations along the beam in order to achieve a desired deflection. The steps followed in the calculation of the transverse loads and beam deformed shape were:

1. for a cantilever beam with N transverse loads applied to it, the generic expression of the deformed shape was obtained from the basic beam equation by using the superposition principle

2. N tentative positions x_i along the beam were selected for the loads and the vertical deflection y_i in these points was set equal to the desired target in x_i

3. substituting the N (x_i, y_i) values in the expression of the deformed shape, a set of N equations in the N unknown loads P_i was obtained and its solution allowed to evaluate the magnitude of the loads in the specified positions

4. once the transverse loads were known, they were applied back to the deformed beam equation in order to evaluate the deflection in all the coordinate locations

A total number of loading points was specified along the beam and the procedure was repeated for all the possible combinations of loading positions. For each load combination, the deflection curve of the beam was determined and its distance from the desired deflection was evaluated over the interval. The configuration with the smaller distance from the target was selected as the optimal one.
In the current analysis, a beam having length L=0.54 m was considered and a total of 35 possible loading positions was analysed. Three different cases were considered of a cantilever beam under three, four and five loads respectively (N= 3, 4 and 5).

8.2.3.1 Beam with Three Loads

The beam was subject to three vertical loads P_1, P_2 and P_3 applied in three generic locations x_1, x_2 and x_3 along the beam, as shown in Figure 8.8.
The deflection curve of the beam can be described piecewise as:

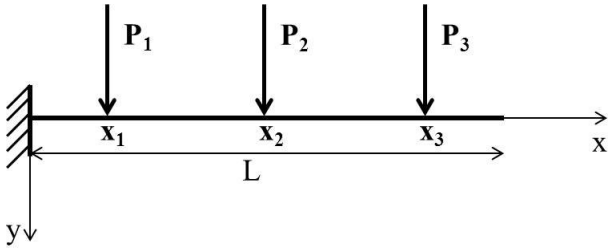

Figure 8.8: Cantilever beam with three concentrated loads

$$y = \frac{(P_1+P_2+P_3)L}{2EI}x^2 - \frac{(P_1+P_2+P_3)}{6EI}x^3 \qquad 0 \le x \le x_1 \tag{8.2.15}$$

$$\begin{aligned} y = &\left[\frac{P_1 L}{2EI}x_1^2 - \frac{P_1}{6EI}x_1^3\right] + \left[\frac{P_1 L}{EI}x_1 - \frac{P_1}{2EI}x_1^2\right](x-x_1) + \\ &+ \frac{(P_2+P_3)L}{2EI}x^2 - \frac{(P_2+P_3)}{6EI}x^3 \qquad x_1 \le x \le x_2 \end{aligned} \tag{8.2.16}$$

$$\begin{aligned} y = &\left[\frac{P_1 L}{2EI}x_1^2 - \frac{P_1}{6EI}x_1^3\right] + \left[\frac{P_1 L}{EI}x_1 - \frac{P_1}{2EI}x_1^2\right](x-x_1) + \\ &+ \left[\frac{P_2 L}{2EI}x_2^2 - \frac{P_2}{6EI}x_2^3\right] + \left[\frac{P_2 L}{EI}x_2 - \frac{P_2}{2EI}x_2^2\right](x-x_2) + \\ &+ \frac{P_3 L}{2EI}x^2 - \frac{P_3}{6EI}x^3 \qquad x_2 \le x \le x_3 \end{aligned} \tag{8.2.17}$$

$$\begin{aligned} y = &\left[\frac{P_1 L}{2EI}x_1^2 - \frac{P_1}{6EI}x_1^3\right] + \left[\frac{P_1 L}{EI}x_1 - \frac{P_1}{2EI}x_1^2\right](x-x_1) + \\ &+ \left[\frac{P_2 L}{2EI}x_2^2 - \frac{P_2}{6EI}x_2^3\right] + \left[\frac{P_2 L}{EI}x_2 - \frac{P_2}{2EI}x_2^2\right](x-x_2) + \\ &+ \left[\frac{P_3 L}{2EI}x_3^2 - \frac{P_3}{6EI}x_3^3\right] + \left[\frac{P_3 L}{EI}x_3 - \frac{P_3}{2EI}x_3^2\right](x-x_3) \qquad x_3 \le x \le L \end{aligned} \tag{8.2.18}$$

The three transverse loads P_1, P_2 and P_3 in the above equations are unknown. Their value can be determined by expressing them as a function of the desired deflections y_1, y_2 and y_3 and of the loading points x_1, x_2 and x_3. The following system of three equations in the three unknowns P_1, P_2 and P_3 was obtained:

$$\{A\}\,[P] = \{B\} \tag{8.2.19}$$

where $[P]$ is a vector containing the three unknown applied loads P_1, P_2 and P_3 and $\{A\}$ and $\{B\}$ are two matrices 3×3 and 3×1 whose terms are known and equal to:

$$
\begin{aligned}
A(1,1) &= 1 \\
A(1,2) &= 1 \\
A(1,3) &= 1 \\
A(2,1) &= \tfrac{9Lx_1^2}{6EI} - \tfrac{4x_1^3}{6EI} - \tfrac{Lx_1x_2}{EI} + \tfrac{x_1^2x_2}{2EI} \\
A(2,2) &= \tfrac{Lx_2^2}{2EI} - \tfrac{x_2^3}{6EI} \\
A(2,3) &= \tfrac{Lx_2^2}{2EI} - \tfrac{x_2^3}{6EI} \\
A(3,1) &= \tfrac{9Lx_1^2}{6EI} - \tfrac{4x_1^3}{6EI} - \tfrac{Lx_1x_3}{EI} + \tfrac{x_1^2x_3}{2EI} \\
A(3,2) &= \tfrac{9Lx_2^2}{6EI} - \tfrac{4x_2^3}{6EI} - \tfrac{Lx_2x_3}{EI} + \tfrac{x_2^2x_3}{2EI} \\
A(3,3) &= \tfrac{Lx_3^2}{2EI} - \tfrac{x_3^3}{6EI} \\
B(1) &= \tfrac{y_1 6EI}{x_1^2(3L-x_1)} \\
B(2) &= y_2 \\
B(3) &= y_3
\end{aligned}
\tag{8.2.20}
$$

It is possible to solve the system 8.2.19 for each combination $(x_1, x_2, x_3, y_1, y_2, y_3)$ to obtain the three loads P_1, P_2 and P_3 to apply.

The resulting best loading positions for the case of three transverse loads is represented in Figure 8.9 and exhibited a total point by point difference of 17.6 mm from the desired deflected shape.

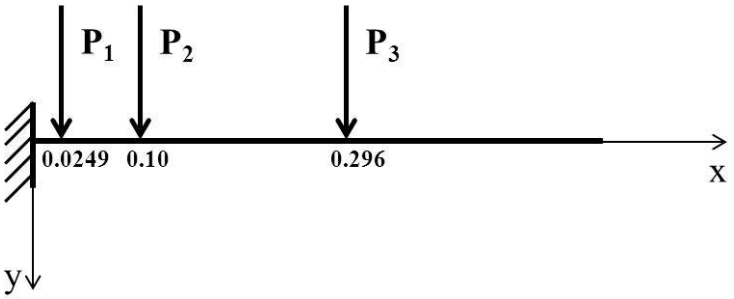

Figure 8.9: Beam with three transverse loads: best loading distribution

As shown in Figure 8.10, the deflected beam shape exhibited a good agreement with the target flap shape in the first part of the structure, in proximity of the loading positions, but not in the final part, which deflected linearly according to the beam approximation adopted and was not able to follow the more cambered target deflection. An increase

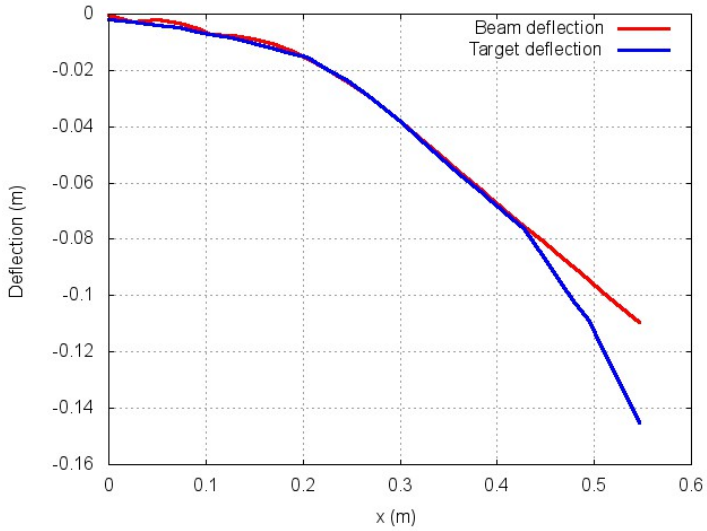

Figure 8.10: Shape approximation using the beam model with 3 transverse loads

in the number of transverse loads applied to the beam would definitely improve the deflection shape achieved by reducing the region of linear deflection.

8.2.3.2 Beam with Four Loads

The analysis was repeated for a cantilever beam subject to four transverse loads, shown in Figure 8.11.

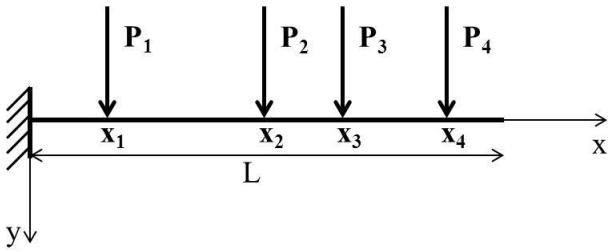

Figure 8.11: Cantilever beam with four concentrated loads

Following a similar approach, the beam deflection curve can be described piecewise as:

$$y = \frac{(P_1+P_2+P_3+P_4)L}{2EI}x^2 - \frac{(P_1+P_2+P_3+P_4)}{6EI}x^3 \qquad 0 \le x \le x_1 \tag{8.2.21}$$

$$\begin{aligned} y = &\left[\frac{P_1 L}{2EI}x_1^2 - \frac{P_1}{6EI}x_1^3\right] + \left[\frac{P_1 L}{EI}x_1 - \frac{P_1}{2EI}x_1^2\right](x - x_1) + \\ &+ \frac{(P_2+P_3+P_4)L}{2EI}x^2 - \frac{(P_2+P_3+P_4)}{6EI}x^3 \qquad x_1 \le x \le x_2 \end{aligned} \tag{8.2.22}$$

$$
\begin{aligned}
y = &\left[\frac{P_1 L}{2EI}x_1^2 - \frac{P_1}{6EI}x_1^3\right] + \left[\frac{P_1 L}{EI}x_1 - \frac{P_1}{2EI}x_1^2\right](x - x_1) + \\
&+ \left[\frac{P_2 L}{2EI}x_2^2 - \frac{P_2}{6EI}x_2^3\right] + \left[\frac{P_2 L}{EI}x_2 - \frac{P_2}{2EI}x_2^2\right](x - x_2) + \\
&+ \frac{(P_3 + P_4)L}{2EI}x^2 - \frac{P_3 + P_4}{6EI}x^3 \qquad x_2 \leq x \leq x_3
\end{aligned}
\tag{8.2.23}
$$

$$
\begin{aligned}
y = &\left[\frac{P_1 L}{2EI}x_1^2 - \frac{P_1}{6EI}x_1^3\right] + \left[\frac{P_1 L}{EI}x_1 - \frac{P_1}{2EI}x_1^2\right](x - x_1) + \\
&+ \left[\frac{P_2 L}{2EI}x_2^2 - \frac{P_2}{6EI}x_2^3\right] + \left[\frac{P_2 L}{EI}x_2 - \frac{P_2}{2EI}x_2^2\right](x - x_2) + \\
&+ \left[\frac{P_3 L}{2EI}x_3^2 - \frac{P_3}{6EI}x_3^3\right] + \left[\frac{P_3 L}{EI}x_3 - \frac{P_3}{2EI}x_3^2\right](x - x_3) + \\
&+ \frac{P_4 L}{2EI}x^2 - \frac{P_4}{6EI}x^3 \qquad x_3 \leq x \leq x_4
\end{aligned}
\tag{8.2.24}
$$

$$
\begin{aligned}
y = &\left[\frac{P_1 L}{2EI}x_1^2 - \frac{P_1}{6EI}x_1^3\right] + \left[\frac{P_1 L}{EI}x_1 - \frac{P_1}{2EI}x_1^2\right](x - x_1) + \\
&+ \left[\frac{P_2 L}{2EI}x_2^2 - \frac{P_2}{6EI}x_2^3\right] + \left[\frac{P_2 L}{EI}x_2 - \frac{P_2}{2EI}x_2^2\right](x - x_2) + \\
&+ \left[\frac{P_3 L}{2EI}x_3^2 - \frac{P_3}{6EI}x_3^3\right] + \left[\frac{P_3 L}{EI}x_3 - \frac{P_3}{2EI}x_3^2\right](x - x_3) \\
&+ \left[\frac{P_4 L}{2EI}x_3^2 - \frac{P_4}{6EI}x_3^3\right] + \left[\frac{P_4 L}{EI}x_3 - \frac{P_4}{2EI}x_3^2\right](x - x_4) \qquad x_4 \leq x \leq L
\end{aligned}
\tag{8.2.25}
$$

The resulting best loading positions for the case of four transverse loads is shown in Figure 8.12.

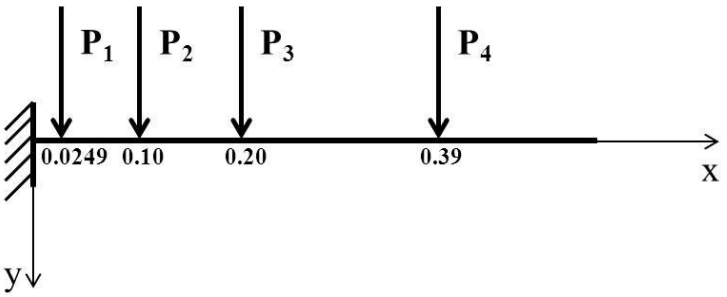

Figure 8.12: Beam with four transverse loads: best loading distribution

Figure 8.13 presents the deflected shape obtained when four loading points were considered. Although the curve showed a better agreement with the target shape than the three loads configuration presented in Figure 8.10, the maximum deflection at the trailing edge was still sensibly different from the desired one.

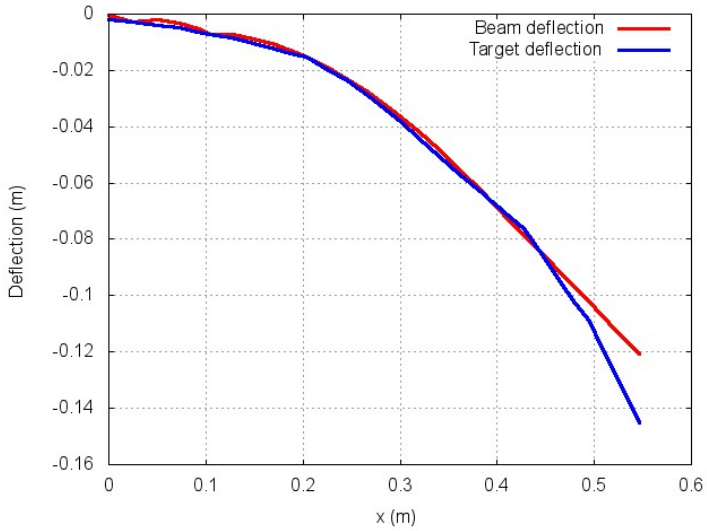

Figure 8.13: Shape approximation using the beam model with 4 transverse loads

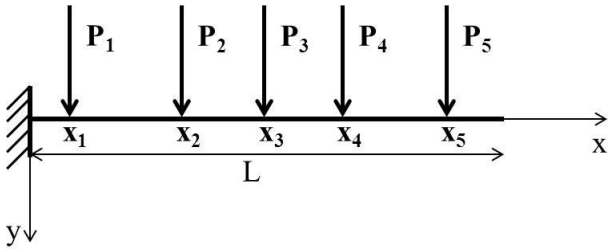

Figure 8.14: Cantilever beam with five concentrated loads

8.2.3.3 Beam with Five Loads

The case of a cantilever beam subject to five transverse loads was also considered (see Figure 8.14). The deflection curve can be described piecewise as:

$$y = \frac{(P_1+P_2+P_3+P_4+P_5)L}{2EI}x^2 - \frac{(P_1+P_2+P_3+P_4+P_5)}{6EI}x^3 \qquad 0 \le x \le x_1 \tag{8.2.26}$$

$$\begin{aligned} y = &\left[\frac{P_1 L}{2EI}x_1^2 - \frac{P_1}{6EI}x_1^3\right] + \left[\frac{P_1 L}{EI}x_1 - \frac{P_1}{2EI}x_1^2\right](x - x_1) + \\ &+ \frac{(P_2+P_3+P_4+P_5)L}{2EI}x^2 - \frac{(P_2+P_3+P_4+P_5)}{6EI}x^3 \qquad x_1 \le x \le x_2 \end{aligned} \tag{8.2.27}$$

$$\begin{aligned} y = &\left[\frac{P_1 L}{2EI}x_1^2 - \frac{P_1}{6EI}x_1^3\right] + \left[\frac{P_1 L}{EI}x_1 - \frac{P_1}{2EI}x_1^2\right](x - x_1) + \\ &+ \left[\frac{P_2 L}{2EI}x_2^2 - \frac{P_2}{6EI}x_2^3\right] + \left[\frac{P_2 L}{EI}x_2 - \frac{P_2}{2EI}x_2^2\right](x - x_2) + \\ &+ \frac{(P_3+P_4+P_5)L}{2EI}x^2 - \frac{P_3+P_4+P_5}{6EI}x^3 \qquad x_2 \le x \le x_3 \end{aligned} \tag{8.2.28}$$

$$
\begin{aligned}
y = &\left[\frac{P_1 L}{2EI}x_1^2 - \frac{P_1}{6EI}x_1^3\right] + \left[\frac{P_1 L}{EI}x_1 - \frac{P_1}{2EI}x_1^2\right](x - x_1) + \\
&+ \left[\frac{P_2 L}{2EI}x_2^2 - \frac{P_2}{6EI}x_2^3\right] + \left[\frac{P_2 L}{EI}x_2 - \frac{P_2}{2EI}x_2^2\right](x - x_2) + \\
&+ \left[\frac{P_3 L}{2EI}x_3^2 - \frac{P_3}{6EI}x_3^3\right] + \left[\frac{P_3 L}{EI}x_3 - \frac{P_3}{2EI}x_3^2\right](x - x_3) + \\
&+ \frac{(P_4 + P_5)L}{2EI}x^2 - \frac{P_4 + P_5}{6EI}x^3 \qquad x_3 \leq x \leq x_4
\end{aligned}
\tag{8.2.29}
$$

$$
\begin{aligned}
y = &\left[\frac{P_1 L}{2EI}x_1^2 - \frac{P_1}{6EI}x_1^3\right] + \left[\frac{P_1 L}{EI}x_1 - \frac{P_1}{2EI}x_1^2\right](x - x_1) + \\
&+ \left[\frac{P_2 L}{2EI}x_2^2 - \frac{P_2}{6EI}x_2^3\right] + \left[\frac{P_2 L}{EI}x_2 - \frac{P_2}{2EI}x_2^2\right](x - x_2) + \\
&+ \left[\frac{P_3 L}{2EI}x_3^2 - \frac{P_3}{6EI}x_3^3\right] + \left[\frac{P_3 L}{EI}x_3 - \frac{P_3}{2EI}x_3^2\right](x - x_3) + \\
&+ \left[\frac{P_4 L}{2EI}x_3^2 - \frac{P_4}{6EI}x_3^3\right] + \left[\frac{P_4 L}{EI}x_3 - \frac{P_4}{2EI}x_3^2\right](x - x_4) + \\
&+ \frac{P_5 L}{2EI}x^2 - \frac{P_5}{6EI}x^3 \qquad x_4 \leq x \leq x_5
\end{aligned}
\tag{8.2.30}
$$

$$
\begin{aligned}
y = &\left[\frac{P_1 L}{2EI}x_1^2 - \frac{P_1}{6EI}x_1^3\right] + \left[\frac{P_1 L}{EI}x_1 - \frac{P_1}{2EI}x_1^2\right](x - x_1) + \\
&+ \left[\frac{P_2 L}{2EI}x_2^2 - \frac{P_2}{6EI}x_2^3\right] + \left[\frac{P_2 L}{EI}x_2 - \frac{P_2}{2EI}x_2^2\right](x - x_2) + \\
&+ \left[\frac{P_3 L}{2EI}x_3^2 - \frac{P_3}{6EI}x_3^3\right] + \left[\frac{P_3 L}{EI}x_3 - \frac{P_3}{2EI}x_3^2\right](x - x_3) + \\
&+ \left[\frac{P_4 L}{2EI}x_3^2 - \frac{P_4}{6EI}x_3^3\right] + \left[\frac{P_4 L}{EI}x_3 - \frac{P_4}{2EI}x_3^2\right](x - x_4) + \\
&+ + \left[\frac{P_5 L}{2EI}x_3^2 - \frac{P_5}{6EI}x_3^3\right] + \left[\frac{P_5 L}{EI}x_3 - \frac{P_5}{2EI}x_3^2\right](x - x_5) \qquad x_5 \leq x \leq L
\end{aligned}
\tag{8.2.31}
$$

The resulting best load position for the case of the five loads is shown in Figure 8.15 and the deflection shape achieved is presented in Figure 8.16. The use of five transverse loads led to a considerably smaller overall distance between the target and the achieved shape, equal to 3.84 mm. From Figure 8.16 it is evident that the use of five loading points led to a very good agreement between the beam model and the target deflection shape, since the last load contributed to deflect the final part of the beam up to the maximum vertical displacement required.

A summary of the best loading positions for the beam model with three, four and five transverse loads is presented in Table 8.2. The use of more loading points contributed to progressively improve the deflection of the beam tip.

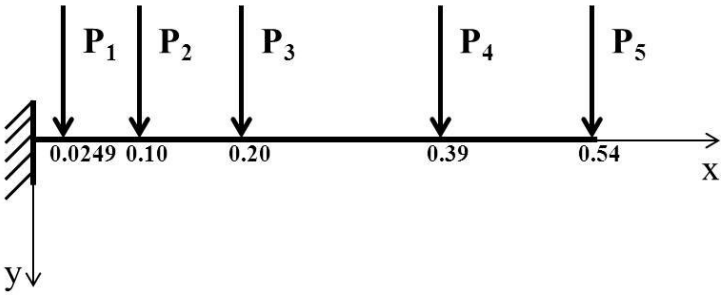

Figure 8.15: Beam with five transverse loads: best loading distribution

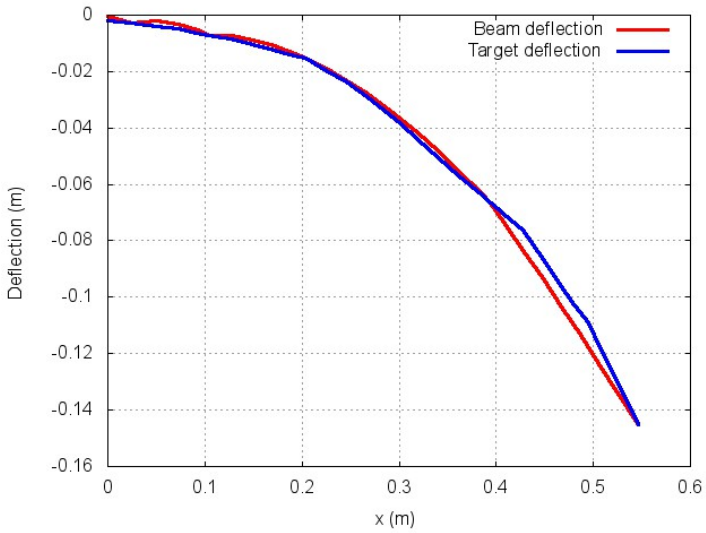

Figure 8.16: Shape approximation using the beam model with 5 transverse loads

No. of Loads	x_1	x_2	x_3	x_4	x_5
3	2.49e-2	0.10	0.296	-	-
4	2.49e-2	0.10	0.20	0.39	-
5	2.49e-2	0.10	0.20	0.39	0.54

Table 8.2: Beam loading positions

The beam approximation adopted in this paragraph provided a simple but effective way to represent the trailing edge deflection under transverse loads and to select the most suitable actuation load distribution for the flap structure. One of the main advantages offered by this approach was to retain a strong connection with a real physical problem by taking into account the material properties of the flap skin. In fact, the beam flexural stiffness EI, figuring in the equations, was chosen equal to the EI of a thin Aluminium strip of skin having rectangular cross section constant along the beam, with unit width and skin equal to the flap skin thickness of 2 mm. The use of the beam equation automatically allowed to achieve a realistic deflection of the structure also in the areas between the different loading positions. The results showed that the use of three or four loads along the flap trailing edge led to an overall difference with the target deflection of 17.6 mm and 12.1 m respectively. The largest discrepancy with the target shape was observed in the final portion of the beam, which deflected linearly rather than following a more cambered profile. The case with five loading positions showed a dramatic improvement in the deflection achieved, which was only 3.84 mm far from the desired morphed shape.

8.2.4 Shape Analysis with the Finite Element Method

The beam model proposed in Section 8.2.3 provided some indication on the best loading positions on the flap structure and on the number of loads required to achieve the desired deflection. However, it did not offer an accurate representation of the trailing edge structure, which is composed of two skins connected together along the chord and able to slide over each other at the trailing edge. In order to provide a more accurate analysis of the load distribution along the flap necessary to achieve the desired deflected shape, a finite element analysis was conducted. The finite element model of the trailing edge structure already used to evaluate the actuation loads in Chapter 5 was considered.
In order to evaluate the actuation loads to apply to the flap skins, the approach described in Section 5.3.6 was adopted:

- the desired deflection was imposed as a forced displacement on the structure and the corresponding reaction force was evaluated
- the calculated reaction forces were reapplied as the actuation load to achieve the desired morphed shape

This time, however, rather than considering a single set of fixed, uniformly spaced loading positions, all the different combinations of loading points were included in the analysis. In order to quickly analyse large number of loading conditions, the whole process was automated by interfacing the Nastran structural solver with a Fortran-based script which was able, at each run, to:

- apply the desired deflection in correspondence of the selected loading positions as an imposed displacement
- evaluate the corresponding reaction force in the loading points
- reapply the reaction force as concentrated actuation forces on the structure
- evaluate the deflection achieved and the total actuation load reqired
- shift the loading positions to the next adjacent node, in order to cover all the possible combinations of loading positions

At each step, the difference between the actual and the target shape was evaluated, together with the actuation load needed to achieve the deflection. The use of a FE model for the detailed representation of the structure ensured a high degree of accuracy. The analysis was repeated for three, four and five loading positions respectively, and the best loading positions determined for each case are summarised in Table 8.3.

No. of Loads	x_1	x_2	x_3	x_4	x_5
3	4.9e-2	0.20	0.296	-	-
4	2.49e-2	0.172	0.20	0.397	-
5	0.094	0.194	0.298	0.348	0.543

Table 8.3: Loading positions evaluated with FE analysis

Figure 8.17 shows a comparison between the initial design and the best loading arrangement for three, four and five loads respectively. Each column represents the minimum total difference between the selected configuration and the target deflected shape. In order to have a local measure of the difference between the current and the target deflection, the average difference per node was evaluated and summarised in Table 8.4. While the three loads distribution generated an average difference per node with the target shape of approximately 3.68 mm, a 5 loads distribution exhibited a 26% improvement over the initial design and a much better agreement with the desired deflected shape with an average difference of 0.63 mm per node with the target.

	Initial Design	3 Points	4 Points	5 Points
Total difference (m)	0.03	0.129	0.07	0.022
Difference per node (mm)	0.85	3.68	0.002	0.63

Table 8.4: Average difference Δ per node with the target deflection

The FE analysis also allowed a quick comparison between the total actuation load required for each case. Figure 8.18 shows the total actuation load needed in each loading configuration. The increase in the number of loads led to higher actuation requirements. Although the arrangements with three and four loads presented the lowest actuation requirements, these configurations were discarded due to the large difference in shape with the desired deflection. The five loads arrangement required an actuation load of 4.69 kN, slighlty higher than the initial value obtained in Chapter 5 of 4.02 kN.

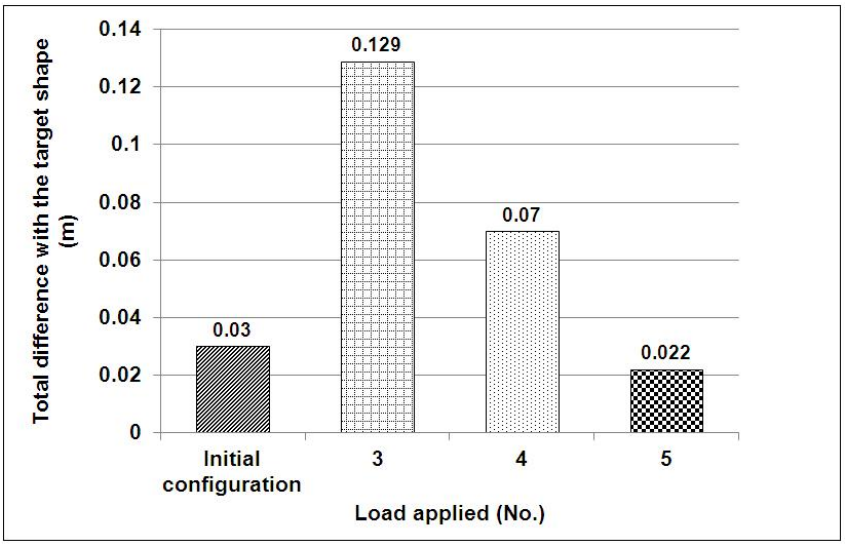

Figure 8.17: Overall difference between the achieved deflection and the desired morphed shape (m)

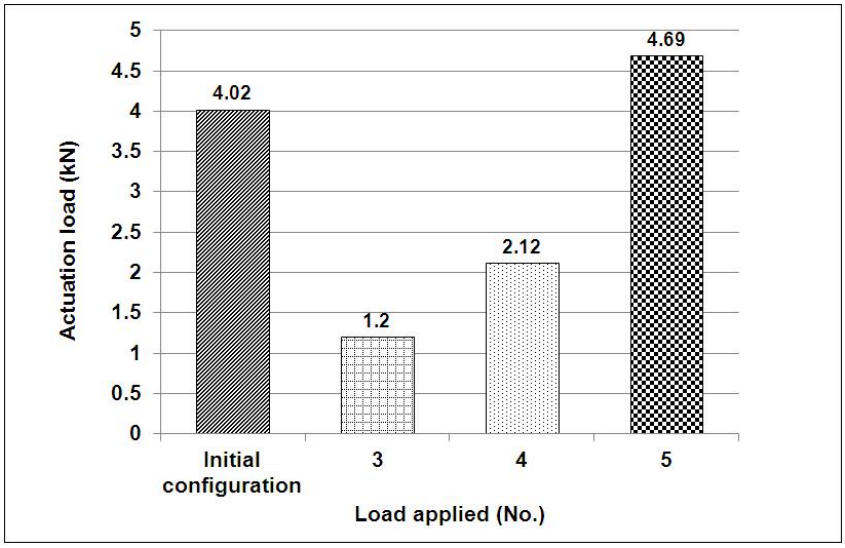

Figure 8.18: Actuation load requirements for the best configurations with three, four and five loads (kN)

The position of the actuation points for the optimal actuation loads distribution using five loading positions differed from the initial, uniformly distributed, design, as shown in Table 8.5. The loading positions along the chord were moved towards the central part of the flap in order to meet the shape requirements.

	x_1	x_2	x_3	x_4	x_5
Initial Design	0.1	0.1938	0.2987	0.39	0.56
Optimal Configuration	0.0939	0.1938	0.2987	0.3481	0.5434

Table 8.5: Position of the actuation load in the initial and optimised design

From the analysis of the results it was also found that the loading positions corresponding to the lower total actuation load were slightly away from the ones for best deflection shape. However, since the total actuation load remained reasonably low in all the various conditions analysed, priority was given to the deflection shape when selecting the best performing load configuration.

A comparison can be drawn between the optimal loading positions obtained using the finite element model of the flap and the findings of the interpolation technique and of the beam approach. The interpolation technique presented in Section 8.2.2 can provide a general idea of the more conventient loading positions on the structure. However, for a complex structure like the morphing flap, a purely theoretical approach which does not take into account the material properties of the structure is too simplified and does not entirely capture the structural behaviour of the flap trailing edge under the effect of the actuation loads.

The use of a beam model and the analysis conducted in Section 8.2.3 allowed to predict the optimal loading positions along the flap chord by considering a realistic structural deflection under concentrated vertical loading. The beam analysis, however, did not take into account the flap internal structure, with the presence of the eccentric beam actuation mechanism and the additional internal connections between the upper and lower skins. Conversely, the use of the finite element model of the morphing flap represents the most complete analysis, since all the structural characteristics of the flap are taken into account. The results have shown that the use of less than five loads leads to unacceptable deflection shapes. On the other hand, the morphing requirements were met with good agreement when five loads were considered. The optimal configuration determined with the finite element approach exhibited a 26% reduction in the difference between actual and prescribed shape compared to the intial uniformly spaced actuation loads. The best loading configuration with five loading positions was selected as the best loading distribution over the flap trailing edge and will be used in the folowing analyses.

8.3 Structural Optimisation of Morphing Structures

Once the characteristics of the actuation mechanism were analysed, the material properties of the morphing flap structure were introduced in the optimisation process. The route selected to optimise the morphing high lift device design and to achieve the desired deflection shape consisted into tailoring the skin properties of the flap trailing edge along

the chord. The trailing edge skin panels could be divided into spanwise strips and each strip thickness could be modified according to the desired deflection and level of stress in the skin. The large number of design variables involved and the need to modify the different thicknesses simultaneously has led to the development of an automated optimisation process rather than attempting any manual change to the skin properties.

8.3.1 The ADS-Nastran Interface for Structural Optimisation

Commercial software for structural optimisation is widely available nowadays, often already integrated within finite element solvers. While this software can be conveniently used in the standard optimisation problems, it does not offer the flexibility required to deal with the non conventional optimisation of morphing structures.

In this research study, a new computer program was developed for the structural optimisation of morphing structures and, more generally, to solve structural optimisation problems having non conventional object functions. The program consists of an interface between the Nastran finite element structural solver and an optimisation module, allowing an iterative analysis of the structure. The objective was to create a tool able to take advantage of the accurate description of the structural behaviour provided by Nastran, and to convey this information into the optimisation module in order to achieve a high degree of accuracy in the evaluation of the objective function and of the constraints.

The optimisation module chosen for the interface problem is the Automated Design Synthesis (ADS) optimisation subroutine, developed at NASA by G. N. Vanderplaats in the 1980s [89]. The ADS subroutine is a general purpose optimisation program allowing great flexibility in the choice of possible strategies, optimizing algorithms and one dimensional search methods, in order to obtain a combination that is suitable for the specific optimisation problem considered. The ADS subroutine was written in FORTRAN and can be easily modified and adapted to suit different types of problems.

Figure 8.19 shows a flowchart of the interface program. A FE model of the structure is created and analysed using Nastran. The displacements and stresses in the structure obtained from the analysis are passed to the optimisation module, which evaluates the objective function and the gradients and generates a new set of design variables. These parameters are used to modify the structure accordingly and a new structural model with the tentative design variables is fed back to the Nastran structural solver. The procedure is iterated until convergence is reached. For the optimisation of the trailing edge skin properties, the flap was divided into thin strips extending in spanwise direction and the various thicknesses were selected as the design variables of the problem.

8.3.1.1 Structure of the Interface

- **Input files for the interface program**
  First, an input file for the structural FE solver (bdf file) was generated from the FE model of the structure to be optimised. Suitable initial values were considered as the set of design variables involved in the optimisation. Some additional text files containing the design variables were also generated and linked to the bdf file. Since

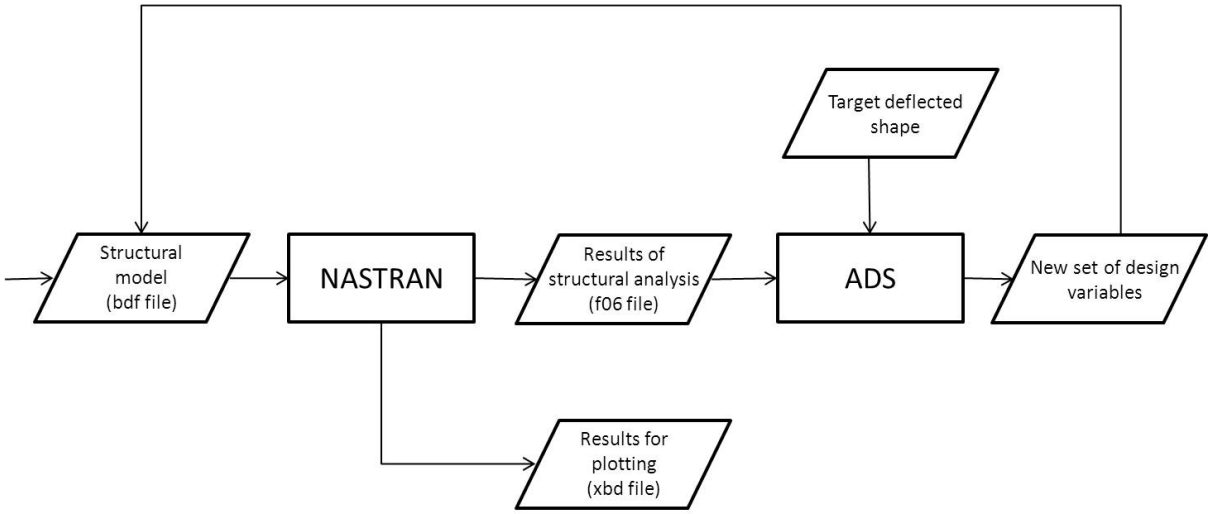

Figure 8.19: Structure of the optimisation interface program

these files contain the design variables, they will be modified at each iteration by the ADS/NASTRAN interface. This would allow to quickly modify the bdf input file without actually entering the file itself, with computational savings especially for large structures ([105], [106]). Finally, for this specific problem, a data file containing the details of the desired deflected shape was also created to contain the parameters required for the evaluation of the objective function $F(\overline{x})$: at each step of the iteration the interface program was able to read from external data files and to determine $F(\overline{x})$.

- **The interface program**
  The interface program was written using the FORTRAN language, in order to be fully compatible with the ADS subroutine [131]. The first step was to invoke the NASTRAN structural solver to perform the structural analysis. Once the structural run was completed, the interface program read directly in the NASTRAN output file (the .f06 file) and extracted the data required for the evaluation of the objective function. These data consisted in the deflection at specified points of the structure and the stress values in the elements. The actual deflection of the structure was compared to the desired deflection of the structural points The ADS subroutine evaluated the objective function and the optimisation constraints based on the results of the structural analysis. The subroutine was also able to automatically perform gradient evaluation by using finite differences. Although it would be possible to include a different gradient calculation subroutine, the ADS computations were considered sufficiently accurate. The gradient evaluation was used to generate the next set of design variables and the optimisation loop was repeatd. When ADS indicated that the convergence was had been achieved, the execution was completed.

- **Output files**
  The interface generated an output file containing the summary of all the iterations of the optimisation process, recalling the initial values of the design variables, their upper and lower bounds, the results of the optimisation complete with information on the optimisation algorithm and its convergence. The actual deflection and the stress values were read directly from the NASTRAN output file (f06 file). A second

ouptut file was represented by the NASTRAN output file (xdb file), allowing to quickly plot and visualize the results.

8.4 Thickness Optimisation of a Cantilever Beam

The interface program was initially tested on a case study represented by a cantilever beam, made of aluminium, modelled in Patran using QUAD4 elements. The beam was divided into transversal sections representing areas where the material properties were constant and the objective of the problem was to optimise the thickness of each of these areas to achieve a prescribed deflection. The design variables considered for this problem were the 5 thickness values along the beam. The minimum and maximum bounds for the thicknesses were selected equal to 1 and 5 mm respectively. A uniform initial thickness value of 1 mm was selected for all the sections. The target deflected shape consisted of a parabola having maximum deflection of 0.175 m at the free end of the strip.

Optimisation results
Table 8.6 shows the optimal values of the thickness for each section, obtained after 17 iterations.

Section N.	Optimal Thickness (mm)
1	4.944
2	3.034
3	1.788
4	1.518
5	1.518

Table 8.6: Optimal thickness distribution of the cantilever beam under a prescribed parabolic deflection

Figure 8.20 illustrates the deflection achieved. The maximum deflection of the beam and the levels of stress and strain in the structure are presented in Table 8.7. The stress values in the x direction, along the beam length, were slightly higher than the initial non optimised ones, but still acceptable.

	Initial Design	Optimal Design
Deflection (m)	0.226	0.165
Stress x (MPa)	101	185
Stress y (MPa)	30	8.44
stress xy (Mpa)	5.54	5.10

Table 8.7: Initial and optimised parameters for the cantilever beam

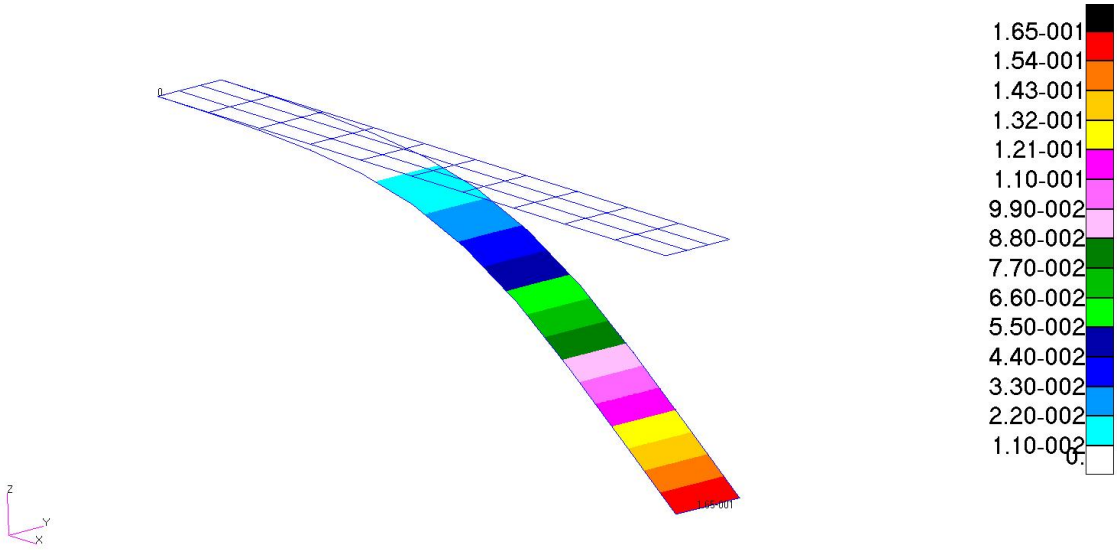

Figure 8.20: Beam final deflection

8.5 Thickness Optimisation of the Morphing Trailing Edge Flap

The optimisation procedure implemented in the ADS/NASTRAN coupled interface was applied to the design of the morphing rear part of the trailing edge flap in order to achieve a deflected shape which was the closest possible to an prescribed target shape without violating the stress limits in the material. This type of optimisation problem can be stated as: minimize the objective function W

$$W = \sum abs\left(z_i - x_{3_i}\right) \tag{8.5.1}$$

subject to stress and design constraints

$$\sigma_i \leq \sigma_i^U$$

$$t_i^L \leq t_i \leq t_i^U$$

where n is the total number of points in the chordwise direction, z_i is the desired deflection and x_{3i} is the vertical displacement in the i-th point.
The objective function W expresses the difference between the actual and the target deflected shape. Acting on the skin thicknesses, which were considered as the design variables, can have a great impact on the flexibility of the flap trailing edge, which in turn affects the actuation loads required. In turn, thinner trailing edge skins could potentially reduce the structural weight of the flap, not only because less material would be used, but mainly because a more flexible structure would require less powerful, lighter actuators. The aerodynamic load on the flap structure gradually decreases moving towards the trailing edge, while the internal actuation loads increase from the rear spar to the trailing edge, suggesting opposite variations in the skin thickness.

Initial non-optimised results
The initial non optimised design has been already analysed in Section 6.1.2 of Chapter 6. The flap skin panels were made of aluminium 2 mm in thickness. The total actuation load required to deflect the flap structure was 4.02 kN and the flap model was able to meet the desired shape with acceptable stress levels. The initial stress results showed that the flap loading conditions were still far from being critic and there was a certain margin for skin thickness reduction.

8.5.1 Thickness optimisation

The first step in the optimisation of the flap structural design consisted in dividing each of the flap upper and lower skin panels into 6 different regions, with the possibility to modify the material properties of each section independently from the others. The design variables considered were the thicknesses, hence the design variables vector $\underline{x}$ had 12 components. A minimum and maximum allowable thicknesses were selected for this study, equal to 1 and 3 mm respectively. All the other material properties were assumed constant.

The optimization problem expressed by Equation 8.5.1 for the flap skin thickness was analysed considering a uniform initial thickness value of 1 mm for all the strip sections. The displacements and the stress values required to evaluate the design constraint were read directly from the Nastran output file. The final optimized values for the skin thickness, shown in Table 8.8, were obtained after 184 iterations.

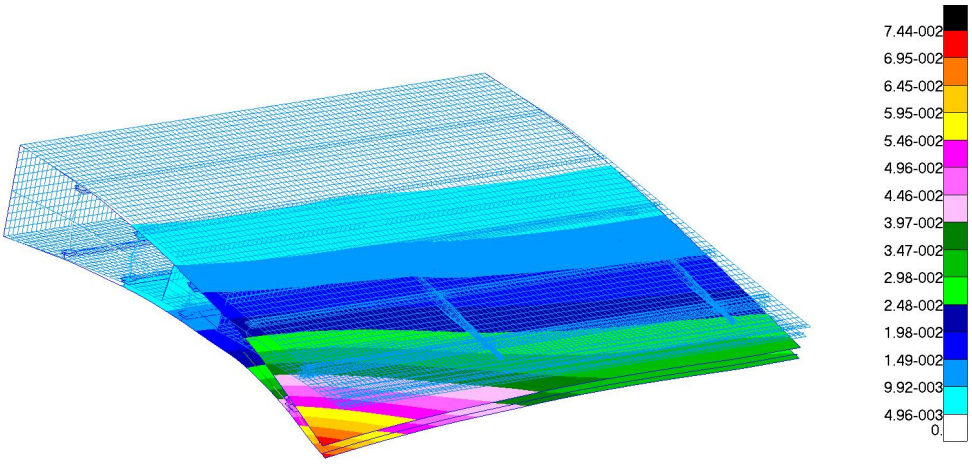

Figure 8.21: Deflection achieved by the flap with optimised skin thickness

Section N.	1	2	3	4	5	6	7	8	9	10	11	12
t (mm)	1.75	1.75	1.75	1.75	2.60	3.00	1.75	1.75	1.75	1.75	2.37	3.00

Table 8.8: Optimised thickness distribution in the different flap sections (mm)

The objective function Equation 8.5.1 for the optimised thicknesses presented in Table 8.8 was equal to 0.3186, lower than the value of 0.3274 obtained for the initial design presented in Section 6.1.2. As it can be noted from Table 8.8, the optimal thickness values

obtained resulted lower than the initial non optimized value of 2 mm in all the strips, apart from the two skin panels close to the trailing edge, where the optimal thickness was higher than the non-optimal one. This result can be explained by considering the stress distribution in the FE model, which showed some stress concentration in correspondence of the actuation loads in the section close to the trailing edge. The peak stress were equal to 260 MPa in the chordwise direction. These values remained within the limits for the material, hence they did not cause any concern, however they affected the optimization procedure in the sense that the skin thickness in that region was higher than anywhere else in the flap. It is expected that, in the full span model of the trailing edge flap, the more realistic load distribution along the span will avoid the presence of such stress concentrations.

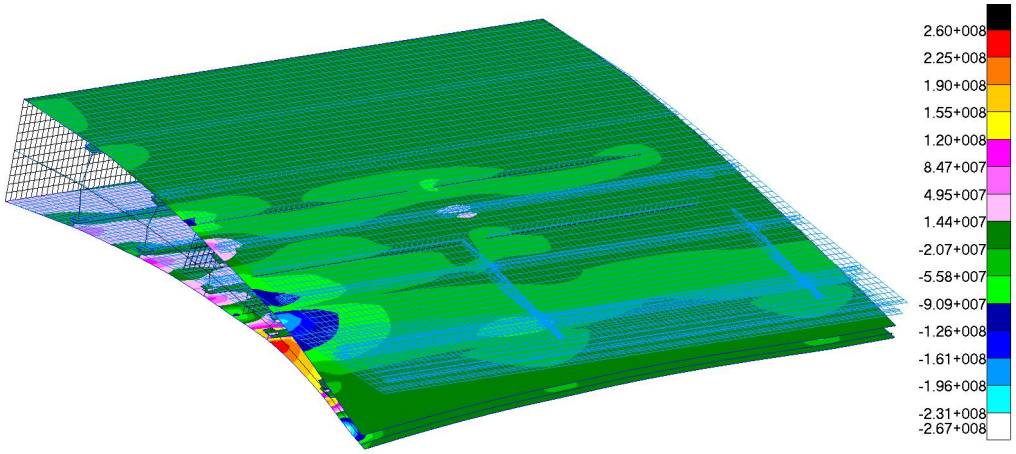

Figure 8.22: Stress distribution in the trailing edge flap with optimised thickness

As a consequence of the modified thickness distribution discussed above, it can be noted that the peak stresses, obtained in correspondence of the stress concentration points, resulted lower in the optimised design than in the initial non optimized one (peak tensile stress in chordwise direction of 370 MPa in the lower skin). On the other hand, if the points of stress concentration were not taken into account, then the stress in the skins resulted generally higher in the optimized design, as expected following a thickness reduction. The results show there is the potential to achieve a weight reduction while remaining within the strength safety limits of the structure.

As already shown in Section 6.1, the use of a 1 m spanwise section of the trailing edge device could lead to pessimistic results due to the different supporting condition considered for the structure. The optimised thickness values were hence applied to the full span inboard flap model.

8.5.2 Thickness and Loading Position Combined Optimisation

The ADS-Nastran coupled analysis presented in Section 8.5.1 has shown the possibility to optimise the skin thickness of the trailing edge flap in order to achieve a desirable deflection shape while conforming to the stress constraints on the structure. In this section, the thickness optimisation analysis is combined to the results presented in Section 8.2.4 in order to take a step further towards the optimisation of the morphing flap structure.

The analysis conducted in Section 8.5.1 is repeated for the full span inboard flap with optimal loading positions and a uniform skin thickness of 2 mm, in order to tailor the skin thickness for the new loading positions.

Table 8.9 presents the optimised skin thicknesses obtained for the different skin sections. It can be noted that applying the ADS/Nastran optimisation procedure to the flap with loads in optimal position, rather than uniformly distributed, gave the possibility to further reduce the skin thicknesses with consequent benefit for the whole wing.

Section N.	1	2	3	4	5	6	7	8	9	10	11	12
t (mm)	1.59	1.46	1.19	1.19	1.39	2.00	1.19	1.19	1.19	1.19	1.32	2.48

Table 8.9: Optimised thickness distribution in the different flap sections

Figure 8.23 shows the final deflected shape achieved by the flap with morphing trailing edge. The combination of tailored skin thicknesses and best loading positions allowed to easily reach the morphed deflected shape. The flap skins deflected uniformly along the span. The stress levels in the skins remained below the maximum allowed for the aluminium, as imposed by the constraint applied in the optimisation process.Figure 8.24 shows the stress distribution in the skins. Discarding the local stress concentrations, a maximum tensile stress of 315 MPa was achieved in chordwise direction, which is safely below the allowable value for the aluminium and is also lower than the stress in the trailing edge section due to a better redistribution of the stresses over the whole flap.

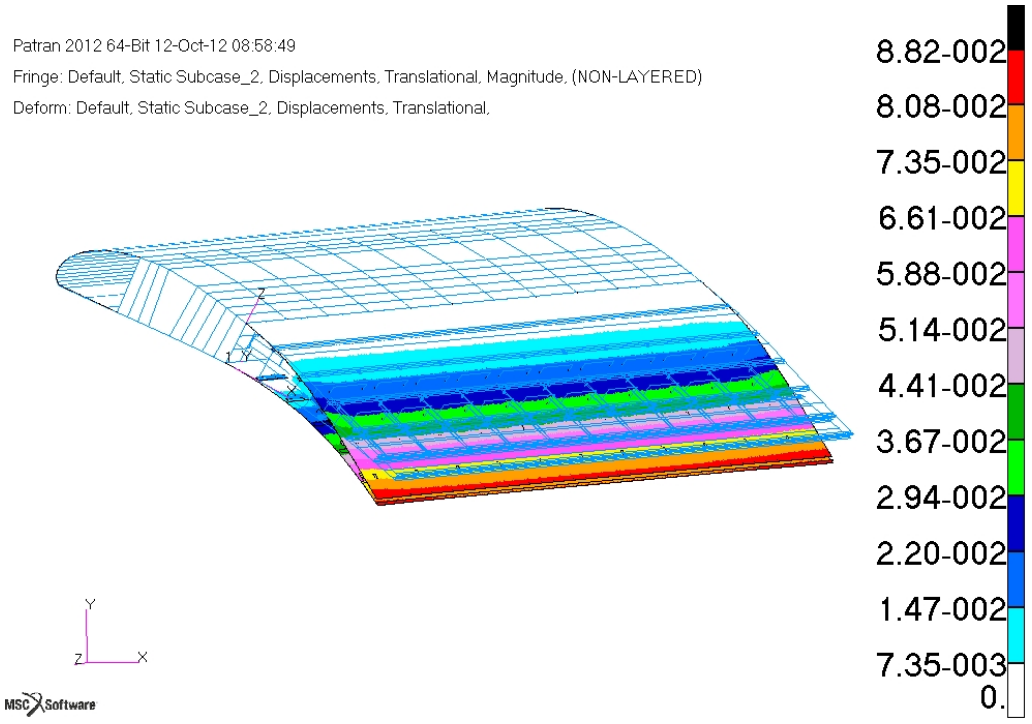

Figure 8.23: Deflection of the flap with optimised loading positions and skin thickness

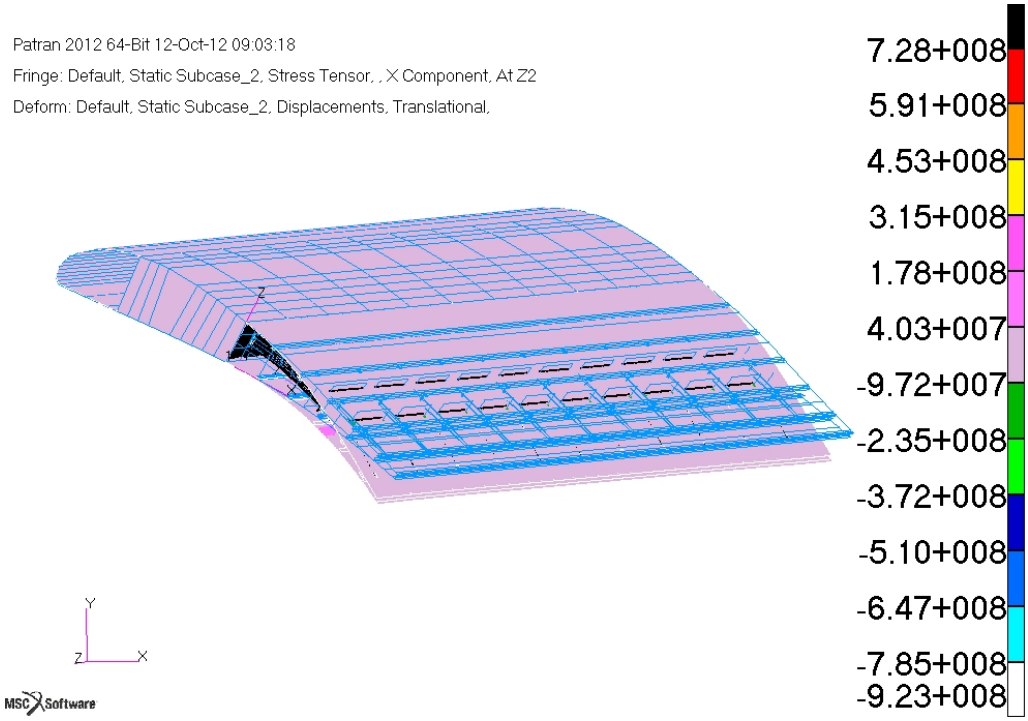

Figure 8.24: Stress distribution in the flap with optimised loading positions and skin thickness

8.6 Thickness Optimisation of the Morphing Leading Edge

As described in Chapter 4, the SADE wing is equipped not only with a smart flap with morphing trailing edge, but also with a morphing leading edge device. A detailed analysis of the leading edge structure has been already conducted by Morishima [108] and goes beyond the scope of this current research work. However, in order to test the optimisation procedure developed in this chapter, and in particular the ADS/Nastran interface program, the design presented in [108] for the SADE morphing leading edge device has been considered and its skin thickness has been optimised.
A detailed description of the geometry and target deflected shape for the leading edge structure has been provided in Section 4.2.1. Figure 8.25 shows a schematic representation of the leading edge deflection requirements, as presented in Section 4.2.1.

The leading edge structure, with its 0.86 m chord, was larger than the flap trailing edge flap and a step-by step analysis of all the possible loading configurations proved to be less effective in finding the optimal loading positions because small changes in the position of the actuation points did not influence much the final morphed shape achieved. Hence, it was decided to consider the loading configuration selected in [108] and shown in Figure 8.26, which led to an actuation load per beam equal to 4.51 kN.

An optimization problem analogous to the one defined for the trailing edge was considered, in order to determine the optimal skin thickness for best deflected shape under minimum stress.

The thickness optimisation was set up using the ADS/Nastran interface program and a

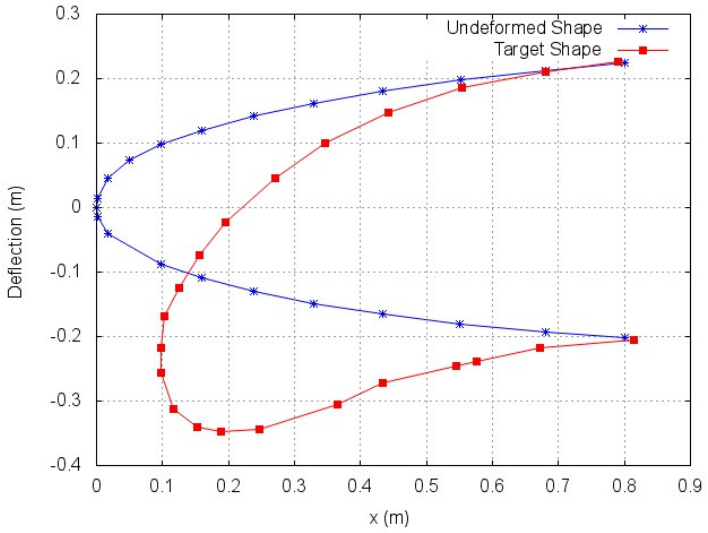

Figure 8.25: Deflection shape requirements for the leading edge

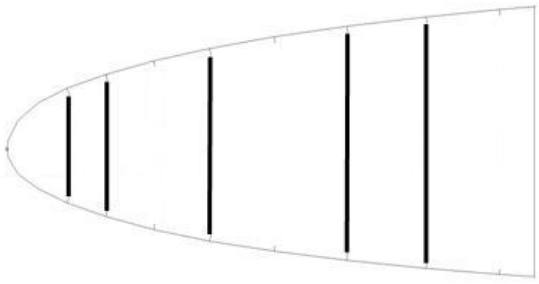

Figure 8.26: Loading positions for the leading edge [108]

minimum and maximum allowable thicknesses equal to 1 and 3 mm respectively were chosen for the leading edge study. A preliminary analysis showed that the leading edge device exhibited very high stress values in correspondence of the nose lower skin, where a change of curvature was required together with a vertical deflection. The high stresses influenced the overall thickness in the optimization process, leading to values equal to the upper bound set for the design variables, hence equal to the maximum skin thickness allowed by the optimisation problem, no matter its exact value. For this reason, the optimization was focused only to the nose area, where a thickness reduction would most help to better follow the demanding shape requirements.

The optimal thickness in the nose region was found to be uniform and equal to 1.5 mm, while in the rest of the leading edge the skin panels remained unchanged from the initial design and equal to 2 mm. Figure 8.27 shows the non optimised deflected shape and stress results while Figure 8.28 presents the stress results obtained for the modified leading edge skin thickness.

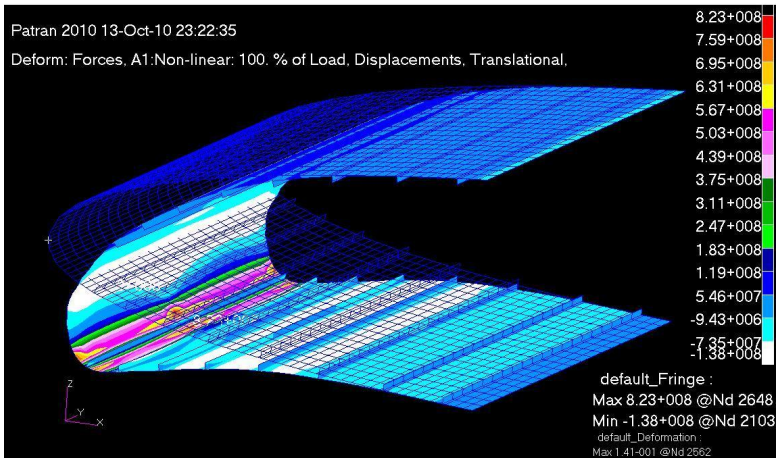

Figure 8.27: Non optimised leading edge: stress [108]

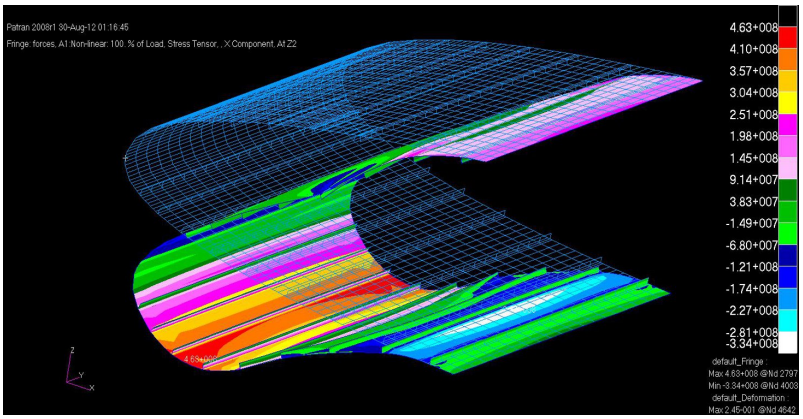

Figure 8.28: Stress distribution in the leading edge with optimal design

A maximum stress in chordwise direction equal to 463 MPa was achieved, higher than the maximum chordwise tensile stress of 439 MPa obtained by Morishima. Comparing the modified leading edge design with the initial one, however, despite the overall higher stress distribution, the thickness reduction contributed to the the deflection of the lower skin into a shape closer to the target morphed configuration.

This page is intentionally left blank.

CHAPTER 9

Conclusions and Future Work

An innovative design of a morphing flap device with flexible trailing edge has been developed, modelled and analysed to improve the aerodynamic efficiency of a commercial aircraft wing.

The main findings of this research work are hereby summarised with emphasis on the novel aspects of this study and the contribution to knowledge generated.

9.1 Eccentric Beam Actuation Mechanism

An innovative actuation mechanism concept has been developed for the trailing edge flap of a commercial aircraft. The proposed design is based on the principle of eccentuation and consists in an eccentric beam actuation mechanism called EBAM.

The EBAM mechanism has been able to provide the actuation load needed for morphing and also to replace the conventional internal structure of the flap. The novel design features of the actuation mechanism and the changes implemented in the conventional flap structure are listed below:

- The actuation mechanism consists of a curved beam mounted onto the rear spar and set into rotation by an actuator. Discs with varying radii (cams) are fixed along the beam and push the skins in the desired shape when the beam is rotated. The eccentric beam is designed with a curvature that meets the desired deflected shape at each angle of rotation.
- The upper and lower skins were disconnected at the flap trailing edge in order to allow them to slide one respect to the other during the flap deflection. The open sliding trailing edge allows to achieve a uniform deflected shape.
- Additional connections are set between the upper and lower skins in order to ensure the correct transfer of the actuation load from the eccentric beam to the flap skins.

The skin connections ensure the functionality and effectiveness of the design and preserve the structural integrity of the flap with the open trailing edge under the effect of the aerodynamic load.

9.2 Modelling and Analysis Methodology

As no explicit and univocal guidance is available in literature on the subject, the modelling techniques and the analysis methodology adopted for the morphing structure were novel aspects of this research. The innovative aspects of the study conducted on the morphing flap include the modelling of the proposed design and the estimation of the actuation loads required for morphing. Furthermore, an iterative analysis was set up to investigate the interaction of the flap structure with the surrounding airflow. An optimisation process was also proposed and used to tailor the characteristics of the actuation mechanism and flap structure to achieve the desired deflected shape with maximum accuracy and minimum weigh penalty.

9.2.1 Structural Modelling

- The parts constituting the eccentric beam actuation mechanism and the open trailing edge feature were modelled including sliding constraints to account for the relative motion of the parts during morphing. Multi Point Constraints were set in the finite element model to restrain the fixed degrees of freedom and to offer an accurate representation of the flap internal structure.

- The parametric analysis of several types of skin connections has shown that the use of thin layers of fabric-like material extending spanwise in the mid sections of the flap trailing edge contributes to achieve a uniform and smooth deflected shape. This type of connection performed better than point to point types of connection but determined an increase in the actuation load required for morphing.

9.2.2 Nonlinear Static Analysis

- A 2-step procedure was implemented to evaluate the actuation load required to deflect the structure up to the target morphed shape. A finite element model of the trailing edge skin was created and the desired deflected shape was imposed to the structure in the form of displacements along the flap chord. In the first step of the analysis, the actuation loads for the morphing structure were evaluated as the reaction forces of the flap to the imposed desired deflections. In the second step, the estimated reaction forces were reapplied to the structure to prove they were effectively able to deflect it into the desired morphed shape.

- A nonlinear static analysis was conducted to account for the large deflections in the morphing structure and to evaluate the stresses and strains in the skin materials.

9.2.3 Dynamic Analysis

- The dynamic behaviour of the morphing flap structure was investigated and the presence of the actuator was taken into account by varying the stiffness of the curved beam root

9.2.4 Aeroelastic Analysis

- The Nastran structural solver was interfaced with the Xfoil software for aerodynamic analysis of airfoils using panel method. An iterative analysis was set up to investigate the effect of the air pressure load on the flap trailing edge deflection. At each step the flap deformed configuration under the effect of the loading was used to evaluate the new aerodynamic load to be applied to the structure. The process was repeated until convergence was reached.

9.2.5 Optimisation of the Morphing Structure

- A polinomial interpolation was initially used to provide an approximation of the optimal loading positions for the flap structure.

- A better approximation of the morphing flap defected shape was obtained by representing the trailing edge structure as a cantilever beam deflected by transverse loads. The analysis considered a number N of loading points equal to 3, 4 and 5 respectively. The optimal loading positions were determined based on the knowledge of the desired morphed shape at different locations by solving a system of N equations.

- The analysis conducted to determine the optimal loading positions along the flap structure was further refined by using a finite element model of the flap and evaluating all the different loading combinations. The procedure described in Section 9.2.2 was used for the determination of the actuation loads in various positions. The process was automated by writing a Fortran program able to move the load step by step during the process.

- A suitable formulation for the structural optimisation problem for a morphing structure has been developed. The deflection shape requirements have been included in the optimisation objective function, while a maximum stress constraint has been considered as additional condition.

- An interface program between the Nastran structural solver and the ADS optimisation code has been generated and an iterative analysis has been conducted to minimize difference between the achieved and the desired shapes. The skin thickness was considered as the state variable and a maximum stress constraint was included in the process.

9.3 Results of the Analysis

The main research objective of achieving a feasible design for a next generation large aircraft wing morphing trailing edge actuation mechanism has been achieved. Specifically:

- The flap with morphing trailing edge is able to achieve the desired deflected shape under the actuation load applied by a series of eccentric beam mechanisms spanwise distributed and to achieve a uniform and smooth deflection of the trailing edge
- The analysis has been conducted in parallel for both aluminium and carbon fibre/epoxy skin materials in order to investigate the performance of both metallic and composite skins under morphing. Both the internal actuation loads and the external air pressure loads have been applied to the structure. The results show that both skins meet the target shape without violating the strength limits.
- A dynamic response analysis conducted on the flap with integrated actuation mechanism has shown that the proposed actuation mechanism provides adequate stiffness to the trailing edge structure to withstand the aerodynamic pressure loads and also to maintain a high degree of stability in the event of gust encounter.
- The aeroelastic analysis of the flap has shown that the interaction between flap structure and airflow has an overall positive effect on the wing structure. In fact, despite an additional actuation load contribution required to overcome the air pressure loads, the flap contributes to the wing structural stability by counteracting the increase of angle of attack generated by the leading edge device.
- The optimisation process has defined the optimal loading positions along the flap chord to achieve the desired morphed shape.
- The structural optimisation conducted with the ADS software has shown the potential to improve the deflected shape achieved while obtaining a skin thickness reduction, with consequent weight saving.

9.4 Future Work

Additional work could be conducted on the morphing flap to extend the knowledge of its structural behaviour and to improve the modelling technique. Possible future investigations are listed below.

- Model the nonlinear effects connected to the presence of loose hinges, freeplay phenomena in the actuator and friction between the sliding contacts.
- Structural optimisation of the morphing flap with composite skin by tailoring the layup of the skin panels.
- Create a complete demonstrator model of the flap with morphing trailing edge to experimentally investigate its static and dynamic structural behaviour.

- Couple the flap structural model to a CFD tool for an accurate aeroelastic analysis.
- Model the whole wing plus droop nose and flap with morphing trailing edge to conduct a high fidelity aeroservoelastic analysis.
- Develop a concept for a flap with flow blowing devices at the open trailing edge to further enhance the aerodynamic performance.

This page is intentionally left blank.

Bibliography

[1] Arguelles, P., Bischoff, M., Busquin, P., Drost, B. A. C., Evans, R., Kroll, W., Lagardere, J., Lina, A., Lumsden, J., Ranque, D., Rasmussen, P., Reutinger, P., Robins, R., Terho, H., Wittlov, A., *European aeronautics: a Vision for 2020 - Meeting society's needs and winning global leadership*, European Commission for Research, 2001.

[2] Global Aviation Industry and the Air Transportation Action Group (ATAG), The right flight path to reduce aviation emissions, *Position Paper at the UNFCC Climate Talks*, Durban, South Africa, 2011.

[3] Intergovernmental Panel on Climate Change (IPCC), Historical, present-day, and 2015 forecast emissions inventories, online resource: http://www.ipcc.ch/ipccreports/sres/aviation/134.htm (Last access: September 2012).

[4] Babikian, R., Lukachko, S. P., Waitz, I. A., The historical fuel efficiency characteristics of regional aircraft from technological, operational, and cost perspectives, *Journal of Air transport Management*, Vol. 8, Iss. 6, 2002, Pages 289-400.

[5] Goldin, D. S., "Three pillars for success. NASAs response to achieve the national oriorities in aeronautics and space transportation", *NASA Presidential Report on Aeronautics*, March 1977.

[6] Committee to Identify Potential Breakthrough Technologies and Assess Long-Term R&D Goals in Aeronautics and Space Transportation Technology, Commission on Engineering and Technical Systems, National Research Council, *Maintaining U.S. leadership in aeronautics: breakthrough technologies to meet future air and space transportation needs and goals*, National Academy Press, Washington, D.C. 1998.

[7] Dowell, E. H., Bliss, D. B., Clark, R. L., Aeroelastic wing with leading and trailing edge control surfaces, *Journal of Aircraft*, Vol. 40, No. 3 (2003), pp. 559-565.

[8] Spillman, J., The use of variable camber to reduce drag, weight and costs of transport aircraft, *Aeronautical Journal*, January 1992, pp. 1-9.

[9] Niu, M. C. Y., *Aircraft structural design*, 7th Ed. Hong Kong: Conmilt Press Ltd., 1993.

[10] Rudolph, P. K. C., High lift systems on commercial subsonic airliners, NASA Report CR-1996-4746.

[11] Rudolph, P. K. C., Mechanical design of high lift systems for high aspect ratio swept wings, NASA Report CR-1998-196709.

[12] Szodruch, J., Hilbig, R., Variable wing camber for transport aircraft, *Progress in Aerospace Science*, 1988, Vol. 25, pp. 297-328.

[13] Smith, A. M. O., High lift aerodynamics, *Journal of Aircraft*, Vol. 12 No. 6, June 1975.

[14] van Dam, C. P., Shaw, S. G., Vander Kam, F. C., Rudolph, P. K. C., Kinney, D., Aero-mechanical design of high-lift systems, *Aircraft Engineering and Aerospace Technology* Vol. 71 No. 5 (1999) pp. 436-443.

[15] Ford, T., Actuation systems development, *Aircraft Engineering and Aerospace Technology* Vol. 70 No. 4 (1998) pp. 265-270.

[16] Pires, R. M. M., *Design methodology for wing trailing edge device mechanisms*, Cranfield University, PhD Thesis, 2007.

[17] Scavini, J., Comparison of flap mechanisms of Boeing B787 and Airbus A320, Wikimedia Commons, 2012, *http : //en.wikipedia.org/wiki/File : $Flaps_Mechanism_B787_A320.png$* (Last access: August 2012).

[18] Ricketts, R. H., Experimental aeroelasticity: history, status and future in brief, NASA Technical Memorandum 102651, April 1990

[19] Forster, E., Sanders, B., Eastep, F., Synthesis of a variable geometry trailing edge control surface, 44^{th} *AIAA/ASME/ASCE/AHS/ASC Structures, Structural Dynamics and Materials Conference*, 7-10 April 2003, Norfolk, Virginia.

[20] Forster, E., Sanders, B., Eastep, F., Modelling and sensitivity analysis of a variable eometry trailing edge control surface, 44^{th} *AIAA/ASME/ASCE/AHS/ASC Structures, Structural Dynamics and Materials Conference*, 7-10 April 2003, Norfolk, Virginia, pp. 1-11.

[21] Kuzmina, S., Amiryantis, g., Schweiger, J., Cooper, J., Amprikidis, M., Sensberg, O., Review and outlook on active and passive Aeroelastic design concepts for future aircraft,23^{rd} *International Congress of Aeronautical Sciences Proceedings*, 2002.

[22] Weisshaar, T. A., Morphing aircraft technology - New shapes for aircraft design, *Multifunctional Structures/Integration of Sensors and Antennas. Meeting Proceedings RTO-MP-AVT-141, Overview 1*, Neuilly-sur-Seine, France 2006 Available from: http://www.rto.nato.int/abstracts.asp.

[23] Voracek, D., Pendleton,E., Reichenbach, E., Griffin, K., Welch, L., The Active Aeroelastic Wing phase I flight research through January 2003, NASA/TM-2003-210741, NASA, Edwards, California.

[24] Boehm, B., Flick, P., Sanders, B., Pettit, C., Reichenbach, E., Zillmer, S., Static aeroelastic response predictions of the Active Aeroelastic Wing (AAW) flight research vehicle, 42^{nd} *AIAA/ASME/ASCE/AHS/ASC Structures, Structural Dynamics, and Materials Conference and Exhibit*, 16-19 April 2001, Seattle, Washington.

[25] Lind, R., Abdulrahim, M., Boothe, K., Ifju, P., Morphing for flight control of micro air vehicles, *European Micro Air Vehicle Conference*, Braunschweig, Germany, July 2004.

[26] Kudva, J. N., Martin, C. A., Scherer, L. B., Jardine, A. P., McGowan, A. R., Lake, R. C., Sendeckyj, F., Sanders, B., Overview of the DARPA/AFRL/NASA Smart Wing Program, *SPIE Proceedings*, Vol. 3674, No. 230, 1999.

[27] Bartley-Cho, J., Wang, D. P., Martin, C. A., Kudva, J. N., West, M. N., Development of high-rate, adaptive trailing edge control surface for the Smart Wing Phase 2 wind tunnel model, *Journal of Intelligent Material Systems and Structures*, Vol. 15 , No. 4, 2004, pp. 279-291.

[28] Jardine, A. P., Bartley-Cho, J., Flanagan, J., Improved design and performance of the SMA torque tube for the DARPA Smart Wing program, *SPIE Proceedings*, Vol. 3674, No. 260, 1999.

[29] Love,M. H., Zink, P. S., Stroud, R. L., Bye, D. R., Chase, C., Impact of actuation concepts on morphing aircraft structures", 45_{th} *AIAA/ASME/ASCE/AHS/ASC Structures, Structural Dynamics and Materials Conference*, 19-22 April 2004, Palm Springs, California, pp. 1-12.

[30] Joshi, S. P., Tidwell, Z., Crossley, W. A., Ramakrishnan, S., Comparison of morphing wing strategies based upon aircraft performance impacts, 45^{th} *AIAA/ASME/ASCE/AHS/ASC Structures, Structural Dynamics and Materials Conference*, 19-22 April 2004, Palm Springs, California, pp. 1-7.

[31] Stanewsky, E., Aerodynamic benefits of Adaptive Wing Technology, *Aerospace Science and Technology*, Vol. 4, 2000, pp. 439-452.

[32] Schweiger, J., Suleman, A., Kuzmina, S., Chedrik, V. V., MDO Concepts for an European research project on Active Aeroelastic Aircraft, 9^{th} *AIAA/ISSMO Symposium on Multidisciplinary Analysis and Optimization*, 4-6 September 2002, Atlanta, Georgia

[33] Moorhouse, D., Sanders, B., von Spakovsky, B., Butt, J., Benefits and design challenges of adaptive structures for morphing aircraft, *The Aeronautical Journal*, March 2006, pp. 157-162.

[34] Patel, S.C., Majji, M., Koh, B. S., Junkins, J. L., Rediniotis, O. K., Morphing wing: a demonstration of aero servo elastic distributed sensing and control, *Texas Institute for Intelligent Bio-Nano Materials and Structures*, 2005, pp.1-8.

[35] Barbarino, S., Bilgen, O., Ajaj, R. M., Friswell, M. I., Inman, D., A Review of Morphing Aircraft, *Journal of Intelligent Material Systems and Structures*, Vol. 22, June 2011, pp. 823-877.

[36] Vos, R., Hodigere-Siddaramaiah, V., Cooper, J., Aeroelastic flight control for subscale UAVs, 48^{th} *AIAA/ASME/ASCE/AHS/ASC Structures, Structural Dynamics and Materials Conference*, 23-26 April 2007, Honolulu, Hawaii, pp. 1-12.

[37] Bae, J. S., Seigler, T. M., Inman, D. J., Lee, I., Aerodynamic and aeroelastic considerations of a variable-span morphing wing, 45^{th} *AIAA/ASME/ASCE/AHS/ASC Structures, Structural Dynamics and Materials Conference*, 19-22 April 2004, Palm Springs, California Newport Rhode Island, pp. 1-9.

[38] Monner, H. P., Sachau, D., Breitbach, E., Design aspects of the elastic trailing edge for an adaptive wing, 1999, *RTO AVT Specialists' Meeting on Structural Aspects of Flexible Aircraft Control*, 18-20 October, Ottawa, Canada, Report ADP10488, pp 14.1-14.8.

[39] Campanile, L. F., Anders, S., Aerodynamic and aeroelastic amplification in adaptive belt-rib airfoils, *Aerospace Science and Technology*, Vol. 9, 2005, pp.55-63.

[40] Ricci, S., Scotti, A., Terraneo, M., Design, manufacturing and preliminary test results of an adaptive wing camber model, 47^{th} *AIAA/ASME/ASCE/AHS/ASC Structures, Structural Dynamics and Materials Conference*, 1-4 May 2006, Newport Rhode Island, pp. 1-12.

[41] Monner, H. P., Realization of an optimized wing camber by using formvariable flap structures, *Aerospace Science and Technology*, Vol. 5, 2001, pp. 445-455.

[42] Cesnik, C. E. S., Last, H. R., Martin, C. A., A framework for morphing capability assessment, 45^{th} *AIAA/ASME/ASCE/AHS/ASC Structures, Structural Dynamics and Materials Conference*, 19-22 April 2004, Palm Springs, California, pp. 1-11.

[43] Johnston, C. O., Neal, D. A., Wiggis, L. D., Robertshaw, H. H., Mason, W. H., Inman, D. J., A model to compare the flight control energy requirements of morphing and conventionally actuated wings, 44^{th} *AIAA/ASME/ASCE/AHS/ASC Structures, Structural Dynamics and Materials Conference*, 7-10 April 2003, Norfolk, Virginia, pp. 1-9.

[44] Thill, C., Etches, J., Bond, I., Potter, K., Weaver, P., Morphing skins, *The Aeronautical Journal*, Vol. 112, No. 1129, 2008, pp. 117-139.

[45] Ghandi, F., Anusonti-Inthra, P., Skin design studies for variable camber morphing airfoils, *Smart Materials and Structures*, Vol. 17, 2008, pp. 1-8.

[46] Cooper, J., Adaptive aeroelastic structures. In: Adaptive Structures Engineering Applications edited by Wagg, D., Bond, I., Weaver, P., Friswell, M. Southern Gate, Chichester: John Wiley and Sons Ltd., 2007, p. 137-162.

[47] Carlsson, M., Cronander, C., Efficient roll control using distributed control surfaces and aeroelastic effects, *Aerospace Science and Technology*, Vol. 9, 2005, pp.143-150.

[48] Monner, H. P., Kintscher, M., Lorkovski, T., Storm, S., Design of a smart droop nose as leading edge high lift system for transport aircrafts, 50^{th} *AIAA/ASME/ASCE/AHS/ASC Structures, Structural Dynamics, and Material Conference*, Palm Springs, California, 4-7 May, 2009.

[49] Reckzeh, D., Aerodynamic design of Airbus high lift wings, Online reource: http://www.dlr.de/as/Portaldata/5/Resources/dokumente/veranstaltungen/ehemaligentreffen2005/reckzeh-aero-design-of-high-lift-wings.pdf, (Last accessed: September 2012).

[50] Lajux, V., Methodology for the design of leading edge devices applied to variable camber, Cranfield University PhD Thesis, 2007.

[51] Amprikidis, M., Cooper, J. E., Rogerson, C., Vio, G., On the use of adaptive internal structures for wing shape control, 46^{th} *AIAA/ASME/ASCE/AHS/ASC Structures, Structural Dynamics and Materials Conference*, 18-21 April 2006, Austin, Texas, pp. 1-11

[52] Wildschek A., Havar T., Plotner, K.,An all-composite, all-electric, morphing trailing edge device for flight control on a blended-wing body airliner, *Proc. IMechE, Part G: Journal of Aerospace Engineering*, Vol. 224, 2009 .

[53] Musgrove, R. G., Apparatus for producing pivotal movement, Patent US 3944170, June 1974.

[54] Musgrove, R. G., Eccentric actuator, Patent US 4286761, November 1979.

[55] Mller, D., The horn concept, realisation of a flexible wing camber for optimisation of the aerodynamic performance of future airliners, University of Stuttgart, PhD Thesis, 2000.

[56] Perera, M., Guo, S., Optimal design of an aeroelastic wing structure with seamless control surfaces, *Proceedings of the Institution of Mechanical Engineers, Part G: Journal of Aerospace Engineering*, Vol. 223 No. 8, 2009, pp. 1141-1151.

[57] Kikuta, M. T., Mechanical properties of candidate materials for morphing wings, Virginia Polytechnic Institute and State University, MSc Thesis, 2003.

[58] Botelho, E. C., Silva, R. A., Pardini, L. C., Rezende, M. C., A review on the development and properties of continuous fibre/epoxy/aluminium hybrid composites for aircraft structures, *Materials Research*, Vol. 9 No. 3, 2006.

[59] Yousefi-Koma, A., Zimcik, D. G., Applications of smart structures to aircraft for perfomance enhancement, *Canadian Aeronautics and Space Journal*, Vol. 49, No. 4, December 2003.

[60] Anhalt, C., Monner, H. P., Breitbach, E., Interdisciplinary wing design - Structural aspects, *SAE International*, 2003, Vol. 112, No. 1, pp. 521-530.

[61] Guo, S., Aeroelastic optimization of an aerobatic aircraft wing structure, *Aerospace Science and Technology*, Vol. 11, No. 5, 2007, pp. 396-404.

[62] Iannucci, L., Fontanazza, A., Design of morphing wing structures, 3^{rd} *SEAS DTC Technical Conference*, Edinburgh 2008.

[63] Wu, G., Yang, J. M., The mechanical behavior of GLARE laminates for aircraft structures, *Journal of the Minerals, Metals and Materials Society*, Vol. 57, N. 1, 2005, pp. 72-79.

[64] Asundi, A., Choi, A. Y. N., Fiber metal laminates: an advanced material for future aircraft, *Journal of Materials Processing Technology*, Vol. 63, 1997, pp. 384-394.

[65] Chopra, I., Review of state of art of smart structures and integrated systems, *AIAA Journal*, Vol. 40 No. 11, 2002.

[66] Rocha, J., Costa, P. A., Suleman, A., On active aeroelastic control of an adaptive wing using piezoelectric actuators, *Journal of Aircraft*, Vol. 41 No. 1, 2005.

[67] Berton, B., Shape Memory Alloys application: trailing edge shape control, *Multifunctional Structures / Integration of Sensors and Antennas, Meeting Proceedings RTO-MP-AVT-141*, Neuilly-sur-Seine, France, Paper 13, pp. 13-1 13-16. Available from: *http* : *//www.rto.nato.int/abstracts.asp*.

[68] Keefe A. C., Carman, G. P., Thermo-mechanical characterization of shape memory alloy torque tube actuators, *Smart Materials and Structures*, Vol. 9, 2000, pp. 665-672.

[69] Barbarino, S., Dettmer, W. G., Friswell, M. I., Morphing trailing edges with shape memory alloy rods, 21^{st} *International Conference on Adaptive Structures and Technologies (ICAST)*, University Park, Pennsylvania, 4-6 October 2010.

[70] Bisplinghoff, R. L., Ashley, H., Halfman, R. L., *Aeroelasticity*, Addison -Wesley Publishing Company, US, November 1957.

[71] Fung, Y. C., *An introduction to the theory of aeroelasticity*, New York: Dover Publications Inc., 1969.

[72] Dowell, E. H., Crawley, E. F., Curtiss Jr, H. C., Peters, D. A., Scanlan, R. H., Sisto, F., *A modern course in aeroelasticity* 3^{rd} Ed. Dordrecht: Kluwer Academy Publishers Group, 1995.

[73] Megson, T. H. G., *Aircraft structures for engineering students*, 3^{rd} Ed. Woburn: Butterworth-Heinemann, 2001.

[74] Battoo, R. S., An introductory guide to literature in aeroelasticity, *The Aeronautical Journal*, Vol. 103, No. 1029, 1999, p. 511-518.

[75] Wright, J. R., Cooper, J. E., *Introduction to aircraft aeroelasticity and loads*, John Wiley and Sons, 2007.

[76] Noll, T. E., Aeroservoelasticity, NASA Technical Memorandum 102620, March 1990.

[77] Noll, T. E., Perry, B., Gilbert, M. G., Recent activities in aeroservoelasticity at the NASA Langley Research Center, NASA Technical Memorandum 101582, May 1989.

[78] Librescu, L., Qin, Z., Na, S., Yoon, G., C., Aeroelastic response and active control of aircraft wings modeled as thin walled beams, 47^{th} *AIAA/ASME/ASCE/AHS/ASC Structures, Structural Dynamics and Materials Conference*, 1-4 May 2006, Newport, Rhode Island.

[79] Azoulay, D., Karpel, M., Characterisation of methods for computation of aeroservoelastic response to gust excitation, 47^{th} *AIAA/ASME/ASCE/AHS/ASC Structures, Structural Dynamics and Materials Conference*, 1-4 May 2006, Newport, Rhode Island.

[80] Gold, P., Karpel, M., Reduced-size aeroservoelastic modeling and LCO simulations with structurally non-linear actuators, 47^{th} *AIAA/ASME/ASCE/AHS/ASC Structures, Structural Dynamics and Materials Conference*, 1-4 May 2006, Newport, Rhode Island.

[81] Dimitriadis, G., Cooper, J., Characterisation of the behaviour of a simple aeroservoelastic system with control nonlinearities, *Journal of Fluids and Structures*, Vol 14, 2000 pp. 1173-1193.

[82] Moulin, B., Karpel, M., Modeling of aeroservoelastic systems with nonlinear strain actuation, 47^{th} *AIAA/ASME/ASCE/AHS/ASC Structures, Structural Dynamics and Materials Conference*, 1-4 May 2006, Newport, Rhode Island.

[83] Moulin, B., Karpel, M., Models for aeroservoelastic analysis with smart structures,43^{rd} *AIAA/ASME/ASCE/AHS/ASC Structures, Structural Dynamics and Materials Conference*, 22-25 April 2002, Denver, Colorado.

[84] Vanderplaats, G. N., Thirty years of modern structural optimisation, *Advances in Engineering Software*, Vol. 16, 1993, P. 81-88.

[85] Gartmeier O., Dunne L. W., Structural Optimisation in Vehicle Development, from the MSC online library, http://www.mscsoftware.com/support/library/conf/auto99/p00899.pdf, Last access: Sept. 2011.

[86] Sikiotis E., Saouma V., Long M., Rogger W., Finite element based optimisation of complex structures on a Cray X-MP supercomputer, *Computers and Structures* (1990), Vol. 36 No. 5, pp. 901-911.

[87] Balling R. J., Parkinson A. R., Free J. C., Methods for Interfacing Analysis Software to Optimisation Software, *Computers and Structures* (1986), Vol. 22 No. 1, pp. 87-98.

[88] Vanderplaats G. N., Structural Optimisation by Methods of Feasible Directions, *Computers and Structures*, Vol. 3, 1973, pp. 739-755.

[89] Vanderplaats G. N., ADS - A Fortran program for automated design synthesis, NASA Contractor Report 177985, September 1985.

[90] Friswell, M. I., Herencia, J. E., Baker, D., Weaver, P. M., The optimisation of hierarchical structures with applications to morphing aircraft, *Second International Conference on Multidisciplinary Design Optimisation and Applications*, 2-5 September 2008, Gijon, Spain.

[91] Skillen, M. D., Crossley, W. A., Modeling and optimisation for morphing wing concept generation, NASA Technical Report, CR-2007-214860, March 2007.

[92] Morphing Structures. The OMSAMA programme. http://michael.friswell.com/research/morphing.html. Last access: Sept. 2011.

[93] Report on the potential of innovative active materials, SADE Project internal report (unpublished), 2009.

[94] Lee, B. H. K., Price, S. J., Wong, Y. S., Nonlinear aeroelastic analysis of airfoils: bifurcation and chaos, *Progress in Aerospace Sciences*, Vol. 35, 1999, pp. 205-334.

[95] Breitbach, E., Effects of structural non-linearities on aircraft vibration and flutter, AGARD Report No. 665.

[96] Cantiani D., Theoretical and numerical analysis for the limit cycle oscillations of the EADS/CASA refuelling boom system, Sapienza University, MSc Thesis (2007)

[97] Marsden, C. C., Price, S. J., Transient and limit cycle simulation of a nonlinear aeroelastic system, *Journal of Aircraft*, Vol. 44, No 1 (2007) pp. 60-70.

[98] Kim, S. H., Lee, I., Aeroelastic analysis of a flexible airfoil with a freeplay nonlinearity, *Journal of Sound and Vibration*, Vol. 193, No. 4, (1996), pp. 823-846.

[99] Price, S. J., Alighanbari, H., Lee, B. H. K., The aeroelastic response of a two-dimensional airfoil with bilinear and cubic structural nonlinearities, *Journal of Fluids and Structures*, Vol. 9, (1995), pp. 175-193.

[100] Yang, Z. C., Zhao, L. C., Analysis of limit cycle flutter of an airfoil in incompressible flow, *Journal of Sound and Vibration*, Vol. 123, No. 1 (1988), pp. 1-13.

[101] Guo, S., Composite Structures Course Notes, Cranfield University, 2008, (unpublished).

[102] Kollar, L. P., *Mechanics of composite structures*, Cambridge University Press, New York, 2003.

[103] Zienkiewicz, O. C., Taylor, R. L. *The finite element method, Volume 1: the basis*, 5^{th} Ed. Woburn: Butterworth-Heinemann, 2000.

[104] Zienkiewicz, O. C., Taylor, R. L. *The finite element method, Volume 1: solid mechanics*, 5^{th} Ed. Woburn: Butterworth-Heinemann, 2000.

[105] MSC NASTRAN 2005 Linear Static Analysis User's guide.

[106] MSC NASTRAN 2005 Installation and Operations Guide.

[107] Patran 2010 Reference Manual, Part 3: Finite Element Modelling.

[108] Morishima, R., Analysis of composite wing structures with a morphing leading edge, PhD Thesis, Cranfield University, 2011.

[109] Flap (aircraft), from Wikipedia. http://en.wikipedia.org/wiki/. Last access: March 2013.

[110] SADE - Smart High Lift Devices for Next Generation Wings WP2: Smart leading edge, FNG target shapes: description of results, SADE Technical Report, DLR, 2009 (unpublished).

[111] Smart Single Slotted Flap (SSSF) final target shapes, SADE Technical Report, CIRA, 2009 (unpublished).

[112] Ahmed, S., Personal correspondence.

[113] Brazier, L. G., On the flexure of thin cylindrical shells and other "thin" sections, *Proceedings of the Royal Society of London, Series A, Containing Papers of a Mathematical and Physical Character*, Vol. 116 No. 773, 1927, pp. 104-114.

[114] Cecchini, L. S., Weaver, P. M., The Brazier effect in multi-bay aerofoil sections, 45^{th} *AIAA/ASME/ASCE/AHS/ASC Structures, Structural Dynamics and Materials Conference*, Palm Springs, California, 2004.

[115] Military Handbook. Metallic materials and elements for aerospace vehicle structures. MIL-HDBK-5H, December 1998.

[116] Howe, D., *Aircraft Loading and Structural Layout*, Professional Engineering Publishing, United Kingdom 2004.

[117] ESDU 94028, Increments in aerofoil lift coefficient at zero angle of attack and in maximum lift coefficient due to deployment of a plain trailing edge flap, with or without a leading edge high lift device, at low speeds, December 1994.

[118] ESDU 94030, Increments in aerofoil lift coefficient at zero angle of attack and in maximum lift coefficient due to deployment of a single slotted trailing edge flap, with or without a leading edeg high lift device, at low speeds, April 1995.

[119] ESDU Wings 01.01.05, Slope of lift curve for two-dimensional flow, January 1955.

[120] ESDU Controls 01.01.03, Rate of change of lift coefficient with control deflection in incompressible two-dimensional flow, $(a_2)_0$, May 1956.

[121] ESDU Controls 04.01.02, Rate of change of hinge-moment coefficient with control deflection for a plain control in incompressible two-dimensional flow, $(b_2)_0$, May 1956.

[122] Xfoil website, http://web.mit.edu/drela/Public/web/xfoil/, Last accessed: September 2012.

[123] Drela, M., Xfoil: an analysis and design system for low Reynolds number airfoils, *Conference on Low Reynolds Number Airfoil Aerodynamics*, University of Notre Dame, June 1989.

[124] Anderson, J. D. Jr., *Fundamentals of Aerodynamics*,McGraw-Hill International, Fifth Edition, 2010.

[125] Guruswamy, G. P., A review of numerical fluids/structures interface methods for computations using high fidelity equations, *Computers and Structures*, Vol. 80, 2002, pp. 31-41.

[126] Maman, N., Farhat, C., Matching fluid and structure meshes for aeroelastic computations: a parallel approach, *Computers and Structures* Vol. 54, No.4, 1995, pp 779-785.

[127] Cavagna, L., Quaranta, G., Ghiringhelli, G. L., Mantegazza, P., Efficient application of CFD aeroelastic methods using commercial software, *International Forum on Aeroelasticity and Structural Dynamics IFASD 2005*, Munich, Germany, 28 Jun - 1 Jul 2005.

[128] Lafountain, C., Cohen, K., Abdallah, S., Use of Xfoil in design of camber - controlled morphing UAVs, Wiley Periodicals, Published online in Wiley InterScience (www.interscience.wiley.com); DOI 10.1002/cae.20437.

[129] Chapra S. C., Canale R. P., *Numerical methods for engineers*, McGraw-Hill, 2005.

[130] O. Rhodes, M. Santer, Optimal Problem Definition for Optimization of Morphing Structures, 51^{st} *AIAA/ASME/ASCE/AHS/ASC Structures, Structural Dynamics, and Materials Conference*, 12-15 April 2010, Orlando, Florida.

[131] Kupferschmid, M., *Classical Fortran : programming for engineering and scientific applications*, Marcel Dekker Ed., New York, 2002.

[132] Weisshaar, T. A., Duke, D. K., Induced drag reduction using aeroelastic tailoring with adaptive control surfaces, *Journal of Aircraft*, Vol. 43, No. 1 (2006), pp. 157-164.

[133] M. D. Conner, D. M. Tang, E. H. Dowell, L. N. Virgin, Nonlinear Behaviour of a Typical Airfoil Section with Control Surface Freeplay: a Numerical and Experimental Study, *Journal of Fluids and Structures*, Vol. 11 (1997) pp. 89-109

[134] T. Theodorsen, General Theory of Aerodynamic Instability and the Mechanism of Flutter, NACA Report No. 496

[135] D. Tang, E. H. Dowell, L. N. Virgin, Limit Cycle Behaviour of an Airfoil with a Control Surface, *Journal of Fluids and Structures*, Vol. 12 (1998), pp. 839-858

[136] C. C. Marsden, S. J. Price, The Aeroelastic Response of a Wing Section with a Structural Freeplay Nonlinearity: An Experimental Investigation", *Journal of Fluids and Structures*, Vol. 21, (2005), pp. 257-276

[137] D. Tang, M. D. Conner, E. H. Dowell, Reduced-Order Aerodynamic Model and Its Application to a Nonlinear Aeroelastic System, *Journal of Aircraft*, Vol. 35 No. 2, March-April 1998, pp. 332-338

[138] J. W. Edwards, J. V. Breakwell, A. E. Bryson Jr., Active Flutter Control Using Generalized Unsteady Aerodynamic Theory, *Journal of Guidance and Control*, Vol. 1. No. 1, January-February 1978, pp. 32-40

[139] L. O. Brase, W. Eversman, Application of Transient Aerodynamics to the Structural Nonlinear Flutter Problem, *Journal of Aircraft*, Vol. 25, No. 11, (1987), pp. 1060-1068

[140] L. Liu, E. H. Dowell, Harmonic Balance Approach for an Airfoil with a Freeplay Control Surface, *AIAA Journal*, Vol. 43 No, 4, April 2005, pp 802-815

[141] L. Liu, Y. S. Wong, B. H. K. Lee, Non-Linear Aeroelastic Analysis Using the Point Transformation Method, Part 1: Freeplay Model, *Journal of Sound and Vibration*, Vol.253 No.2 (2002) pp. 447-469

[142] L. Liu, Y. S. Wong, B. H. K. Lee, Non-Linear Aeroelastic Analysis Using the Point Transformation Method, Part 1: Hysteresis Model, *Journal of Sound and Vibration*, Vol.253 No.2 (2002) pp. 471-483

[143] D. Li, S. Guo, J. Xiang, N. Di Matteo, Control of an Aeroelastic System with Control Surface Nonlinearity, 51^{st} *AIAA/ASME/ASCE/AHS/ASC Structures, Structural Dynamics and Materials Conference*, 12-15 April 2010, Orlando, Florida

[144] SADE Project Year 2 Work Package 3 Internal Report

[145] R. Morishima, S. Guo, S. Ahmed, A Composite Wing with a Morphing Leading Edge, 51^{st} *AIAA/ASME/ASCE/AHS/ASC Structures, Structural Dynamics and Materials Conference*, 12-15 April 2010, Orlando, Florida

[146] R. Morishima, Aeroelastic Analysis of Composite Wing Structures with High Lift Devices, Technical Report, May 2009

[147] Certification Specifications for Large Aeroplanes CS-25, European Aviation Safety Agency, September 2008